Control of organic semiconductor nanoparticles morphology for water-processable photovoltaic solar cells

Hugo Laval

université de BORDEAUX

THÈSE PRÉSENTÉE

POUR OBTENIR LE GRADE DE

DOCTEUR DE L'UNIVERSITÉ DE BORDEAUX

ÉCOLE DOCTORALE DES SCIENCES PHYSIQUES ET DE L'INGENIEUR

SPÉCIALITÉ : ELECTRONIQUE

Par Hugo LAVAL

Contrôle de la morphologie de nanoparticules de semi-conducteurs organiques pour des cellules solaires photovoltaïques fabriquées par encres aqueuses

Control of organic semiconductor nanoparticles morphology for water-processable photovoltaic solar cells

Sous la direction de : Dr. Sylvain CHAMBON

(co-directeur : Pr. Guillaume WANTZ)

Soutenue le 6 novembre 2024.

Membres du jury :

M. RAVAINE Serge,	Professeur, Université de Bordeaux	Président
M. CAMPOY-QUILES Mariano,	Professeur, Materials Science Institute of Barcelona	Rapporteur
Mme. HEBRAUD Anne,	Maitresse de conférence, ICPEES-CNRS, Strasbourg	Rapporteuse
Mme. BRUNETTI Francesca,	Professeure, University of Rome	Examinatrice
Mme. SEGUY Isabelle,	Chargée de recherche LAAS-CNRS, Toulouse	Examinatrice

Abstract

In order to improve the sustainability of the organic photovoltaics, the use of toxic solvents for processing organic solar cells needs to be replaced by a cleaner alternative. The present thesis tackles this issue by exploring a way of replacing these solvents by water. As most organic semiconductors are not soluble in water, the strategy to overcome this constraint is to form nanoparticles from these materials, that are thus able to be dispersed in water. Two main methods are employed in the community to obtain such an aqueous dispersion, the miniemulsion and the nanoprecipitation. Nanoparticles synthesised with the latter method are known to present a more favourable internal morphology between the donor and acceptor materials as compared to the former method. As a result, water-processable organic solar cells prepared from nanoprecipitation demonstrate much higher efficiencies. The work undertaken in this thesis aims to understand and overcome the limitations arising from the internal morphology of the nanoparticles prepared by miniemulsion. In particular, we studied the influence of the interfacial energy between the donor and acceptor material on the nanoparticle internal morphology. Composite nanoparticles of PTQ10 associated with various acceptor small molecules were formed and studied with advanced microscopy techniques (STXM, AFM, cryo-TEM). The analysis showed that having a system with a low interfacial energy, such as PTQ10:Y6, is beneficial in obtaining nanoparticles with intimate morphology. As a result, organic solar cells fabricated with nanoparticles of PTQ10:Y6 have hence reached a power conversion efficiency of 9.98 %. A thermal treatment at high temperature was necessary in order to sinter the nanoparticles while keeping a favourable morphology and crystallinity. Such a high temperature is yet not suitable for an industrial process. To reduce this temperature, the alkyl chains length of both the donor and acceptor materials was found to play an important role. Through the screening of polymers having short and long alkyl chains associated with the acceptor material Y6, the polymer with the longer chains enabled processing at a lower temperature, achieving efficiencies exceeding 10%. Moreover, this work explores the link between nanomorphology and charge transport within nanoparticles by developing nanogap devices. Dielectrophoresis force has been successfully used to insert core-shell nanoparticles in the nanogap. This result shows that nanoparticle morphology and shell composition do not have a dramatic impact on the charge mobility within the nanoparticle or the overall performance of the solar cells.

Résumé

Pour rendre le procédé de fabrication des cellules solaires organiques plus écoresponsable, l'utilisation de solvants toxiques doit être remplacée par une solution plus propre. Cette thèse aborde cette problématique en explorant l'utilisation de l'eau comme alternative. Comme la plupart des semi-conducteurs organiques ne sont pas solubles dans l'eau, la stratégie pour surmonter cette contrainte consiste à former des nanoparticules à partir de ces matériaux, qui peuvent ainsi être dispersées dans l'eau. Deux méthodes principales sont utilisées dans la communauté pour obtenir de telles dispersions aqueuses : la mini-émulsion et la nano-précipitation. Les nanoparticules synthétisées par cette dernière présentent une morphologie interne plus favorable entre les matériaux donneurs et accepteurs par rapport à la mini-émulsion. De ce fait, les cellules solaires fabriquées à base de dispersions aqueuses préparées par nano-précipitation montrent des rendements beaucoup plus élevés. Le travail entrepris dans cette thèse vise à comprendre et à surmonter les limitations liées à la morphologie interne des nanoparticules préparées par mini-émulsion. En particulier, nous avons étudié l'influence de l'énergie interfaciale entre les matériaux donneurs et accepteurs sur la morphologie interne des nanoparticules. Des nanoparticules composites de PTQ10 et de différents matériaux accepteurs ont été formées et étudiées à l'aide de techniques de microscopie avancées (STXM, AFM, cryo-TEM). L'analyse a montré qu'un système donneur/accepteur avec une faible énergie interfaciale tel que le PTQ10:Y6 est bénéfique pour obtenir des nanoparticules avec une morphologie inter-mixée. Par conséquent, les cellules solaires fabriquées avec des nanoparticules de PTQ10:Y6 ont atteint une efficacité de conversion énergétique de 9,98 %. Un traitement à haute température a été nécessaire pour fritter les nanoparticules tout en maintenant une morphologie et une cristallinité favorables. Cependant, une telle température élevée n'est pas adaptée à un processus industriel. Pour réduire cette température, la longueur des chaînes alkyles des matériaux donneurs et accepteurs a été identifiée comme un facteur clé. En examinant des polymères avec des chaînes alkyles courtes et longues, il a été observé que le polymère avec les chaînes les plus longues permettait un traitement à une température plus basse, atteignant des efficacités supérieures à 10 % lorsqu'il est associé au Y6. Cette thèse a aussi exploré le lien entre la morphologie et le transport des porteurs de charges au sein des nanoparticules en développant dispositifs à canal nanométrique. Dans ces canaux, nous avons réussi à piéger des nanoparticules de type cœur-écorce à l'aide de la force diélectrophorétique. Ce résultat a montré que la morphologie des nanoparticules et la composition de l'écorce n'ont pas d'impact significatif ni sur la mobilité des charges dans les nanoparticules, ni sur les performances finales des cellules solaires.

“Créer, vivre, inventer, imaginer, c'est toujours composer avec une frontière. Nous ne sommes pas dieu. La finitude est notre lot. La beauté s'élabore toujours dans la contrainte.

Ce n'est pas triste, c'est être en vie.”

Aurélien Barrau.

Acknowledgments

It has been a long journey, and I would like to acknowledge and thanks everybody who has directly or indirectly contributed to this work and helped me.

My most deep and sincere gratitude goes to my two supervisors, Dr. Sylvain Chambon and Prof. Guillaume Wantz. First of all, for agreeing to have me as your PhD student. I know I was not the most obvious and appropriate candidate in the first place. But I guess life requires some risky bets sometimes. Thank you so much for that. You gave me a fantastic opportunity, and I hope I did everything possible to show you that you made the right choice. During these 3 years I have learned so much from you two, and received all the support I needed to complete this journey. Thanks to you, I have been able to explore so many aspects of my subject because of the freedom you gave me. I know my carbon footprint is bad, very bad, but I am thankful that you allowed me to travel so much to collect results and then present them in conferences. At the end, the most important thing of all is the relation we have created together. It is priceless, I know that, and I hope we will remain close in the future.

Sylvain, having you as my main supervisor was probably the reason why I felt so peaceful and safe during this PhD. You have put your trust in me and made my “impostor syndrome” disappear so many times. You are also the best example of a scientist I could give to anyone. I guess you probably know how my experience in Japan changed my life, and I owe you that. Thank you. I will always remember our moments there, and Mount Fuji will forever be linked to you.

Guillaume, I know you were not into me in the first place, but I am glad I made you change your mind. I have always considered you as a great researcher, and this has always been confirmed with your pertinent remarks during my PhD. I really appreciated the time and help you gave me, especially for the defense, you were so encouraging and reassuring, thank you for that. See you soon in Porquerolles.

This work is the result of many collaborations, and it is beautiful to see that science also emerged from human relationships. First of all, thanks to the team of Pau led by Dr. Antoine Bousquet and Dr. Christine Lartigau-Dagron for the fruitful collaborative work and their warm welcome during my visit at IPREM. Boss Alexandre, you will remain the heart of this OPV nanoparticles project, and I am so happy we did this together. You are a true inspiration for me, and I hope we will have the opportunity to work in the future. Now, the nanoparticles team has a bright future ahead of it with you Bea, Alejandro and Matthieu. I wish you the best. During my PhD I had the honour to work with Dr. Natalie P. Holmes for

the STXM characterisation. I am deeply grateful for the wonderful opportunity you provided me with, especially the unforgettable trip to Berkeley to work at the Advanced Light Source synchrotron facility. It was such a peak time in my professional life, I learned so much from you during those few days together. These night shifts were so challenging and still feel unreal now. Thank you to Dr. Matthew A. Marcus for your help and expertise, and for making this beamtime a success. A warm thank you to Dr. Marc Schmutz for the cryo-TEM images. I am honoured I started a collaborative work with Prof. Martin Heeney and Dr. Martina Rimmele from ICL, thank you for your amazing FOx-T polymers. Martina, it was so nice to have you during my PhD, I will always remember our trip to NYC and all the moments we shared together. I truly hope we will keep in touch, even from so far away now. Thank you, Dr. Giorgio Mattana, for the opportunity to stay at ITODYS and for our interesting discussions. Dr. Christophe Schatz for allowing me to use his equipment for the DLS characterisation.

My stay at the Institute of Industrial Science in Japan would not have been possible without Prof. Kazuhiko Hirakawa. Thank you for hosting me in your lab and for the warm welcome from the whole Hirakawa group. A big thanks to Yue Tian for your help and your time. My nano-gap and I are very grateful. To all the members of LIMMS, and its director Dr. Sebastian Volz, thanks again for making me feel in France from time to time. A warm thanks to the LIMMS secretariat, and especially to Eiko, you made my stay so easy and your help was so precious. I am happy to join the LIMMS once again for my post-doc. See you soon in Tokyo. I was also able to conduct part of my research at RCAST, and I would like to thank Prof. Takaya Kubo, Dr. Fumiyasu Awai, and Dr. Takaya Kubo for granting me access to the equipment and for their help during my stay.

I owe my happiness and mental health during these three years to all my close friends: Louis, Cécile, Lise, Ophélie, Clémence, Jb, Adrien, Quentin, Mathis, Boubou, Skavout, Camélia, Elliot, Abdoul and Ines. I also managed to get over this thesis without becoming insane thanks to you, Arthur and Eliot. You were so supportive and I was so lucky to live with you. Both of you will remain the best memory I have from Bordeaux. I wish I could thank you more. Same goes for Manon and Pauline of course. I hope I was a decent flatmate. To all the wonderful persons I have met through my PhD, I am glad you were by my side during this quest. Francis, thank you for welcoming me the way you did three years ago when I arrived in Bordeaux. I owe you a lot. Chloé, we probably had one of the worst possible starts for a friendship, but I am happy to call you my friend now. You helped me so much. Wish you to be C.R. soon and please, be happy. Gilles, you were for me the main pillar of this lab, and I was sad to see you left. Best luck for the future. Reem, I wish I had a sister like you. Like brother and sister, we had our ups and downs, but I will only keep the good times and all the laughs we had. I wish you the best for the end of your PhD, and I

cannot wait to call you Doctor El Attar. To all the new people I have met over the past year, especially Joan and Rebecca, my office mates. Joan, your precious liquor is almost finished now, but I hope our friendship will last. Rebecca, thank you for being friends with a grumpy doctor like me. To the other members of IMS, please know that you are also part of this work: Lionel, Damien, Marie, Laurence, Isabelle, Martial, Sophie, Mamatimin, Harmony, Chélia, Zuzanna, Ayoub, Barth, Ewen, Nhung, Suwapat, Sarah. I would also like to thank my two interns, Virginia and Darwin, whom I had the chance to supervise during my PhD. I hope I was a good tutor.

Kona, even though the distance between us was 10,202 km this past year, I feel you were with me every single second to support me. I am so happy and lucky to have met you, and I cannot wait for what is ahead of us now. ありがとう.

To the few teachers I have met in my life who somehow believed in me by saying “If he wants, he can”. Thank you. I guess this time, I wanted.

À mère. Celle qui s'est battue toute sa vie pour faire de moi la personne que je suis aujourd'hui. Merci infiniment.

Table of content

General introduction

Defining the obstacle that the world is currently facing by the simple use of “climate change”, “global warming” or even “environmental crisis” is perhaps minimising the actual gravity of the situation. More than everything, we are witnessing the collapse of life on earth. From a recent article, scientists are updating the situation with respect to the planetary boundaries framework proposed more than a decade ago.[1,2] Their study concludes that we are now beyond six out of the nine planetary boundaries, and even if climate change is the boundary we are often pointing out, this is not the most dramatic transgression made up to now (**Figure 0-1**).

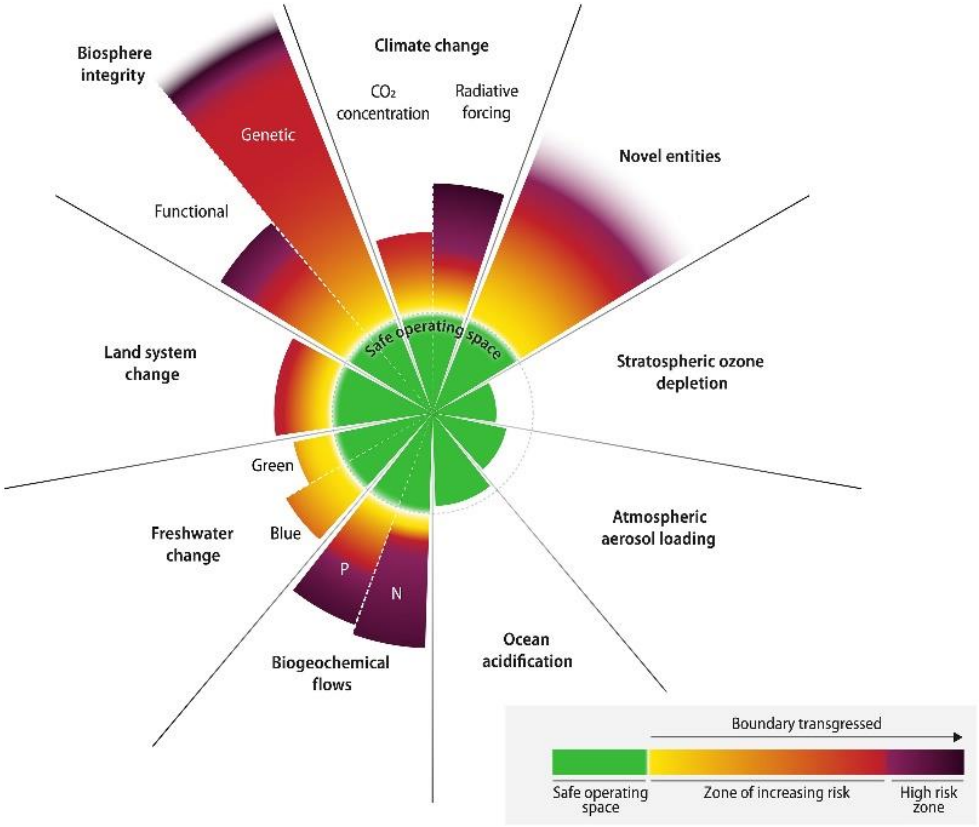

Figure 0-1: Current status of control variables for all nine planetary boundaries. Reproduced from Richardson *et al*.[2]

The recent and important report from the intergovernmental organization IPCC has established a synthesis of the critical changes arising from this climate change, its major causes and future consequences.[3] Since the end of the 19th century, the global surface temperature has increased by 1.1°C, primarily due to different human activities (unsustainable energy use, land use, over consumption and production…). Since the Paris agreement signed in 2016, the world has the objective to keep this rise below 1.5°C, which

seems now unlikely to happen. Based on the IPCC report, the greenhouse gases emissions should be reduced by 43% from 2019 emission levels. However, greenhouse gases emissions (mainly CO_2) coming from fossil fuels are directly related to our fossil fuel consumption. And looking at **Figure 0-2**, our consumption of oil, coal and gas does not seem to slow down. As a matter of fact, the global CO_2 emission from energy combustion and industrial processes increased by more than 2% since 2019.[4]

In 2023, more than 80 % of the energy consumption in the world still comes from fossil fuels. And by looking at the current trend, major alternatives to fossil fuels must be adopted. The present and modest thesis is obviously not here to address all the problems listed above, the work would go beyond what is feasible. But it is to contribute and bring solution to a part of the equation we need to solve, which is the energy production part, and more specifically the electricity production.

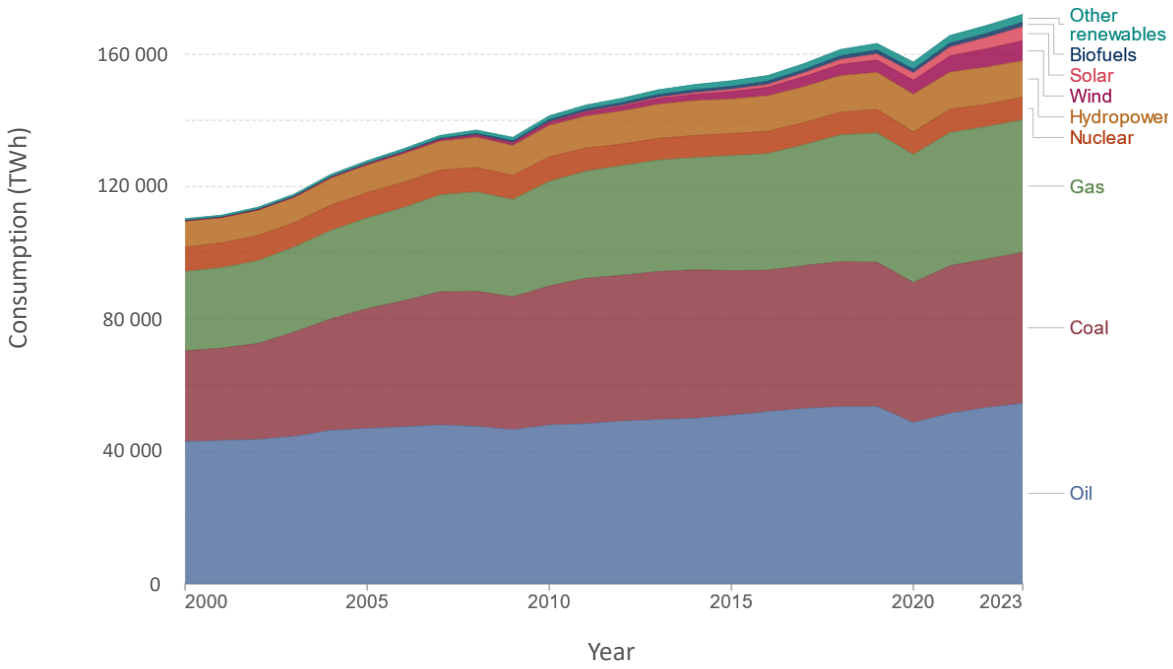

Figure 0-2: Energy consumption in the world by source from 2000 to 2023. Reproduced from ref [5].

Concerning the use of resources for electricity production only, the trend is still alarming with about 60 % of the electricity generation in the world that comes from fossil fuels (**Figure 0-3a**). However, it is still concerning as the trend of the electricity demand keeps rising over the years. Thanks to recent developments and energy policies, the growth in renewable energies over the last two decades is impressive and gives hope for the future.

The three primary renewable sources are hydro, wind and solar power accounting today for 27 % of the electricity generation. Note that it can be very different from a region to another as this value raise to 38 % in the European Union (EU) and decrease to 22% in Africa. Among these three sources, solar energy is the one generating the less electricity, and this tendency is almost true on every continent (**Figure 0-3b**). Yet, a complete opposite trend is observed when considering the yearly potential of these renewable energies. The solar energy reaching our planet and could be potential use is around 23 000 TW-yr, whereas for wind and hydro it is 25-70 TW-yr and 3-4 TW-h respectively.[6] Hence it easy to understand the massive room for improvement in the development of solar energy production, and the expansion of the installed capacity that is almost exponential is a good marker (**Figure 0-3c**).

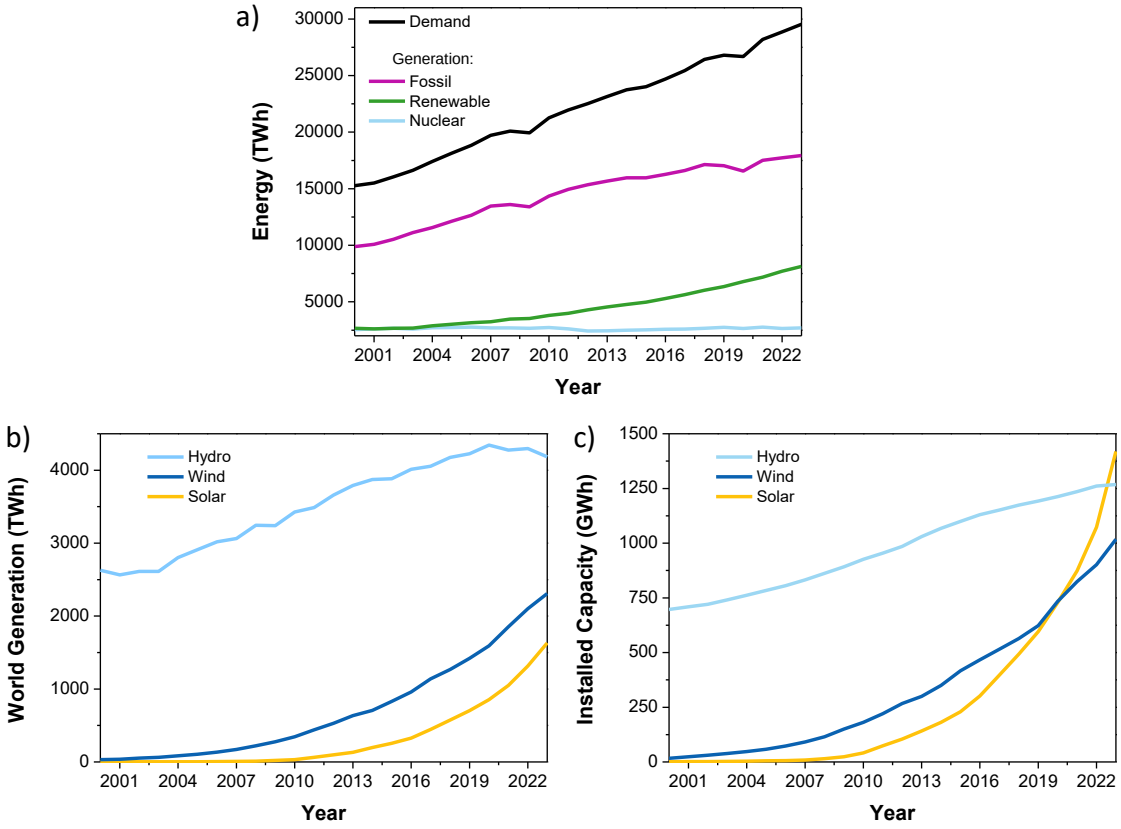

Figure 0-3: Evolution of (**a**) the energy demand and generation coming from electricity production with different sources in the world, (**b**) the electricity generation from different renewable energy sources and (**c**) of the different renewable energy capacity production. Data have been taken from EMBER website.[7]

When referring to solar energy for the electricity production, the photovoltaic (PV) technology dominates over other technologies such as the concentrated solar thermal power technology. Compared to other renewable energy technologies, the PV technology

presents several advantages such as having versatile integrations and easy installations, less maintenance and service costs, being safe and silent. We usually classify PV panels into three generations and the evolution of their best research-cell efficiency chart provided by NREL is shown in **Figure 0-4**.[8,9]

1st generation: Includes the technologies based on monocrystalline (mc-Si) and polycrystalline (poly-Si) silicon, as well as III-V materials (e.g. gallium arsenide (GaAs)).

2nd generation: Describes the inorganic thin-films technologies based on copper indium gallium di-selenide (CIGS), cadmium telluride and sulphide (CdTe & CdS) and amorphous silicon (a-Si) among others.

3rd generation: Contains the emerging thin-films technologies based on new materials or new architectures. The principal technologies are the organic photovoltaics (OPV), perovskite solar cells, quantum dots (QD) solar cells and dye-sensitized solar cells (DSSCs).

Among all of these PV technologies, the OPV is particularly having an intensive research development over the last decades, and is now at the dawn of a wide industrial development. This great interest is coming from the ability of this technology to produce transparent, lightweight and flexible solar cells with a low production cost. The last feature allows organic solar cells to have a short energy payback time, which is contributing greatly to the sustainability of the products.[10] Furthermore, the materials embedded in organic solar cells are carbon-based, which have an advantage in terms of toxicity over the lead-based materials used in perovskite solar cells for instance. The fabrication processes involved in this technology have a great impact on lowering the cost. Indeed, some layers of an OPV solar cell are solution-processed films, which are suitable for high throughput manufacturing technology such as roll-to-roll processes. However, this wet-processing requires the use of organic solvent which are toxic to the human health and harmful to the environment. The present thesis tackles this issue by exploring a way of replacing these solvents by water.

This chapter aims to introduce the general motivation and context of this thesis, in both societal and scientific dimensions. The OPV technology is now broken down in the next chapter, from its working principle to a global and brief look at its state-of-the-art.

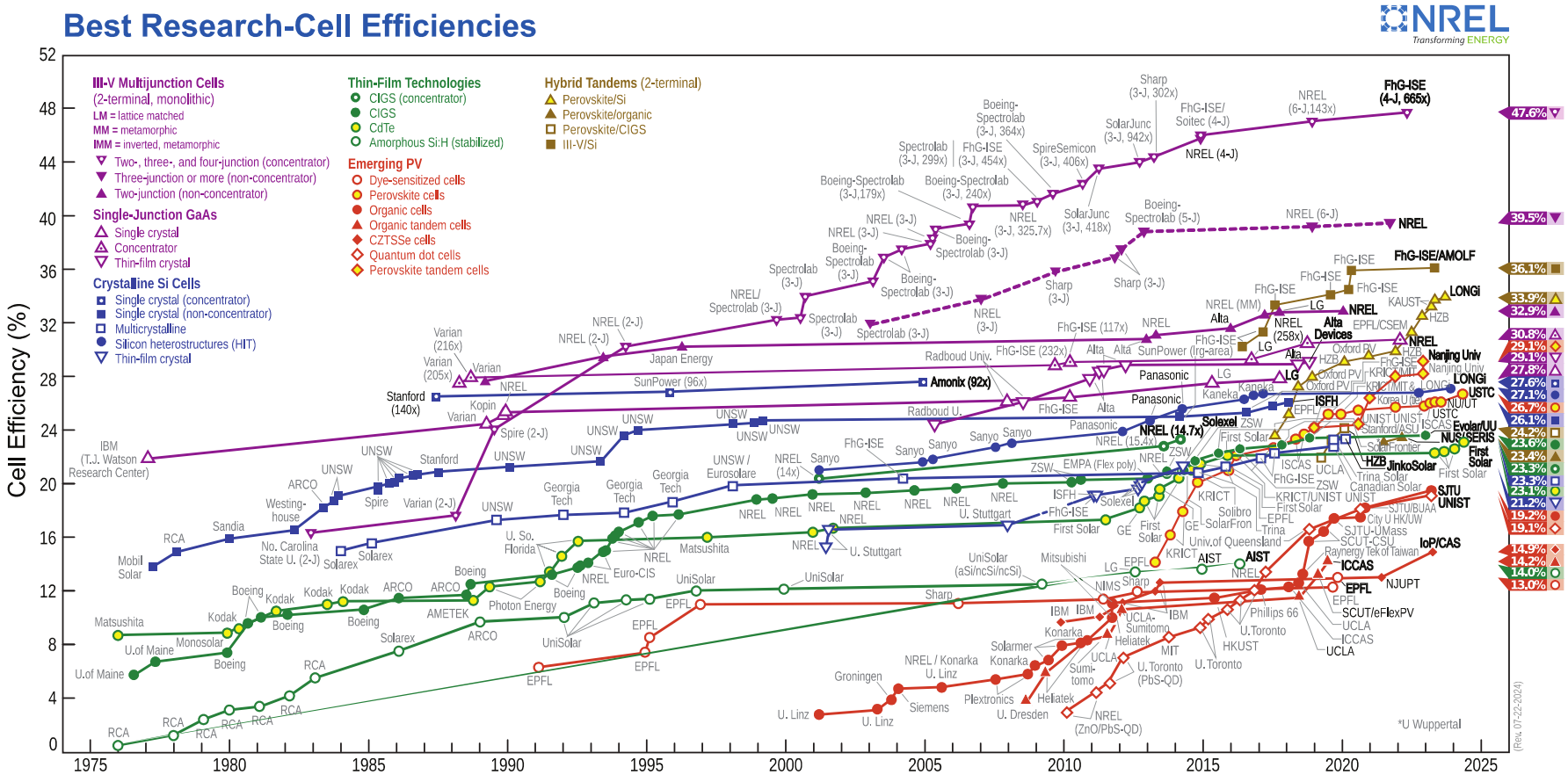

Figure 0-4: Best research-cell efficiency chart provided by NREL.[8]

Chapter 1

Organic photovoltaics

1.1. Introduction

Like every PV technology, the journey of OPV finds its core almost 200 years ago by A. E. Becquerel discovered the photovoltaic effect in 1839.[11] A wonderful phenomenon that allows the conversion of photons into electricity. After this discovery, it took more than 50 years for the first solar cell to be introduced by C. Fritts in 1883 following the work of W. Smith on Selenium.[12],[13] Until then, only inorganic materials were involved, and concerning synthetic materials, the way was opened in the early 1900s with the investigation of the conductivity and photoconductivity of anthracene, an organic compound.[14],[15] Again, several decades were needed to develop and finally introduce the organic semiconductors thanks to the development of many organic compounds.[16] The PV technology was primarily developed with inorganic materials, mostly silicon, with the first pn junction solar cell reported by Bell Laboratories in the 1950s and showing an efficiency of 6%.[17] With organic semiconductors, due to the low concentration and mobility of free charge carriers, as well as the poor exciton dissociation, further decades were needed to finally introduce the OPV technology. It was finally introduced in the 1990s with the important contributions of A. J. Heeger and R. H. Friend developing the concept a phase-separated mixture of two-component polymers for efficient charge photogeneration.[18–21] In the early 2000s, an efficiency of 2.5% was achieved, hence promoting OPV to the rank of a highly interesting technology.[22] At that time, over 25% efficiency was already achieved using single crystals silicon solar cells, and III-V multijunction technology was showing more than 30% efficiency, hence approaching the theoretical Schockley-Queisser limit.[23] Despite its lower efficiency as compared to other technologies, the OPV technology has known a tremendous development and a fast growing, approaching the symbolic barrier of 20% efficiency very recently in 2024. The interest in this technology lies into numerous advantages over the inorganic technology counterparts such as the promise of low-cost fabrication, the semi-transparency of OPV modules, their flexibility and lightweight (**Figure 1-1**).

Before taking a brief look on the current state-of-the-art of OPV, it is important to provide the scientific background of this technology by firstly defining the core material of an organic solar cell, and presenting the physics of the device.

Figure 1-1: Principle advantages of OPV

1.2. Working Principles

1.2.1 Organic semiconductors

In order to understand how an organic semiconductor works (also named as a π-conjugated material), it is here essential to put the carbon atoms in the centre of the discussion. Starting from the electronic structure of carbon, the latter has the following electron configuration in its ground state: $1s^2\ 2s^2\ 2p_x^1\ 2p_y^1\ 2p_z^0$. Whenever one of the 2s electrons is promoted to the empty orbital $2p_z$, the atom is able to form four covalent bonds. Upon interaction with three hydrogens and a carbon (ethane), new hybrid orbitals are formed from the 2s and 2p orbitals, leading to four hybridised $2sp^3$ orbitals (**Figure 1-2a**). Taking now the example of the ethene molecule, the carbon only hybridises three $2sp^2$ orbitals that are σ-orbitals. Two of the σ-orbitals form σ-bonds with the two hydrogens, and the third one a σ-bond with the other carbon. The last orbital ($2p_z$) is unhybridised and represents a π-orbital. Each π-orbital of the two carbon can now overlap above and below the carbon-carbon σ-bond to create a new π-bond. This overlap can create a bonding molecular orbital (π) and an anti-bonding molecular orbital (π^*), depending on where the two electrons are located, which gives its name to the *π-conjugated materials* (**Figure 1-2b**).

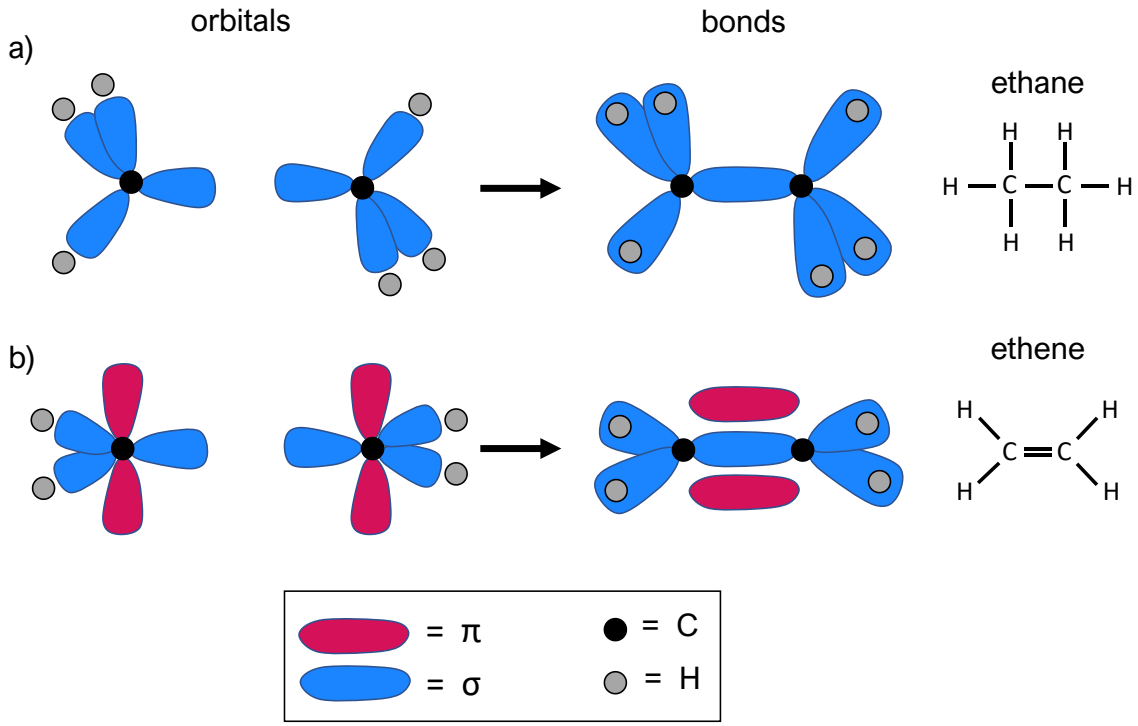

Figure 1-2: The combination of six hydrogen atoms and two sp^3 hybridised carbon atoms to yield the molecule ethane and four hydrogen atoms and two sp^2 hybridised carbon atoms to give ethene (ethylene) showing the pi-conjugation. Redrawn from ref [24].

In more complex π-conjugated systems, simple and double carbon-carbon bonds alternate to form repeat units where the electrons are weakly bound and delocalised along the conjugated chain. This confers to the electrons the ability to easily move through the material and its semiconductor properties.

In terms of energetic level, a linear combination of the π-orbitals from each repeat unit produces a π-band. This large band has two sub-bands, a filled low energy π-band and an empty high energy π^*-band separated with an energy gap (Eg). These two bands originate from the bonding molecular orbitals energies and the anti-bonding molecular orbitals energies. The highest energy level of the π-band is called the highest occupied molecular orbital (HOMO), and the lowest energy level of the π^*-band is called the lowest unoccupied molecular orbital (LUMO) (**Figure 1-3**).[25]

An excited state is created when an electron from the HOMO level is promoted to the LUMO level. Many kinds of excitation can produce an excited state, but in an organic solar cell, the dominant one is the photoexcitation produced from the absorption of a photon by the organic semiconductor.

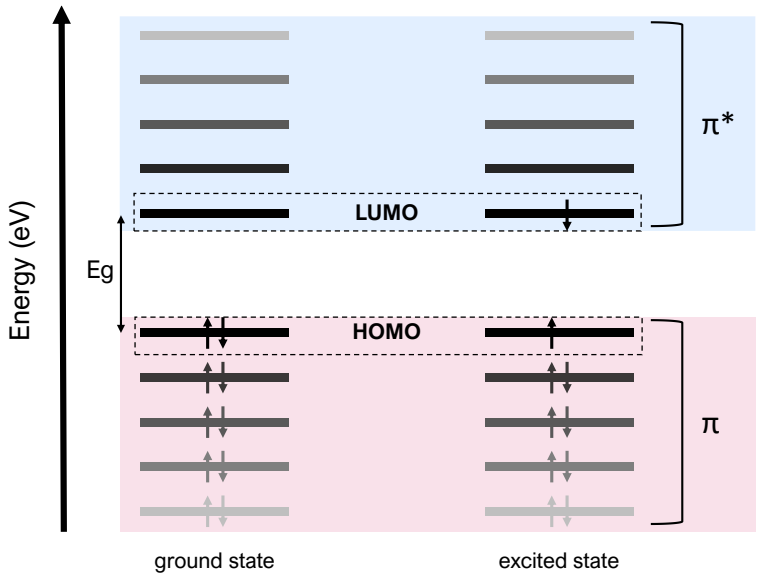

Figure 1-3: Simplify energy level diagram resulting from the linear combination of π-orbitals of a π-conjugated polymer (or small molecule) in the ground sates and excited state.

1.2.2 Organic solar cells

If a photon has an energy greater than or equal to the energetic band gap ($h\nu \geq Eg$), it is then absorbed and creates an exciton. This quasi-particle is a bonded electron-hole pair often referred to as a Frenkel exciton, which is specific to low dielectric constant materials such as organic semiconductors.[26] The Coulomb potential energy between the electron and hole is quite high, resulting in a large binding energy (0.1 eV – 1 eV). Unlike inorganic semiconductors, the energy at room temperature, kT, is not sufficient to dissociate the exciton and produce a free electron and hole. Therefore, to fully use the photovoltaic effect with organic materials, an additional energy is needed. A way to obtain this energy is to contact two materials with a sufficient energy difference, which results in a built-in potential. The photo-active layer (PAL) of an organic solar cell is thus forms with two materials: an electron donor and an electron acceptor material, and is called a bulk heterojunction (BHJ). The electron donor material (often a polymer) has the ability to transfer an electron from its LUMO to the LUMO of the acceptor which has a lower energy level. The acceptor material (often a small molecule) can transfer a hole located in its HOMO to the HOMO if the donor material has a higher energy level. Therefore, a good BHJ lies in the association of two materials having their energy levels compatible for the charge transfer. The photogeneration of charges and their transport in a BHJ can be described as follows: (**1**) once the photon is absorbed, (**2**) an exciton is generated in the

donor (or the acceptor) and (**3**) diffuses until it reaches an interface. When the exciton reaches an interface, a charge transfer (CT) state is formed with the electron in the acceptor material and the hole in the donor material. Once the binding energy of the CT state is overcome, (**4**) the exciton finally dissociates into free charges (**5**) able to be transport toward their respective electrodes (**Figure 1-4b** & **1-4c**). In order to collect these charges, the PAL is placed in between an anode and cathode, which together form the solar cell. Depending of the energetic levels of the PAL, the cathode and anode can be tuned for a better extraction of electrons and holes thanks to an appropriate electron transport layer (ETL) and hole transport (HTL). Two architectures are possible and are shown in **Figure *1-4*a**. In both architecture, one of the electrodes is a transparent conductive layer (TLC), which allow the light to reach the PAL, and is usually formed with indium tin oxide (ITO). In the presence thesis, only the inverted architecture is used and built as follows: **ITO/ZnO(ETL)/PAL/MoO_3(HTL)/Ag**. The details of the fabrication can be found in ***Methods***.

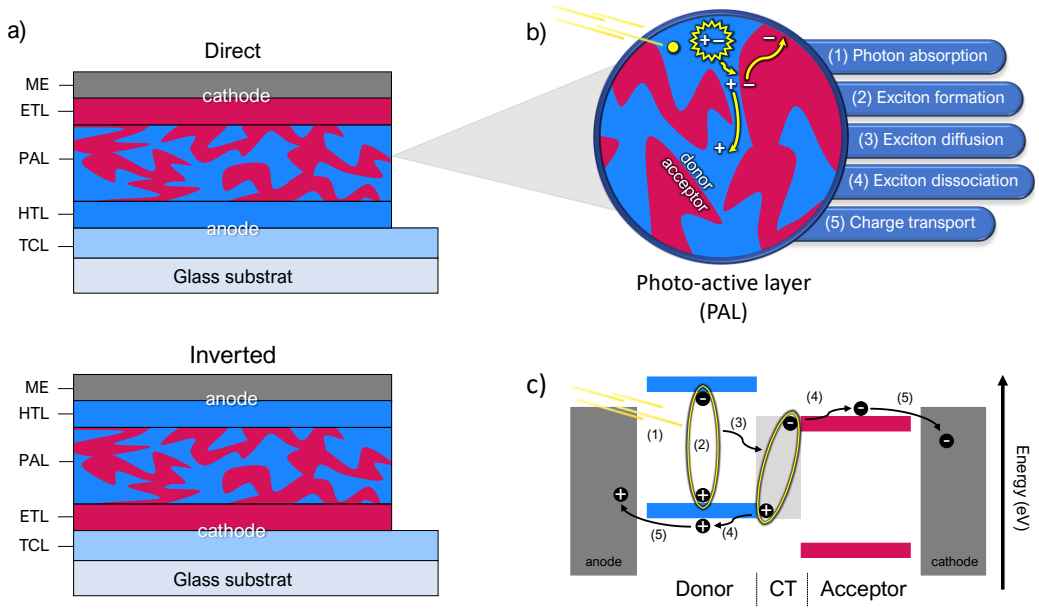

Figure 1-4: (**a**) Two different architecture used in OPV and (**b**) the photogeneration processes in the active layer made from a BHJ. (**c**) Represents the charge generation and transfer from a band diagram point of view.

1.2.3 Loss mechanisms in organic solar cells

Considering an ideal organic solar cell, every photon absorbed by the PAL would generate free charges collected at the electrodes. In a non-ideal solar cell, each step

described and illustrated in **Figure 1-4b** & **1-4c** would encounter several loss mechanisms. It is essential to understand these different mechanisms as they are setting the limit of the OPV performances.

The first type of loss is called geminate recombination and takes place when an electron and a hole coming from the same photon recombine before being separated into free charges. It can firstly happen during the diffusion of the exciton. Each exciton has a diffusion length which can vary (10-40 nm) depending on the material in which the exciton has been generated.[27,28] This length, way smaller than the PAL thickness, gives to the exciton a few ns to reach an interface before relaxing to the ground state. Photoluminescence measurement is very efficient for probing this recombination which is radiative. Secondly, a geminate recombination might occur when the exciton has reached an interface and a CT state is formed. At this point, the electron and hole are still coulombically bond and can recombine through CT state relaxation directly to the ground state or via a molecular triplet state. Probing the radiative recombination from the CT state can still be done through PL or EL measurements by analysing a red-shift signature. For the non-radiative recombination, it is quite challenging as the kinetic involved is around the sub ns scale, and fast spectroscopy is needed such as transient absorptions spectroscopy (TAS).[29]

Recombination happening after the charge separation are called non-geminate recombination. This type of recombination can be summarised in two categories with a first one referred to as Langevin or bimolecular recombination. This model characterises the chance that a free electron encounters a free hole leading to their recombination. In low charge carrier mobility materials, mostly the case for organic semiconductors, the Langevin recombination rate is generally high and proportional to the charge carrier density as well. The second category is the so-called Shockley-Read-Hall (SGR) recombination, also known as trap-assisted recombination which are favour by disorder and impurities. The trapped charge carrier recombines if the energy level of the trap lies below E_g, or can be realised if the energy is higher. Non-geminate recombination involves free charge carriers, so the time scale of this recombination is longer (ns - µs) than geminate recombination and various electrical and optical measurements are used to investigate these recombination mechanisms.[30]

1.2.4 Characterisation

Numerous types of experiments are carried out to characterise the various mechanisms and extract their parameters. Only the basic characterisation of an organic solar cell is presented in this part, and more specific one can be found in **Methods** or throughout the thesis. Once the solar cell is fabricated, it behaves like a diode with a resistance in parallel called the shunt resistance (R_{SH}) and a resistance in series called the series resistance (R_S) (**Figure 1-5a**). A low R_{SH} can indicate a poor film quality (pin holes, inhomogeneity…) as well as unintentional doping of the active layer resulting in leakage currents at reverse bias in the dark. R_S represents the resistance of each layer at forward bias, indicating the quality of contacts in the device. In the ideal case, R_{SH} is very high ($R_{SH} \rightarrow \infty$) and R_S very low ($R_S \rightarrow 0$), giving the characteristic current voltage (J-V) of the diode described by the Shockley equation (1.1) where J_0 is the saturation current of the diode, n its ideality factor, q the elementary charge, k the Boltzmann constant and T the temperature. Once the cell is placed under illumination, a photocurrent is generated through the absorption of light, and the current density is now given by equation (1.2). In the real case, the current density is given by equation (1.3) where the overall performances are dictated by the series and shunt resistances.

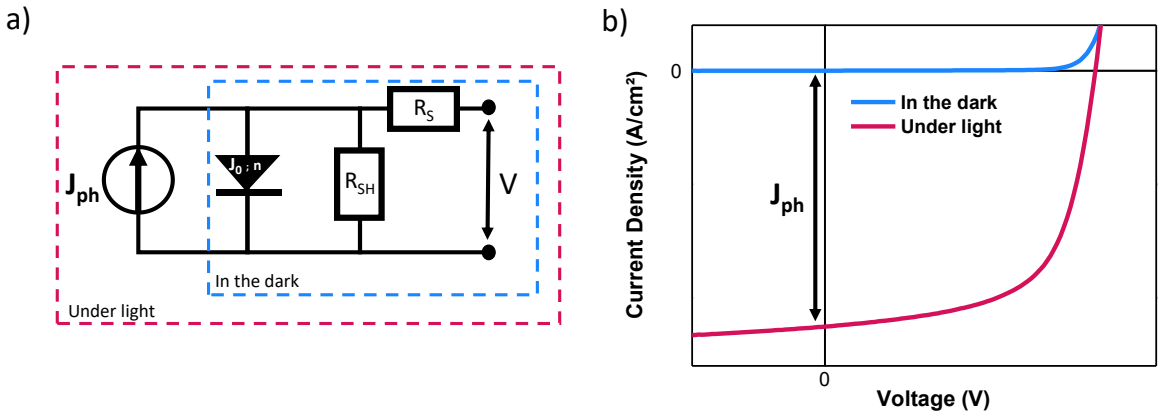

Figure 1-5: (**a**) Equivalent circuit of a solar cell including a Shockley diode, a photocurrent source and the two parasitic resistances. (**b**) Typical current – voltage characteristics of an organic solar cell in the dark and under illumination.

$$J = J_0\left(e^{\frac{qV}{nkT}} - 1\right) \quad (1.1)$$

$$J = J_0\left(e^{\frac{qV}{nkT}} - 1\right) - J_{ph} \quad (1.2)$$

$$J = J_0\left(e^{\frac{q(V-JR_S)}{nkT}} - 1\right) + \frac{V - JR_S}{R_{SH}} - J_{ph} \quad (1.3)$$

The main PV parameters are extracted from the J-V curves obtained when the OPV cell is characterised under an incident light with a power-density of 100 mW cm^{-2} corresponding to 1 sun. It is the typical power density received from the sun on the earth after passing through 1.5 times the thickness of the atmosphere. The spectrum of this light corresponds to the Air Mass 1.5 Global (AM 1.5G) which tries to reproduce the solar spectrum as closely as possible (see **Methods**). Using this specific light spectrum is essential to extrapolate the real operating behaviour of the cell, as well as for a rigorous comparison between the laboratories around the globe.

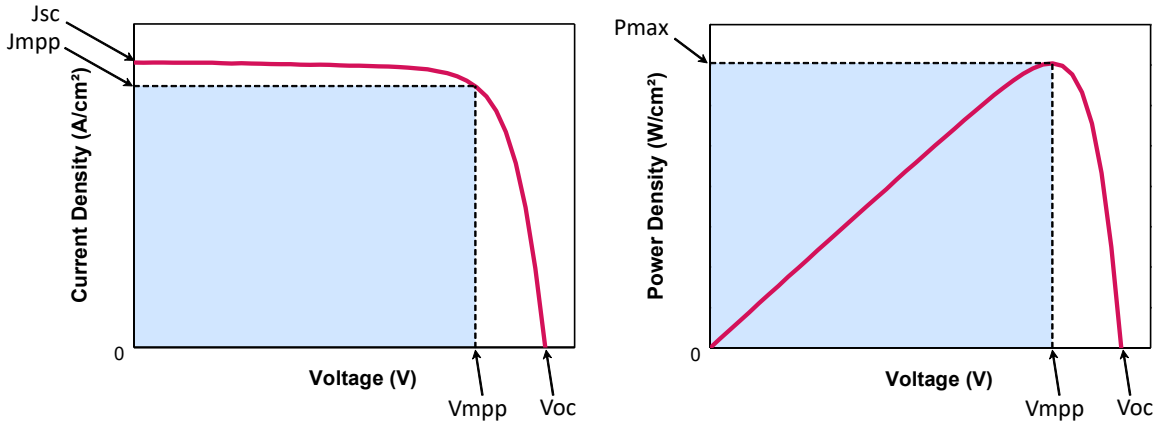

Figure 1-6: Typical (**a**) current - voltage and (**b**) power - voltage characteristics of an organic solar cell with the principal parameters.

From the J-V curves, four points are crucial in order to extract the overall efficiency (J_{SC}, V_{OC}, J_{MPP} and V_{MPP}). The V_{OC} is the voltage across the solar cell at open-circuit condition (J = 0) (equation (1.4) and the J_{SC} is the current density measured at short-circuit condition (V = 0) (equation (1.5). The J_{SC} is mainly set by the spectral signature of the active layer and subsequently how efficient photogenerated excitons diffuse and separate. The V_{OC} is related to the energetic level of the active materials, and in specially to how the electron and hole quasi-Fermi levels are splitted under illumination. The architecture also plays an important role of setting the V_{OC} due to the role of the HTL and ETL in the creation of the built-in field. The last two points (J_{MPP} and V_{MPP}) are the operating condition point of the solar cell, where the power density supplied by the cell is maximum (P_{MAX}). With these four values,

the fill factor (FF) is obtained and has a value between 0 and 1, where a FF close to 1 represents an ideal solar cell (equation (1.6).It is the result of the combination of many parameters in the cell such as the charge carriers extraction efficiency, the electrons and holes mobility and the balance between the two.[31] Finally, the important figure of merit of a solar cell is expressed by the power conversion efficiency (PCE) which is the ratio of the input power given by the light intensity to the maximum output electrical power (equation (1.7).

$$J_{SC} = -J_{ph} \qquad (1.4) \qquad V_{OC} = \frac{nkT}{q}\ln\left(\frac{J_{ph}}{J_0} - 1\right) \qquad (1.5)$$

$$FF = \frac{J_{MPP}.V_{MPP}}{J_{SC}.V_{OC}} \qquad (1.6) \qquad PCE = \frac{P_{MAX}}{P_{IN}} = \frac{J_{SC}.V_{OC}.FF}{P_{IN}} \qquad (1.7)$$

Another important characterisation of a solar cell is done through the external quantum efficiency (EQE) measurement. Also called the incident photon to electron conversion efficiency, the EQE is useful to correlate the photocurrent (I_{ph}) at a certain wavelength (λ). As expressed by equation (1.8) at a given λ, the EQE is the ratio between the measured photocurrent and the theoretical current obtained if all photons of the flux (Φ_{ph}) are converted into free charges. By doing the EQE measurement over the AM 1.5G spectrum range and integrating the whole, the J_{SC} can be calculated from equation (1.9).

$$EQE\ (\lambda) = \frac{I_{ph}(\lambda)}{q.\Phi_{ph,\lambda}} \qquad (1.8)$$

$$J_{SC} = -q\int_{\lambda_2}^{\lambda_1} EQE(\lambda).\Phi_{ph}^{AM\ 1.5G}\ d\lambda \qquad (1.9)$$

1.3. A brief state-of-the-art and motivations

Before presenting the core and the motivation of the present thesis, a brief introduction to the current state of organic photovoltaic in the research field is necessary.

As previously shown by the NREL chart relating the best research-cell efficiencies, the OPV community is on the eve of reaching and going beyond the 20% power conversion efficiency (PCE) milestone. Two recent published works even report PCEs reaching 20.17% and 20.22%, although certified PCEs still below 20% in both cases.[32,33] The latest major milestone was the development of non-fullerene acceptors (NFAs), which led to surpassing the highest efficiency obtained with historical fullerene acceptors in 2016 (PCE > 12%).[34,35] From that point, NFAs have played an important role in the rise of organic solar cell efficiencies. Firstly, through the development of the A–D–A-type fused-ring small molecules such as IDIC, ITIC and their derivatives (PCE > 13%).[36] And since 2019 with the low-bandgap A-DA'D-A fused-ring small molecules represented by the Y6 (PCE > 15%).[37] Benefiting from the electron deficient 2,1,3-benzothiadiazole (BT) based core, the Y6 and its derivatives present high electron mobility as well as enhance intermolecular interactions due to its U shape. Furthermore, its complex but tunable chemical structure enables a wide molecular engineering potential from the end-groups to the side chains.[38] Doing so, in 2019 the derivative L8-BO was synthesised and gave a PCE of 18.32% by switching from linear side chain to the 2-butyloctyl bulky branched-side chains.[39]

Though NFAs are highly efficient photoactive semiconductors, they need donor polymer materials to their sides in order to reach such efficiencies. Starting from the early 2000s, P3HT has been for more than a decade the most used donor polymer in the OPV community thanks to its good light absorption and its reasonably good mobility. [40] However, P3HT's limited V_{OC} (with most acceptors) and FF, together with a limited absorption spectrum, have pushed the research toward polymers with a downshifted HOMO and LUMO level, while decreasing as well the donor bandgap.[41,42]. To this end, numerous low-band gap polymers have been developed during the early 2010s to finally achieve in 2015 one of the most high-performing donor polymer known until now the PM6.[43] Almost 10 years after, PM6 is today one of the mostly used donor polymer in bulk heterojunction showing PCE over 19%. Associated with Y6, this blend is unanimously considered as the P3HT:PC_{61}BM blend of the new era of OPV. Because of this status, many studies have explored the different mechanisms of this efficient blend and identified several interesting features: longer exciton diffusion lengths, simultaneous lower radiative and non-radiative recombination compared to other polymer:NFA systems and even a lower energetic disorder.[44] However, our understanding of this system is still far from the mature P3HT:PCBM system as many debates on physical processes of NFA-based solar cells are

still ongoing.[45] With such efficiencies, these materials were making the OPV technology more and more attractive, but the "low-cost" advantage often emphasised was getting less relevant. Due to the high synthesis complexity a thus high cost of these materials, a new pan of the research has led to propose in 2018 the low cost and high efficient donor polymer PTQ10.[46] The two-step reactions and one-time purification of the PTQ10 give to this polymer a similar low synthetic complexity than P3HT, which makes it of great interest for commercial application.[47] Furthermore, a tremendous power conversion efficiency over 18% with a simple binary blend was recently achieved.[48]

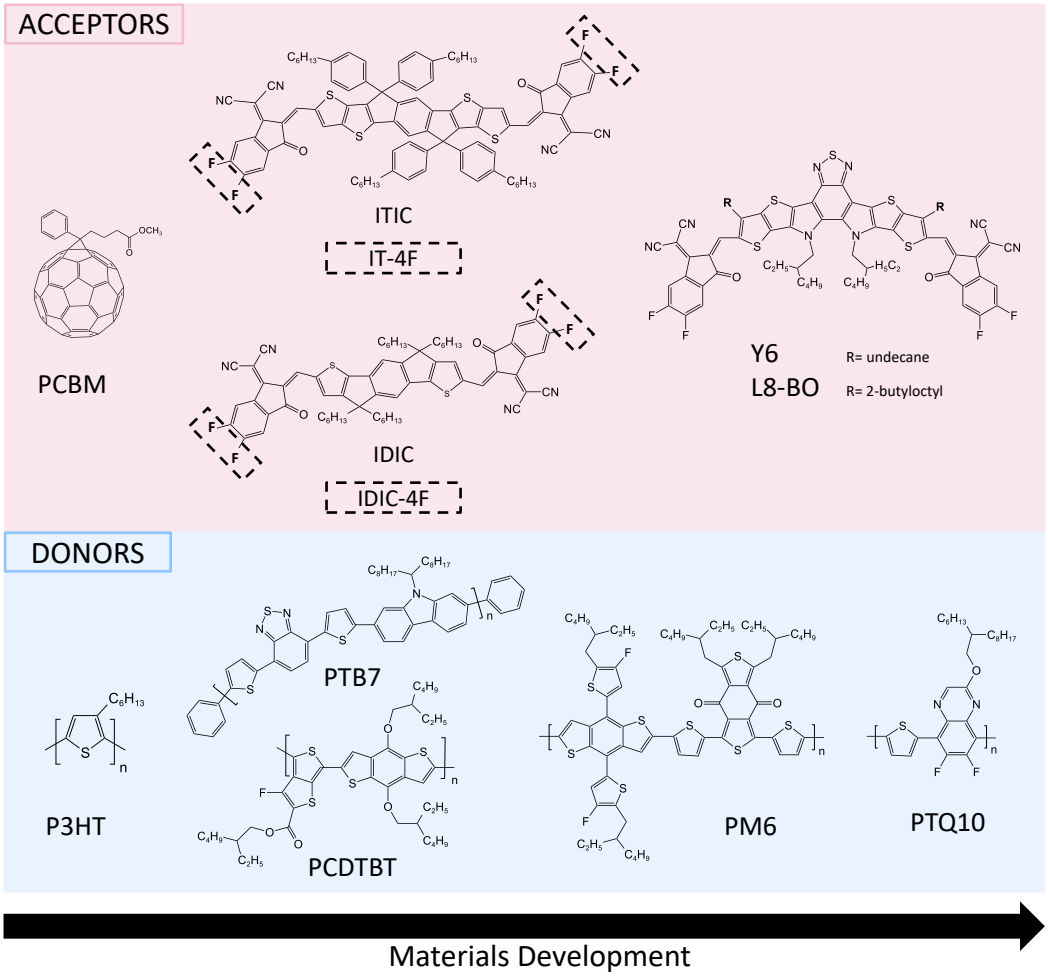

Figure 1-7: Chemical structures of some of the more important π-conjugated materials over the history of OPV

To successfully realise the lab-to-fab transition, and start to spread out efficient OPV modules for our daily electricity need, this technology is expected to show higher stability. Along with the PCE and the synthetic complexity, Min *et al*. have also included the

photostability in their industrial figure of merit (i-FoM), which makes it a central parameter in the transition. An organic solar cell is highly sensitive to external parameters such as oxygen, moisture, light, heat and mechanical stress. This sensitivity causes chemical degradation as well as physical degradation through mechanical failures, explains short lifetimes of an organic solar cell as compared to a silicon solar cell.[49] An efficient encapsulation can effectively prevent water and oxygen from penetrating in the active and induce photo oxidation.[50] However, photochemical reactions due to UV light and chemical degradation can still occurs with a good encapsulation. A recent and complete published review has summarised the progress made in the OPV community for stability of organic solar cells since 2020.[51] Despite the low number of publication reporting stability data as compared to the number of publication in the OPV field, this number is increasing since 2020 stressing out the interest of the community and its importance (**Figure 1-8a**). However, when comparing the stability test conditions of these results, a lot of differences are observed such as the type of light, the temperature or the T_{80}. This parameter has been introduced in 2011 to create an universal comparison methodology.[52] It represents the time at which the solar cell has lost 20% of its initial efficiency. From **Figure 1-8b**, the PCE of a selection of high efficiency solar cells published in the last four years are plotted with their respective T_{80}. It shows the great potential of OPV to achieve long lifetimes using different strategies such as material design (ternary blend, HTL or ETL material…) and device engineering (interlayer modification, electrode modification…).

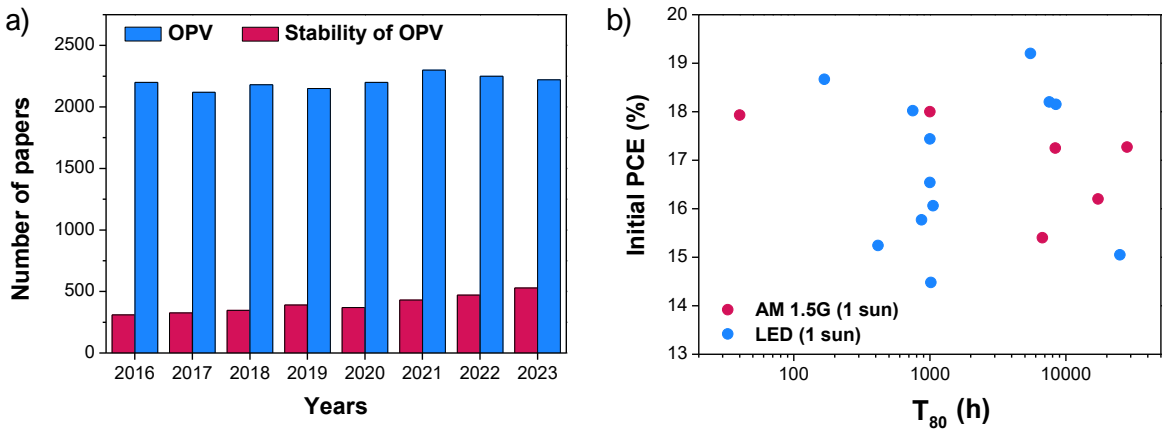

Figure 1-8: (**a**) Number of papers published on OSCs and the stability of OSCs from 2016 to 2023. (Reproduced from Ding *et al.*[51]). (**b**) Selection of the highest PCE reported for OPV and their T_{80} value under illumination (LED or AM 1.5G) (inspired from Ding *et al.* [51]).

Shifting to commercial products also requires an upscaling of the organic solar cells, which involves moving from laboratory cells (≤ 1 cm²) to modules. However, from **Figure *1-9***, we can observe that such a transition is yet not possible without losing performances. The larger the area, the more challenging it becomes to maintain the best device efficiencies obtained with cells areas < 0.1 cm².

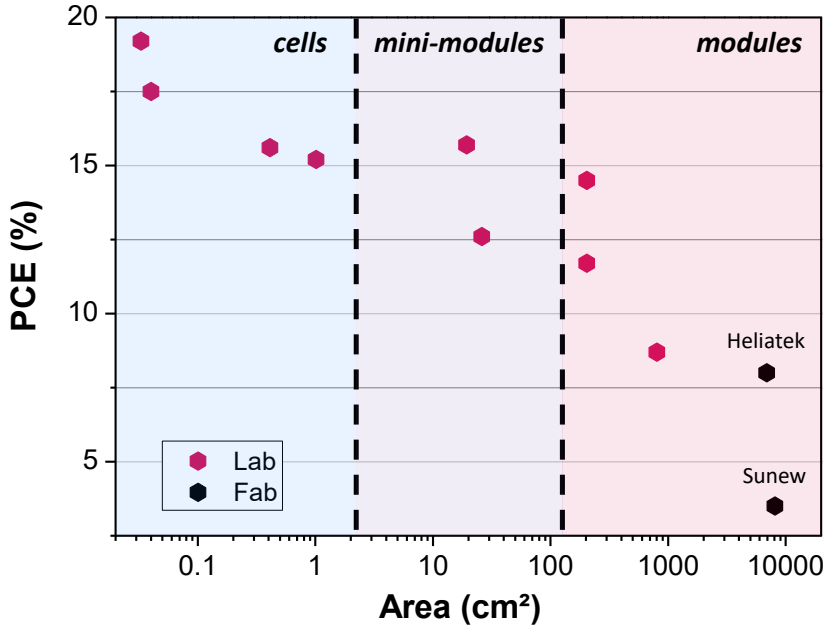

Figure 1-9: Best PCE reported for OPV devices as function of their active area. (all efficiency are certified and extracted from different reports[9,53,54]).

First of all, the spin coating technique is the major coating technique to achieve highest performances for lab-scale organic solar cells. Widely spread in the research field to deposit several organic solar cell layers, it is a very convenient technique to optimise the process as we are working with small area and many devices per batch. However, when it comes to scalable coating techniques, the key parameters that are uniformity, thickness, crystallisation and subsequently morphology are much harder to control as compared to the spin coating technique. Because the BHJ is a complex system where donor and acceptor are randomly distributed through the layer, the upscaling is quite challenging as a BHJ is very sensitive to thickness variation.[55] The sequential deposition strategy, which enables the formation of pseudo-planar heterojunctions, has emerged as a good candidate to control the morphology while upscaling.[56] Another source of losses when shifting to large area OPV comes from the electrical and geometrical losses.[57] Modules are essentially

several single cells connected together in series, which add to the internal resistance of the cell an interconnection resistance. In addition, for flexible modules the internal resistance of the cells integrated in a module is much higher due to the higher resistance of the flexible transparent electrodes. And the geometrical losses correspond to the inactive photo-active areas that are used for interconnections.

Willing to address these different obstacles, Basu *et al*. have recently reported a world record efficiency for large area OPV with modules >200 cm².[58] Their extensive optimisation of the coating process as well as the module layout through computational simulations enabled a 14.5% PCE with 204 cm² module. While this represents substantial progress compared to lab-scale devices, the journey toward the fab is still ongoing as it is still far from the modules commercialised by the Heliatek and Sunew (> 6000 cm²). However, their efficiencies remain below the symbolic 10% PCE already achieved in the lab more than 10 years ago.

Along all these considerations of high performances, stability and upscaling, the success of OPV commercialisation won't be fully complete without sustainability considerations. Many parameters cover the question of sustainability, and it is not straightforward to make a qualitative assessment on the sustainability of an electronic product.[59] For industries and investors, it is clear that the main parameter is the production cost. OPV has shown great potential of producing economically feasible products, but major concerns about the cost of high efficiency active materials must be addressed.[60] As we expect the OPV production to grow exponentially in the next decades, a strategy for recycling OPV modules is essential. Unlike silicon PV, where recycling methods are already well established, OPV still needs to develop this side of its research.[61] Recent results from R. Sun and co-workers have demonstrated a cost-efficient protocol to recycle an OPV solar cell by reusing photo-active and conductive materials.[62]

The use of wet-process fabrication instead of a dry-process presents the advantage of using low-cost techniques, and versatility in producing large-area and flexible devices.[63–65] A wet-process also means to handle deposition solvents, which in the field of OPV are often hazardous organic solvents that present many issues (e.g. halogenated solvents). Numerous research works are claiming the use of "green solvents" to deposit the photoactive materials, often considering the toxicity.[66],[67] However, the term of "green solvents" should contain more than this only parameter. The sustainability of a deposition

solvent also involves other factors, such as its environmental impact and safety.[68] Several solvent selection guides aim to provide tools in order to assess the sustainability of a solvent. Based on one of these, the GlaxoSmithKline (GSK) solvent sustainability guide, the best PCE obtained with common solvents, including "green solvent", are displayed as a function of their sustainability score (**Figure 1-10**).[69]

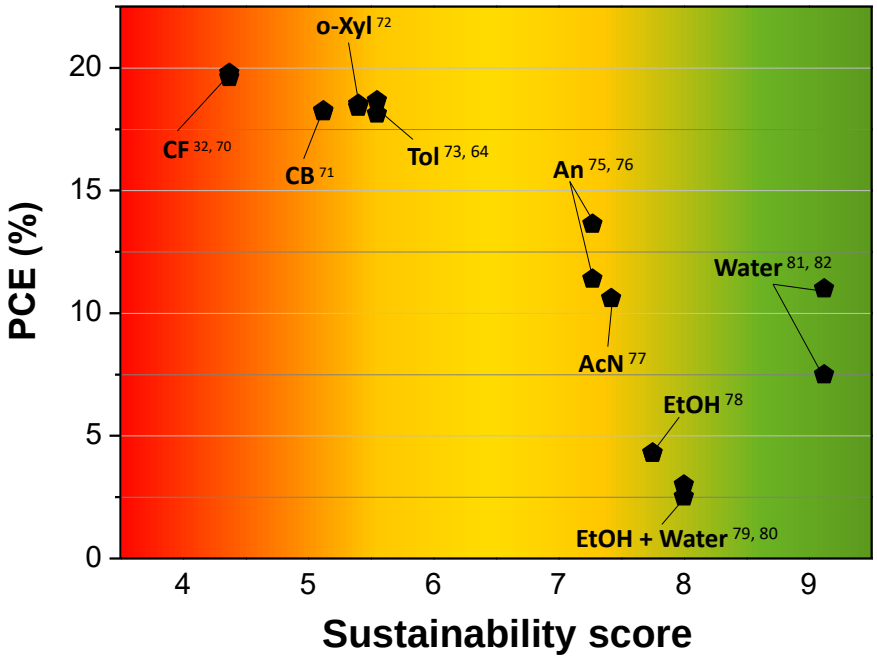

Figure 1-10: Sustainability versus highest power conversion efficiency of OPV devices active layer processed with common solvent including "green solvents". Data are from ref [32,70–82]

Without any surprises, from the above figure we observed that high efficiencies are obtained from chloroform, which happens to be the less sustainable. Good performances associated with a deposition from chloroform (CF) or chlorobenzene (CB) are due to the extremely high solubility with the best performing π-conjugated materials. Shifting to more sustainable solvent, some considerations must be taken into account to match the solvent and the material such as the Hansen solubility parameters which is a good tool for the solvent selection.[83] Often introduced as green solvents reaching PCE over 18%, o-xylene (o-Xyl) and toluene (Tol) are yet relatively low in the sustainability scale, even though the former is now industrially compatible in the EU. Looking now at a more sustainable solvent recommended by the United Nations, the anisole (An) as shown high efficiency up to 13.6 % PCE.[79] This result was made possible via the modification of a polymer by changing C=C

bonds to B–N covalent bonds with highly polar characteristics. This strategy often leads to complex synthetic routes, which can impact the sustainability of the whole study. It is worth noting to mentioned the novel class of solvents recently adopted in OPV: terpenes. In particular, they are interesting for their potential negative carbon footprint, as they are derived from renewable bio-sources. Based on the system PM6:BTP-eC9 and using terpene-based solvents, Corzo *et al.* have obtained an efficiency similar to their control cell made out of chloroform and DIO of 15.1 % PCE.[67] Because the GSK guide does not report data concerning solvents reported in the article, which are eucalyptol and tetralin, the data are not included in **Figure 1-10**. Nevertheless, the only type of terpene rated by the GSK guide is the limonene. Although it presents an advantage due to its production, it still presents some risks when looking at the environment category which described the air and aqueous impact.

From the sustainability scale, few are the solvents falling in the category of "green solvents", to be fair, water is the greenest solvent overall there is no doubt about water being the best choice. However, using water as a solvent is not an easy task because most of the organic semiconductors are not soluble in water. The strategy of solubilising organic semiconductors in a water/alcohol mixture for the photoactive layer has been explored but suffers from weak efficiencies and requires the synthesis of new materials that are not commercially available.[84],[85] Most of them bearing water compatibiliser moieties that are bulky and strongly decreasing electrical properties. However, remarkable works have been published on water and water/alcohol soluble conductive polymers for transport layers.[86,87] Overall, the strategy that gave the best efficiencies so far is based on the elaboration of aqueous dispersions of organic semiconductor nanoparticles.[88,89] The work done in the present thesis is following this strategy, and before presenting the results obtained during this PhD, an overview of the literature of water-based OPV is presented in the next chapter.

Chapter 2

Nanoparticles-based organic photovoltaics

2.1. Introduction

In **Chapter 1**, an introduction of the OPV technology has been provided as well as its working principle and the main characterisation of an organic solar cell leading to its various figures of merit. A brief overview of the current state-of-the-art has illustrated the main challenges of the field in order to achieve the fab-to-lab transition. One of the keys is sustainability, which is, to some extent, related to the use of really “green” solvents when processing an organic solar cell. Water being by far the best solvent in term of sustainability, the present chapter is presenting the main strategy employed to develop water-processable OPV through the use of nanoparticles dispersions. From the synthesis of the latter and the different morphologies of nanoparticles reported in the literature, an overview of the current performances obtained along with their limitations is presented.

Water-processable OPV is referring to the process of using water as a solvent to deposit one or several layers when building an organic solar cell. More specifically, this term is used to describe the deposition of the active layer with aqueous colloidal dispersion. Herein, the water is not a solvent in the sense where the active materials are solubilised in water, but nanoparticles are formed dissolving first active materials in a given solvent (not water) and then dispersed in water for the thin film deposition. Two main strategies are employed in the community to elaborate these colloidal inks, within which many parameters and variation allow the formation of a large variety of nanoparticles. As previously seen when looking at the best efficiency of different solvent, the water-based OPV still falls below the state-of-the-art of OPV processed from chlorinated/halogenated solvents. Many reasons can explain this gap among which stand the use of surfactants, the quality of the nanoparticulate active layer or its final nanoscale morphology. To start, an overview of the two main methods for the synthesis of nanoparticles is presented, followed by a focus on the resulting internal morphology of these nanoparticles. Then, a focus is given at the process for fabricating an organic solar cell with these colloidal inks and the subsequent OPV performances. Finally, the aim and outline of the present thesis are presented before getting into the main results obtained during the last three years.

2.2. Nanoparticles elaboration

Organic semiconductor nanoparticles can be obtained using the *bottom-up* approach. In contrast with the *top-down* approach where the formation of nanoparticles is achieved from processing the source material at the macroscale or microscale, the *bottom-up* approach consists in using the self-organisation of molecules to end up with the nano-object. The latter is the most convenient in our case as it offers a better control of the size along with its dispersity. The self-organisation leading to a nanoparticle is made possible by a solvent displacement leading to a solid state (i.e. the nanoparticle) in a liquid environment.

2.2.1 Mini-emulsion

Mini-emulsion is the first method discussed as it is the most used to form organic semiconductor nanoparticles since its introduction for OPV by K. Landfester and co-workers back in the early 2000s (**Figure 2-1**).[90,91]

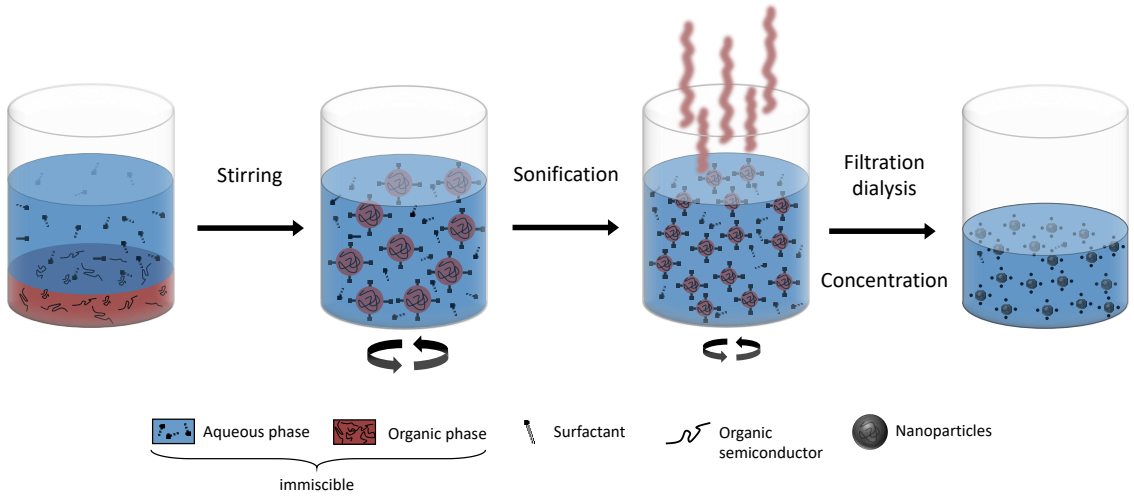

Figure 2-1: Schematic of the elaboration of nanoparticles via the mini-emulsion method.

The method, originally proposed as an emulsion polymerisation in 1973, consists in preparing two immiscible phases: an aqueous phase, by dissolving a surfactant into water, and an organic phase, by dissolving the active material into an organic solvent.[92] As the organic solvent needs to have a low boiling point, ii. be immiscible with water and iii.

solubilise most of the material, the chloroform is the main choice as it checks all criteria. Nevertheless, the use of higher boiling point such as o-Dichlorobenzene is however still possible but less employed.[93] In the aqueous phase, when the right concentration of surfactant is utilised, which must be above the critical micelle concentration (CMC), micelles are formed to thus create of a macro-emulsion. The latter is obtained by mixing the two phases (aqueous and organic) under vigorous stirring. The organic phase is now forming small droplets (around the µm scale) with the hydrophobic tail of the surfactant pointing toward the organic phase and the hydrophilic one oriented toward the aqueous phase.

Next, the obtained macro-emulsion is further emulsified using a sonifier to form a mini-emulsion. At this point, nanodroplets (sub µm scale) of organic phase are dispersed in the aqueous phase. Subsequently, the evaporation of the organic solvent takes place leading to the formation of the nanoparticles. While the organic solvent is evaporating, the active materials start to precipitate inside the nanodroplets until no more solvent is left and nanoparticles are then formed from the material precipitation. After this, surfactants are still present at the surface of the nanoparticles which allow the electrostatic repulsion of the particles and the stabilisation of the dispersion. In addition to these surfactants attached to the nanoparticles, the aqueous dispersion still contains some remaining free surfactants. When depositing the colloidal ink, these remaining surfactants are considered to be impurities that act as charge trapping sites.[94] Therefore, an additional step of the mini-emulsion process is the removal of this excess of surfactant by either simple dialysis or centrifugal dialysis. The latter is particularly convenient as it offers the possibility to concentrate the dispersion at the same time which favours the deposition of the particles. While it is bound to be removed, the surfactant has a crucial role in the mini-emulsion process. As such, even if a wide range of them have been investigated, sodium dodecyl sulfate (SDS) remains the most used (**Figure 2-2**).[95–97]

This method has been widely used in the community to form nanoparticles of various size as this latter can be finely tuned upon addressing various process parameters.[88] While it is essentially used in OPV, the OFET community has also started to show some interest for mini-emulsion.[98,99] More recently, pure PM6 nanoparticles were synthesised and used to develop a sequential layer-by-layer (LBL) deposition in organic solar cell.[100,101] The LBL strategy is getting more and more attention from the community

because it allows the fabrication of a well-controlled and interdiffused pseudo-bilayer.[102] By forming a layer with PM6 nanoparticles onto which an NFA is spin-coated from an organic solvent solution, C. Xie and co-workers achieved a mesoporous interface. The latter unlocked a fine tuning of the interdiffusion between the donor and acceptor domains. Different surfactants than SDS were involved such as CTAB which produced a more stable and homogenous dispersion by suppressing flocculation and Ostwald ripening. The study shows that the use of nanoparticles has more to offer than just being a sustainable strategy, it can actually help the control of the final active layer morphology.

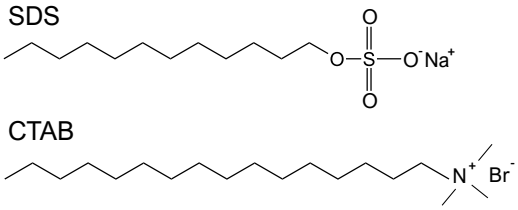

Figure 2-2: Chemical structure of SDS and CTABS.

2.2.2 Nanoprecipitation

The second method to produce colloidal dispersion is the so-called "nanoprecipitation", which takes its name from the re-precipitation method, firstly demonstrated with the preparation of π-conjugated microcrystals (**Figure 2-3**).[103]

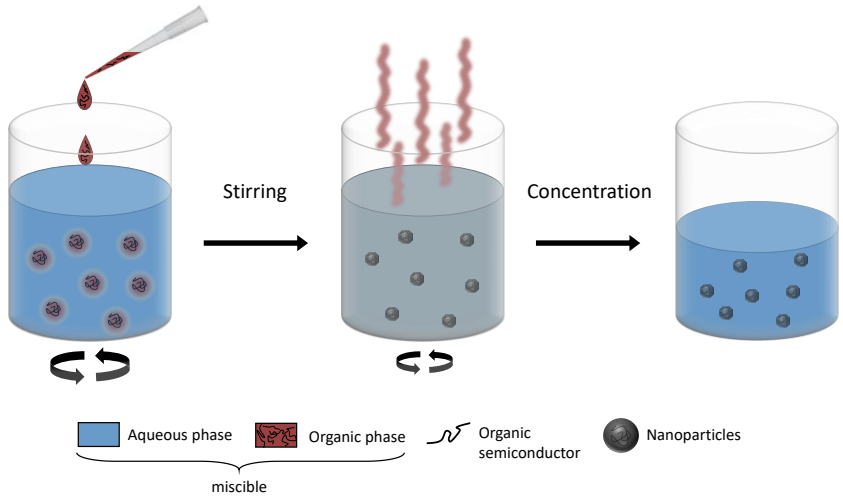

Figure 2-3: Schematic of the elaboration of nanoparticles via the nanoprecipitation method.

For the first step of this method, the organic semiconductor is solubilised in an organic solvent (organic phase) and injected into the water (aqueous phase). Unlike the mini-emulsion method, the solvent and the non-solvent (water) must be miscible. Under constant stirring, the organic phase is forming droplets, in which the concentration gradually increases as the organic solvent is slowly getting dissolved into water. When reaching the super-saturation stage, nuclei are formed and ultimately grow to form nanoparticles. The formation of a nanoparticle is hence quite similar to the mini-emulsion, but implies a much faster formation step because of the quicker solvent displacement. The dissolved organic solvent is then evaporated to obtain the final aqueous dispersion. Note that the non-solvent which is here described as water can also be an alcohol such as ethanol or methanol.[82,104–108]

Before being integrated into organic solar cells, some studies have reported the synthesis of organic semiconductors nanoparticles prepared via nanoprecipitation and their optical and electronic properties.[109–112] For instance, J. Gesquiere and co-workers have studied with fluorescence spectroscopy single composite nanoparticles of P3HT:$PC_{61}BM$.[110,111] Doing so, there were able to prob the formation of two types of P3HT crystalline nanodomains in P3HT:$PC_{61}BM$ composite nanoparticles depending of the amount of $PC_{61}BM$. Using P3HT to from pure nanoparticles, Millstone *et al.* have demonstrated the successful integration of the nano-objects in organic field effect transistors showing a similar mobility obtained with P3HT deposited from organic solvents.[112] In 2014, Darwis *et al.* have reported working solar cells using P3HT:$PC_{61}BM$, reaching a PCE of 1.09 % by applying a proper thermal annealing. They emphasised that higher performances were obtained with surfactant-free nanoparticles as compared to nanoparticles prepared via mini-emulsion, hence containing a surfactant.[113] Furthermore, even if the nanoprecipitation is a quick and easy method, it comes with disadvantages such as low dispersion stability and concentration. This is arising from aggregates formation and fullerene sedimentation, which makes it not suitable for all active materials.[108]

In 2018, Xie *et al*. have introduced the use of a surfactant during the nanoprecipitation synthesis without impacting the performances as they reached the record PCE for water-processed OPV of 7.5 % with the PBQ-QF:ITIC system.[74] Their strategy is based on the use of the poloxamer Pluronic F127 which has a temperature-sensitive CMC. This property allows to switch from F127 micelles to poloxamers, and thus

allows the removal of all excess F127 while preserving a stable aqueous dispersion without aggregation (**Figure 2-4**). Using this method, they have recently reported the up-to-date highest efficiency for water-based OPV by forming PM6:BTP−eC9-based nanoparticles and adding 1,8-diiodooctane (DIO) in the organic phase. With this additive, they reached a PCE of over 11%, currently holding the world record for water-based OPV.[73]

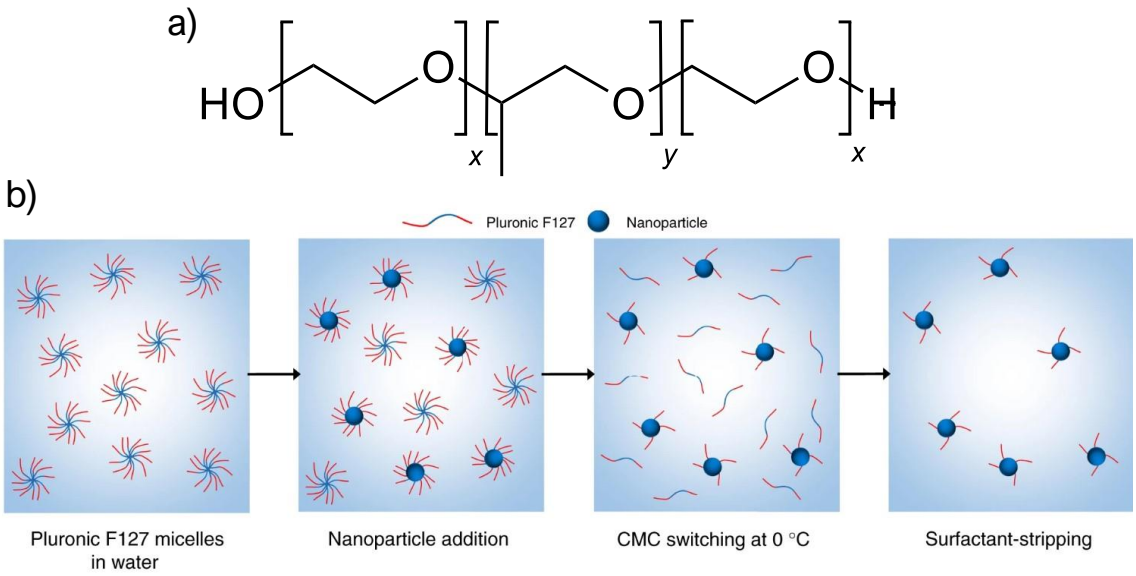

Figure 2-4: (**a**) Chemical structure of Pluronic F127. (**b**) F127 retention as function of centrifugal washes at freezing and room temperature in water (Reproduced from Xie *et al.* [74])

Stable dispersion can also be achieved using the surfactant-free nanoprecipitation by doing a slight concession on sustainability. Indeed, by switching to alcohol-based dispersion such as ethanol or methanol, a good stability dispersion stability can be obtained according to literature.[104,107] By doing so, and using the P3HT:ICBA system, PCE exceeding 4% were achieved using a similar process.[82,104] Enhancing dispersion stability has been studied even more by A. Colsmann's group employing the strategy of permanent or reversible electrostatic stabilisation (PES or RES).[81,106] In both cases, p-doping of the colloidal ink was found to enhance the electrostatic repulsion of the nanoparticles and hence the dispersion stability. In particular, the RES based on the iodine doping method allowed them to reach PCEs of 10.6% using the donor:acceptor blend J71:Y6. However,

the dispersions used in their studies are based on acetonitrile and not water, which here again goes against sustainability.

2.3. Nanoparticle morphology

For organic solar cell applications, a nanoparticle is generally formed of the donor and the acceptor together, leading to composite nanoparticles. The special distribution of these two materials can take many forms, which dictates the morphology of the nanoparticle. However, as it is shown later in the chapter, pure nanoparticles of either the donor or the acceptor have also been used. The performances of organic solar cells are extremely dependent of the active layer morphology as it directly influences the exciton dissociation as well as the charge carriers transport mechanisms. By forming the active layer with nanoparticles, the resulting morphology strongly depends of the initial morphology of the composite nanoparticles. Therefore, this morphology has been often investigated by the community in order to correlate the optical properties of the nanoparticles and the obtained OPV performances. Back in 2004, photoluminescence measurement was the first tool used to determine the morphology of a composite nanoparticle made with F8BT and PFB using the mini-emulsion method.[114] The results have led T. Kietzke and co-workers to describe a nanoparticle with a phase composed almost exclusively of F8BT and another one, more intermixed, with phase-separated PFB and F8BT. Three years later, the same group has reported on a biphasic morphology (Janus) for a PS:PPC-based composite nanoparticle using transmission electron microscopy (TEM), where they ended up extrapolating this finding to the PFB:F8BT nanoparticle system.[115] However, following these results, P. C. Dastoor's group has shown a completely different morphology for these PFB:F8BT nanoparticles and demonstrated that the scanning transmission X-ray microscopy (STXM) technique is capable of mapping conjugated polymers on a sub-20/40 nm length scale.[116] Doing so, they obtained core-shell morphology images for PFB:F8BT nanoparticles. This kind of morphology can exist if one of the two materials (material 1) has a stronger interaction with the aqueous phase during the solvent evaporation. As a result, a low interfacial tension between the material 1 and the aqueous phase would push the material 2 to form a core while the material 1 would form a shell around it. The same group has reported the same core-shell morphology for two other donor/acceptor systems (i.e. P3HT:PC_{61}BM and P3HT:ICBA), again determined

using STXM (**Figure 2-5**). They observed that the P3HT was found to be systematically in the shell of the particle and the fullerene ($PC_{61}BM$ or ICBA) in the core.

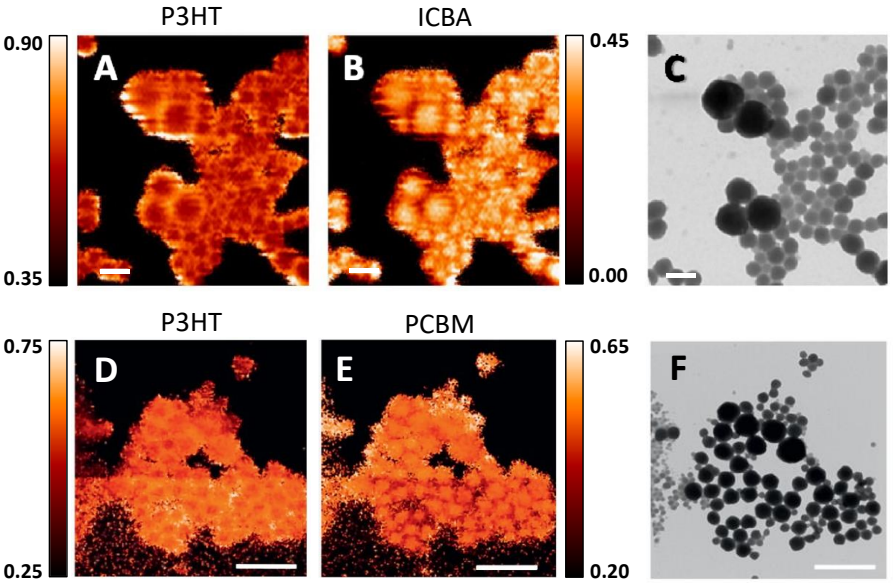

Figure 2-5: (**A**) P3HT and (**B**) ICBA STXM compositional maps for the unannealed P3HT:ICBA NP film and (**C**) the corresponding TEM image (scale bars: 200 nm). (**D**) P3HT and (**E**) $PC_{61}BM$ STXM compositional maps for the unannealed P3HT:$PC_{61}BM$ NP film and (**F**) the corresponding TEM image (scale bars:1 µm). Reproduced from Holmes *et al.* and Ulum *et al.*[117,118]

The opposite distribution, i. e. P3HT in the core and the fullerene in the shell, has also been observed using the nanoprecipitation combined with successive solvent displacements.[96,119] For instance, Chambon *et al.* have precipitated P3HT from a P3HT:$PC_{61}BM$ tetrahydrofuran (THF) solution into dimethyl sulfoxide (DMSO). While the P3HT formed nanoparticles, the $PC_{61}BM$ molecules were still soluble in DMSO. Therefore, a second solvent displacement in water led to the precipitation of $PC_{61}BM$ around the P3HT nanoparticle. This "inverted core-shell" was thus possible with the nanoprecipitation method but arises from a solvent displacement engineering and this morphology is usually not encounter with nanoprecipitation. Indeed, generic rules about the different morphologies obtained from the mini-emulsion and the nanoprecipitation processes have been proposed by K. N. Schwarz and co-workers (**Figure 2-6a**).

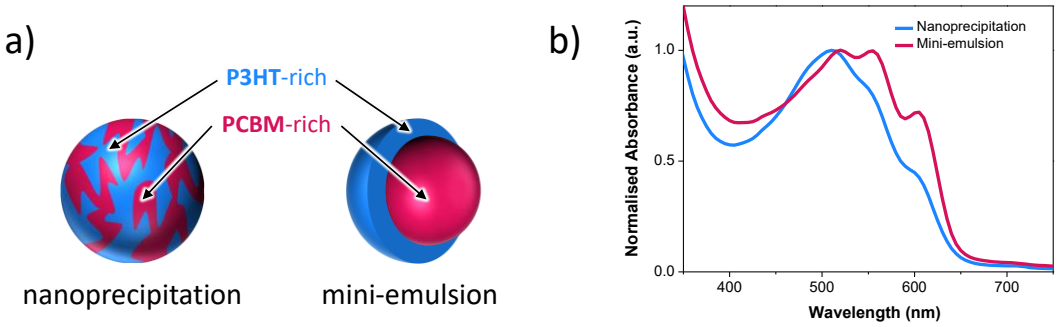

Figure 2-6: Schematic representation of the internal morphology of nanoparticles prepared by nanoprecipitation and mini-emulsion. Redrawn from Schwarz *et al.* work.[120]

In the classical nanoprecipitation method, the solvent displacement (e.g. THF into water) is extremely fast, and does not give time to the donor and the acceptor to arrange themselves and phase separate, hence leading to an intimate morphology. On the other hand, the solvent displacement in the mini-emulsion, that corresponds in that case to the evaporation of the organic phase solvent, takes several hours. Therefore, the role of the different interfacial energies between the organic phase and the aqueous phase is predominant and lead to radial phase separation in the case of the mini-emulsion. This has been well reported by Holmes *et al.* thanks to STXM analysis showing the two type of particles depending of the method used.[113] Through transient absorption spectroscopy, Schwarz *et al.* have illustrated this concept by showing a much more crystalline nature in P3HT:PCBM nanoparticles prepared by mini-emulsion. Whereas P3HT amorphous regions were prevailing over P3HT crystalline regions in P3HT:$PC_{61}BM$ nanoparticles prepared by nanoprecipitation (**Figure 2-6b**). In this regard, they compared the molecular arrangement inside a nanoparticle prepared by mini-emulsion to the arrangement of a film deposited from organic solvents upon thermal treatment. Whereas a more amorphous arrangement is obtained by nanoprecipitation, which is closer to the arrangement obtain in a film deposited from organic solvent without thermal treatment. Therefore, one could think that nanoparticles obtained by mini-emulsion are most likely to have better electronic proprieties due to their crystalline nature. However, the latter might restrain efficient charge collection in OPV cells as it is more difficult to change the initial core-shell morphology with thermal treatment without the formation in some cases of gross phase segregation.[113,121] For instance, the same P3HT:ICBA system prepared either by mini-emulsion or nanoprecipitation exhibits a maximum PCE of 2.5 % or 4.1 % respectively.[104,118]

Concerning the mini-emulsion, this core-shell morphology has been exclusively observed for donor/fullerene systems. This observation was emphasised by M. G. Barr and co-workers to originate from the higher surface energy of the fullerene acceptor compared to that of the donor material.[122] On the other hand, when looking at the new non-fullerene acceptors (NFAs), they present lower surface energies than their fullerene counterparts. As a consequence, the morphology of donor/acceptor nanoparticles is not always acceptor-rich core/donor-rich shell (**Figure 2-7**). Furthermore, as for TQ1:N220, they can even present donor/acceptor intermixed shell. These findings pave the way toward a fine tuning of the morphology of nanoparticles synthesised via mini-emulsions by a careful analysis of surface energies.

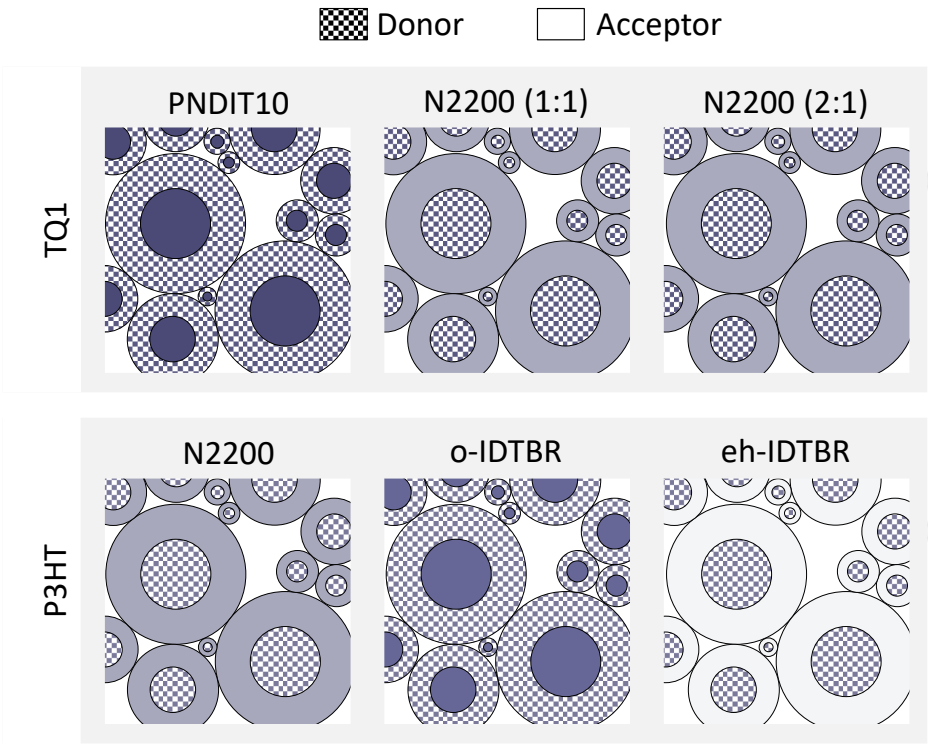

Figure 2-7: Conceptual schematic incorporating core–shell structure observed for different donor–acceptor system (Redrawn from ref [122]).

However, in addition to these core-shell morphologies, other types of morphology have been reported when using the mini-emulsion method as well. It is for instance the case when stabilising the nanoparticles with a different surfactant than SDS. In particular,

the water-soluble thiophene 2-(3-thienyl)-ethyloxy-4-butylsulfonate sodium salt (TEBS) has been reported as a surfactant for the mini-emulsion method (**Figure 2-8**).[97,123,124]

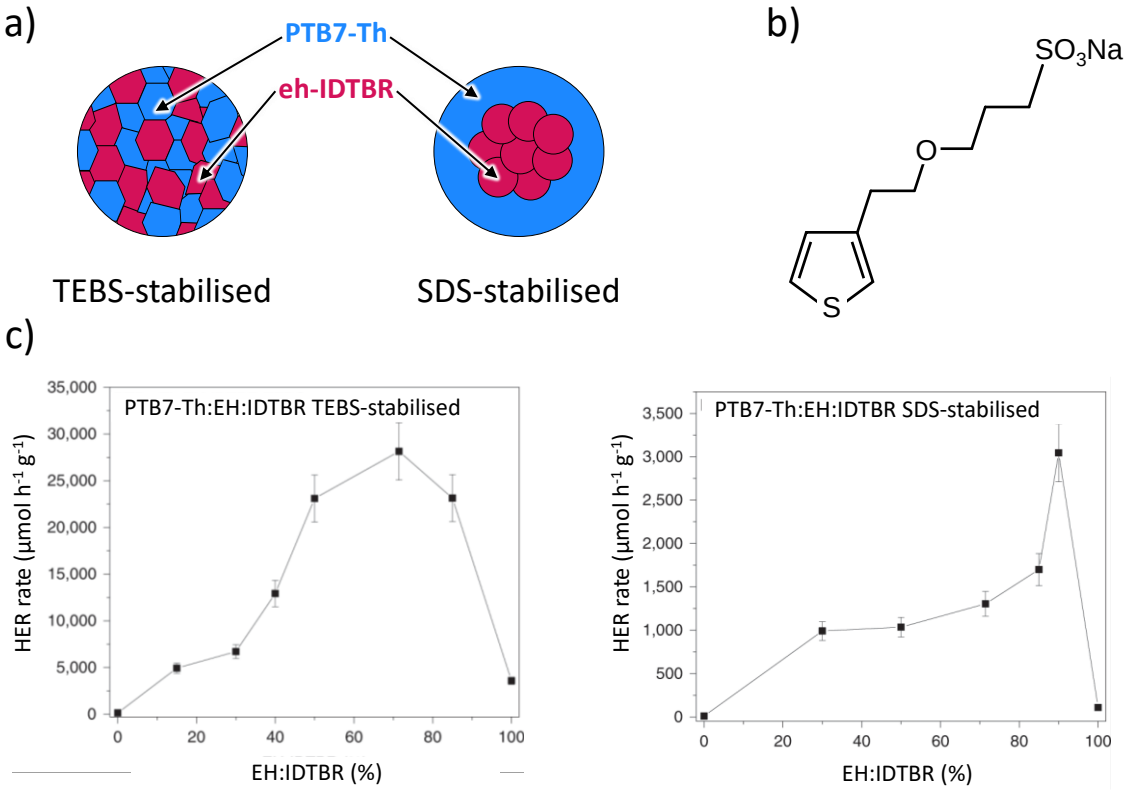

Figure 2-8: (**a**) Schematic representation of the internal morphology of P3HT:$PC_{61}BM$ nanoparticles stabilised by TEBS and by SDS. (Reproduced from Subianto *et al.* [97]). (**b**) Chemical structure of TEBS. (**c**) Average H_2 evolution rates of PTB7-Th/EH-IDTBR nanoparticles formed using TEBS or SDS surfactant over 16 h as a function of blend composition (Reproduced from Kosco *et al.* [123]).

TEBS is the monomer derived from the water-soluble polymer PTEBS.[125] In each case, the authors compare nanoparticles stabilised with SDS and TEBS, and they identify a more intermixed donor/acceptor morphology of the nanoparticles stabilised with TEBS than the those stabilised with SDS (**Figure 2-8a & b**). In the first study, Subianto and co-workers attribute this phenomenon to the better miscibility of TEBS with P3HT compared to SDS because of its thiophene units. From electrochemical characterisation they demonstrate that $PC_{61}BM$ was more present on the surface of TEBS-stabilised P3HT:$PC_{61}BM$ nanoparticles whereas for SDS-stabilised nanoparticles the fullerene is not

detected at the surface which is in accordance with the core-shell morphology already obtained in previous works. Following their study, in 2022 Chowdhury *et al.* have confirmed with STXM analysis the more intimate P3HT:$PC_{61}BM$ internal morphology obtained using TEBS. The resulting difference resulted in a PCE enhancement of about 50% compared to conventional SDS-stabilised nanoparticles. This strategy of surfactant engineering has also been explored with nanoparticles for photocatalysis applications and, more specifically, water-splitting. Based on PTB7-Th:eh-IDTBR nanoparticles, Kosco *et al.* used either SDS or TEBS to form their nanoparticles to probe the hydrogen evolution rate (HER), and studied the morphology with cryo-TEM. They observed that the radial segregation of PTB7-Th or eh-IDTBR within the nanoparticle leading to a core-shell with SDS is no longer seen with TEBS, which instead leads to more intermixed morphology. These observations were linked to surface energy measurements, where they showed that PTB7-Th and eh-IDTBR have similar affinity with TEBS in term of interfacial energy. While with SDS, the interfacial energy between PTB7-Th and SDS was measured to be twice lower than the one between eh-IDTBR and SDS. Thus, the radial segregation was no longer thermodynamically favoured with TEBS. As a result, the observed one order of magnitude increases in the HER, which was attributed to an improved charge extraction due to a more mixed blend obtained with TEBS (**Figure 2-8c**).

More recently, and still based on the mini-emulsion, nanoparticle synthesis engineering has led A. Synytska and co-workers to elaborate nanoparticles presenting a Janus-type morphology.[126,127] It describes a particle symmetric in shape but asymmetric in composition and subsequently in properties. In their studies, the authors do not directly obtain Janus nanoparticles but they convert core-shell nanoparticles into Janus particles. Using the PTB7:$PC_{71}BM$ system, they first obtain a core-shell morphology where again the core is mainly composed of the fullerene material and the shell of the donor polymer. When adding N-methyl-2-pyrrolidone (NMP) in the aqueous dispersion, and due the much higher solubility of PCBM in NMP, the core-shell is etched and allows the formation of a Janus-type NP after removal of NMP (**Figure 2-9a**). Internal morphologies of these NPs were investigated using energy-filtered TEM (EFTEM). Performing photoluminescence measurements, the core-shell nanoparticles were found to be highly fluorescent as compared to the Janus particles, along with a much faster decay rate highlighting a better charge transfer. They also compared the OPV performances and found that the core-shell and Janus nanoparticles-based solar cells performances exhibited a 50% and 15% loss

respectively as compared to the control solar cells made from organic solvent DCB. Furthermore, when switching to PTB7-Th:$PC_{71}BM$, a hero-cell with a PCE of 5.11% was obtained, which was at the time the highest efficiency obtained for a water-based solar cell using mini-emulsion.

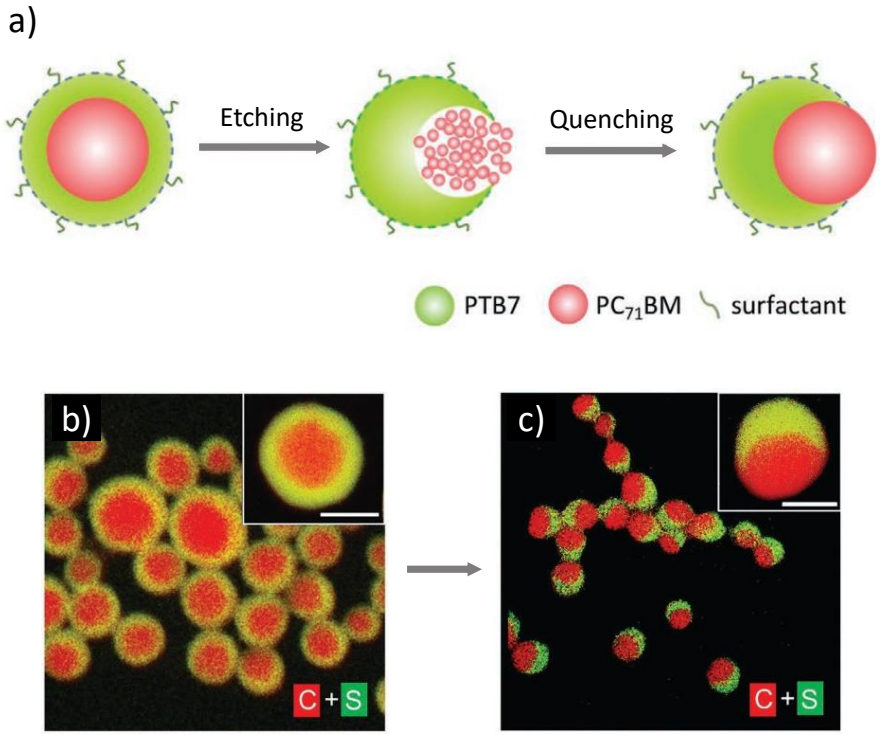

Figure 2-9: (**a**) Conversion of a core-shell nanoparticle into a Janus nanoparticle by solvent etching. (**b**) Color-coded elemental EFTEM maps with chemical mapping of sulfur (green) and carbon (red). Reproduced from Synytska *et al*.[126]

Moreover, it is also possible to obtain Janus morphology while keeping a single step in the mini-emulsion method as shown by Ghazy and co-workers.[128] By changing the initial solvent, from chloroform to a mix of toluene and THF, they enhanced the phase separation between P3HT and $PC_{61}BM$ due to the different solubilities of each materials in the two solvents. Indeed, the solubility of P3HT in THF is higher than the one of $PC_{61}BM$, while $PC_{61}BM$ is more soluble in toluene than P3HT, thus leading to more phase separation. Furthermore, in order to cancelled the radial segregation due to the better affinity of P3HT with the aqueous phase, they drastically increased the SDS concentration leading to a high

SDS coverage on the surface of the nanodroplets. Combining these two strategies, thermodynamically-driven P3HT:$PC_{61}BM$ Janus nanoparticles were obtained.

2.4. Building a nanoparticule active layer

Whatever the morphology of the final nanoparticles, another challenge is to form an active layer from these nanoparticles. It has also been shown that the quality of the film can be highly dependent of the surfactant concentration. Colberts *et al.* monitored the SDS concentration with electrical conductivity and zeta potential measurements. A drop-in conductivity was observed when increasing the dialysis steps as well as the time which is consistent with the removal of SDS. They reported the need to precisely control the dialysis process as dispersions with high conductivity (high concentration of SDS) led to poor film quality with numerous dewetting points. On the other hand, when the dispersions are intensively dialysed, the low SDS concentration of the dispersions increased the formation of aggregates on the deposited films. Turning their attention to the surface tension of the dispersion, Almyahi *et al.* have observed similar results by varying the number of dialysis steps as well as the type of dialysis (crossflow and centrifugal process).[129] They also studied the effect of adding ethanol to their dispersions which was found to enhance the coating quality resulting in an increase of the short circuit current (J_{SC}). This result is in accordance with several other reports and is often associated to closer packing of the nanoparticles leading to lower leakage currents.[130–133] Authors report that this strategy needs to be carefully considered as the addition of ethanol into the dispersion can form aggregates that would lead to dewetting and/or poor film quality.

Up to now, examples of aqueous dispersions deposition has been mainly illustrated through dispersions prepared with the mini-emulsions. Such method is quite convenient as it allows to easily obtain highly concentrated dispersions due to the high solubility of most of the materials in chloroform. On the contrary, the use of THF in the nanoprecipitation method is a limitation to obtain dispersion with high nanoparticles concentration as the solubility limit of most of organic semiconductor in THF is low. This is accentuated for the nanoprecipitation surfactant-free where the formation of aggregation increases at higher concentration. To overcome this limitation, some groups have performed the deposition of their nanoparticles by adopting the spray-coating deposition method.[134] Doing so, Prunet

et al. have obtained layers with thickness of about 100 nm with a high rugosity which was point out to limit device performances. Another strategy is to make successive deposition of low concentrated solution to gradually increase the thickness.[96,113,135]

With their Janus nanoparticles, Synytska *et al.* have adopted a completely different approach to form their active layers without the use of any conventional deposition technique. Close-packed monolayers were built based on the air/liquid interfacial self-assembly. This technique is very interesting as it presents the advantage of not losing any material during the fabrication step. To obtain their films, the nanoparticles are firstly transfer in an alcohol dispersant such as ethanol and butanol, and the resulting dispersion is added on a water surface. Then, the addition of alcohol droplets was found to shrink the sparse nanoparticles (**Figure 2-10**). Preferring a liquid/liquid interface self-assembly (hexane/water), they even increased the film density allowing higher performances when building the organic solar cells thanks to an enhanced absorption and charge transport.

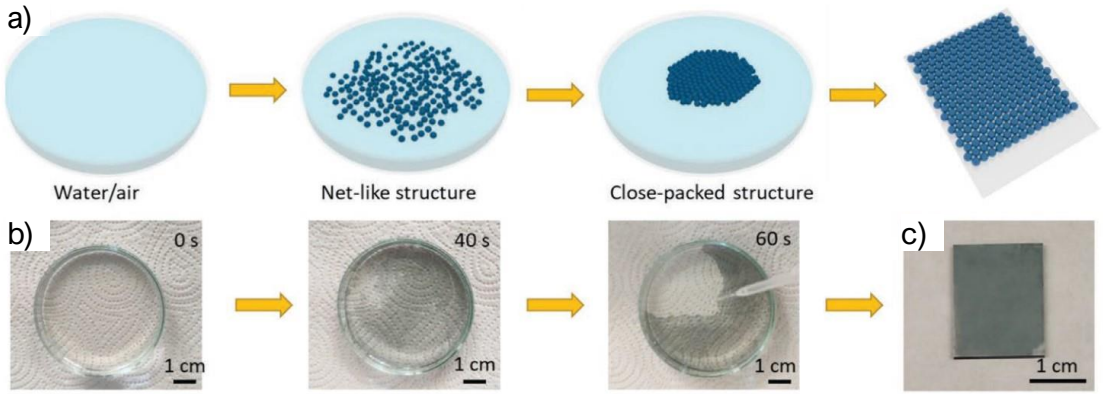

Figure 2-10: (**a**) Schematic of fabrication of hexagonal close-packed nanoparticle films on the water surface and transfer to target substrates. (**b**) Photos of the nanoparticle array, showing the transition from net-like structure to a close-packed structure at air/water interface by dropping butanol onto the water surface and (**c**) of the film transfer on a substrate. Reproduced from Synytska *et al.*[127]

Once the nanoparticulate film is formed, particular care should be given to the treatment of this layer. More specifically, the thermal annealing of the layer is essential and a centre part of many water-based OPV articles.[133,136–138] Holmes *et al.* have synthesised pristine P3HT and PCBM nanoparticles which simply form a two-phase structure when cast

as a layer.[137] Then, they showed how it is possible to switch to a three-phase microstructure, (composed of a pure P3HT phase, pure $PC_{61}BM$ phase and intermixed P3HT/$PC_{61}BM$ phase) by applying the right thermal annealing treatment. The importance of setting the annealing temperature (110 °C) above the glass transition temperature (T_g) of the polymer (80°C) was pointed out in order to generate a three-phase microstructure. Although this temperature is below the T_g of the $PC_{61}BM$ (161°C), the fullerene was still able to diffuse in the amorphous region of the P3HT. As a result, they measured the experimental exciton dissociation efficiency raising from 37% to 64% when switching from a two-phase to a three-phase microstructure. Though an enhanced morphology can be obtained after annealing, the use of pure nanoparticles is generally pointed out to limit performances over composite nanoparticles. For instance, Xie *et al.* have compared core-shell PDPP5T-2:$PC_{71}BM$ nanoparticles with their respective pristine nanoparticles.[138] While halogenated solvent-processed devices still presented a better mobility-lifetime than the two type of nanoparticulate layer, the use of composite nanoparticles with the appropriate treatment favoured the charge collection over the pure particles. The isolated polymer and fullerene domains in the film of pure nanoparticles are insufficiently percolated, which restrict photogenerated polarons from reaching the percolation network. A previous study involving pure nanoparticles has also shown similar trends between pure and blend nanoparticles of PCDTBT:$PC_{71}BM$, where the mixture of pure particles led to poor efficiencies < 0.01% PCE, while the blended particles have better efficiencies (0.70% PCE).[139] Nevertheless, tuning the pure nanoparticles diameter and the ratio between pure P3HT and pure PCBM nanoparticles have reduced the performances gap between active layer of blend and separate nanoparticles. Indeed, Gehan *et al.* showed with conductive AFM measurements that as the ratio of pure P3HT to PCBM nanoparticles increases, the number of hole conducting pathways also increases leading to increased current.[133] As a results, with an optimised ratio, they have succeed to reach a PCE of 1.84% with separate nanoparticles, not so far from the 2.15% PCE obtained with composite nanoparticles. Interestingly, there is no published work that reports on the use of both pure and composite nanoparticles within the same active layer.

As illustrated by Holmes *et al.* with pure nanoparticles[137], the thermal treatment is also highly necessary in order to create pathways between composite nanoparticles and allow a better transport of charge carriers. This has been beautifully illustrated with core-shell nanoparticles where an optimised thermal annealing is creating connections between

each core of the TQ1:$PC_{61}BM$ particles (**Figure 2-11a**).[136] A drying step with a temperature (110 °C) above the T_g of the polymer (100 °C) was found to effectively sinter the particles together, but residual nanoparticulate structure was still clearly visible, which could prevent an efficient charge transport. Therefore, rising this temperature to 140 °C allowed the nanoparticulate film to become mildly blended/smoothed on the surface with no evidence of nanoparticle shape. An additional annealing treatment at 140 °C, that followed the drying treatment at 140 °C, increased the formation of connection pathways between $PC_{71}BM$-rich nanoparticles cores. Such a control of the morphology could drive the OPV performances to increase from a PCE of 0.49% (drying at 110 °C) to 2.10 % (drying and annealing at 140 °C (**Figure 2-11b**).

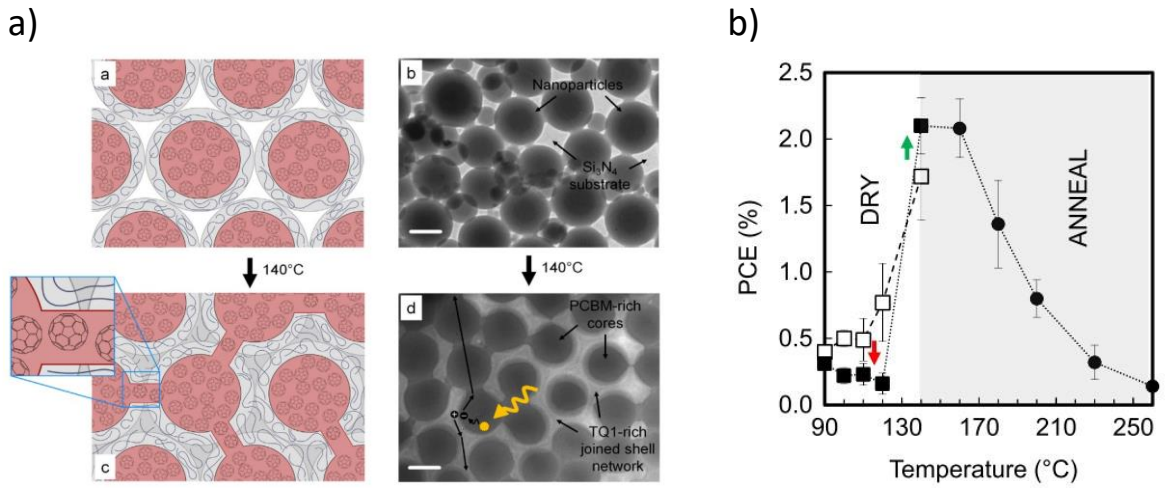

Figure 2-11: (**a**) Schematic and TEM images of TQ1:$PC_{71}BM$ NP film as cast and annealed at 140°C. (**b**) Average PCE of TQ1:$PC_{71}BM$ water-based dried at various temperatures (90-140°C) (open squares); the same devices subsequently annealed at 140°C (closed squares); or dried at a constant temperature of 140°C followed by annealing at various temperatures (140-260°C) (closed circles). Reproduced from Holmes *et al.*[136]

2.5. Conclusions and outline of the thesis

From the fabrication of the organic semiconductor nanoparticles to the deposition of colloidal inks, we have seen that many considerations should be considered to obtain highly efficient OPV devices. And even though plenty of studies have addressed various

aspects, there are still major limitations in water-based OPV. As shown in the previous chapter, there is an almost 10% gap in power conversion efficiency between water-based and chlorinated solvent-based organic solar cells. Nevertheless, based on the recent results and seeing the efficiency continuously getting higher, one can hope to decrease this gap by improving our understandings and control of the nanoparticle formation, deposition and the resulting film processing (**Figure 2-12**).

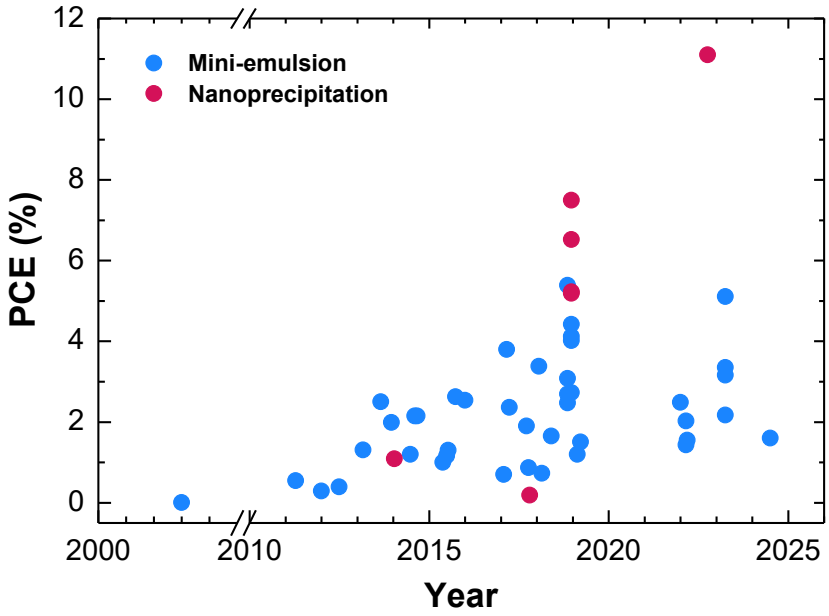

Figure 2-12: Evolution of the PCE obtained from water-based organic solar cells prepared via different method over the years.

The results from J. Kosco and co-workers using the mini-emulsion method and still ending up with intermixed nanoparticles are encouraging in the idea that mini-emulsion does not necessary lead to a core-shell morphology. The control and the investigation of the morphology of nanoparticles prepared via mini-emulsion will hence be at the heart of the present work. Furthermore, except for few recent studies in the literature, the development of water-based OPV is not really incorporating high efficiency materials. This is particularly true for studies based on the mini-emulsion technique, where only Xie *et al.* have reported on the use of NFAs (o-IDTBR and ITIC) allowing them to reach PCEs above 4%. Similar observation can be made on the donor side where the systematic use of

efficient polymer such as PCE10, PBQ-QF or PTB7-Th for nanoparticles based on the mini-emulsion has led to the highest efficiencies reported so far. The use of state-of-the-art materials, *i. e.* champions in organic solvent-based OPV, is quite obviously going to bring water-based OPV to higher efficiencies, which is in itself interesting. However, as these new materials are tested out in NP-based approaches, new insights must be gained on their structure-properties relationships.

Therefore, this thesis aims at investigating high efficiency systems for water-processed OPV using the mini-emulsion by focusing our attention on the internal morphology. Overall, the gap between the performances of these more sustainable devices and the control ones, made with chlorinated solvents, is the principal figure of merit we need to consider. In addition, characterisation techniques such as STXM and cryo-TEM will constitute powerful tools to bring light onto the nanoparticle's internal morphology. It is obvious that the charge transport in a NP film is impacted by the overall morphology of the film and how thermal treatment affects it. Yet, this charge transport is less understood at the nanoparticle scale when it is subject to morphological changes. To explore this propriety, devices based on nano gap electrodes will also be developed along with a method to precisely insert nanoparticles in this submicrometric gap.

Based on these objectives, the present thesis is constituted of four result chapters including the following contents:

Chapter 3: One of the challenges arising from making water-based organic solar cells is to successfully achieve the formation of a nanoparticulate layer. Therefore, in addition to establishing our process for the synthesis of nanoparticles, a careful optimisation of the deposition process will be carried out. Subsequently, using the well-known P3HT:$PC_{61}BM$ system, solar cells will be built and characterised and the impact of thermal treatment will be investigated. Furthermore, this chapter will explore the potential advantages of incorporating pure nanoparticles among a matrix of composite nanoparticles.

Chapter 4: An attempt to control the morphology of composite nanoparticles prepared with the mini-emulsion method will be reported. As the surface energy has been shown to have a significant impact on the morphology, this strategy will be used throughout this chapter. More specifically, the interfacial energy, between the donor and the acceptor

and its impact on OPV performances are assessed for two different systems: PTQ10:Y6 and PTQ10:$PC_{61}BM$ having respectively a low and high interfacial energy. The morphology of the nanoparticles is examined with STXM and further investigation and optimisation are carried out on the newly developed Y6-based nanoparticles. The stability of water-based devices is also probed and compared to the control devices fabricated from chloroform solution.

Chapter 5: The correlation of the morphology with interfacial energies will be further examined with various PTQ10-based nanoparticle systems. To this end, the NFAs IDIC and Y12 are associated with the donor polymer and the resulting morphology is explored as well as the impact on the nanoparticule process and the resulting OPV performances. By studying Y12, it will open the question about the impact of the side chains length on the nanoparticle morphology. Then, the influence of side chains is extended to the new donor polymer FO6-T, developed by collaborators at Imperial College of London, and its derivatives having different alkyl chains length.

Chapter 6: The development of nano-junction devices is carried out to explore the charge transport in nanoparticles. An elegant technique to trap nanoparticles between the electrodes with nanometric gap is proposed. This technique is based on the dielectrophoresis force which applies on particles in a dielectric medium upon an alternative electric field. Using an optimised architecture, the transport of positively charge carriers of composite nanoparticles based on P3HT:eh-IDTBR and P3HT:o-IDTBR will be examined. The aim of this chapter will be to establish a correlation between the different in surface energy of these two systems and the extracted hole mobilities.

Chapter 3

From aqueous colloidal inks to organic solar cells

3.1. Introduction

This chapter's aim is to report the work done during the beginning of this PhD to earn a relative ability to control the fabrication of organic solar cell processed from water-based inks. This task is essential as it is necessary to have homogenous thin film formation to be able to characterise correctly the devices. Herein, from the elaboration of an aqueous dispersion to its deposition, the experimental details are discussed to underline the importance of the fabrication steps. From what we have seen in the literature, various ways are reported for the synthesis of colloidal inks used to fabricate water-based cells. It is divided into two main categories, nanoprecipitation and mini-emulsion, but includes also diverse sub-details which vary for one report to another. It is therefore important to control and understand each step before the deposition. Undoubtedly as important as its formulation, getting an optimised coating from an organic semiconductor nanoparticles water-based ink required a lot of care for many reasons. Therefore, this crucial step is also detailed in this section as it was the key to obtain controlled-coating and reliable devices. The well-known donor:acceptor system P3HT:$PC_{61}BM$ has been chosen as a benchmark to develop the process. In this chapter, I will mainly use composite nanoparticles from a donor and an acceptor blend, which is the standard way to make nanoparticulate organic solar cells. Moreover, I will present the results of devices made with the addition of pure nanoparticles which could be beneficial to create charge transport pathways. Therefore, this chapter also presents the efforts to verify or discard this assumption.

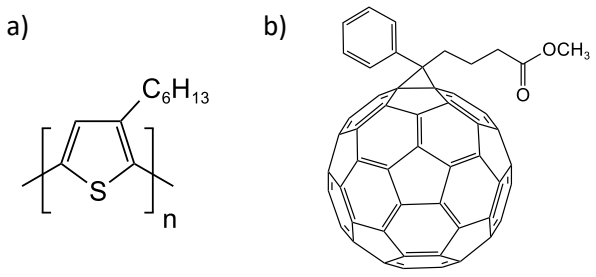

Figure 3-1: Chemical structure of (**a**) poly(3-hexylthiophene) (P3HT) (**b**) [6,6]-Phenyl-C_{61}-butyric acid methyl ester ($PC_{61}BM$)

3.2. Processing organic semiconductor nanoparticles inks

In this section, aqueous colloidal dispersions of P3HT:$PC_{61}BM$ (**Figure 3-1**) are fabricated using the mini-emulsion method described earlier. Three different type of nanoparticles are synthesised, two dispersion containing pure nanoparticles (pNPs) of each material, namely P3HT and $PC_{61}BM$, and a dispersion of composite nanoparticles (cNPs) composed by a blend of P3HT:$PC_{61}BM$ having a donor:acceptor ratio of [1:1].

3.2.1 Dispersions formulation

The three type of nanoparticles were prepared by the mini-emulsion method elaborate by Landfester *et al.*[140]. For the organic phase, 25 mg ml^{-1} of donor:acceptor (e.g. P3HT:$PC_{61}BM$ cNPs wt% of 1:1) mixture, or 25 mg ml^{-1} of pure donor or acceptor (e.g. P3HT pNPs or $PC_{61}BM$ pNPs) was first dissolved in chloroform stirred for 2 h at 65 °C in a nitrogen-filled glovebox. Aqueous phase was obtained by dissolving 5 mg ml^{-1} (17 mM) of surfactant (e.g. SDS) in deionised (D.I.) water and stirred for 30 min at room temperature. We note that the SDS concentration is above the critical micelle concentration (CMC) of SDS in water which is 0.008 mol L^{-1}. The choice of having a concentration slightly above de CMC was made to minimise the amount of SDS as low as possible without compromising the emulsion formation and electronic transport due to excessive amount of SDS in the final active layer. A macro-emulsion was then obtained by adding the organic phase into the aqueous phase (1:5 volume ratio) and stirred for 1 h at room temperature or at 40 °C (1000 rpm). Subsequently, the mini-emulsion dispersion was formed by sonicating the macro-emulsion in an ice-water bath for 2 min. Concerning the sonification power, as well as the macro-emulsion temperature, these parameters have been optimised to target the smallest nanoparticule diameter and the results are shown in **Figure 3-2**.[139] Once the sonification done, chloroform evaporation was done by stirring the mini-emulsion for a minimum of 3 h at 65 °C. Finally, in order to eliminate the excess of surfactant and concentrate the inks at 60 mg ml, centrifugal step was carried out by using centrifuge filter (cut-off 100 kDa). Four centrifugation cycles were done at 2200 rpm for 9 min. The retentate was raised to 15 ml with D.I. water between each step. The parameters of the centrifugal

last cycle were adjusted in order to obtain the desire concentration. Once the two dispersions of pNPs were done, the two were mix together to reach a final wt% of 1:1.

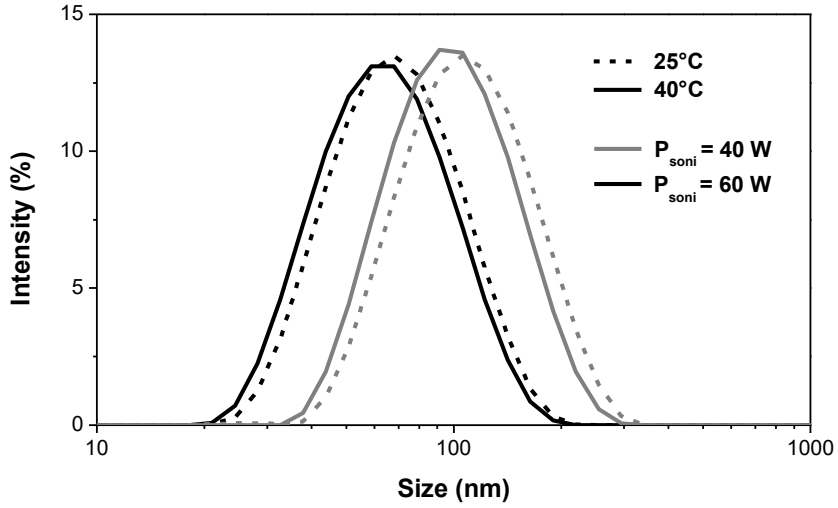

Figure 3-2: DLS particle size distributions of P3HT:$PC_{61}BM$ cNPs dispersions fabricated with varying temperature during formation of the macro-emulsion and sonification power.

Table 3-1: Particle diameters from DLS measurements for P3HT:$PC_{61}BM$ cNPs fabricated with varying temperature during formation of the macro-emulsion and sonification power.

Power (W)	Macro-emulsion Temperature (°C)	Mean diameter (nm)
40	25°C	116 ± 40
	40°C	105 ± 40
60	25°C	74 ± 30
	40°C	69 ± 30

From **Table 3-1**, we can observe a large influence of the sonification power on the nanoparticle diameter. With only a slight increase of the power by 20 W, the nanoparticle diameter decreases from 116 nm to 74 nm when forming the macro-emulsion at room temperature (25°C), and from 105 nm to 69 nm by setting the temperature at 40 °C during the macro-emulsion. The decrease of the diameter when having the temperature set at 40 °C can be due to a better macro-emulsion formation which results in smaller macroscopic organic phase droplets due to a decrease of the chloroform density at 40°C. These results were obtained with P3HT:$PC_{61}BM$ cNPs, while P3HT pNPs and $PC_{61}BM$ pNPs

are showing an overall higher diameter for the same mini-emulsion process parameters, 100 ± 30 nm and 78 ± 40 nm respectively.

Zeta potential measurements were also performed after each cycle to quantify the removal of SDS (**Figure 3-3**). The zeta potential underwent a small decrease from 49 mV to 42 mV. The final zeta potential shows that electrostatic repulsive forces are high enough to prevent aggregation[141]. Nevertheless, the washing remains essential to remove excess free surfactants in the dispersion. It is worth mentioning that zeta deviation for each cycle is large (± 40% of the average zeta potential) and it is thus not easy to extract reliable information from this measurement[142]. Since charges are photo-generated upon the absorption of the 633 nm wavelength of the probe laser, the measurement can be affected as the potential around the nanoparticles is modified.

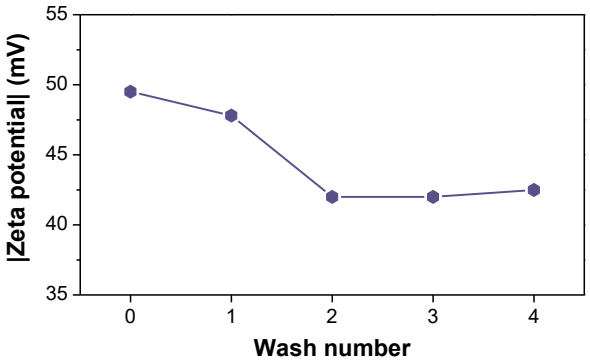

Figure 3-3: Zeta potential of P3HT:PC_{61}BM cNPs dispersions during centrifugal washes.

First, the two final dispersions, namely pure P3HT:PC_{61}BM NPs (mixture of P3HT pNPs and PC61BM pNPs) and composite P3HT:PC_{61}BM NPs, are characterised using UV-visible absorbance spectroscopy as well as photoluminescence spectroscopy (**Figure 3-4**). For both systems, we note a decrease of the PC_{61}BM signature between 300 and 450 nm after centrifugal washing. A similar observation in ethanol has been made when reducing the dispersion volume of P3HT:fullerene nanoparticles, leading to a severe fullerene sedimentation and therefore a decrease in the absorbance[108]. However, as the reduction volume here is different (centrifugal dialysis and not solvent evaporation), another

possibility is a loss of $PC_{61}BM$ through the dialysis filter as a molecule of $PC_{61}BM$ could easily pass through a 100 kDa cut-off filter if the latter did not participate to the formation of the nanoparticles.

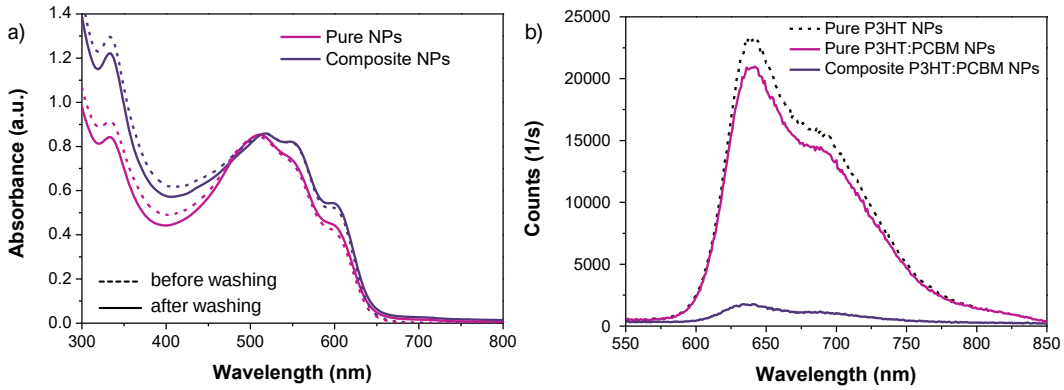

Figure 3-4: (**a**) UV-visible absorption spectra of P3HT:$PC_{61}BM$ pure nanoparticles and composite nanoparticles dispersions before and after washing. (**b**) Photoluminescence emission of P3HT pNPs, P3HT:$PC_{61}BM$ pure nanoparticles and composite nanoparticles dispersions excited at 514 nm. (dispersions concentration = 0.06 mg ml^{-1})

Looking now in the P3HT region, the composite nanoparticles present a typical vibronic peaks associated with interchain order in the P3HT, resulting from π conjugation and π-π stacking of the P3HT backbone[143]. This observation is consistent with P3HT based-nanoparticles obtained with mini-emulsion method as materials have time to arrange, and behave like an already organised thin film deposited from organic solvent (i.e. chlorobenzene)[117]. For the dispersion of pure P3HT and $PC_{61}BM$ nanoparticles, the spectra indicate a signature similar to what can be found using the nanoprecipitation, which suggest that ordering and aggregation of P3HT is less important for larger particles. For both colloidal nanoparticle dispersions, photoluminescence emission spectra feature the characteristic P3HT 0 – 0 and vibronic 0 – 1 transitions (at 640 nm and 700 nm respectively)[144]. However, the quenching is much more important (92 %), for composite nanoparticles as compared to pure particles, indicating a close proximity between the donor and the acceptor inside a composite nanoparticle. The little quenching observed for pure P3HT:$PC_{61}BM$ nanoparticles is not due to a charge separation as the donor NP and the acceptor NP are not in contact, but to the contribution of PCBM in the absorbance at 510 nm, which means that less P3HT was photo-excited during the measurement.

3.3. Processing thin-films from organic semiconductor nanoparticles inks

When it comes to processing an organic solar cell from an aqueous dispersion, a major challenge concerns the deposition of the organic semiconductor nanoparticles ink. Indeed, for a good coating, some element should be considered. First, water has a bad wettability with most of the layer onto which the active layer needs to be (ZnO, PEDOT:PSS, PEDINO) due to their hydrophobicity. As observed in the literature, few are the studies that report the precise optimisation of the nanoparticule thin film formation.[130,131,145] Therefore, the development of this process is discussed in the following section. Furthermore, care should be addressed whereas this air processing can impact the properties of the active layer. For instance, Gehan *et al.* have shown an increase in the carrier concentration in the dark in P3HT:$PC_{61}BM$ nanoparticles-based solar cells due to doping effect, which could explain the loss in V_{OC} that they encounter in their work[146]. The use of a direct architecture could increase this effect as charge trapping at the PEDOT:PSS/polymer interface might occurs. Therefore, the choice has been made to work with the inverted architecture, without PEDOT-PSS, in the present work. Before fabricating the OPV devices, optimising the film deposition is essential to form a homogeneous dense film (100-200 nm) in order to have a good reproducibility, a maximum absorption and no leakage current.

3.3.1 Spin coating deposition

The spin coating deposition was the main technique used during this work to form the active layer. At a laboratory scale, this is one of the most spread method in order to optimise a new process or new systems by doing a large parameter screening (thickness, D:A ratios, annealing temperatures…). This technique is based on the rotation of a substrate onto which a solution is dropped. The coating is form through three steps: dispense and spread, spinning and solvent drying. From here, two main way are possible. Either the drop of the solution is done before the rotation of the sample (static dispenses) or during the rotation (dynamic dispense). For solutions made with low boiling point solvent such as chloroform, dynamic dispense is often preferred as the solvent has less time to evaporate before being spread off, while solution based on chlorobenzene are often dispensed before

spinning the substrate. Water has a relatively high boiling point (100 °C), so the static dispense was the first method that has been explored.

Deposition tests were first done on glass substrates by setting the spin speed at 3000 rpm for 60 sec. As mentioned previously, it is quite difficult to obtain a large volume of the dispersion if we want it highly concentrated. Therefore, the use of a 20mg ml^{-1} concentrated dispersion was used in the beginning. UV-O_3 treatment allowing a better wettability of the dispersion thanks to the generation of hydroxyl groups onto the surface was used prior to the deposition of the water-based dispersion. The contact angle with water decreases from 40° to 0° after treatment, showing the complete wettability of the dispersion (**Figure 3-5**). As a result, the homogeneity of the layer was improved with respect to the active layers deposited on non-treated substrates (**Figure 3-6a** et **b**). However, although homogeneous, extremely thin films were obtained (~ 40 nm) as shown in **Figure 3-6b**. Only the combination of highly concentrated dispersion (60 mg ml^{-1}) and the later surface treatment was enough to obtain a homogenous and thick coating (**Figure** 3-6**c**).

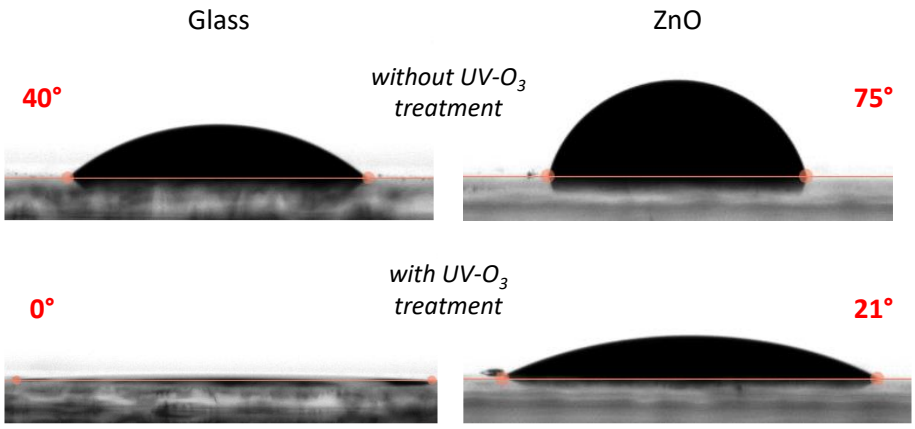

Figure 3-5: Goniometer pictures of contact angles and their values in red of the P3HT:$PC_{61}BM$ nanoparticles dispersion (60 mg ml^{-1}) on a glass (left column) and ZnO (Right column) without (top) and with UV-0_3 treatment (bottom).

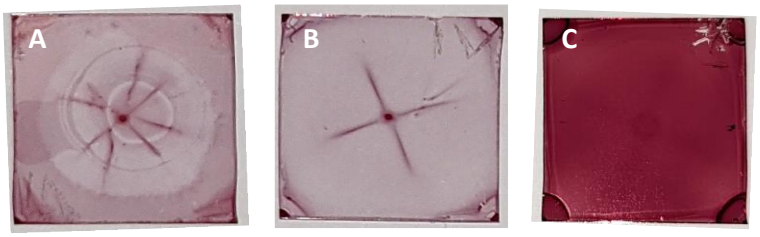

Figure 3-6: Macroscopic images of P3HT:$PC_{61}BM$ *np-BHJ* spin coated with a 20 mg ml^{-1} concentrated dispersion onto glass **A**) without and **B**) with UV-O_3 treatment and **C**) with a 60 mg ml^{-1} concentrated dispersion onto glass with UV-O_3 treatment (static dispense). 40 µl was the volume dispense for each coating.

Moving to a solar cell architecture, the actual layer onto which the colloidal dispersion has to be coated to build an inverted configuration is the ZnO layer. Here again, the UV-O_3 treatment was necessary to enhance the wettability with water, from an angle of 75 ° to 21 ° after treatment (**Figure 3-5**). However, due to the higher surface tension of the ZnO as compared to glass, even after UV-O_3 treatment, the coating over the whole surface was not total when using 40 µl as dispense volume. As a consequence, a larger volume of 80µl had to be used to favour the covering. However, using such large volume led to a large waste of materials and the covering was too inhomogeneous for reliable device batches (**Figure 3-7c**).

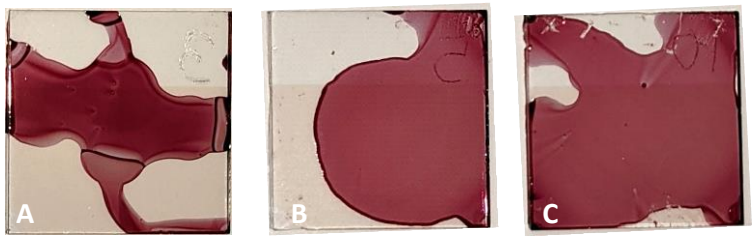

Figure 3-7: Macroscopic images of P3HT:$PC_{61}BM$ np-BHJ spin coated with 50µl of a 60 mg ml^{-1} concentrated dispersion onto ZnO **A**) without and **B**) with UV-O_3 treatment and **C**) with 80µl of a 60 mg ml^{-1} concentrated dispersion onto ZnO with UV-O_3 treatment (static dispense).

In order to save some dispersion volume, and thus the active materials, the dynamic dispense was used, while keeping the UV-O_3 treatment. With only a low dispense volume (20 µl), the coating was greatly improved in term of surface coverage. To help the saving,

10 µl was used as dispense volume, but the surface coverage was found to be deteriorate (**Figure 3-8**). Furthermore, filtration of the dispersion through a syringe filter is also essential as the stability of nanoparticles is quickly compromised by washing cycles, resulting in irreversible aggregation. Indeed, as shown in **Figure 3-9,** the density of dewetting points due to micro aggregates is greatly reduced after filtration. Here again, the dynamic dispense enhance the coating by showing less aggregates as compared to static dispense even after filtration.

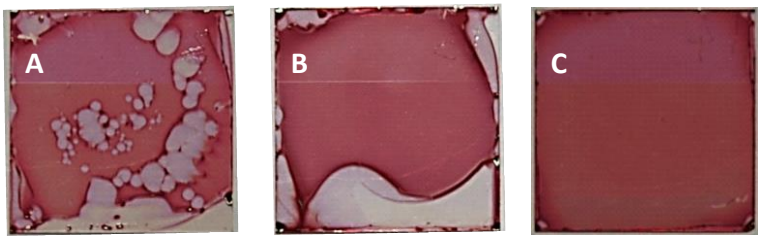

Figure 3-8: Macroscopic images of P3HT:$PC_{61}BM$ np-BHJ spin coated with 10µl of a 60 mg ml^{-1} concentrated dispersion onto ZnO: **A**) without and **B**) with UV-O_3 treatment and **C**) with 20 µl of a 60 mg ml^{-1} concentrated dispersion onto ZnO with UV-O_3 treatment (dynamic dispense).

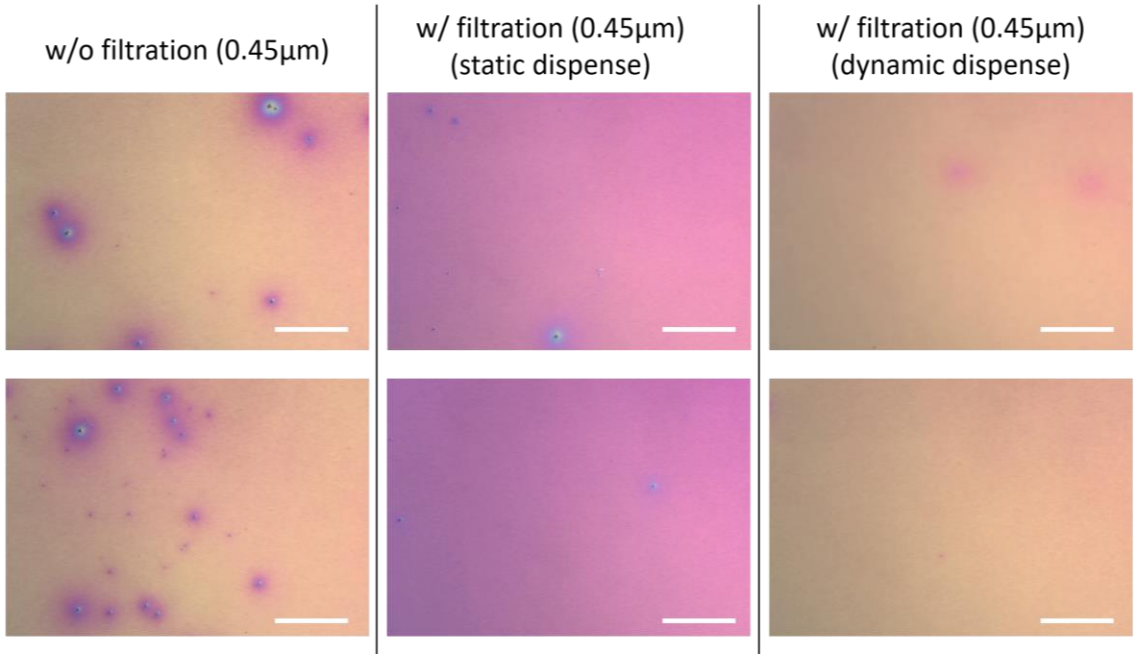

Figure 3-9: Optical microscopic images of P3HT:$PC_{61}BM$ *np-BHJ* films made from non-filtrated and filtrated dispersion using static or dynamic dispense. (Images for each condition have been chosen to be as representative of the overall coating aspect). All scale bars are 50 µm.

Another important improvement in coating quality was developed through the modification of the pipette tip. Indeed, we observed a major difference when enlarging the dispensing spot diameter (wide bore). Widening the pipette tip when dispensing the dispersion shows a better coating repeatability over a large devices batch. In fact, even if the previous optimisation enables correct reproducibility, large dewetting spots and large aggregations unsystematically appeared during a batch process. This might be explained by the sensitivity of the process upon variations in manipulation by the operator such as speed of dispersion dispense, distance from the tip to the substrate or angle of the tip relative to the substrate when dispensing. Changing the tip diameter results in less aggregates formation (**Figure 3-10**).

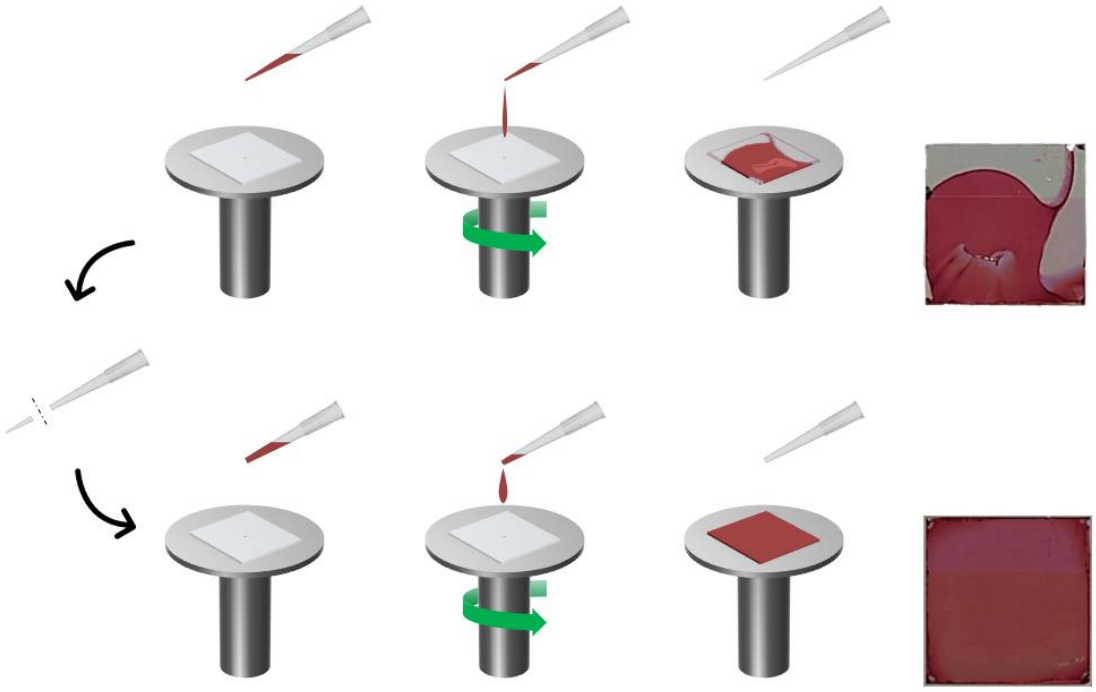

Figure 3-10: Schematic representation of the spin-coating process using two type of pipette tip and resulting deposited film.

3.3.2 Additive for coating optimisation

We have seen that the concentration of the dispersion is a critical parameter to consider to achieve a homogenous and thick layer with minimum of dewetting points.

Nevertheless, high concentrated dispersions (> 60 mg ml^{-1}) are not really economically viable as compare to a process based on organic solvents. To obtain a similar thickness, and better coating, the organic solvent-based solutions are more than half less concentrated that the aqueous dispersions, generally around 20 mg ml^{-1}. Sustainability requirements are mainly based on the environmental impact of a technology, but the cost is also as much important in these requirements. Therefore, an effort needs to be done to decrease the concentration of the aqueous ink, allowing the use of the same amount of active material than organic solvent-based solutions. Several studies have previously shown that adding an inert cost-effective insulating polymer to the donor:acceptor bulk heterojunction allows easier processing and more importantly get rid of dewetting points in the active layer[147]. Such additive can be added up to 50 wt.% without drastically decreasing the OPV performances[148]. In our case, poly(1-vinyl-1,2,4-triazole) (PVT) (**Figure 3-11**) has been used to solve the dewetting issue and increase the thickness of the film even at low dispersions concentration. This non-toxic polymer, biocompatible, thermally stable and easily soluble in water has been reported as a dielectric in OFET[149]. Various wt.% of PVT have been added to a P3HT:$PC_{61}BM$ dispersion while keeping the active material concentration at 20 mg ml^{-1}. Even for the highest PVT concentration (40wt.%), no impact on the optical properties of the ink has been observed (**Figure 3-11a**).

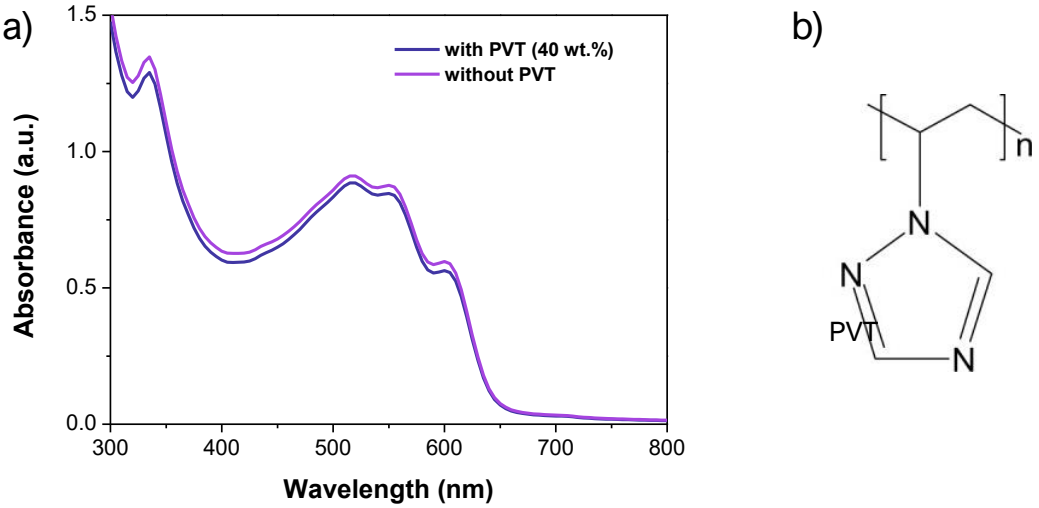

Figure 3-11: (a) UV-visible absorbance spectra of the P3HT:$PC_{61}BM$ nanoparticles dispersion without PVT and with 40wt.% of PVT. (dispersions concentration = 0.06 mg ml^{-1}) (b) Chemical structure of poly(1-vinyl-1,2,4-triazole) (PVT)

Films have been formed following the optimised deposition protocol developed previously (UV-O_3 treatment for 20 min and spin speed at 3000 rpm for 60 sec with thermal annealing treatment of 90 °C during 5 min) and an inverted architecture was used to fabricate organic solar cells with the following architecture (**Figure 3-12**): ITO (150 nm) – ZnO (40 nm) – P3HT:$PC_{61}BM$ *np-BHJ*:PVT (44 – 100 nm) – MoO_x (8 nm) – Ag (80 nm). More details of the organic solar cell fabrication process can be found in **Methods.**

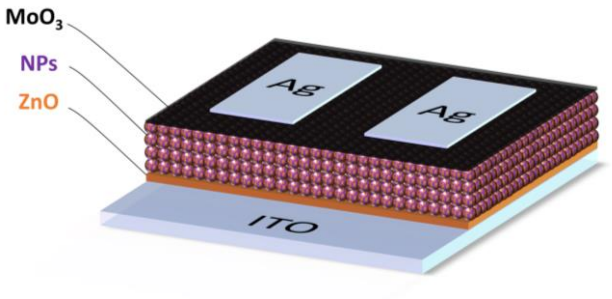

Figure 3-12: Schematic representation of organic photovoltaic devices fabricated from water-based colloidal dispersions

---

Without any PVT addition in the colloidal ink, ultra-thin layer of around 44 nm obtained have been obtained from a 20 mg ml^{-1} dispersion (**Figure 3-13a**). For a P3HT:$PC_{61}BM$-based active layer, such a thin thickness cannot absorbed enough light as the typical optimal thickness for this system is between 75 nm and 100 nm[40],[150]. Furthermore, having nanoparticle with a diameter of around 60 nm forming such a thin layer creates important leakage current in the order of magnitude of 10 mA cm^{-2} due to possible inter-particle spacing and/or pinholes. Adding 10wt.% of PVT already increase the thickness to 65 nm, and up to 113 nm by incorporate 40wt.% of PVT. An increase of the thickness was the major target here, as the dark current density is proportionally decreased which often favour the overall performances (**Figure 3-13b**).[151] Here, an addition of 10wt.% of PVT increases the shunt resistance of more than one order of magnitude (0.30 to 5.99 kΩ), and up to 3 order of magnitude after adding 40 wt.% (257.11 kΩ).

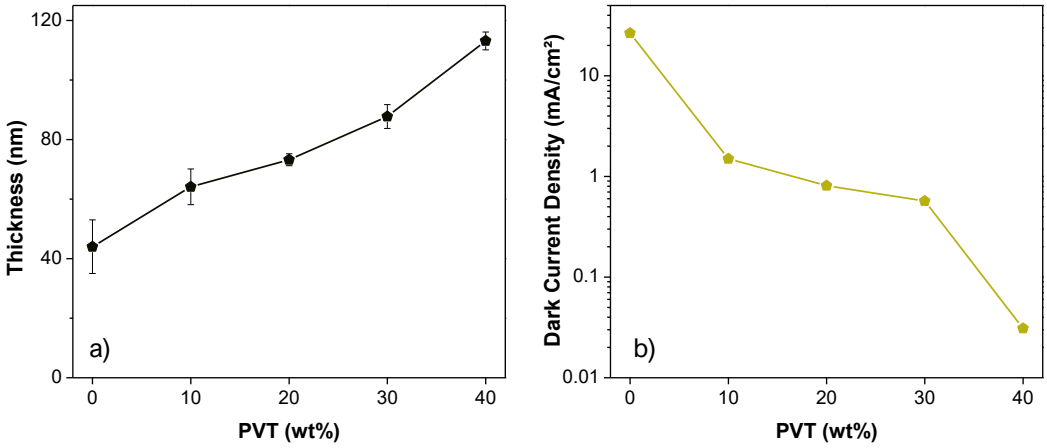

Figure 3-13: (**a**) Dependence of the P3HT:$PC_{61}BM$ *np-BHJ* layer thickness with different PVT wt.%. (**b**) Current density measured in darkness at −0.9 V for P3HT:$PC_{61}BM$ np-BHJ devices from a 20 mg ml^{-1} concentrated dispersion with different PVT wt.%

An addition of 10 wt.% PVT gave the optimal performances, reaching twice the PCE that is obtained without PVT, 0.31 % and 0.15 % respectively (**Table 3-2** & **Figure 3-14**). However, further addition of PVT does not improve the overall performances of the device. Despite continuously decreasing the dark current density, which can be linked to the increase of the V_{OC}, J_{SC} and FF gradually decrease down to 0.1 mA cm^{-2} and 0.24 respectively for 40wt.% of PVT. In the case of a nanoparticulate film, these losses might be explained by the difficulty for the free charges in the nanoparticles to find transport pathways as the PVT progressively form a barrier between each particle. Such effect cannot be seen for a classic bulk-heterojunction having an insulating polymer third component, due to a more intermixed morphology allowing the presence of good transport pathway even at high insulating polymer concentration (50 wt.%).[152]

Table 3-2: Average OPV performances of P3HT:$PC_{61}BM$ np-BHJ devices fabricated from a 20mg ml^{-1} concentrated dispersion of composite nanoparticles with different PVT wt.%

wt.%$_{PVT}$	R_{shunt} (kΩ)	V_{OC} (mV)	J_{SC} (mA cm^{-2})	FF	PCE (%)
0 %	0.30 ± 0.11	96 ± 24	4.80 ± 0.19	0.31 ± 0.02	0.15 ± 0.05
10 %	5.99 ± 0.99	278 ± 9	2.73 ± 0.09	0.41 ± 0.0.	0.31 ± 0.01
20 %	9.54 ± 1.63	321 ± 13	1.99 ± 0.2	0.40 ± 0.00	0.26 ± 0.01
30 %	15.13 ± 2.19	329 ± 15	1.02 ± 0.08	0.35 ± 0.01	0.12 ± 0.01
40 %	257.11 ± 44.15	381 ± 37	0.10 ± 0.00	0.24 ± 0.02	0.01 ± 0.00

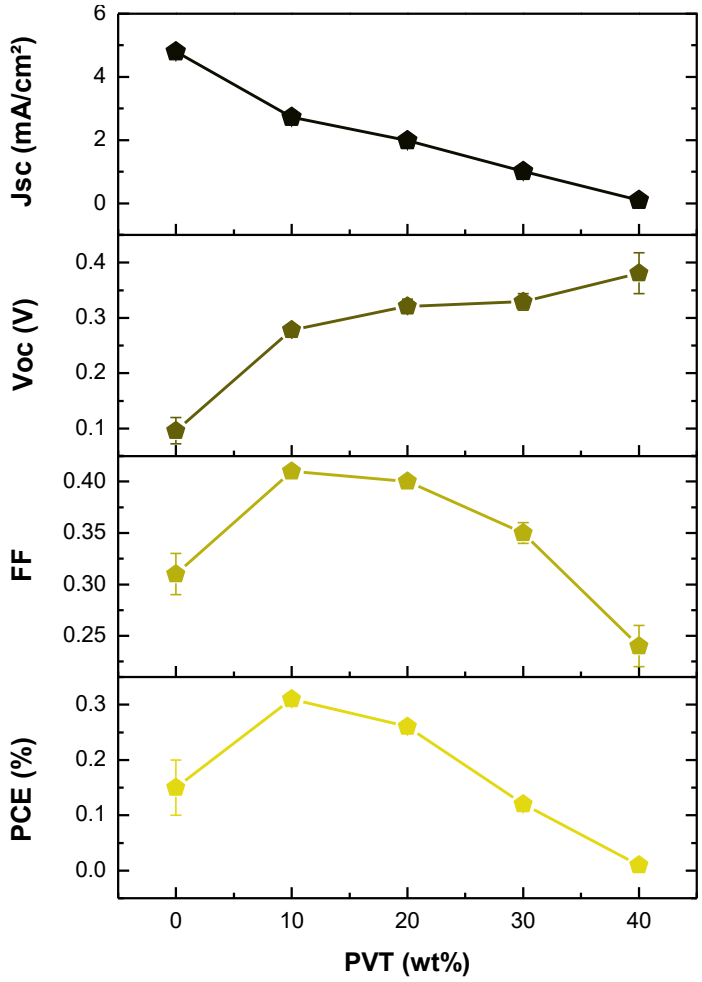

Figure 3-14: OPV performances of P3HT:$PC_{61}BM$ np-BHJ devices fabricated from a 20 mg ml^{-1} concentrated dispersion with different PVT wt.%.

While the method uses in the present section did not shown efficient results, it is highlighting the capability of additives to increase the performances obtained from low concentration aqueous dispersions. More efforts have to be done toward decreasing the concentration to match the sustainability requirements. While it would slightly move the process from its "eco-friendly" nature, the addition of a more volatile solvent such as ethanol might be a possible way to explore. Howse *et al.* have previously shown the formation of holes when spin-coating a low concentration with a low volatility dispersion (water) by the occurrence of capillary drying fronts. By tuning the volatility towards an intermediate value between that of water and ethanol, ordering occurs predominantly via shear forces which prevents the hole formation.[153]

3.3.3 Bar coating deposition

This work, along with many scientific productions in the organic photovoltaic community, is dedicated to giving keys to move the OPV technology toward the industrial world with large area OPV cells using sustainable processes. With this in mind, it was relevant to explore a process that is compatible with the upscaling and to contribute to the so-called "lab-to-fab" development. The spin-coating technique does not allow this development due to several reasons: incompatibility with the R2R process, important waste of the solution, or dispersion in our case, during the spin (> 90 %). Among the different deposition processes suitable for this development, we chose to start with the blade-coating. This method employs a blade or a bar coater having a unidirectional motion on a substrate (**Figure 3-15**).

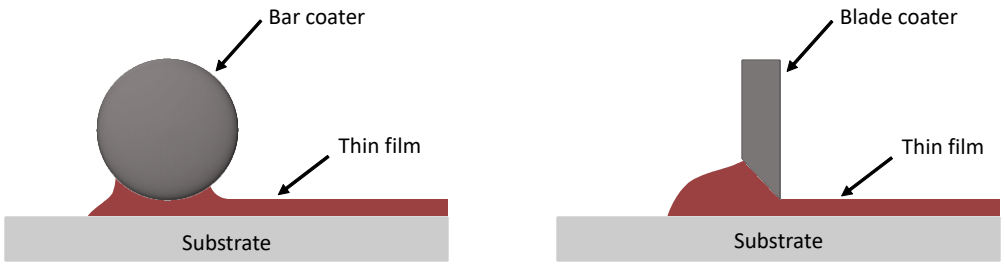

Figure 3-15: Simplified schematic representation of the blade coating technique using (**a**) bar coater or (**b**) blade coater.

The blade coating consists in depositing between the substrate and the blade and spread it all over the surface by displacement of the baled or bar. Therefore, this technique favours the homogenous coating of large area layer with thicknesses up to 1µm, and can be easily adapted for a roll-to-roll process allowing high speed fabrication. Furthermore, in the lab scale point of view, this technique has shown a great ability for the high-throughput screening of the optimal film thickness.[154] Unfortunately, no complete devices were actually fabricated using the blade coating to form the active layer. Therefore, the following results only show the effort that has been done to highlight a potential compatibility for water-based active layer to be form with a blade coater and consequently being a candidate for a future upscaling work.

Standing in lab-to-fab point of view to minimise as possible the use of active materials, a low concentrated dispersion of 20 mg ml^{-1} has been chosen for this study. A

bar coater has been used with a height of 30 µm, the coating plate was set at room temperature and the speed of bar has been set to 10 mm s^{-1}. Very thin layers were obtained with thickness of 40 nm, and a second coating on top of the first layer allowed an increase of the thickness to 90 nm along with the formation of inhomogeneities (**Figure 3-16**). However, since only one bar height of 30 µm was used, increasing this height would probably increase the thickness. The speed of the bar coater is also an important parameter to tune in order to obtained various thicknesses. The speed was thus varied from 10 to 30 mm s^{-1} (**Figure 3-17**). One can observe that the faster the bar coater goes the thicker the film is supposed to be, which is in accordance with the Landau-Levich regime.[155] Unfortunately, large thickness inhomogeneity for the highest speed were observed. After investigation, this probably comes from the motor of the coater that scatters at relatively high speed.

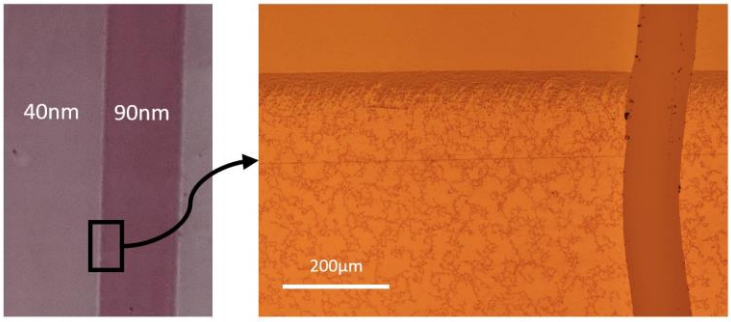

Figure 3-16: Optical (a) macroscope and (b) microscope image of as cast P3HT:$PC_{61}BM$ *np-BHJ* deposited with blade coater with one and two successive depositions.

Speed (mm/s)	10	20	30
Épaisseur (nm)	40 ± 6	49 ± 12	73 ± 32

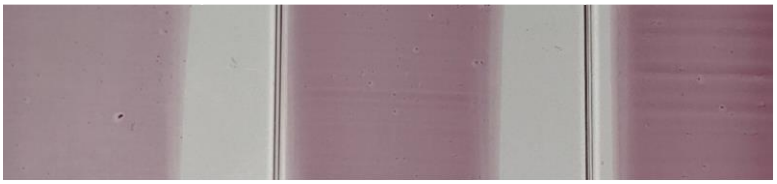

Figure 3-17: Optical macroscope images P3HT:$PC_{61}BM$ np-BHJ deposited with bar coater with varying bar speed.

As we proceed during the spin coating optimisation, the filtration via a RC syringe filter with pore size of 0.45 µm greatly improved the coating by smoothing the surface by getting rid of the dewetting points (**Figure 3-18**). In addition, PVT has also been incorporated in the dispersion which improved as well the coating.

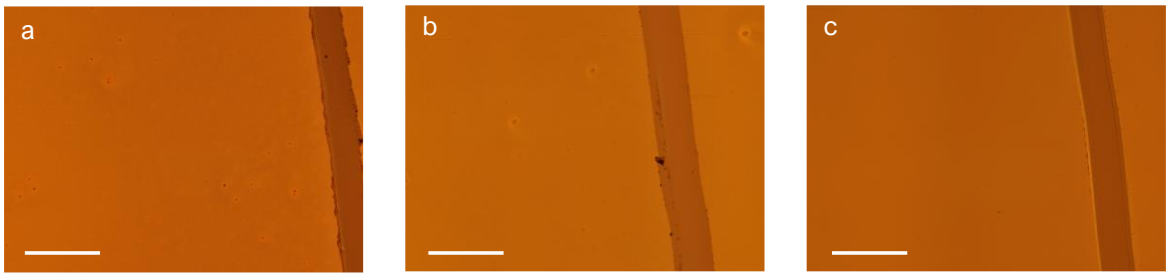

Figure 3-18: Optical microscope images of as cast P3HT:$PC_{61}BM$ np-BHJ deposited with blade coater from dispersion (**a**) without filtration, (**b**) filtrated (0.45 µm) and filtrated (0.45 µm) with 10 wt% of PVT. All scale bars are 200 µm.

3.4. Composite and pure nanoparticles-based organic solar cells

From the literature, blend of pure donor and pure acceptor nanoparticles have been studied, as well as composite donor:acceptor nanoparticles.[133,138] But no works have been carried out on the use of both pure and composite nanoparticles within the same active layer. Using pure donor and acceptor nanoparticles could improve the charge transport in the active layer. Therefore, to assess a possible impact of pure nanoparticles addition with composite nanoparticles on the OPV performances, three different nanoparticles based active layers were fabricated: blend of pure P3HT and pure $PC_{61}BM$ nanoparticles namely P3HT:$PC_{61}BM$ [1:0], blend of pure P3HT, pure $PC_{61}BM$ and composite P3HT:$PC_{61}BM$ nanoparticles namely P3HT:$PC_{61}BM$ [1:1] and composite P3HT:$PC_{61}BM$ NPs namely P3HT:$PC_{61}BM$ [0:1]. The ratios correspond to the ratio [pNPs:cNPs] between pure P3HT and pure $PC_{61}BM$ nanoparticles (pNPs) and composite P3HT:$PC_{61}BM$ nanoparticles (cNPs), note the weight ratio between the donor and the acceptor [D:A] which here remains constant and correspond to 1:1.

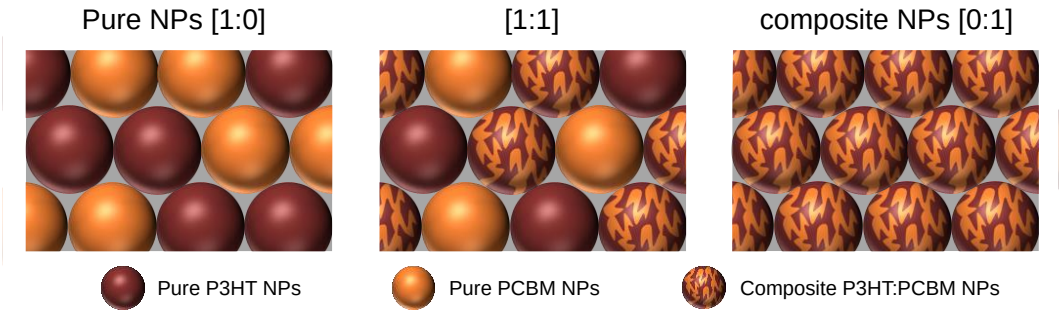

Figure 3-19: Schematic representation of thin films coated with different [pNPs:cNPs] ratio.

3.4.1 UV-visible spectroscopy

Prior to the OPV performances investigation, thin films of pure [1:0], composite [0:1], and a mixing of pure and composite nanoparticles have been formed on a UV-O_3 treated glass substrate with thickness of 130 nm in order to screen their absorption upon different annealing temperature (Figure 3-20). Thermal treatment has been done as a routine procedure to evaporate the remaining water and with the aim of turning the nanoparticule film into a homogenous layer. The annealing conditions were set at 90 °C and 130 °C for 10 min, and film without any annealing are also shown (as cast). As cast, the active layers with different ratio 1:0; 1:1 and 0:1 present similar absorbance compared to their respective dispersion, indicating no change in the nanoparticle arrangement upon deposition. Upon a 90°C annealing, no significant change is observed for the different active layers (P3HT:$PC_{61}BM$ [1:0], [1:1] and [0:1]). When increasing the annealing temperature up to 130°C, for films with ratio 1:0 and 1:1, all three absorption peaks of P3HT slightly increase, a typical behaviour characterising a higher degree of interchain stacking of P3HT. For the composite nanoparticles [0:1], a spectacular increase in the absorbance spectra is observed, indicating a major change in the film morphology. P3HT vibronic peaks remain prominent, but the absorbance in the PCBM region seems to overlap the P3HT one. Note that the optical band gap calculated with Tauc plots did not show any difference between the three layers upon the different thermal annealing temperature with a constant bandgap remaining around 1.99 eV.

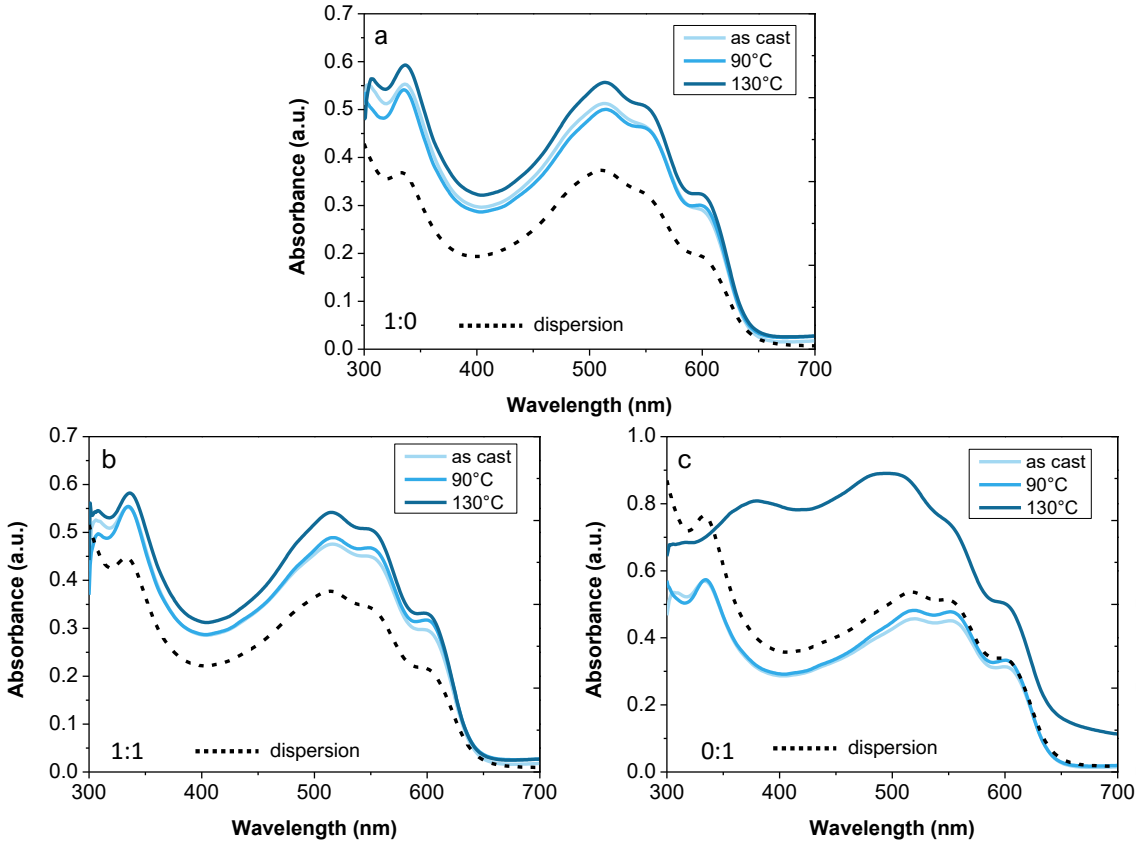

Figure 3-20: UV-visible absorption spectra of P3HT:$PC_{61}BM$ dispersions and films made from (**a**) pure nanoparticles [1:0], (**b**) mix of pure and composite nanoparticles [1:1] and (**c**) composite nanoparticles [0:1] with varying thermal treatment. (dispersions concentration= 0.025 $mg.ml^{-1}$)

3.4.2 Morphological investigation on composite nanoparticles

From optical microscopy, a large phase segregation with small crystals is observable in **Figure 3-21** for P3HT:PC61BM np-BHJ films made from cNPs and annealed at 130°C. The thermal annealing has induced a phase segregation forming what could be aggregates of $PC_{61}BM$ crystallites, thus confirming the previous description related to the optical bandgap.[156] To probe the inner film morphology and get more insight about the remarkable evolution of P3HT:$PC_{61}BM$ composite nanoparticle film, 2D AFM topography measurements have been conducted. As cast, a clear nanoparticle film is obtained resulting in a relatively high surface roughness of 8.0 nm (RMS). With a 90°C thermal treatment, the coalescence of nanoparticles has begun with less visible nanoparticle shapes and boundaries resulting in the decrease of surface roughness to 6.2 nm. At a higher annealing temperature of 130°C, the aggregate observed by optical microscopy are clearly

observable with the AFM images and are found to be around 500 nm large, increasing the RMS value up to 55.3 nm. Such a behaviour at relatively mild annealing temperature that is 130 °C is not often see in the literature. Furthermore, it is normally the average temperature required to obtain the state-of-the-art performances for P3HT:$PC_{61}BM$ nanoparticles solar cells made from mini-emulsion. Such a phase separation is usually observed at higher temperature (160 °C) for fullerene-based nanoparticles layers.[134,135] Yet, Pedersen and co-workers have mentioned a problem related to phase separation when annealing at temperature above 80 °C, but no deep insights are details.[157] It is worth mentioning that Holmes and co-workers have also reported such gross phase segregation with P3HT polymers having low molecular weight (5-12 kDa) but does not correspond to the molecular weight used in my work (53 kDa).[113,121] Thought no morphological analysis were done on the two other ratio (1:1 and 1:0), the UV-vis spectra suggest that for these particles, no such morphological changes is happening. The pure nanoparticles might prevent a large phase separation as it is already existing.

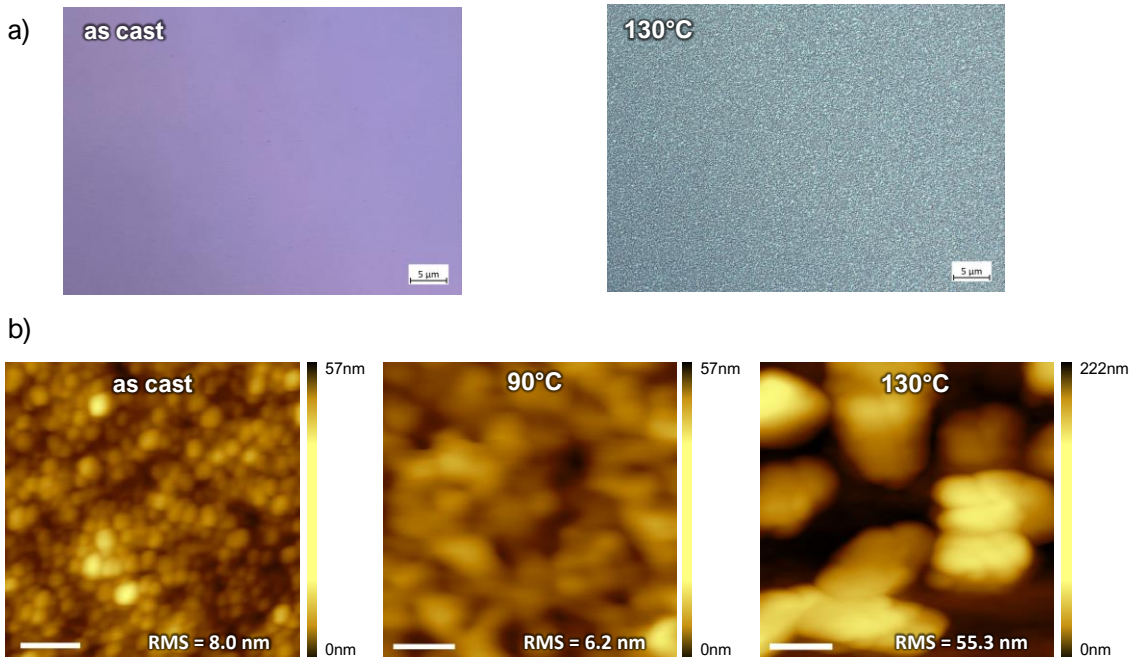

Figure 3-21: (**a**) Optical microscopic images of P3HT:$PC_{61}BM$ np-BHJ films made from cNPs as cast and after 130°C annealing. (**b**) AFM topography images of P3HT:$PC_{61}BM$ np-BHJ films made from cNPs [0:1] with varying thermal treatment. (Scale bar = 300nm)

3.5. OPV performances

J-V curves of the OPV cells with the three different nanoparticulate films treated with different annealing temperature for 5 min are shown in **Figure 3-22**.

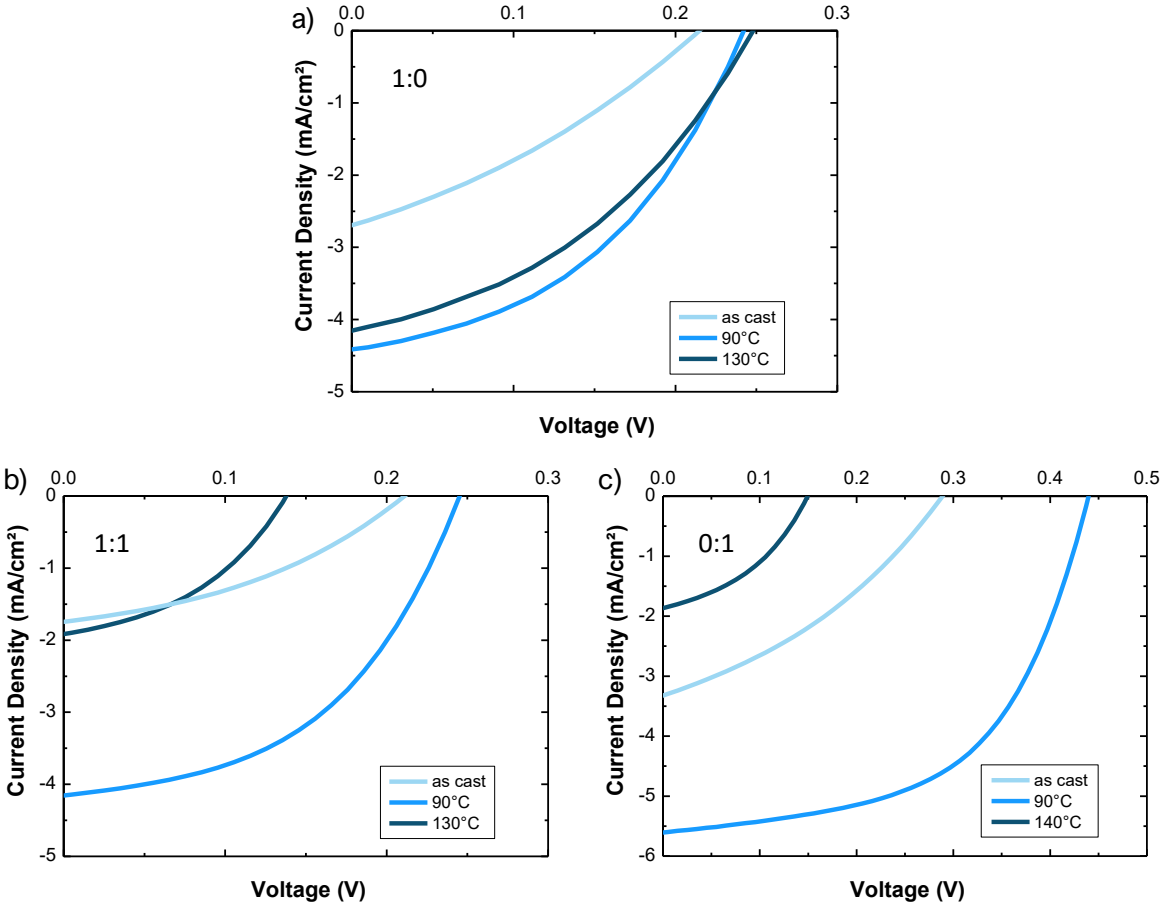

Figure 3-22: J-V curves for P3HT:$PC_{61}BM$ np-BHJ devices made from (**a**) pure nanoparticles [1:0], (**b**) mixing pNPs and cNPs [1:1] and (**c**) cNPs [0:1] with varying thermal treatment. (Selected curves have been chosen to be as close as the average performance for each annealing temperature shown in **Table 3-3**).

For each ratio, the thermal treatment of 90 °C enhanced all three photovoltaic parameters that is J_{SC}, FF and V_{OC}, leading to their optimal PCE of 0.41 %, 0.47 % and 1.26 % for the ratio [1:0], [1:1] and [0:1] respectively. As the AFM already highlighted, this thermal annealing increases the close packing of NPs and thus induces charge transport pathways to the ETL and HTL. This correlation between forming intimate contacts between the nanoparticles and the increase in performances is in accordance to previous work[104]. Ultimately, it shows the decrease of bimolecular recombination because the free charges

are not confined anymore in the nanoparticles but can be transport through the active layer. A higher annealing temperature of 130 °C did not improve the performances of each devices. Interestingly, devices made with pure nanoparticles similar performances that those fabricated with 90 °C annealing temperature, with a modest loss of J_{SC} and FF. For the two other ratio having composite nanoparticles, a dramatic loss in the overall performances is observed, going from 0.47 % to 0.11 % for [1:1] and from 1.37 % to 0.45 % for composite nanoparticles only. As for both system the J_{SC} is the major parameters impacted, the large phase segregation shown earlier for cNPs is likely to have caused this drastic loss. For the mix of pNPs and cNPs, the lack of change in UV-visible absorbance did not show evidence of a possible degradation. Nevertheless, relatively large phase segregation might still occur due to the presence of cNPs but did not show any features in the absorbance spectrum. As the phenomenon is not seen for pure nanoparticles, it indicates that composite nanoparticles are extremely sensitive to high thermal treatment in the case of P3HT:PC_{61}BM. The dramatic loss of V_{OC} observed after annealing the film at 130 °C for the ratio [1:1] and [0:1] can be due to this large-scale phase separation. In term of energy levels as mentioned earlier, but also from a metal–insulator–metal (MIM) model that can represent a solar cell. Indeed, these large aggregate and high roughness saw earlier are increasing possible direct pathways between the transport layers and thus inducing a voltage drop.[158]

Table 3-3: Average OPV performances of P3HT:$PC_{61}BM$ np-BHJ devices made from (a) pure nanoparticles [1:0], mixing pure and composite nanoparticles [1:1] and (c) composite nanoparticles [0:1] with varying thermal treatment (best devices are shown in brackets)

pNPs : cNPs	TA Temperature (°C)	V_{OC} (mV)	J_{SC} (mA cm^{-2})	FF	PCE (%)
1 : 0	none	217 ± 20 (236)	2.83 ± 0.30 (3.16)	0.33 ± 0.01 (0.33)	0.20 ± 0.04 (0.24)
	90°C	229 ± 9 (242)	4.24 ± 0.19 (4.41)	0.42 ± 0.01 (0.44)	0.41 ± 0.04 (0.47)
	130°C	235 ± 16 (239)	4.04 ± 0.07 (4.30)	0.38 ± 0.02 (0.40)	0.39 ± 0.04 (0.41)
1 : 1	none	211 ± 0 (212)	1.79 ± 0.06 (1.75)	0.38 ± 0.02 (0.38)	0.14 ± 0.00 (0.14)
	90°C	244 ± 2 (245)	4.14 ± 0.11 (4.24)	0.47 ± 0.00 (0.47)	0.47 ± 0.02 (0.49)
	130°C	132 ± 11 (138)	2.01 ± 0.08 (1.92)	0.41 ± 0.01 (0.41)	0.11 ± 0.00 (0.11)
0 : 1	none	279 ± 37 (302)	3.29 ± 0.05 (3.24)	0.35 ± 0.02 (0.37)	0.32 ± 0.05 (0.36)
	90°C	424 ± 27 (515)	5.61 ± 0.12 (5.66)	0.53 ± 0.03 (0.54)	1.26 ± 0.13 (1.38)
	130°C	149 ± 7 (165)	1.80 ± 0.46 (1.76)	0.39 ± 0.02 (0.42)	0.11 ± 0.11 (0.58)

Furthermore, to assess a possible impact of pNPs addition with cNPs-based active layer, two supplementary ratios have been studied, [0.5:1] and [0.25:1], and their optimum OPV performances as well as the other ratio are reported in **Figure 3-23**. For the additional ratio, the annealing temperature has been set at 90 °C during 5 min. Interestingly, even with the smallest amount of pNPs [0.25:1] (corresponding to 16 w% of pNPs), the overall performances were still very low as compared to the 100% cNPs-based devices. The difference primarily comes from large open-circuit voltage loss when adding pure nanoparticles. Even at a ratio of [0.25:1], an important V_{OC} loss of more than 100 mV is observed. Short-circuit current density is also higher when having only composite nanoparticles and can be explained by a decrease of geminate recombination due to the absence of large domains of both $PC_{61}BM$ and P3HT represented by pure nanoparticles. Overall, all parameters are enhanced when increasing the amount of composite

nanoparticles, highlighting the importance of having small domains found in composite nanoparticles. Drastically decreasing the size of pure nanoparticles could be a good way to complete the study in order to correlate this loss to domain sizes.

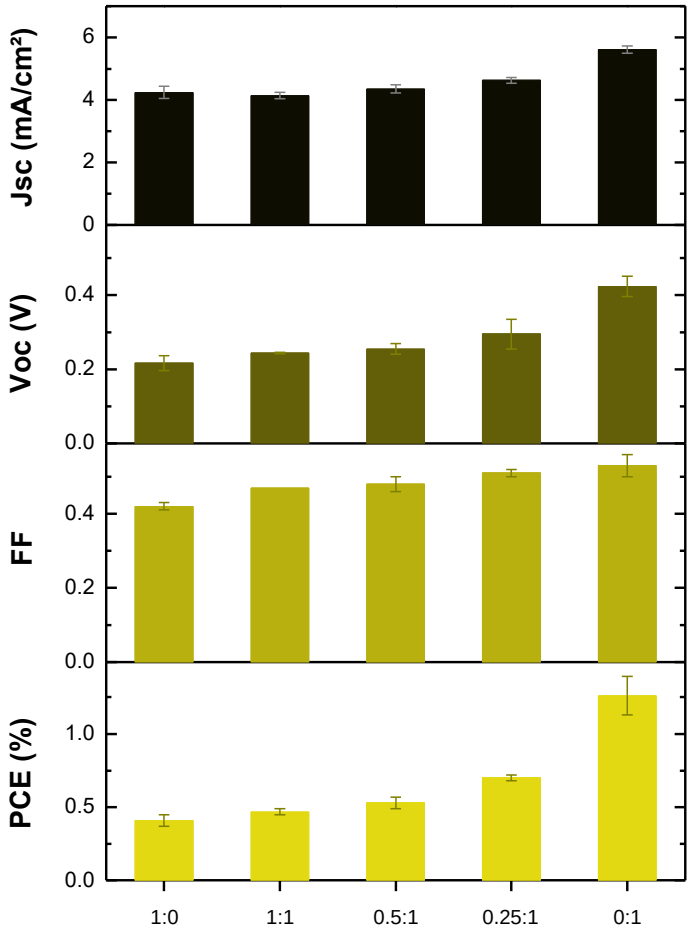

Figure 3-23: OPV performances of P3HT:$PC_{61}BM$ np-BHJ devices fabricated from different ratio between pure nanoparticles and composite nanoparticles [pNPs:cNPs].

An effective way to evaluate a water-based solar cell is to directly compare its performances with a solar cell using the same D:A system, but which has been deposited from an organic solvent. OPV devices have been fabricated from a chlorobenzene solution at the concentration of 16 mg ml^{-1} and spin-coated on the ZnO layer at 1000 rpm. Herein, J-V curves and EQE curves of both water-based and organic solvent-based devices are shown in **Figure 3-24** and details can be found in **Table 3-4**. The two measurements are showing the overall large loss of performances when using nanoparticles as an active layer.

Less than half of the performances achieved with P3HT:$PC_{61}BM$ *BHJ* devices are reached with P3HT:$PC_{61}BM$ *np-BHJ* devices. Even though the thermal annealing of 90 °C reduced the roughness, large grain boundaries are still present with an RMS value of 6.2 nm, this surface morphology is preventing the charge carrier to be efficiently transported and extracted from the active layer. The later might explained the large gap in the J_{SC} and FF observed with control devices. V_{OC} is also impacted with the water-based devices with an average V_{OC} loss of 150 mV. This loss is apparently not related to a change in the bandgap energy E_g as both processes are showing similar value extracted from the EQE of 1.92 eV and 1.91 eV for the water-based process and the organic solvent process respectively. Many reasons could explain this loss, such as the use of a surfactant and the none optimal morphology which can favour a large trap density. The results from the literature are showing minor V_{OC} loss for this system prepared with mini-emulsion. However, taking the example of Holmes *et al*. work, optimal performances (including optimal V_{OC}) have been obtained when annealing the nanoparticulate film at 140 °C. When using a lower temperature (110 °C), a much lower V_{OC} was obtained (310 mV).[159] In addition to this phenomenon, the increase of the molecular weight (M_W) of P3HT was found to decrease the V_{OC} at similar M_W that the P3HT used in my work.[160] However they did not focus the discussion around this V_{OC} gap between water-processed and organic solvent-processed OPV devices. In our case, the impossibility of doing a thermal annealing above 90 °C due to large phase segregation might limited the formation of an optimal morphology.

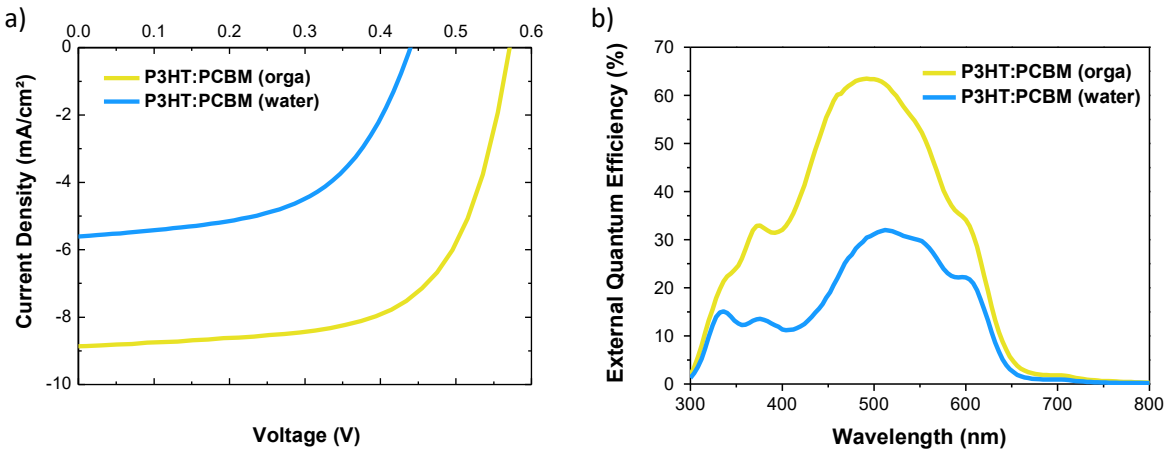

Figure 3-24: J-V curves and b) EQE for P3HT:$PC_{61}BM$ *np-BHJ* [cNPs] (blue) and P3HT:$PC_{61}BM$ BHJ (yellow) at the optimal thermal annealing temperature. Note that the selected curves have been chosen to be as close as the average performance shown in **Table 3-4**.

Table 3-4: Average OPV performances of P3HT:$PC_{61}BM$ np-BHJ and BHJ devices (best devices are shown in brackets)

Active layer	V_{OC} (mV)	J_{SC} (mA cm^{-2})	FF	PCE (%)
P3HT:PCBM np-*BHJ*	424 ± 27 (453)	5.61 ± 0.12 (5.66)	0.53 ± 0.03 (0.54)	1.26 ± 0.13 (1.38)
P3HT:PCBM *BHJ*	575 ± 5 (579)	8.85 ± 0.29 (9.13)	0.66 ± 0.02 (0.68)	3.34 ± 0.21 (3.60)

3.6. Conclusion of chapter 3

In summary, the elaboration of organic semiconductor nanoparticles has been described and will represent from now on the standard fabrication process for the next results presented in this work. Furthermore, this chapter has laid the foundations for processing homogenous and thick layers from aqueous dispersions of organic semiconductor nanoparticles. For deposition with spin-coating technique, an optimisation has been done to decrease as low as possible the amount of active materials while preserving a good coating. For the same purpose, a low concentration dispersion (20 mg ml^{-1}) has been employed with an addition of PVT to maintain thick and homogenous layer. An addition of 10 wt.% PVT had shown an improvement compared with devices without PVT due to decrease of the leakage current. However, these devices fabricated from low concentration (20 mg ml^{-1}) remain less performing than devices made out with a high concentrated dispersion (60 mg ml^{-1}). Further tests with different weight ratio of the insulating additive might be worth trying as well as different type of insulating polymers.[161,162] Finally, based on the P3HT:$PC_{61}BM$ system, we have studied the incorporation of pure nanoparticles in composite nanoparticles dispersions at different ratio. The aim was to assess a possible benefit of small amount of pure nanoparticle in a composite nanoparticles-based solar cell to improve the charge transport. However, the solar cells prepared with 100 % of composite nanoparticles have shown much higher efficiencies compared to all the other kind of dispersion incorporating pure P3HT and PCBM NPs. This can be explained by the larger domains induce by pure nanoparticles and poor transport between particles. Overall, an average PCE of 1.26 % has been demonstrated with P3HT:$PC_{61}BM$ *np-BHJ* which is in accordance with the efficiency reported in the literature for mini-emulsion. An incomplete sintering of the nanoparticles might prevent higher performances. The thermal annealing at temperate above 100 °C

could have solve this problem, however a large phase segregation has been seen for the composite nanoparticles. For similar temperature, such effect is not seen for classic bulk heterojunction or even for pure nanoparticles. Therefore, it highlights that a confined donor:acceptor morphology inside a nanoparticle has an important role and is highly sensitive to thermal annealing. A care should hence be given to control the nanoparticle morphology, as well as to the film processing and treatment to end up with the desire morphology as close as possible to a bulk-heterojunction one.

Chapter 4

Controlling the morphology with surface energies

Part of the following chapter has been published in a peer-reviewed journal [163]:

H. Laval, A. Holmes, M. A. Marcus, B. Watts, G. Bonfante, M. Schmutz, E. Deniau, R. Szymanski, C. Lartigau-Dagron, X. Xu, J. M. Cairney, K. Hirakawa, F. Awai, T. Kubo, G. Wantz, A. Bousquet, N. P. Holmes, S. Chambon, *Adv. Energy Mater.* **2023**, *13*, 2300249

4.1. Introduction

From the previous section, the fabrication of reliable OPV cells from water-processed active layer has been carried out. Meanwhile, I was able to highlight the importance of having donor/acceptor composite nanoparticles instead of having pure donor and acceptor nanoparticles mixed together or added with composite nanoparticles to form the active layer. This indicates that the initial nanoparticle morphology strongly determines the resulting active layer morphology and therefore the final photovoltaic performances. More specifically, the contrast between pure and composite nanoparticles emphasise the importance of domain size and donor/acceptor interfaces. From the literature, we observe a similar contrast in term of performances between blend nanoparticles obtain from mini-emulsion and nanoprecipitation and we believe the causes might be similar. One can argue that such difference comes from the use of surfactant with a dielectric behaviour, but I propose in this chapter to focus more on the initial nanoparticle morphology.

Undeniably, kinetics implied during the formation of a nanoparticle made by mini-emulsion and nanoprecipitation are different. The slow kinetic of the mini-emulsion tends to increase the phase segregation as materials have more time to arrange/crystallise in the nanoparticles. That being said, the optimisation of a water-processable organic solar cell should obviously start with a precise control of the nanoparticle morphology considering its proprieties. These proprieties will also set the post-deposition process strategy as the annealing temperature plays a major role for achieving the final nanoparticle-based active layer. In order to achieve high efficiency water-based solar cells, candidates have to be carefully chosen among the colossal π-conjugated materials library for OPV. The polymeric donor PTQ10 has been chosen as the common donor material based on its performances in the literature but also a good energetic compatibility with a wide variety of acceptors. This choice has to be made based on some of the material properties, and we have first chosen to give our interest to the surface energy as this parameter can strongly influence the interaction between two materials. Special attention is also given to further optimisations of water-based devices and the physico-chemical properties of the chosen materials. This chapter aims to provide keys for targeting and understanding properties that are essential when processing active layer with nanoparticles formed by mini-emulsion.

4.2. Surface and interfacial energies

Self-organisation of materials inside a composite nanoparticle made with mini-emulsion is not straightforward to predict as it involves a synthesis in a complex thermodynamic and chemical environment. Therefore, being able to corelate a nanomorphology with photovoltaics performances and dynamics is still not under control. Yet, the study of Barr and co-workers has shown a notable impact of the surface energy difference between the donor and the acceptor material on this self-organisation.[122] This imply a possibility of tuning the morphology by doing a careful selection of active materials, especially the acceptor. Almost a decade has passed since the non-fullerene acceptors (NFAs) have changed the OPV destiny, and in the water-processable OPV point of view, they have the ability to help tuning the morphology since they present a large variety of surface energies.[164]

Fullerene derivatives-based donor/acceptor composite nanoparticles prepared by mini-emulsion present essentially core–shell morphology due to higher surface energy of the acceptor compared to that of the donor material. On the other hand, NFAs present lower surface energies than fullerene derivatives and, as a consequence, the morphology of donor/acceptor nanoparticles is not always acceptor-rich core/donor-rich shell. These findings are encouraging in our journey to control the internal morphology of the nanoparticles, and to explore the use of NFAs.

When blending a donor and an acceptor material, their surface energies can give good indications about the miscibility between them. From their values, an additional parameter that is the interfacial energy between a material A and B (γ_{AB}) can be extracted to further quantify their miscibility following the equation ((4.**1**) where γ_A and γ_B are the total surface energy of the material A and B respectively, $\gamma_{\mathrm{A}}^{\mathrm{d}}$ and $\gamma_{\mathrm{B}}^{\mathrm{d}}$ their respective depressive component and $\gamma_{\mathrm{A}}^{\mathrm{p}}$ and $\gamma_{\mathrm{B}}^{\mathrm{p}}$ their polar component.[165] We thus have decided to study the impact of surface energies and interfacial energies on the morphology of NP-based active layers.

$$\boldsymbol{\gamma_{AB} = \gamma_A + \gamma_B - \frac{4\gamma_A^d \gamma_B^d}{\gamma_A^d + \gamma_B^d} - \frac{4\gamma_A^p \gamma_B^p}{\gamma_A^p + \gamma_B^p}} \quad (4.1)$$

The surface energy of a liquid can directly be measured from several techniques such as the pendant drop or the Wilhelmy plate method. However, a direct measurement of the surface energy of a solid is not possible due to the bulky nature of a solid, its complex surface properties and interactions. Nevertheless it is possible via an undirect method of contact angle measurements of liquids onto a solid described by the well-known Young's equation ((4.**2**) established in 1805 and describing the contact angle (θ) of a liquid drop on a plane solid surface.[166] The three boundaries forces at the equilibrium are the surface energy at liquid-vapour interface γ_{lv}, the solid-liquid interface γ_{sl} and the solid-vapour interface γ_{sv}. The two component Wu model resulting from the combination of the interfacial energy equation and the Young's equation is used in this work to calculate these energies (4.3) where γ_l^d is the dispersive component of the surface tension of a liquid, γ_l^p its polar component, γ_s^d is the dispersive component of the surface energy of a solid, γ_s^p its polar component. In order to solve this equation, the contact angle data with two liquids are required. In our case, water and ethylene glycol have been chosen.

$$\boldsymbol{\gamma_{lv}\cos(\theta) = \gamma_{sv} - \gamma_{sl}} \tag{4.2}$$

$$\boldsymbol{\gamma_{lv}\cdot(1+\cos(\theta)) = \frac{4\gamma_l^d\gamma_s^d}{\gamma_l^d+\gamma_s^d} + \frac{4\gamma_l^p\gamma_s^p}{\gamma_l^p+\gamma_s^p}} \tag{4.3}$$

In **Table 4-1**, the surface energies (dispersive, polar and total) of PTQ10 and several acceptors are listed. With these values, the interfacial energy $\gamma_{D:A}$ between PTQ10 and each acceptors have been calculated from equation (4.3). From these six donor:acceptor systems, various interfacial energies are obtained, with a maximum value of 13.1 mN m^{-1} for PTQ10:$PC_{61}BM$ and a minimum of 4.4 mN m^{-1} for PTQ10:Y6. In order to study the impact of this interfacial energy on the morphology of a nanoparticle, these two systems have been selected and aqueous colloidal dispersions have been synthesised from those. The values listed in Table 1 have been taken from the PhD thesis work of Robin Szymanski[167]. It is

important to note that different batches of PTQ10, $PC_{61}BM$ and Y6 have been used in the present thesis. Therefore, contact angles and surface energies calculations have been performed once again on the materials specifically used in this work. New values are shown in **Table 4-2** and were calculated from the contact angle measurements presented in **Figure** 4-1. Very similar values have been obtained and the large difference of interfacial energy between PTQ10:$PC_{61}BM$ and PTQ10:Y6 is confirmed.

Table 4-1: Surface energies (polar, dispersive and total) of PTQ10 and a series of acceptor materials. $\gamma_{D:A}$ represents the interfacial energy between PTQ10 and the respective acceptor. Values have been taken from the PhD thesis of Robin Szymanski [167].

Material	γ_D (mN m^{-1})	γ_P (mN m^{-1})	γ (mN m^{-1})	$\gamma_{D:A}$ (mN m^{-1})
PTQ10	21.2	2.0	23.2	/
$PC_{61}BM$	15.7	17.0	32.7	13.1
ITIC-Th	15.8	11.4	27.23	7.4
4TIC-4F	17.4	9.5	26.8	6.4
IT-4F	15.2	10.9	26.1	5.9
Y9	15.5	8.5	25.0	4.7
Y6	19.2	8.0	27.2	4.4

Table 4-2: Surface energies (polar, dispersive and total) of PTQ10, $PC_{61}BM$ and Y6. $\gamma_{D:A}$ represents the interfacial energy between PTQ10 and the respective acceptor. Measured values in this work.

Material	γ_D (mN m^{-1})	γ_P (mN m^{-1})	γ (mN m^{-1})	$\gamma_{D:A}$ (mN m^{-1})
PTQ10	21.3	1.7	23.1	/
$PC_{61}BM$	17.1	17.9	35.1	13.8
Y6	19.6	8.5	28.1	4.5

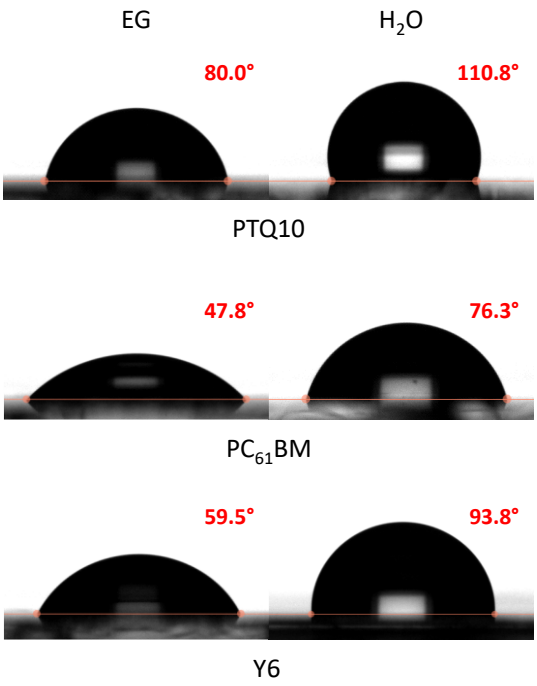

Figure 4-1: Goniometer pictures of contact angles and their values in red of ethylene glycol (left) and water (right) on PTQ10, $PC_{61}BM$ and Y6 films deposited from chloroform.

4.3. Nanoparticles synthesis

Composite nanoparticles with PTQ10:$PC_{61}BM$ and PTQ10:Y6 were synthesised following the usual procedure described in **Methods**: For the organic phases, 25 mg ml^{-1} of PTQ10:Y6 [1:1.2] mixture, or 25 mg ml^{-1} of PTQ10:$PC_{61}BM$ [1:1] mixture, was first dissolved in chloroform and stirred for 2 h at 65 °C in a nitrogen-filled glovebox. The ratios were set based on the literature for their optimised counterpart organic solvent-based devices. Which are [1:1.2] for PTQ10:Y6[168] ; and [1:1] PTQ10:$PC_{61}BM$. Note that for the ratio PTQ10:$PC_{61}BM$ we performed the optimisation ourselves as no results had been identified in the literature. The aqueous phase was obtained by dissolving 5 mg ml^{-1} (17 mM) of SDS in deionised water and stirred for 30 min at room temperature. The concentration of both dispersions was adjusted through the parameters of the last centrifugal cycle in order to obtain a concentration of 60 mg ml^{-1}.

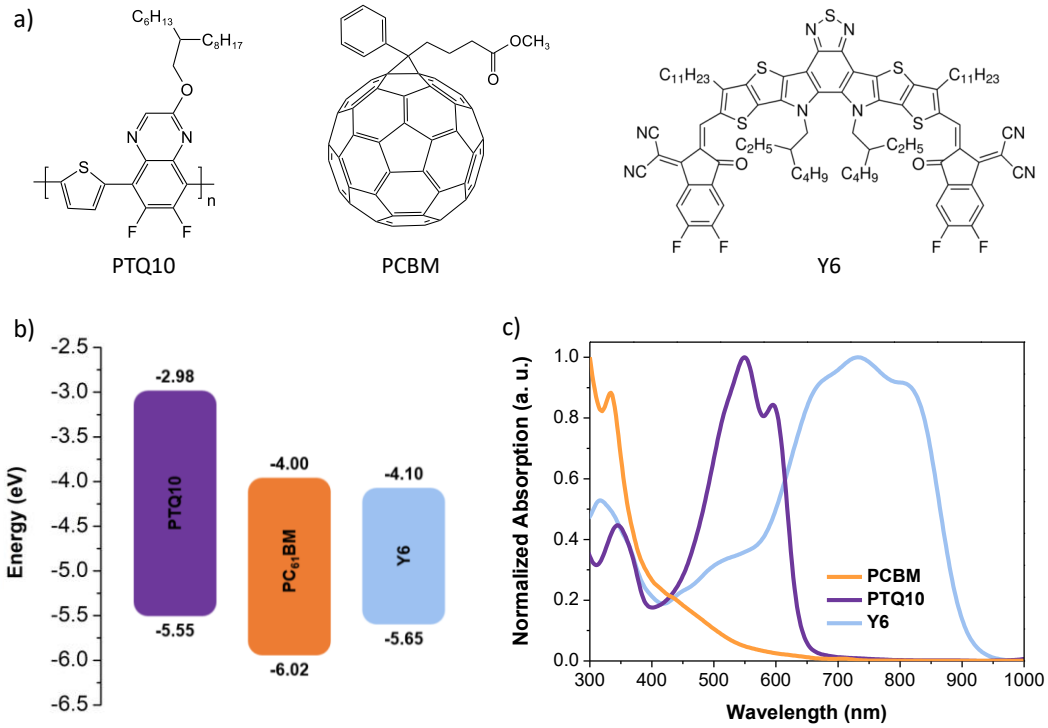

Figure 4-2: (**a**) Chemical structures of the donor material (PTQ10) and the two acceptor materials ($PC_{61}BM$, Y6). (**b**) Highest Occupied Molecular Orbital (HOMO) and Lowest Unoccupied Molecular Orbital (LUMO) of PTQ10, $PC_{61}BM$, and Y6. (**c**) Absorption spectra of $PC_{61}BM$ NPs, PTQ10 NPs, and Y6 nanoparticles (dispersions). (dispersions concentration = 0.06 mg ml^{-1})

After the synthesis of the NPs, we performed UV-visible absorption (**Figure 4-3a**) as well as the photoluminescence (PL) of the nanoparticles in dispersion (**Figure 4-3b**). The average diameter (Z-average) from the DLS measurements are also listed in **Table 4-3**. Following our synthesis process, the nanoparticle size does not seem to be material dependent and is quite similar to the sizes obtain with P3HT:$PC_{61}BM$ nanoparticles. As it has been observed for P3HT:PCBM when forming a nanoparticle, PTQ10:Y6 nanoparticle seems to have a similar absorption spectrum than its solid film made from organic solvent, which here again highlight a possible high degree of ordering inside the nanoparticle.[46] Concerning the PL, with the objective of this characterisation is to investigate a possible difference of morphology through the fluorescence of the common material PTQ10. We thus applied a photoexcitation at 540 nm, in the PTQ10 region and recorded the emission of four different nanoparticles: pure PTQ10, pure Y6, composite PTQ10:Y6 and composite PTQ10:$PC_{61}BM$. For the reference emission of PTQ10 pure nanoparticles, the peak at 735 nm is typical of a band-to-band transition in the PTQ10 polymer. For PTQ10:$PC_{61}BM$, the

quenching of the PTQ10 fluorescence is very effective and up to 96%, indicating that exciton dissociation is highly efficient in the PTQ10 region. In the case of PTQ10:Y6 nanoparticles, PTQ10 fluorescence is totally quenched, which might indicate a slightly more intimate morphology which favours the exciton dissociation generated in the polymer. On the other hand, one can clearly still see that the fluorescence of Y6 (800– 1150 nm) is only partially quenched by 70%. This result indicates that the Y6 domains might be larger than the exciton diffusion length and that the morphology is not yet optimised for all the exciton formed in the Y6 to be fully dissociated. Care will be given later in this chapter to understand the possible reason to the remaining fluorescence.

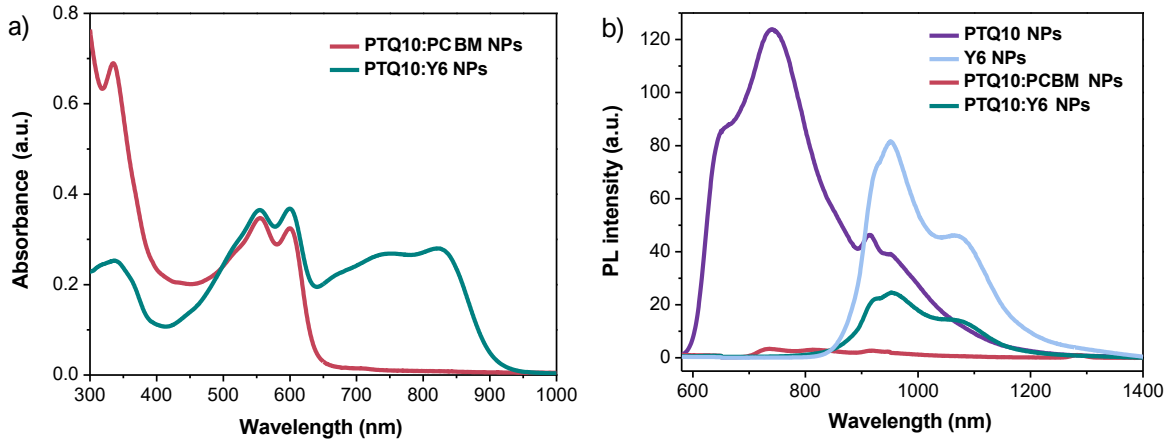

Figure 4-3: (**a**) Absorption spectra of PTQ10:PC_{61}BM NPs and PTQ10:Y6 NPs (dispersions) and (**b**) photoluminescence spectra of PTQ10 NPs, Y6 NPs, PTQ10:PC_{61}BM NPs and PTQ10:Y6 NPs (dispersions). (dispersions concentration = 0.03 mg ml^{-1})

Table 4-3: Average diameter of PTQ10:Y6 NPs and PTQ10:PC_{61}BM NPs measured with DLS

System	Z-average (d.nm)
PTQ10:Y6	65
PTQ10:PC_{61}BM	67

4.4. OPV performances

Water-based OPV solar cells (*np-BHJ*) from PTQ10:Y6 and PTQ10:PC_{61}BM nanoparticles dispersions have been fabricated following the optimised deposition process

described in the previous chapter with P3HT:$PC_{61}BM$ *np-BHJ*. For each system, the most favourable annealing temperatures have been selected through a temperature screening and their resulting OPV performances are analysed. In this first section, a constant annealing time of 5 min is done for each temperature. Care has to be ensured to compare what is comparable. Therefore, our approach here again (as it was when comparing P3HT:$PC_{61}BM$ *np-BHJ* with P3HT:$PC_{61}BM$ *BHJ*) is not to compare directly the performances of the two water-based devices (PTQ10:Y6 *np-BHJ* vs. PTQ10:$PC_{61}BM$ *np-BHJ*) but to compare each of them with their respective counterpart processed with an organic solvent (*BHJ*). Indeed, $PC_{61}BM$ having a much less capability of absorption in the visible and near-infrared region, both systems are far to be analogous. Organic solvent-based OPV cells have thus also been prepared. The annealing temperature optimisation process and the final comparison between the two processes are described in the following sections.

4.4.1 PTQ10:$PC_{61}BM$ – high $\gamma_{D:A}$ system

For the first system, namely "high $\gamma_{D:A}$ system" due to PTQ10:$PC_{61}BM$ high interfacial energy ($\gamma_{D:A}$ = 13.8 mN m^{-1}), the evolution of the J-V curves with varying the thermal annealing temperature and the resulting PCE are plotted in **Figure 4-4** and the different photovoltaic parameters are listed in **Table 4-4**. From a pristine film to a film thermally annealed at 200 °C for 5 min, no clear dependency has been observed in the power conversion efficiency value that remains around 1% for 100 °C annealing temperature and higher. As mentioned in **Chapter 3**, the only noticeable difference comes from the drying at low temperature (here at 100°C) that favour removal of any remaining water and a possible change in the inter-nanoparticles spacing. The latter might possibly be the cause of the increase in the FF values from 0.42 to 0.56 upon annealing. Thermal treatment might induce on the one hand a film shrinkage and a change the domain spacing in the *np-BHJ* film, allowing an appropriate charge transport and extraction and on the other hand induce at the same time phase separation.[138] Without this shrinkage, morphological traps created by the film morphology could induce an increase of recombination and /or low charge carrier mobility explaining the low FF.[169],[170] While it favours the FF, the J_{SC} obtained when varying the thermal annealing condition is remaining the same, indicating that there is no significant change in the charge photogeneration process. Nonetheless, the increase of FF

upon annealing is compensated by a large V_{OC} loss, falling from 0.90 V at 140°C to 0.69 V at 200°C, and does not induce a raise in efficiency. However, the significant evolution of FF and V_{OC} can question a possible change in the active layer morphology and/or at the ETL/active layer interface.

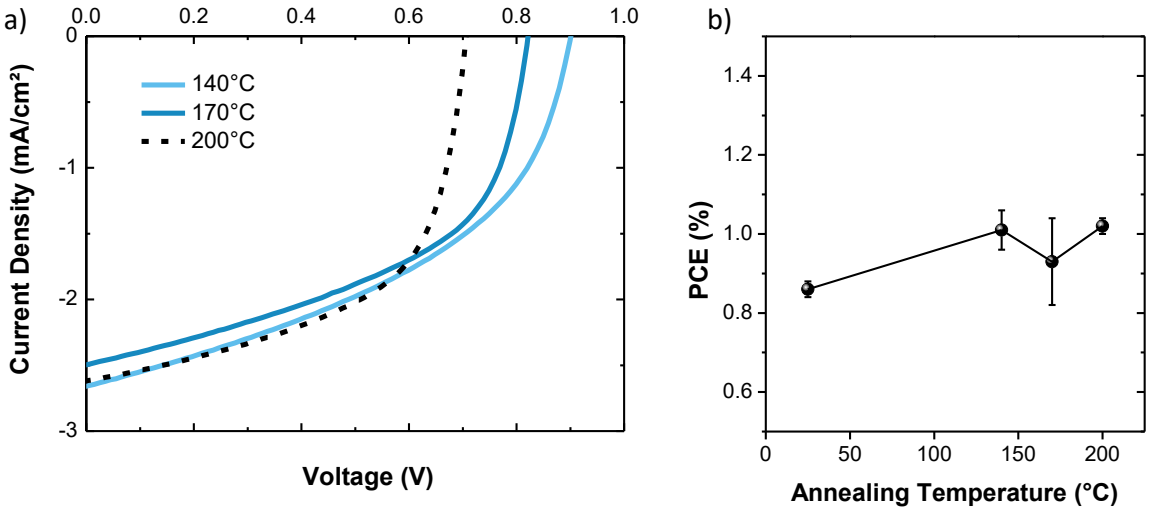

Figure 4-4: (**a**) J-V curves for PTQ10:PC_{61}BM np-BHJ devices with varying the thermal annealing temperature from no annealing to 200°C for 5 min. Note that the selected curves have been chosen to be as close as the average performance for each annealing temperature shown in **Table 4**. (**b**) represents PCE with varying the thermal annealing temperature for PTQ10:PC_{61}BM np-BHJ OPV devices.

Table 4-4: Average OPV performances of PTQ10:PC61BM np-BHJ extracted from a minimum of 8 devices with different thermal annealing (TA) temperatures (best devices are shown in brackets).

TA Temperature (°C)	V_{OC} (mV)	J_{SC} (mA cm^{-2})	FF	PCE (%)
none	820 ± 10 (814)	2.51 ± 0.05 (2.56)	0.42 ± 0.01 (0.42)	0.86 ± 0.02 (0.87)
140	900 ± 10 (901)	2.54 ± 0.11 (2.66)	0.44 ± 0.01 (0.45)	1.01 ± 0.05 (1.08)
170	830 ± 20 (821)	2.43 ± 0.05 (2.50)	0.50 ± 0.01 (0.50)	0.93 ± 0.11 (1.03)
200	690 ± 10 (707)	2.65 ± 0.33 (2.62)	0.56 ± 0.01 (0.57)	1.02 ± 0.02 (1.05)

From these results, no clear optimised temperature was found. Nevertheless, the water-based device annealed at 140°C gives a hero cell with 1.08% PCE (J_{SC} = 2.66 mA cm^{-2}, V_{OC} = 901 mV and FF = 0.45). In order to assess and quantify this performance, we compare it with its control device made from a tetramethylbenzidine (TMB) solution (BHJ). J-V curves and EQE from the two optimised process (**Figure 4-5**) clearly show a different behaviour. In particular, the J_{SC} obtained from PTQ10:$PC_{61}BM$ *np-BHJ* devices is much lower than that of PTQ10:$PC_{61}BM$ *BHJ*, decreasing from 4.83 mA cm^{-2} down to 2.54 mA cm^{-2} as well as FF, decreasing from 0.58 to 0.44 (**Table 4-5**). EQE results confirm a much lower efficiency for the *np-BHJ* active layer in terms of photo-conversion since only a maximum of 22% of incident photons generate charges in the PTQ10 absorption region, almost twice lower than for the organic solvent-processed active layer in the same region of interest (**Figure 4-5b**). This result is quite surprising as we observed previously a complete quenching in the PL measurement. Therefore, it indicates that bimolecular recombination are dominant in the process. Furthermore, the fact that the *np-BHJ* devices do not present any V_{OC} loss as compare to the *BHJ* devices is a sign that radiative recombination might be dominant.[171] When it comes to compare only the PCE, the water-based strategy presents a loss of 60% (± 3%) in PCE as compare to the classical strategy employing an organic solvent.

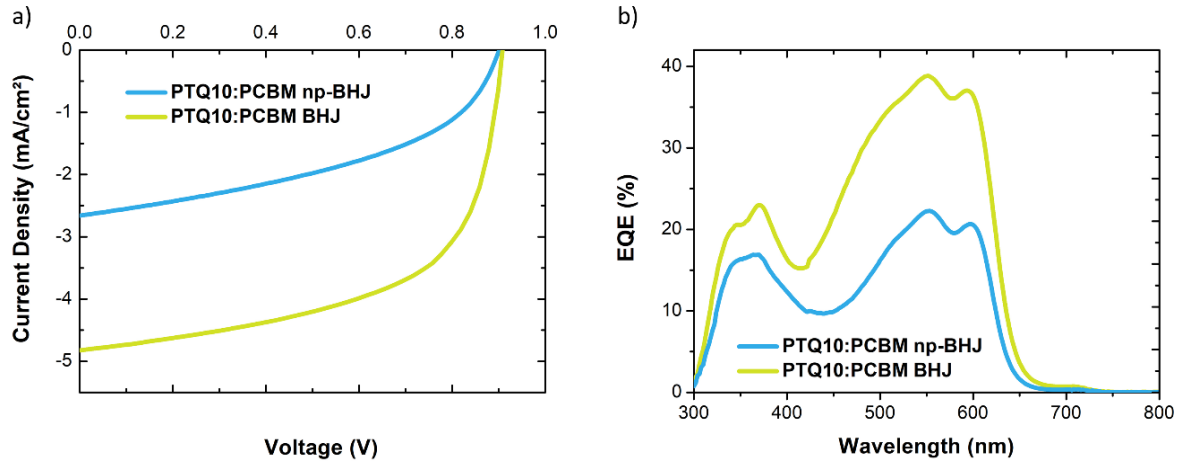

Figure 4-5: (a) J-V curves and (b) EQE for PTQ10:$PC_{61}BM$ np-BHJ (blue) and PTQ10:$PC_{61}BM$ BHJ (yellow) at the optimal thermal annealing temperature. Note that the selected curves have been chosen to be as close as the average performance shown in Table 4.

Table 4-5: Average OPV performances of PTQ10:$PC_{61}BM$ BHJ PTQ10:$PC_{61}BM$ np-BHJ extracted from a minimum of 8 devices at the optimal thermal annealing temperature (best devices are shown in brackets)

	V_{OC} (mV)	J_{SC} (mA cm^{-2})	FF	PCE (%)
PTQ10:$PC_{61}BM$ *BHJ*	897 ± 11	4.83 ± 0.03	0.58 ± 0.01	2.52 ± 0.06
PTQ10:$PC_{61}BM$ *np-BHJ*	900 ± 10	2.54 ± 0.11	0.44 ± 0.01	1.01 ± 0.05

4.4.2 PTQ10:Y6 - low $\gamma_{D:A}$ system

Now taking a look to the "low $\gamma_{D:A}$ system", a different behaviour was observed for devices made from PTQ10:Y6 nanoparticles. The overall performances are continuously enhanced by the increase of the thermal annealing temperature until they reach an average of 8.08% PCE, with J_{SC} = 18.13 mA cm^{-2}, V_{OC} = 714 mV and FF = 0.62 at 200 °C. The spectacular rise of both J_{SC} and FF, from 7.97 mA cm^{-2} to 18.13 mA cm^{-2} and from 0.40 to 0.62 respectively, was essential to obtain such an increase in the efficiency (**Figure 4-6** and **Table 4-6**).

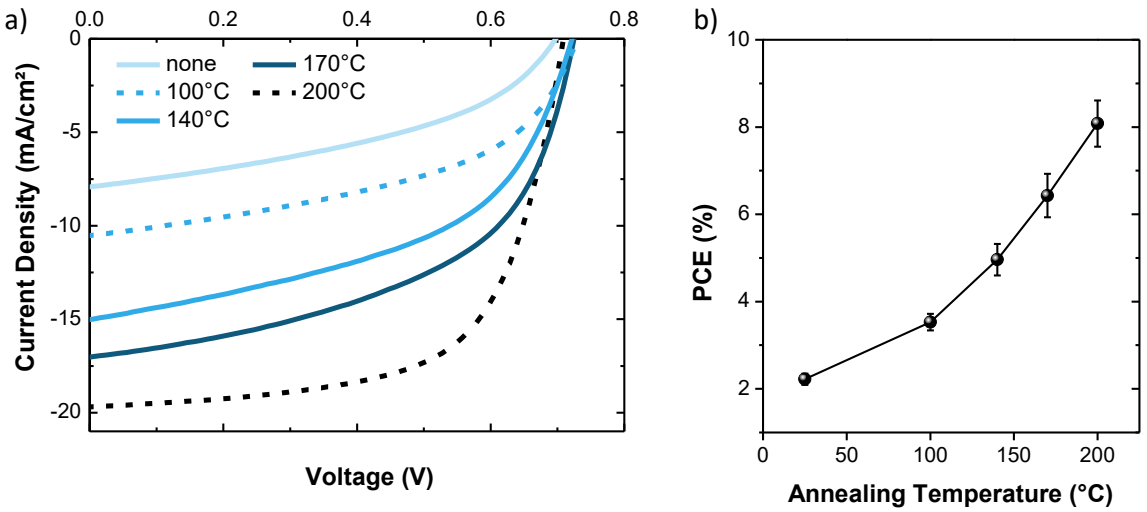

Figure 4-6: (a) J-V curves for PTQ10:Y6 np-BHJ devices with varying the thermal annealing temperature from no annealing (light blue) to 200°C (dark dashed line. Note that the selected curves have been chosen to be as close as the average performance for each annealing temperature shown in **Table 4-6**. And (b) represents PCE vs thermal annealing temperature for PTQ10:Y6 np-BHJ OPV devices.

Table 4-6: Average OPV performances of PTQ10:Y6 np-BHJ extracted from a minimum of 8 devices with different thermal annealing (TA) temperatures (best devices are shown in brackets)

TA Temperature (°C)	V_{OC} (mV)	J_{SC} (mA cm^{-2})	FF	PCE (%)
none	688 ± 13 (697)	7.97 ± 0.11 (7.92)	0.40 ± 0.02 (0.42)	2.22 ± 0.13 (2.34)
100	716 ± 17 (730)	10.43 ± 0.18 (10.53)	0.47 ± 0.02 (0.48)	3.53 ± 0.19 (3.71)
140	705 ± 11 (722)	14.34 ± 0.82 (15.02)	0.49 ± 0.01 (0.50)	4.96 ± 0.36 (5.39)
170	714 ± 13 (725)	16.90 ± 0.56 (17.03)	0.47 ± 0.03 (0.52)	5.64 ± 0.50 (6.43)
200	714 ± 15 (709)	18.13 ± 1.15 (19.70)	0.62 ± 0.01 (0.64)	8.08 ± 0.53 (8.93)

J-V and EQE spectra of PTQ10:Y6 based devices (*BHJ* and *np-BHJ*) are presented in **Figure** 4-7. For PTQ10:Y6 *BHJ*, up to 70% of incident photons generate electrons, with PTQ10 contributing to 70% and Y6 to 65%. On the other hand, for PTQ10:Y6 *np-BHJ* we obtain a maximum EQE of 61% in the PTQ10 region but only 56% in the Y6 region. Although lower than for organic solvent-based devices, these high EQE values suggest an appropriate active layer morphology of PTQ10:Y6 *np-BHJ*. Devices prepared from organic solvent present also higher V_{OC} than those prepared from water-based colloidal inks, 0.82 and 0.73 V, respectively, but lower FF, 0.50 and 0.65, respectively. Although many factors can affect those characteristics, one can suggest that the change is attributed here to the nanoscale morphology. Indeed, it has been shown that higher degree of organisation of the donor and/or the acceptor generally leads to lower V_{OC} due to energy level splitting and higher FF due to better charge transport.[172–174] Another possible reason for this V_{OC} loss might come from a different molecular orientation of the Y6 molecules in the thin films obtain from water-based and organic solvent-based processes. **Figure 4-7c** is showing a much lower absorbance of PTQ10:Y6 *np-BHJ* than PTQ10:Y6 *BHJ* despite their similar thickness (~115 nm). Such a difference could also be attributed to more mixed orientations of Y6 molecules in PTQ10:Y6 *np-BHJ* reducing the in-plane absorption as reported for another polymer:Y6 system involving two different solution process.[175]

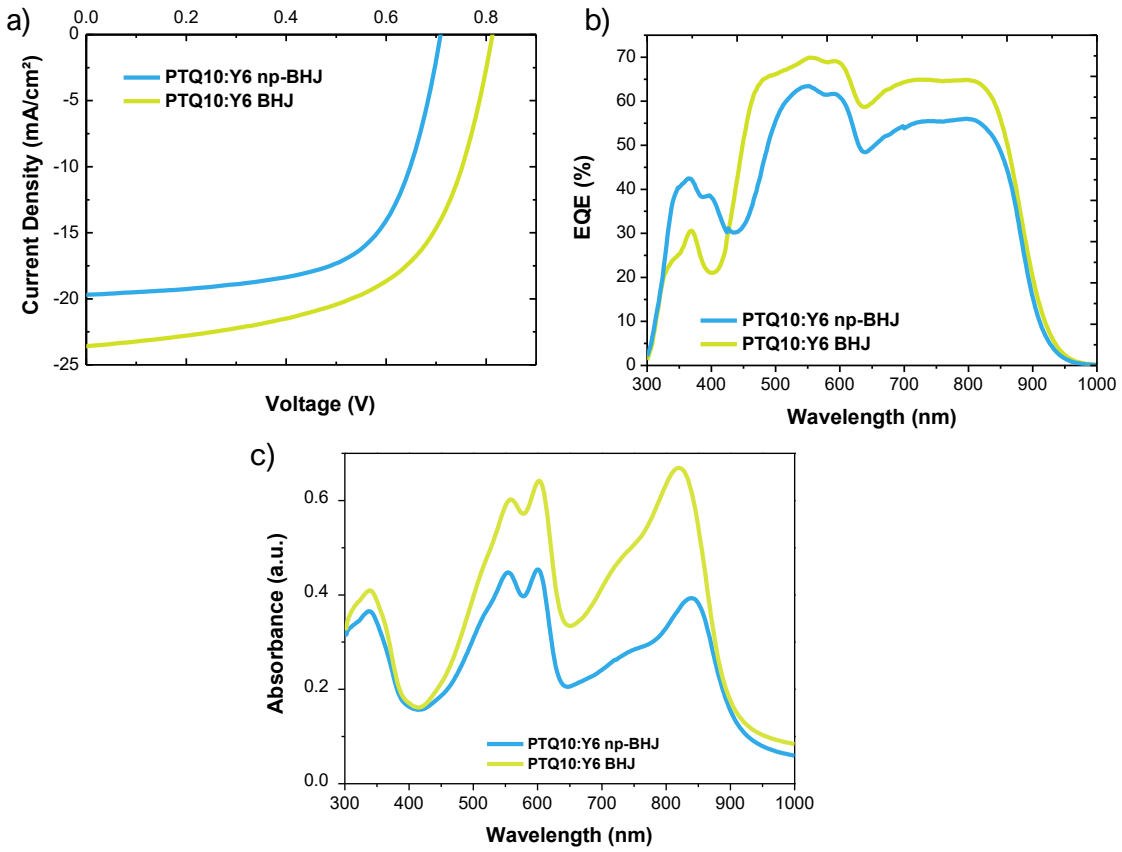

Figure 4-7: (**a**) J-V curves (**b**) EQE and (**c**) UV-vis spectrum for PTQ10:Y6 *np-BHJ* and PTQ10:Y6 *BHJ* at the optimal annealing temperature. Note that the selected curves have been chosen to be as close as the average performance shown in **Table 4-7** and both films measured for the absorbance are ~115 nm thick.

Table 4-7: Average OPV performances of PTQ10:Y6 BHJ PTQ10:Y6 np-BHJ extracted from a minimum of 8 devices at the optimal thermal annealing (best devices are shown in brackets)

	V_{OC} (mV)	J_{SC} (mA cm^{-2})	FF	PCE (%)
PTQ10:Y6 *BHJ*	809 ± 5	23.15 ± 0.07	0.60 ± 0.02	11.19 ± 0.26
PTQ10:Y6 *np-BHJ*	714 ± 15	18.13 ± 1.15	0.62 ± 0.01	8.08 ± 0.53

4.4.3 Discussion

From their OPV devices performances, different behaviour for each system have been observed. PTQ10:$PC_{61}BM$ *np-BHJ* generate much less free charges upon illumination

as compared to the organic solvent-processed devices prepared with 1,2,4-Trimethylbenzene. This poor capability to generate charges is reflected by the low J_{SC} measured. Several thermal treatments have been performed, but none was successful to narrow the gap between the two processes. The EQE measurement highlights a possible high bimolecular recombination rate for the water-processed device, which might be due to the morphology of the active layer. On the contrary, with the low interfacial energy system, the water-processed devices succeed to achieve performances close to the organic solvent-processed counterpart. An important amount of charges are photo-generated and harvested in PTQ10:Y6 *np-BHJ*, an amount which is really close to what is also generated and harvested from the same donor:acceptor system deposited with chloroform (PTQ10:Y6 BHJ). For this system, thermal annealing plays a major role on this spectacular gain of J_{SC} and FF. And despite a lower V_{OC}, more than 70% of the performances obtained with the control cells are reached with PTQ10:Y6 *np-BHJ*.

4.5. Morphological investigation

Results obtained from the OPV cells suggest that there is a morphological difference between both nanoparticle-based systems. For the low $\gamma_{D:A}$ system PTQ10:Y6 *np*-BHJ, this difference still exists initially (i.e. before thermal treatment) but is partially reduced as the annealing temperature increases. The observed differences seem to be even more important when increasing the interfacial energy. Morphological studies were undertaken to explore whether the device performances trends observed could be attributed to a structural change of the nanoparticle-based active layer films. In this respect, two microscopy techniques have been used. First, we have recorded AFM images to gain insights on the surface structure of each *np-BHJ* film system and their evolution with temperature. In order to explore the internal and intraparticle morphology and special composition, the scanning transmission X-ray microscopy (STXM) technique has been use. This technique allows us to map the spatial distribution of each materials in the nanoparticles thanks to their near-edge X-ray absorption proprieties.[176] Transmission electronic microscopy (TEM) images are also combined with STXM for a better understanding of the nanoparticles evolution upon annealing. The primary aim here is to corelate these morphologies to OPV cells performances and/or interfacial energy.

4.5.1 AFM analysis

Figure 4-8 shows 2 µm² topography AFM images of PTQ10:$PC_{61}BM$ *np-BHJ* and PTQ10:Y6 *np-BHJ* for with or without thermal treatment (i.e. none and 200°C).

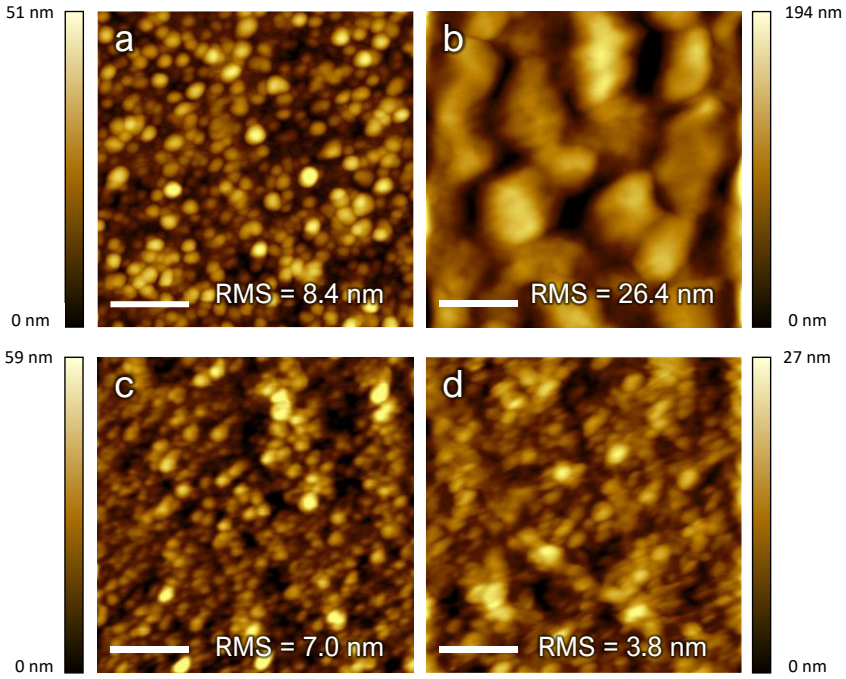

Figure 4-8: AFM topography images (height) of PTQ10:$PC_{61}BM$ (**a**, **b**) and PTQ10:Y6 (**c**, **d**) *np-BHJ* without annealing (**a**, **c**) and with a thermal annealing at 200°C for 5min (**b**, **d**). (Scale bar = 500nm)

We note that for both systems, a relatively high surface roughness is present in the first place (as cast), which is due to the spherical shapes of the nanoparticles. This can imply a poor charge transport between the nanoparticles, thus favouriting the bimolecular recombination that could explain the lower FF and V_{OC} for both type of devices without annealing. For PTQ10:$PC_{61}BM$ *np-BHJ*, despite no significant change in the performances of upon annealing, a drastic modification of the surface morphology is observed. We can clearly observe the surface roughness increases from 8.4 nm to 26.4 nm upon annealing. Such a high roughness coming from a strong phase separation could explain the loss V_{OC} from 0.90 V to 0.69 mV.[177] The opposite trend is observed for PTQ10:Y6 *np-BHJ* as the RMS roughness decreases from 7.0 nm to 3.8 nm. These opposite behaviours upon annealing might come from the interfacial energy difference.

4.5.2 STXM and TEM analysis

In order to get some insights on the composition of the different nanoparticles as well as on the thin films fabricated from the NPs, STXM experiments have been conducted. However, prior to the STXM measurements, the near-edge X-ray absorption fine structure (NEXAFS) spectra of pristine samples of each material (PTQ10, Y6, and $PC_{61}BM$) were recorded and analysed to extract their key absorption energy. Overlaying the spectra of the donor and acceptor of each system is necessary in order to make the selection of their orthogonal energies. From the NEXAFS shown in **Figure 4-9**, the overlay of the PTQ10 and PCBM spectra shows the dissimilarities due to the difference atomic composition between the polymer and the fullerene. Therefore, the choice of two key absorption energies that are 288.1 eV (PTQ10) and 284.4 eV ($PC_{61}BM$) has been made. Looking now at the second spectrum for PTQ10:Y6, both NEXAFS are showing comparable signature, which is not surprising as we find the same type of atoms in both materials. With only a simple choice of two orthogonal energies, it has been thus impossible to obtain reliable compositional maps. A selection of three energies has been made in order to correctly build the compositional maps: 284.0 eV (Pre-edge), 285.1 eV and 293.0 eV. Sequentially using these energies during the STXM measurement leads to generate a compositional map of each blend. More description about NEXAFS and STXM are available in the **Methods** section.

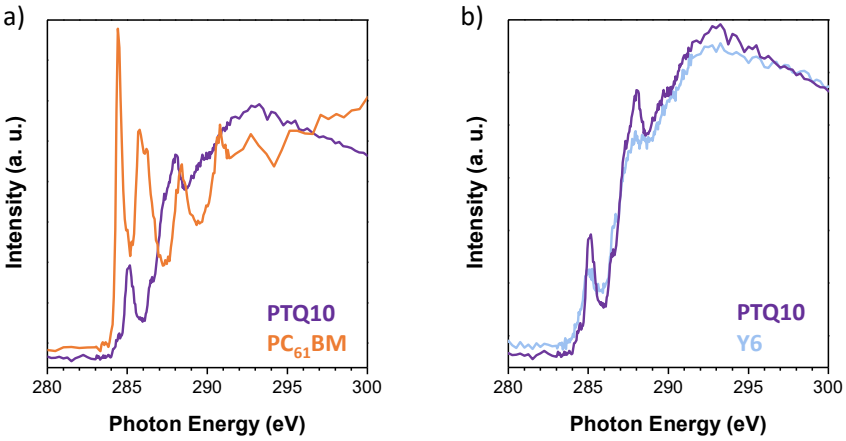

Figure 4-9: NEXAFS spectra for the pure materials (a) PTQ10 and $PC_{61}BM$ overlapped (purple and orange respectively, (b) PTQ10 and Y6 overlapped (purple and blue respectively).

Consecutively, samples were prepared for STXM measurements following the preparation process described in the **Methods** section. It is important to mention that due

to the spectral resolution available for STXM (~25 nm), bigger particles were synthesised for this study than the actual nanoparticles diameter used for the solar cells. With the aim of identifying the nanoparticles morphology down to the resolution limit, we propose to interpret trends in smaller nanoparticle data with the results of STXM studies on large nanoparticles, assuming that the morphology does not change with the size of the nanoparticle. Therefore, high polydisperse nanoparticle inks (100 nm – 400 nm) were prepared using a much lower SDS concentration (0.01 mg ml^{-1}).

First measurements were done on "as cast" nanoparticle films, in order to observe the internal morphology of each system right after their synthesis. Taking a first look at PTQ10:$PC_{61}BM$ NPs (**Figure 4-10a**), a core–shell type morphology is observed. While the shell is PTQ10-rich (75–90%), it is interesting to note that the composition of the core is more intermixed, but still acceptor-rich with around 60% of $PC_{61}BM$ and 40% of PTQ10 (**Figure 4-13a**). In **Table 4-2** one can observe that $PC_{61}BM$ has a much larger surface energy (35.1 mN m^{-1}) than PTQ10 (23.1 mN m^{-1}), similarly to other kinds of donor/fullerene systems (P3HT:$PC_{61}BM$, TQ1:$PC_{61}BM$). This difference explains the nanomorphology of the PTQ10:$PC_{61}BM$ nanoparticles, with the outer shell predominantly composed of the lower surface energy element. Even though core–shell with a highly donor-rich core, previous PL results showed that exciton dissociation is highly efficient in the PTQ10 region. Nevertheless, this morphology driven by the surface energies seems not adapted to a nanoparticles-based organic photovoltaic device. The presence of an almost pure PTQ10 shell around the intermixed core can impede the electron transport. Thermal annealing should in theory allow the creation of transport pathways, but the strong phase separation upon annealing is predominant as previously seen in AFM images.

The thermal annealing at 200 °C has a dramatic effect on the phase separation between PTQ10 and $PC_{61}BM$ as previously observed in the AFM images. **Figure 4-10b** & **10d** shows large clusters (2 - 4 µm) composed mostly of PCBM (≈ 62%) surrounded by PTQ10 highly rich areas (≈ 89%). This tendency to phase segregate is the result of the high interfacial energy between the donor and the acceptor in addition to the high energy brought by the annealing. One can notice that the spherical shape cannot be seen anymore, indicating that the nanoparticles have merged in the form of a thin film. As expected, this evolution of the active layer morphology with large scale separated domains did not lead to an improvement of the OPV performance. Thermal annealing at 140°C, 170°C or 200°C of

PTQ10:$PC_{61}BM$ *np-BHJ* resulted in devices with 1.01%, 0.93% and 1.02% PCE, respectively.

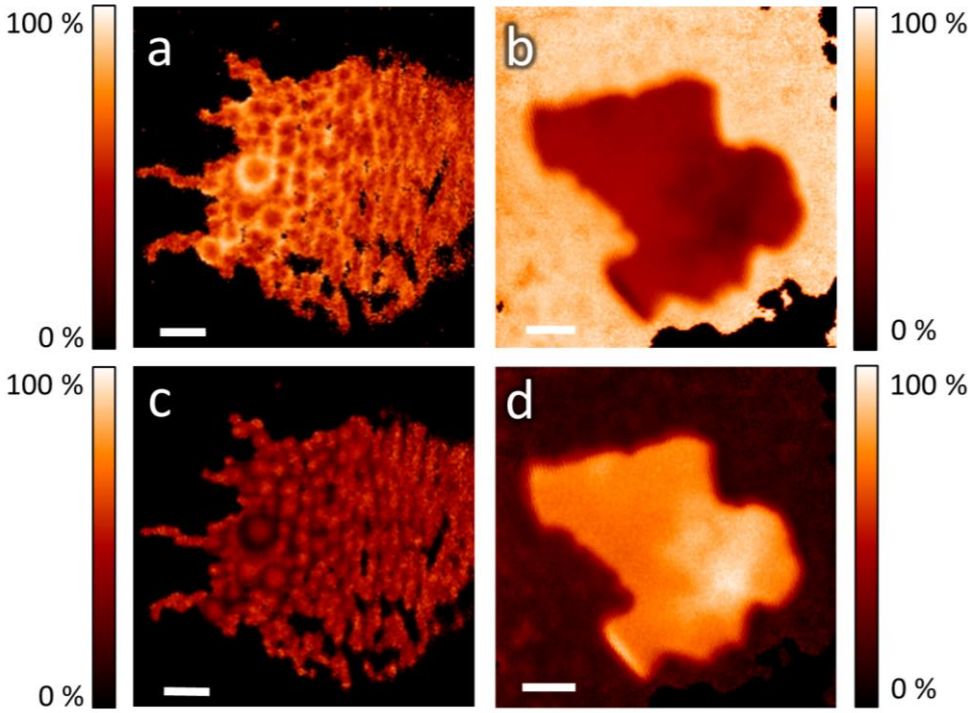

Figure 4-10: STXM composition maps of PTQ10:$PC_{61}BM$ NPs without thermal treatment: relative concentration of (a) PTQ10 and (c) $PC_{61}BM$. With a 200 °C thermal treatment for 5 min: relative concentration of (b) PTQ10 and (d) $PC_{61}BM$. All scale bars are 500 nm. The color contrast is scaled such that light colors correspond to higher component concentrations.

Now moving to the promising PTQ10:Y6 nanoparticles nanomorphology, the STXM images do not show a clear phase separation within the nanoparticles for which the morphology seems to be intermixed. The radial composition profile for this donor:acceptor system (**Figure 4-13b**) is showing no clear trend in phase separation within the error bars, indicating non-defined domains. This analysis reveals that the initial morphology of PTQ10:Y6 nanoparticles is intermixed or with very small subdomains below the resolution limit of STXM. This kind of morphology, already observed for nanoparticles synthesised by nanoprecipitation, is rather uncommon for mini-emulsion based nanoparticles.[113] In few cases intermixed morphology was identified as for PTB7-Th:eh-IDTBR nanoparticles synthesised by the mini-emulsion process using TEBS as a surfactant. In the case of PTQ10:Y6, the surface energy difference between the donor and the acceptor is much lower than that of PTQ10:$PC_{61}BM$, 5 mN m^{-1} and 12 mN m^{-1} respectively (**Table 4-2**).

According to Barr *et al.*, the lower the surface energy difference, the closer the nanomorphology is to an intermixed morphology which is a first explanation of the morphology observed for the PTQ10:Y6 system.

Compared to the higher $\gamma_{D:A}$ system, the thermal annealing has a totally different effect on PTQ10:Y6 *np-BHJ*. As seen in Figure 4-11**b** & **e**, with a thermal annealing treatment at 170 °C, it is still possible to detect the intermixed morphology within a single composite nanoparticle, with here again randomly distributed donor-rich and acceptor-rich domains. With a thermal annealing treatment at 200 °C, nanoparticles partially sintered together, thus removing the grain boundaries. Interfacial energy between PTQ10 and Y6 is only 4.5 mN m^{-1} and such a low value can explain the stability of the nanoscale morphology and the absence of large phase separation upon thermal treatment. TEM images of unannealed samples and samples annealed at 100, 140, 170 and 200 °C, reveal that high temperatures are necessary to merge the nanoparticles (**Figure 4-12**). Without thermal treatment, nanoparticles are well separated and the boundaries between two particles are still visible. At low annealing temperatures of 100 and 140 °C, the particle shape is still clearly visible but coalescence of the nanoparticles starts: the boundaries between them are not as clear as for unannealed nanoparticles. At 170 °C, the coalescence process is more pronounced as the boundaries between the particles are fading away, but the shape of the nanoparticles is still clearly observable. Finally, at 200 °C, the coalescence of the particles is fully effective. Although, it is still possible to identify the original nanoparticle shape, they have all merged into a homogeneous thin film. The evolution of the photovoltaic performance reflects that of the morphology detected by STXM and TEM. Concomitantly, the nanoscale morphology is not affected even at high annealing temperature and nano-domains of donor and acceptor materials with size approaching the resolution of STXM are still detected within a single nanoparticle.

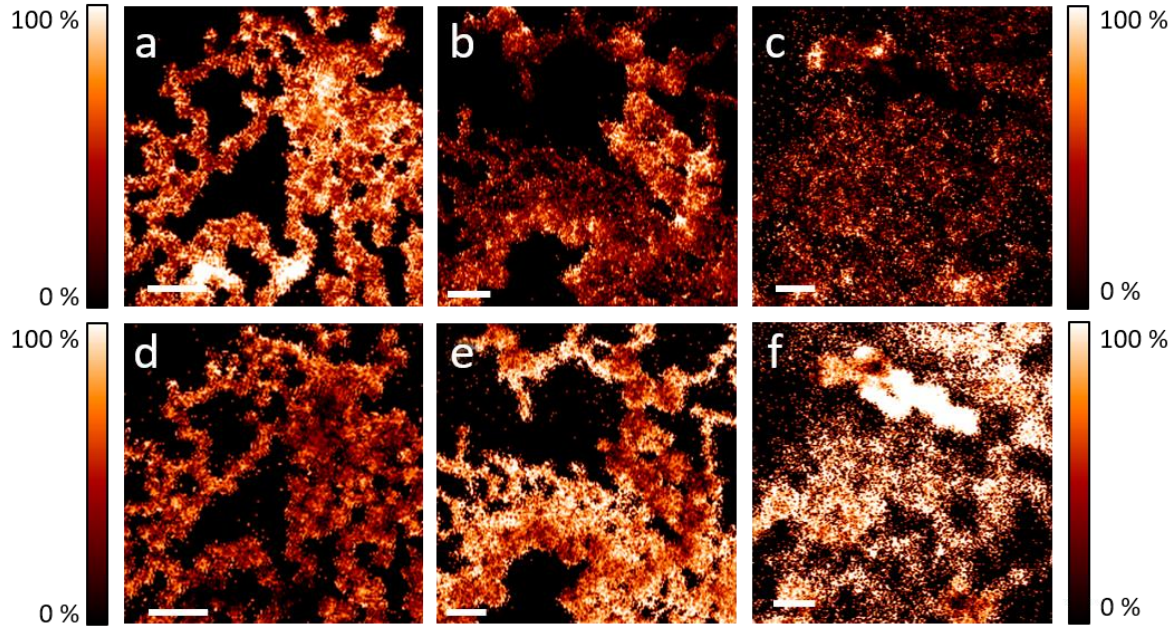

Figure 4-11: STXM composition maps of PTQ10:Y6 nanoparticles without thermal treatment: relative concentration of (a) PTQ10 and (d) Y6. With a 170 °C thermal treatment for 5 min: relative concentration of (b) PTQ10 and (e) Y6. With a 200 °C thermal treatment for 5 min: relative concentration of (c) PTQ10 and (f) Y6. All scale bars are 500 nm. The color contrast is scaled such that light colors correspond to higher component concentrations.

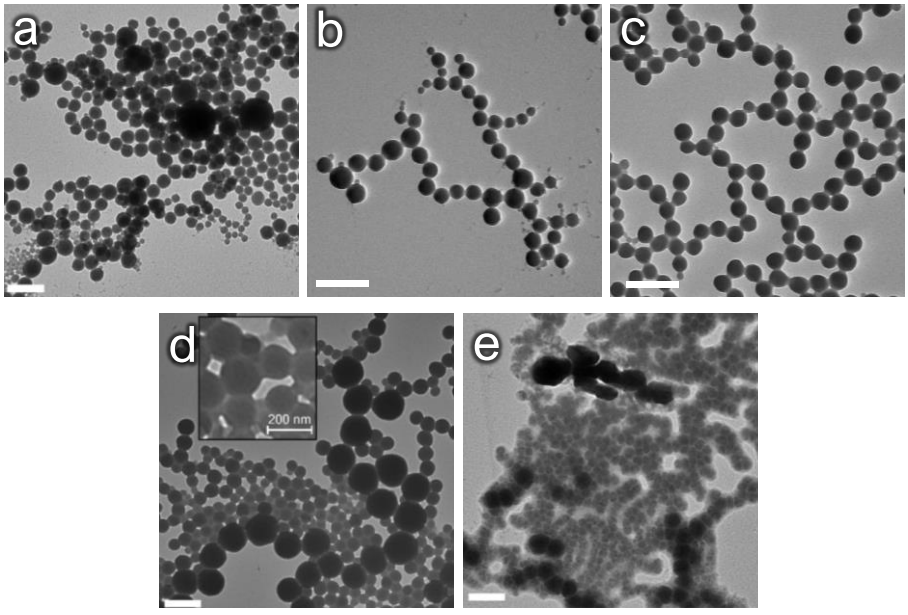

Figure 4-12: TEM images of PTQ10:Y6 NPs without thermal annealing (**a**) and annealed at (**b**) 100 °C, (**c**) 140 °C, (**d**) 170 °C and (**e**) 200 °C. All scale bars are 500 nm.

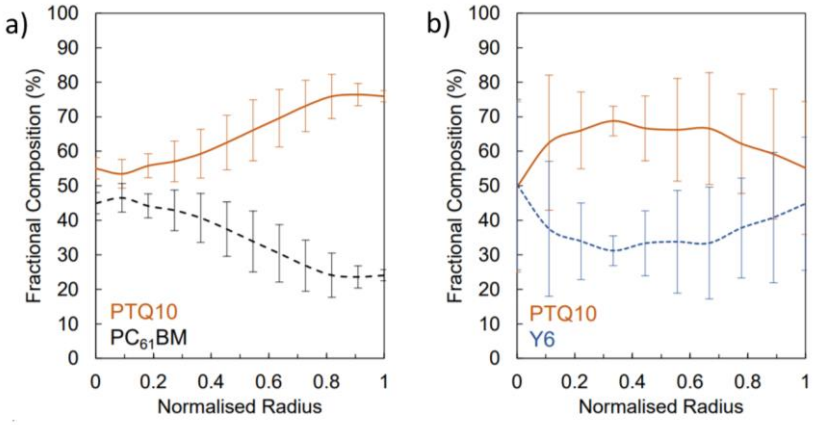

Figure 4-13: (**a**) Average radial composition profiles of (**a**) PTQ10:$PC_{61}BM$ nanoparticle (unannealed) and (**b**) PTQ10:Y6 nanoparticle (unannealed). The error bars represent the standard deviation between multiple particles of the same type.

4.5.3 Discussion

The results obtain from this morphological investigation lead us to propose the following tentative mechanism (**Figure 4-14**). PTQ10:$PC_{61}BM$ nanoparticles present initially a core–shell morphology due to high surface energy difference between the donor and the acceptor. Upon high thermal annealing (200°C), a large phase separation is observed due to high interfacial energies which already tend to noticeably separate the two materials. As a result, PTQ10:$PC_{61}BM$ nanoparticle-based devices present low efficiency as compared to those prepared from organic solvent, only 40% of the PCE achieved from PTQ10:$PC_{61}BM$ *BHJ* is obtained with PTQ10:$PC_{61}BM$ *np-BHJ*. Without a sufficient annealing, transport pathways are limited by the nanoparticle's boundaries. These boundaries are broken with a high temperature annealing, but it also creates the large phase segregation. A good balance is thus hard to obtain and almost impossible with that kind of high interfacial energy system. On the contrary, PTQ10:Y6 nanoparticles prepared by mini-emulsion present initially a donor:acceptor morphology that is intermixed. However, performances of the devices are poor if the active layer is only annealed at low temperature, due to a lack of transport pathways. Therefore, a high annealing temperature is necessary in order to sintered the nanoparticles together and allowed the photogenerated charges to reach their respective electrodes. In order to achieve its full photovoltaic efficiency, interconnection of the nanoparticles, and ultimately of the domains, while preserving an intermixed

morphology between the donor and the acceptor is required. As the performances of PTQ10:Y6 *np-BHJ* devices get really close to PTQ10:Y6 *BHJ* devices, it is safe to argue that the final morphology of these water-based devices is really close to a bulk-heterojunction morphology obtained by depositing the active layer with chloroform.

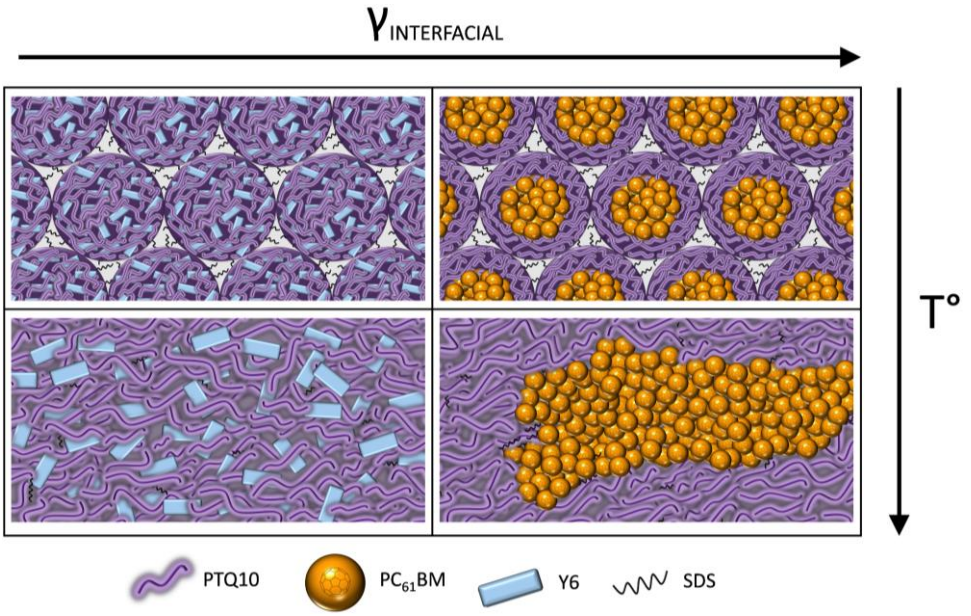

Figure 4-14: Schematic diagram of morphological changes in PTQ10:Y6 (left) and PTQ10:$PC_{61}BM$ (right) films upon thermal annealing

4.6. Towards improvement of PTQ10:Y6 *np-BHJ*

At this point of this study, PTQ10:Y6 *np-BHJ* is undoubtedly the most performing nanoparticles system studied until now. With an average PCE of 8.08%, it is already the highest value reported for an OPV device made from nanoparticles synthesised by the mini-emulsion technique. Up to now, only the optimisation of the thermal annealing temperature has been done. We propose in this section to extend the study of PTQ10:Y6 *np-BHJ* through several optimisation steps (e.g. thickness, nanoparticle size, annealing duration…). Doing so, we aim to reduce the gap with its organic solvent-processed counterpart and bring to light the manifest potential of water-based process for the photoactive layer. A further understanding about the dependence of the performances with the annealing temperature is also needed and will be discussed using differential scanning calorimetry (DSC) and thermogravimetric (TGA) analysis. Cryo-TEM has been also used as well to gain so insight on the arrangement of the material within the nanoparticle.

4.6.1 Thickness dependency

One of the main challenges for OPV devices remains their ability to meet the lab-to-fab processing requirements and lower the large efficiency gap between the experimental results in laboratories and the practical commercial production. This gap is largely due to the thickness difference between what is done in research laboratories and the upscaling requirements. In the literature, most optimal thickness of the active layer are found to be around 100 nm.[178] However, such thin films are extremely challenging to realise at a larger scale and are not compatible with high-throughput processing. Therefore, to accomplish this lab-to-fab transition, we need materials with constant performances despite changes in thickness. Increasing thickness can obviously boost the absorption, but there are multiple drawbacks such as limited charge mobilities or the increase in recombination rates.[179] Studying the impact of the active layer thickness on the performances of PTQ10:Y6 *np-BHJ* devices will allow to gain insight in the system resiliency when changing thickness.

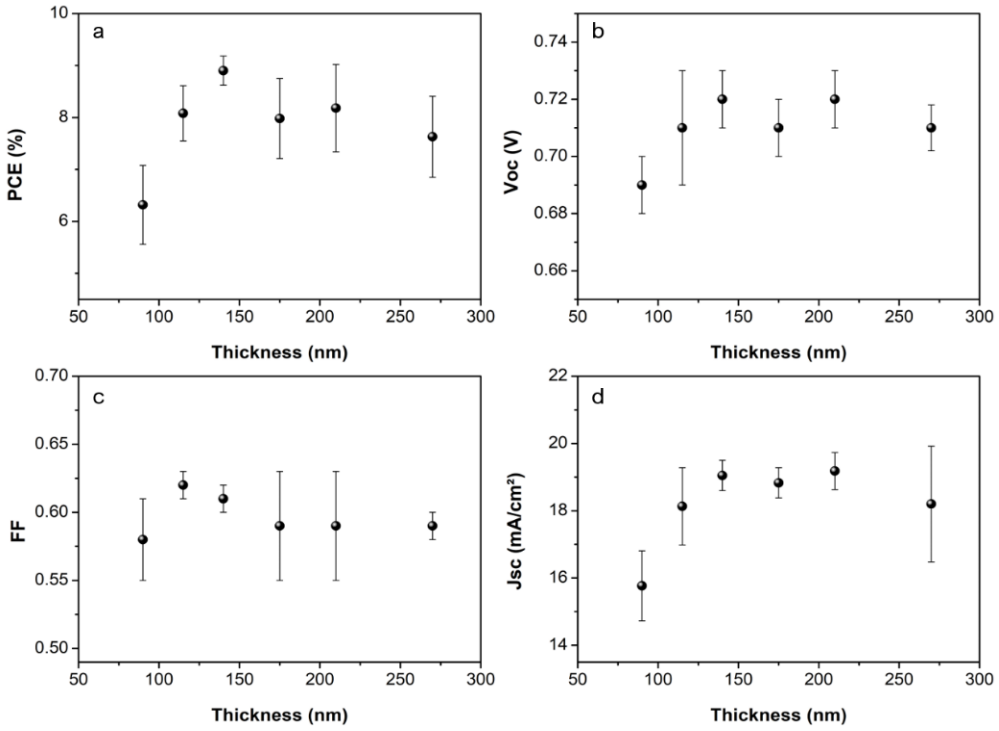

Figure 4-15: (**a**) PCE, (**b**) V_{OC}, (**c**) FF and (**d**) J_{SC} vs thickness of PTQ10:Y6 np-BHJ. Error bars represent the standard deviation for a minimum of 4 replicate devices

Table 4-8: OPV parameters vs thickness of PTQ10:Y6 *np-BHJ*. Error values represent the standard deviation for a minimum of 4 replicate devices

	Thickness (nm)	Shunt R (kΩ)	V_{OC} (mV)	J_{SC} (mA cm^{-2})	FF	PCE (%)
PTQ10:Y6 *np-BHJ*	90	38	689 ± 16	15.77 ± 1.15	0.58 ± 0.03	6.32 ± 0.76
	115	243	714 ± 15	18.13 ± 1.15	0.62 ± 0.01	8.08 ± 0.53
	140	168	723 ± 7	19.05 ± 0.45	0.65 ± 0.01	8.90 ± 0.28
	175	131	714 ± 14	18.83 ± 0.45	0.59 ± 0.05	7.98 ± 0.77
	210	202	720 ± 14	19.18 ± 0.55	0.59 ± 0.05	8.18 ± 0.84
	270	3.7 10^4	710 ± 8	18.17 ± 1.76	0.59 ± 0.01	7.63 ± 0.78

Figure 4-15 and **Table 4-8** show the evolution of the performances of the *np-BHJ* devices having the active layer varying from 90 nm to 200 nm. A thermal annealing was performed at 200°C for 5 min for each device. An increase of the J_{SC} and the V_{OC} with increasing the thickness from 90 nm to 140 nm is observed, resulting in an optimal PCE of 8.90%. As previously mentioned, a water-processable active layer is easily subject to de-wetting point when spin-coating the dispersion, and the thinner the film is the easier is the formation of dewetting points. For 90 nm, the low V_{OC} measured might result to a dependency with the low shunt resistance observed for such a thin film. Interestingly, PTQ10:Y6 *np-BHJ* demonstrates a broad thickness tolerance as only a loss of 14% of the maximum PCE is observed for a thick film of 240 nm. In this regard, this water-based system is comparable to its counterpart organic solvent-based as it experiences similar resiliency to thickness changes and remains a good candidate for a potential upscaling.[180] This is not surprising as the performances dependence on the thickness is usually arising from a morphology dependence. But in our case, the morphology is set by the nanoparticles should not change upon increasing the thickness.

4.6.2 Annealing duration dependency

The time duration during which the nanoparticulate film was annealed has also been investigated (**Table 4-9**). However, only the optimal annealing temperature of 200°C previously shown has been consider in this section, no time-dependency for the lower temperature are presented here. Three annealing duration have been carried out that are 2 min, 5 min and 10 min. A clear trend is observed when varying the treatment duration, the shorter the annealing is, the higher are the performances. Except for the FF which is identical for 2 and 5 min, both the J_{SC} and the V_{OC} are enhanced when annealed for only 2 min. When increasing the time to 10 min, this sustained thermal annealing might induce the separation of the donor and acceptor phase leading to a degraded morphology. However, it is hard to determine the exact reason as no similar trend has been reported at such a high temperature. Another pathway of degradation could be the diffusion of the ZnO layer into the active layer.[181]

Table 4-9: Average OPV performances of PTQ10:Y6 np-BHJ (active layer thickness = 140 nm). Influence of the thermal annealing (TA) time. Average values given for 8 individual devices (record cell in brackets)

	TA (min)	V_{OC} (mV)	J_{SC} (mA cm^{-2})	FF	PCE (%)
PTQ10:Y6 *np-BHJ*	2	731 ± 3 (733)	19.93 ± 0.07 (19.96)	0.65 ± 0.00 (0.66)	9.49 ± 0.10 (9.60%)
	5	723 ± 7 (727)	19.05 ± 0.45 (19.52)	0.65 ± 0.01 (0.66)	8.90 ± 0.28 (9.36%)
	10	725 ± 3 (727)	19.30 ± 0.33 (19.49)	0.63 ± 0.01 (0.62)	8.77 ± 0.06 (8.85%)

4.6.3 Nanoparticles diameter

Herein, PTQ10:Y6 nanoparticles diameter have been varied to assess the impact of the later on OPV performances. In order to change the size of the nanoparticles, we used two different strategies. For the first one, the sonification parameters have been varied through the power and the duration involve during the sonification step, which has proven to be an efficient way to easily change the average nanoparticles diameter.[139]

We have focused our study on two different sonification power that are 40 W and 70 W, as well as two sonification duration, 1 min and 2 min. From these parameters, we have obtained three different diameters of 84 nm, 72 nm and 63 nm (**Table 4-10** & **Figure** 4-16**a**)**.** No devices have been fabricated with these batches, but the UV-visible spectra along with the PL emission spectra for the varying diameters are presented in **Figure 4-16b** & **Figure 4-16c** respectively.

Table 4-10: Evolution of the nanoparticle size according to different sonification parameters.

Power (W)	time (min)	Average NPs diameter (nm)
40	1	84 ± 40
40	2	72 ± 30
70	2	63 ± 30

Looking at the UV-visible spectroscopy measurements, the spectral signatures of the three dispersions are similar and are showing the same features as previously seen. The PL emission spectra are showing much more difference when varying the diameter as a clear reduction of the Y6 emission signal is observed with the decrease of the diameter. This is particularly obvious when going from the sonification parameter of 1 min at 40 W (84 nm) to 2 min at 40 W (72 nm) for which we observed a decrease of the emission signal by 15 %. In this case, a decrease of the nanoparticle size might imply a decrease of the Y6 domains, minimising therefore the radiative recombination and thus improving the exciton dissociation rate. Concerning the PTQ10 signal, for all nanoparticle diameters, no emission is observed even for the large particle, indicating smaller PTQ10 domain size than Y6 are present in the nanoparticles. As a consequence, radiative recombination in PTQ10 is not affected by the nanoparticle diameter.

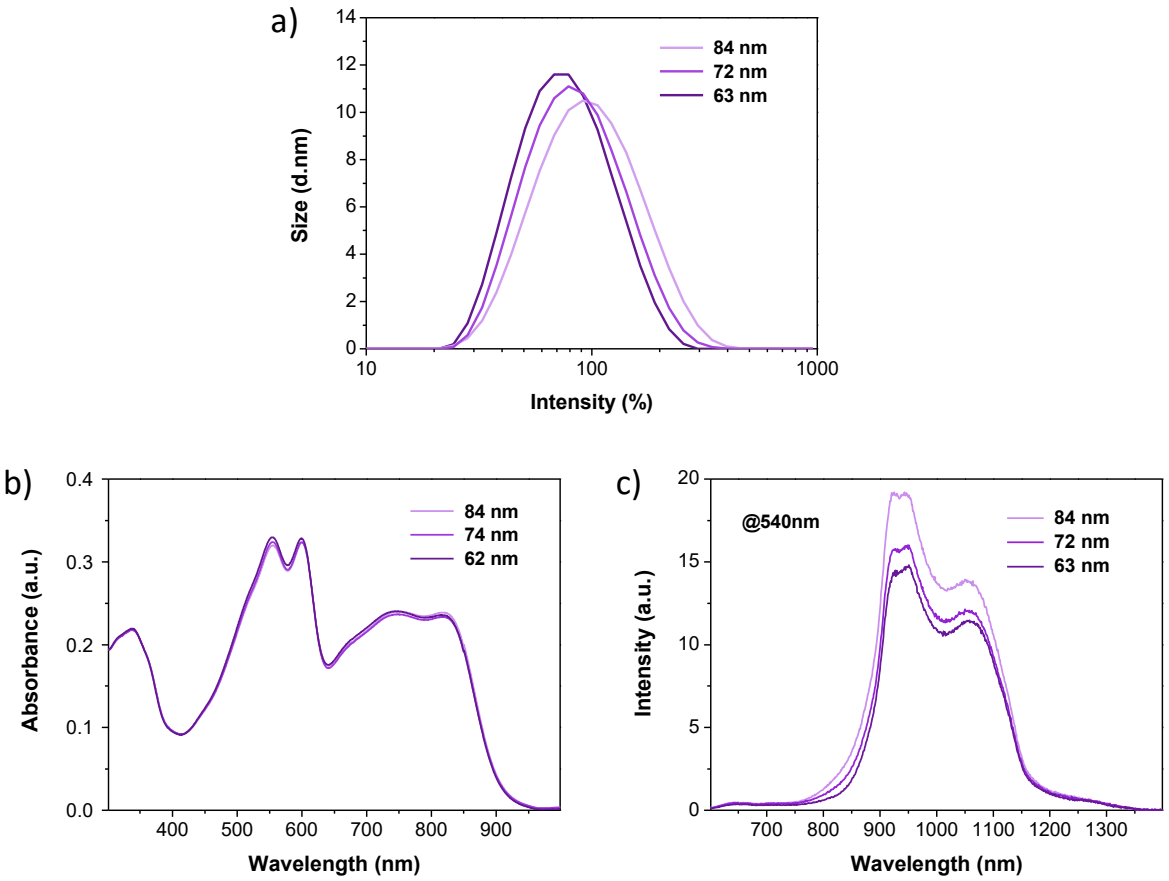

Figure 4-16: (**a**) DLS measurements with varying the sonification conditions. (**b**) Absorption spectra of PTQ10:Y6 nanoparticles dispersions for three different nanoparticle diameter and (**c**) photoluminescence spectra of PTQ10:Y6 nanoparticles dispersions for three different nanoparticle size after excitation at 540 nm. (dispersions concentration = 0.03 mg ml^{-1})

For the second strategies, only the concentration of the organic phase has been varied as this one has a strong impact on the nanoparticle size.[182] Using three different concentrations (i.e. 35 mg ml^{-1}, 25 mg ml^{-1} and 15 mg ml^{-1}) it was expected to measure a decrease in the nanoparticle's average diameter with a decrease of the organic phase concentration. However, in order to facilitate and to keep the centrifugal dialysis step unchanged, the total active material weight has been kept constant. As a consequence, the volume of the organic phase with the lowest concentration was larger than for the highly concentrated one (see **Figure 4-17**), resulting in three different volumes of macro-emulsion.

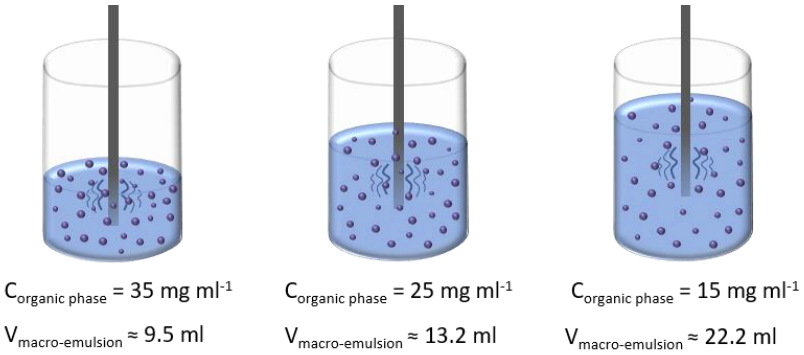

Figure 4-17: Schematic representation of water-based dispersions during the sonification step illustrating the difference in power density due to a volume change in the macro-emulsion solution.

Despite this change in the volume, the duration of the sonification and its power were kept the same (60 W, 2 min). In other words, the power density per volume unit applied was higher for the low volume macro-emulsion (35 mg ml^{-1}) than for the large volume macro-emulsion (15 mg ml^{-1}). Therefore, the obtained trend in the average nanoparticle diameter was the opposite to the expected one. A decrease in the average diameter of the nanoparticles was obtained with a diameter as low as 55 nm for the small volume batch (C = 35 mg ml^{-1}, V = 9.5 ml), while increasing this volume gave rise to nanoparticle diameter of 65 nm (C = 25 mg ml^{-1}, V = 13.2 ml) and 80 nm (C = 15 mg ml^{-1}, V = 22.2 ml). The smaller diameter was found to give the best performances with a remarkable increase in the J_{SC} from 18.86 mA cm^{-2} for the large particles to 21.14 mA cm^{-2} with 55 nm diameter, leading to 9.55% average PCE. This trend is in accordance with the previous PL measurements that are showing a better quenching of the Y6 emission when the diameter is smaller, leading to higher charge generation.

Table 4-11: Average OPV performances of PTQ10:Y6 *np-BHJ* (active layer thickness = 140 nm). Influence of the average nanoparticle diameter. Average values given for 8 individual devices (record cell in brackets)

	NPs average diameter (nm)	**V_{OC} (mV)**	**J_{SC} (mA cm^{-2})**	**FF**	**PCE (%)**
PTQ10:Y6 *np-BHJ*	80 ± 30	723 ± 11 (723)	18.86 ± 0.48 (19.38)	0.62 ± 0.01 (0.63)	8.40 ± 0.27 (8.83)
	65 ± 30	723 ± 7 (727)	19.05± 0.45 (19.52)	0.65 ± 0.01 (0.66)	8.90 ± 0.28 (9.36)
	55 ± 30	722 ± 4 (728)	21.14 ± 0.24 (21.39)	0.62 ± 0.02 (0.64)	9.55 ± 0.27 (9.98)

Nonetheless, looking closely to the EQE (**Figure 4-18b**), the contributions of both PTQ10 and Y6 have been enhanced by the reduction of the nanoparticles diameter. Therefore, as the charge generation from the photon absorbed in PTQ10 was already very efficient, an additional phenomenon might be occurring. Decreasing the size of the particles could be beneficial for the sintering of the nanoparticles, which would lead to more favourable charge transport pathways.

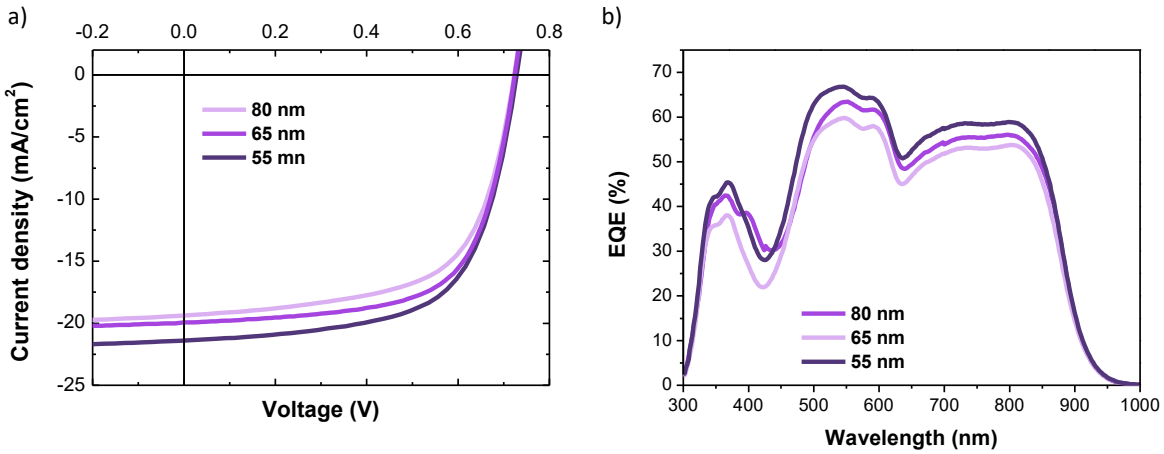

Figure 4-18: (a) J-V curves and (b) EQE for PTQ10:Y6 *np-BHJ* with varying the nanoparticles diameter. Note that the selected curves have been chosen to be as close as the average performance shown in **Table 4-11**.

4.7. Further understanding of PTQ10:Y6 *np-BHJ*

In order to understand the necessity of having high thermal annealing temperature to reach the optimised efficiencies, we investigated the transitions happening at 170°C, and most importantly at 200°C. We showed that this temperature is essential to sinter the nanoparticles and thus to reach such high efficiencies for a water-based device. Two effective analytical tools have been used, thermogravimetric analysis (TGA) and differential scanning calorimetry (DSC) measurements. The first one has been performed to get information on the temperature at which the active layer materials and the surfactant degrade. The second is helpful to understand the different transitions in the pure material or blends such as the determination of melting and crystallisation temperature. More discussion and details about these techniques are available in the **Methods** section.

4.7.1 TGA analysis

TGA was performed on pure materials SDS, Y6 and PTQ10 (**Figure 4-19a**) and on PTQ10:Y6 NPs with different annealing conditions: no annealing, 2 min at 200 °C and 5 min at 200 °C (**Figure 4-19b**). Focusing on single materials, one can observe that the main degradation of the two organic semiconductors happens at high temperatures, 350 – 450 °C for PTQ10 and between 300 – 475 °C for Y6. On the other hand, SDS degradation begins much sooner, between 180 and 300 °C.

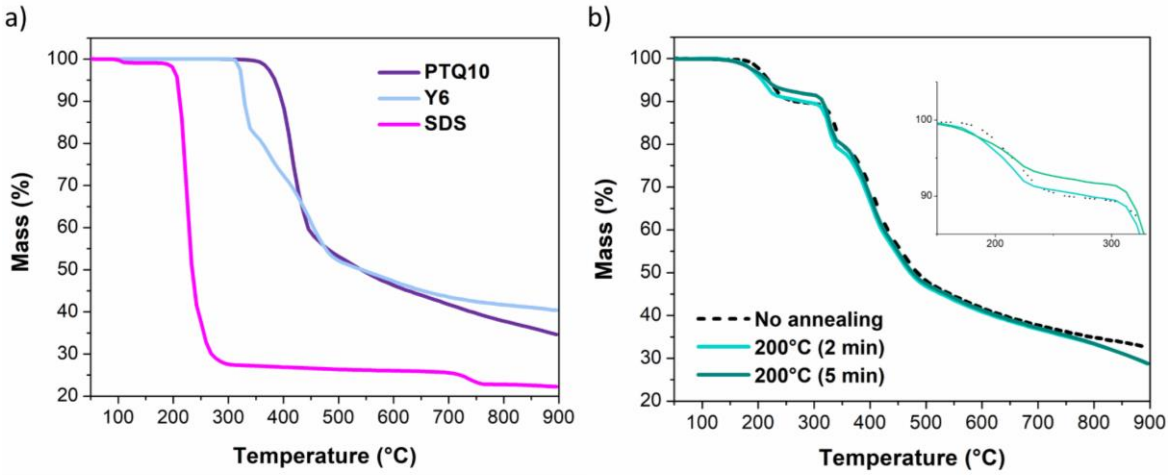

Figure 4-19: (a) Thermogravimetric analysis on PTQ10, Y6 and SDS and (b) as well as on PTQ10:Y6 NPs with different thermal treatment: no annealing, 2 min at 200 °C and 5 min at 200°C. Inset in panel (b) zoom in the degradation of SDS between 150 and 330 °C.

For PTQ10:Y6 NPs, the aim is to detect and estimate the remaining SDS content. For unannealed materials, the proportion of SDS (weight%) with respect to the overall mass is estimated at 15w% according to TGA. This SDS value is expected to be the minimal SDS amount required for stabilisation of the nanoparticles since five washing steps were performed. Interestingly, when the nanoparticles are exposed to a thermal annealing treatment at 200 °C prior to TGA, this proportion decreases down to 14w% and 11w% for 2 min and 5 min at 200 °C respectively. Therefore, the thermal annealing at 200 °C seems to favour the elimination of SDS surfactant through a degradation process. Yet, it seems that 14w% remaining SDS is already sufficiently low not to impact the performances. Indeed, based on this analysis, a thermal treatment at 200°C for 5 min will give a lower SDS

amount (11w%) in the film than the same treatment but for a shorter time of 2 min (14w%). However, we observed higher performances for the shortest duration thermal treatment in the annealing duration study (**Paragraph 4.6.2**). We would have expected that the decrease of SDS amount would enhance the performances as we reduce the presence of an insulating material in the active layer. However, the trade-off time-temperature of the annealing might dominate in this case as the optimised morphology is reached for a short annealing duration and the decrease of 3w% might not be significant to see any improvement.

4.7.2 DSC analysis

Differential scanning calorimetry (DSC) measurements have be ran under a nitrogen environment on four different samples that are PTQ10, Y6, SDS and PTQ10:Y6 nanoparticles. For each sample, the temperature was increased from 25°C to 200°C at 10 °C min^{-1}, then cooled down to 25 °C following the same ramp. For pure materials (PTQ10, Y6 and SDS), this process was repeated for a second cycle. For PTQ10:Y6 NPs, only one cycle was performed, in order to observe the transitions happening during the thermal annealing when preparing OPV devices.

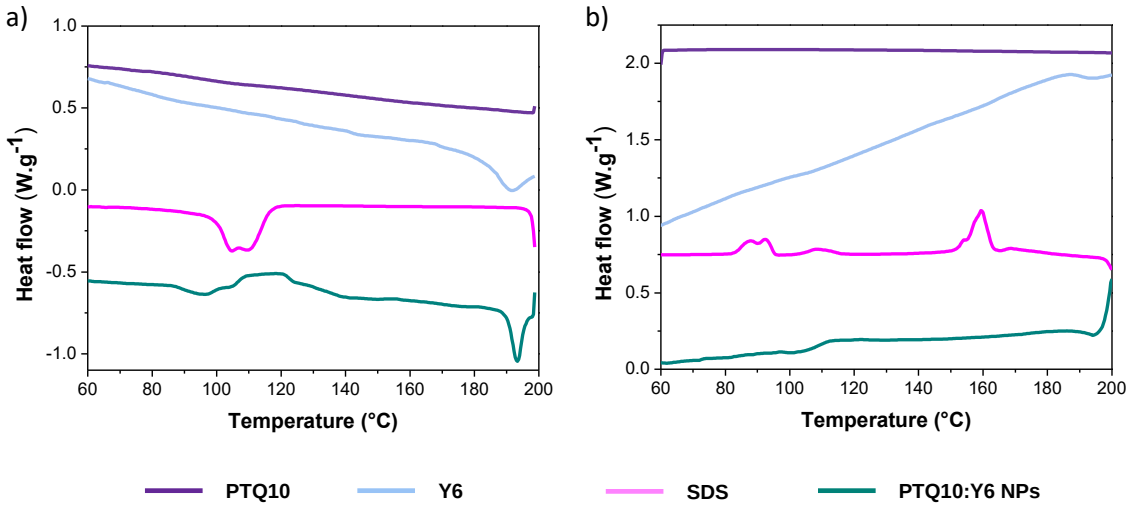

Figure 4-20: (**a**) Heating and (**b**) cooling thermograms of PTQ10, Y6, SDS and PTQ10:Y6 NPs.

The DSC thermogram of PTQ10 did not show any features during heating and cooling ramps in the range of temperature measured in accordance with previous

literature,[46,183] indicating that no measurable phase transition happens up to 200 °C (**Figure** 4-20**).** Neat Y6 is clearly different and present an endothermic peak at 192 °C on the heating trace (**Figure** 4-20**a**) and exothermic one at 183 °C on the cooling traces (**Figure** 4-20**b**). They correspond respectively to the melting and recrystallisation of Y6 crystals[184,185]. The heating thermogram of SDS reveals that the surfactant shows a broad endothermic peak centred around 105 °C, attributed to the fusion of SDS crystals (**Figure** 4-20**a**). PTQ10:Y6 NPs first heating thermogram present three peaks: an endothermic peak centred at 96 °C which corresponds to the fusion of SDS crystals, quickly followed by an exothermic broad peak centred at 120 °C. The origin of this second peak can be related to Y6 cold crystallisation,[186] probably helped by the mobility gained from SDS melting. The cold crystallisation means that the mini-emulsion process and the interaction with PTQ10 or SDS does not allow complete crystallisation of the acceptor. This also reveals that the crystalline volume of Y6 in the nanoparticles can be increased by thermal annealing. Finally, a third endothermic peak is measured at 193 °C, corresponding to the melting of Y6 crystalline domains. This temperature corresponds precisely with the sharp increase of OPV performance and the sintering of the PTQ10:Y6 nanoparticles observed in TEM images. Therefore, one can suggest that the sintering of the nanoparticles is linked to the degree of crystallinity in the nanoparticles.

4.7.3 Cryo-TEM analysis

Cryogenic Transmission Electronic Microscopy (Cryo-TEM) is a powerful tool allowing the characterisation of organic semiconductor assemblies in solution. This technique has shown good capability to reveal the orientation of several material and highlighted theirs crystallinity[187],[123]. Here, images were taken on water dispersed PTQ10:Y6 NPs to confirm the presence of crystalline domains within the composite nanoparticles prepared by mini-emulsion (**Figure 4-21**). Images do not show any contrast but clearly show lamellar arrangements in different areas for a single composite PTQ10:Y6 nanoparticle, confirming therefore its poly-crystalline nature. One can observe a homogenous distribution of these crystalline domains in the nanoparticle, which is suggesting more a distributed nano-domains morphology than a closely intermixed morphology as previously described.

It is therefore quite manifest that the high temperature required to reach the optimal performances is set by the poly-crystalline nature of the PTQ10:Y6 nanoparticles prepared with the mini-emulsion method. The crystalline domain can only be melted at high temperature, and this melting is crucial to sintered the nanoparticles together. As we have already pointed out, the appropriate temperature for the annealing differs a lot from the same nanoparticles prepared with the nanoprecipitation method. It was therefore interesting to compare the physio-chemical features of PTQ10:Y6 prepared by the two methods. In **Figure 4-22a**, the thermograms collected from the two methods are shown. The previously observed Y6 melting and crystallisation features for the mini-emulsions based nanoparticles do not appear for the nanoparticles prepared with nanoprecipitation, resulting in a featureless thermogram in both cooling and heating trace. Another major difference can be spotted when looking at the cryo-TEM images in **Figure 4-22b**. The featureless thermogram for the nanoprecipitation-based nanoparticles matches the absence of crystalline domains in the cryo-TEM image, showing instead fully amorphous nanoparticles. This can explain the much lower temperature needed to sintered the nanoparticles in the case of the nanoprecipitation method (130°C). As previously suggested in **Chapter 2**, the different kinetics of the two methods (slow nanoparticles formation for mini-emulsion and a fast one for nanoprecipitation) greatly impacts the internal structure of the nanoparticle. Because of the slow kinetic and the formation of nanoparticle upon 3h, the formation of Y6 crystalline domains are possible, whereas the almost direct formation of the nanoparticles when using nanoprecipitation keeps an amorphous structure inside the nanoparticle.

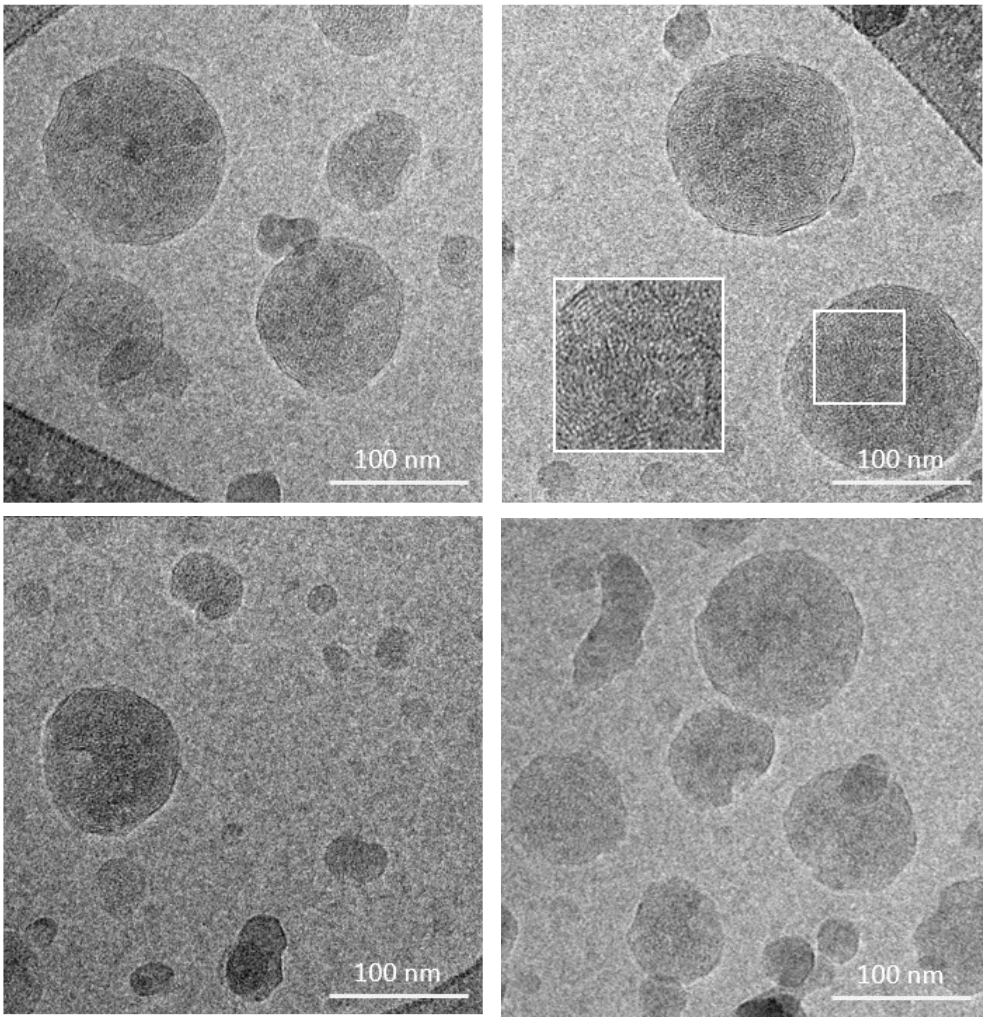

Figure 4-21: Cryo-TEM images of PTQ10:Y6 nanoparticles prepared via mini-emulsion

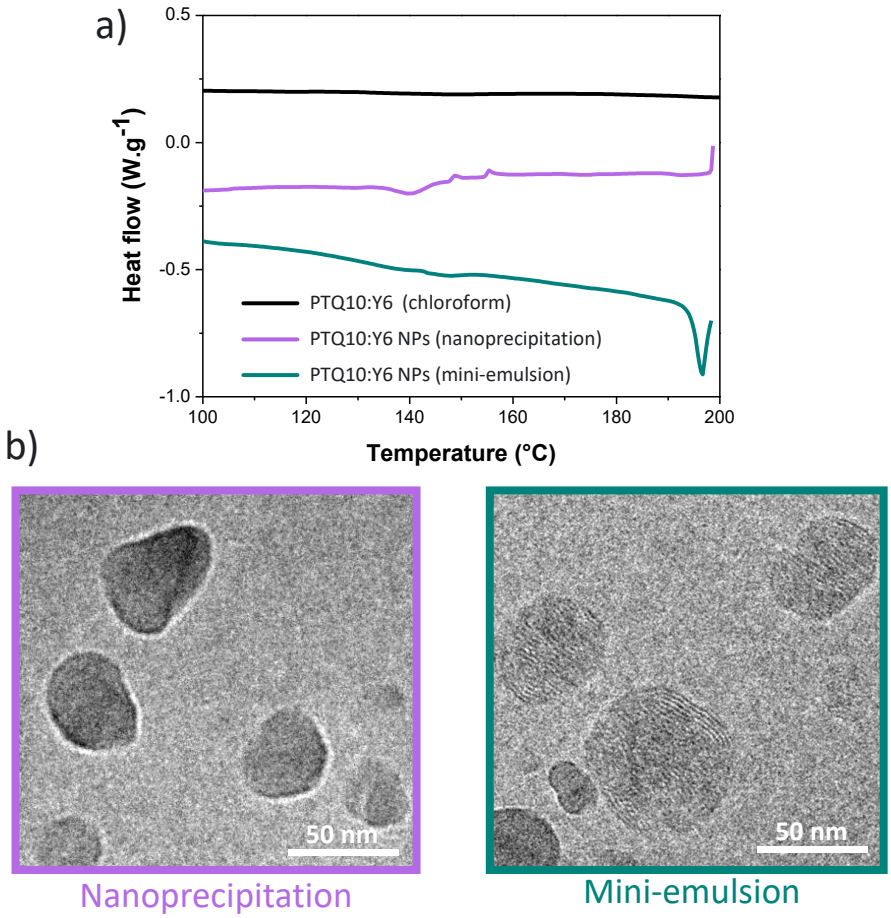

Figure 4-22: (a) Heating thermograms of PTQ10:Y6 NPs prepared by nanoprecipitation and mini-emulsion. (b) Cryo-TEM images of PTQ10:Y6 NPs prepared by nanoprecipitation (left) and mini-emulsion (right). Reproduced with permission.[188] Copyright 2024, Royal Society of Chemistry

4.7.4 Photo-stability

Being a very promising donor:acceptor system for water-based OPV, the lifetime of these devices is an important aspect to assess. A preliminary investigation has been conducted in order to understand the possible impact of the remaining surfactant and/or difference in the morphology on the stability of the OPV devices. The use of a UV-O_3 treatment on ZnO was also questionable on the stability behaviour as a recent study have shown that hydroxyl groups on the surface of ZnO films was proved to enhance the photocatalytic activity and lead to fast degradation of Y6[189]. The devices were submitted for up to 530 h to continuous illumination (AM 1.5G, 1000 W/m², open-circuit condition, at

~50°C, with UV filter). The evolutions of the different photovoltaic parameters are plotted in **Figure 4-23**.

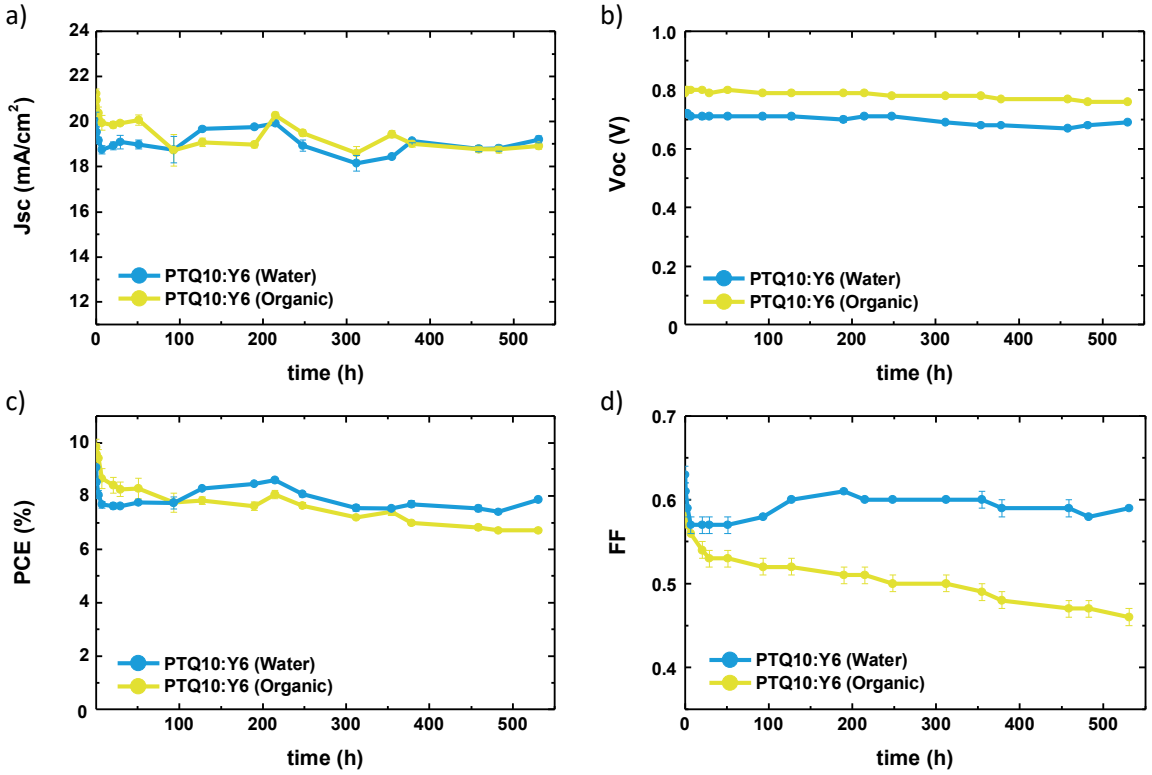

Figure 4-23: Evolution of the photovoltaic performances of OPV devices prepared from chloroform and water-based colloidal inks over 530h: (**a**) J_{SC} , (**b**) V_{OC} , (**c**) PCE, and (**d**) FF.

For both kinds of devices, water-processed and organic solvent-processed, a fast burn-in is observed in the first 10 h, leading to ≈15% loss of efficiency; mainly due to large loss in J_{SC} and FF (**Figure 4-23**). Interestingly, it can be seen that no degradation of the V_{OC} is observed for both of them. After this first degradation phase, the PCE stabilises at around 8% and a slower degradation takes place. We can also quantify the degradation by reporting typical points, defining OPV device stability according to Reese *et al.*[52]. One of them is T_{80}, which is the time taken by the devices to lose 20% of its efficiency from the initial testing measurement. For the control devices fabricated from organic solvent, this value has been measured at +74h. In contrast, this value has never been reached for water-processed devices and is therefore over 530h. This difference is quite remarkable, and mainly comes from the FF of devices fabricated from water-based dispersion that seems to be more stable than the control device. Hypothetically, two main explanations could be given. The first one is that the presence of a surfactant either stabilises the active layer

morphology by crosslinking[190], or creating a pseudo-interfacial layer between the active layer and the ZnO. The layer could act as a Na-doped ZnO layer, and thus removes defects that act as trap states similarly from what has been seen in other type of ZnO doping.[191,192] Alternatively, the more stable morphology of PTQ10:Y6 *np-BHJ* is induced by Y6 crystalline-like nature, thus decreasing the diffusions and demixing kinetics[193],[194].

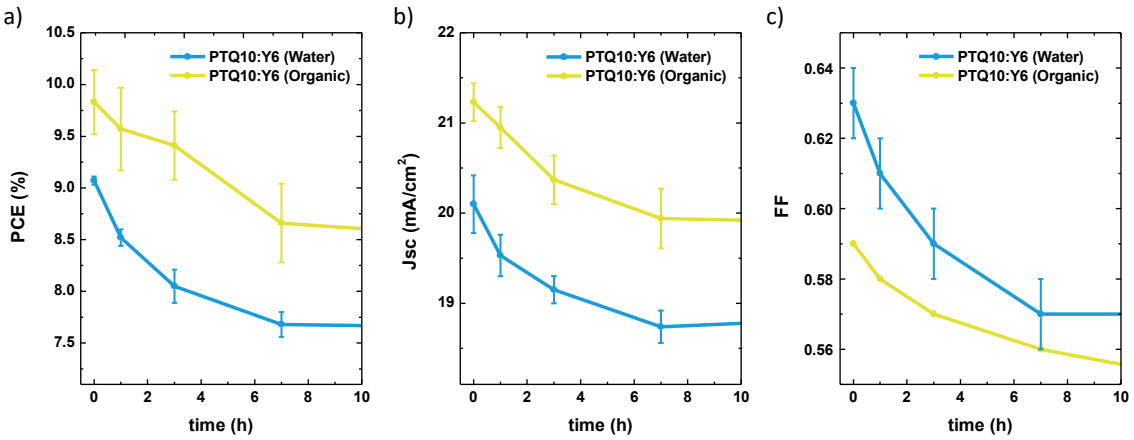

Figure 4-24: Burn-in of the photovoltaic performances of OPV devices prepared from chloroform (yellow) and water-based colloidal inks (blue) : (**a**) PCE , (**b**) J_{SC} and (**c**) FF.

To gain more insight onto the charge carrier dynamic processes, photocurrent density (J_{ph}), versus effective voltage (V_{eff}) curves during ageing of the optimised PTQ10:Y6 *BHJ* and PTQ10:Y6 *np-BHJ* were investigated and are shown in **Figure 4-25**. Initially, the saturation regime of the photocurrent is hardly achieved for both devices considering the low maximum effective voltage (1.7 V). Nevertheless, this saturated current density (J_{sat}) is higher for the PTQ10:Y6 *BHJ* than PTQ10:Y6 *np-BHJ* (21.90 vs. 19.17 mA cm^{-2}) which agrees with the previous EQE results as J_{sat} is driven by the total photogenerated exciton density. Indeed, when the saturation regime is obtained, it is considered that all the photogenerated bound electron–hole pairs (G_{MAX}) dissociate into free charge carriers. Otherwise, the generation rate G is given by $G(T, E) = G_{MAX} \times P(T, E)$ where $P(T,E)$ is the probability of charge separation[195]. In **Figure 4-25c** and **d**, we can clearly see that $P(T, E)$ is much more stable over time in the case of PTQ10:Y6 *np-BHJ* than its organic solvent-processed counterparts. After 454h, the later presents a strong field-dependence at high V_{eff} while this dependence is much lower for PTQ10:Y6 *np-BHJ* (**Figure 4-25e**). This result indicates higher recombination (geminate and/or bimolecular) and/or less efficient charge extraction in PTQ10:Y6 *BHJ* devices upon ageing, thus decreasing FF[196],[197].

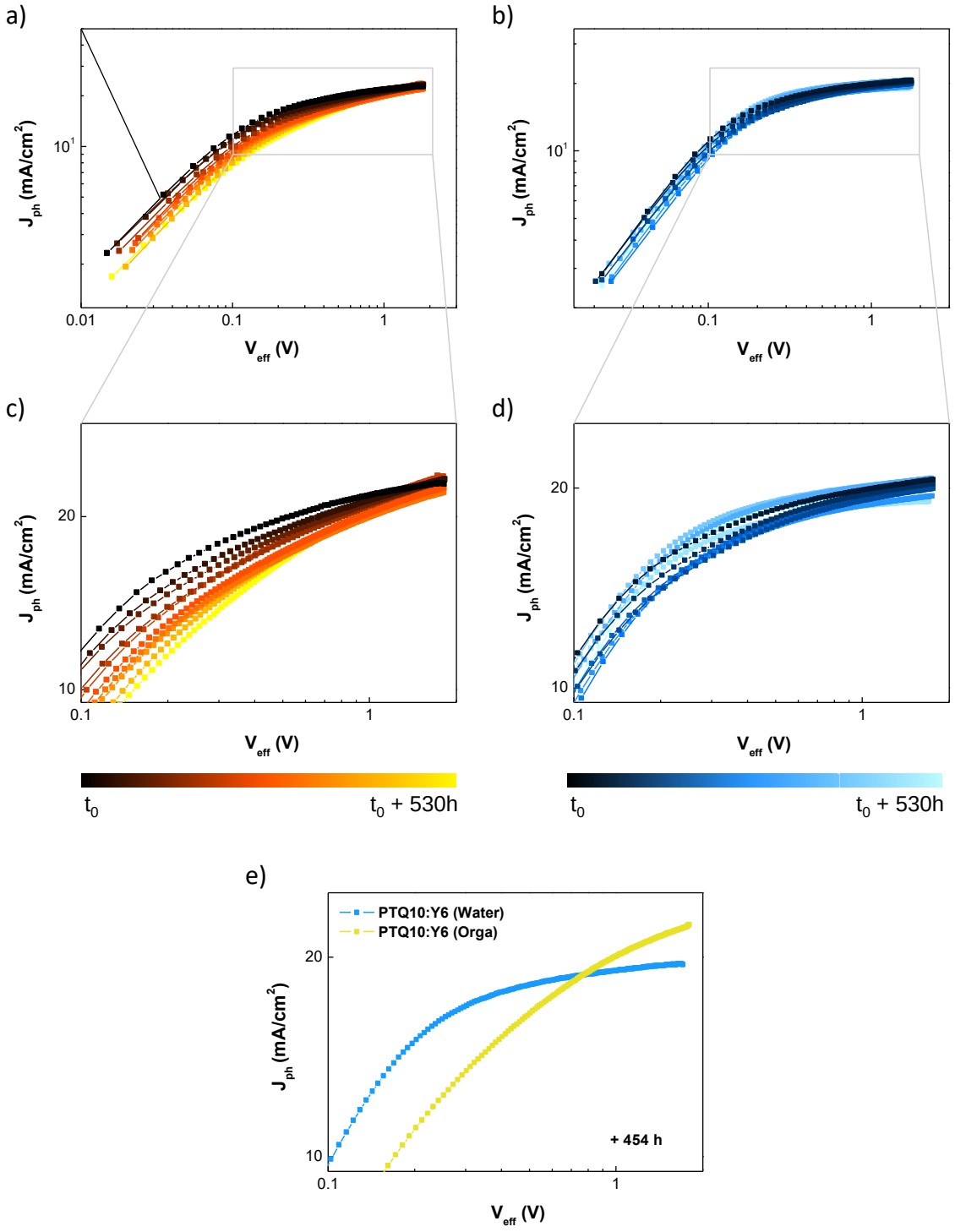

Figure 4-25: Photocurrent density versus effective voltage (Jph–Veff) characteristics for (**a**)-(**c**) PTQ10:Y6 BHJ and (**b**)-(**d**) PTQ10:Y6 np-BHJ. (**e**) is comparing both devices after 454h under incident light intensity (1 sun).

This preliminary study on stability highlights that efficient OPV devices, up to 9.98% PCE, can be fabricated from water-based dispersions with stability comparable to control devices fabricated from organic solvent. This important result highlights that the remaining surfactant is not detrimental for the device stability under these ageing conditions and could even be beneficial.

4.8. Conclusion of chapter 4

Efficient organic solar cells with PCE up to 9.98% were fabricated from water-based organic semiconductor colloidal dispersions prepared by mini-emulsion. In this chapter, we have shown that the choice of the donor/acceptor is critical to achieving high performance organic solar cells made from water-based dispersions. Indeed, the low surface energy difference as well as low interfacial energy, available for PTQ10:Y6, allows for the fabrication of donor/acceptor nanoparticles with low phase segregation and intermixed morphology. In addition, the internal morphology of the nanoparticle was not dramatically modified upon thermal annealing, contrary to donor/acceptor nanoparticles that have a high surface energy difference such as PTQ10:$PC_{61}BM$. Although the internal morphology of the PTQ10:Y6 nanoparticles is suited for organic photovoltaics, thermal annealing up to 200 °C is necessary to achieve high performance. Extensive thermal analysis revealed the different critical temperatures, such as melting temperature of Y6 crystalline domains, at which the PTQ10:Y6 nanoparticles films start to change in term of molecular arrangement. At the optimal temperature, the nanoparticles sintering occurs, and it perfectly correlates with the melting temperature of Y6 crystalline nanodomains present in the nanoparticles. Furthermore, the beginning of SDS degradation happened to match the optimal annealing temperature, and its elimination could contribute also to the high performances achieved. This finding opens the strategy of molecular engineering in order to develop a surfactant that would help the formation of nanoparticles and subsequently be removed during the active layer processing. The combination of these three phenomena: i) stable donor/acceptor intermixed morphology, ii) melting of Y6 crystallites and nanoparticle sintering, and iii) degradation/elimination of SDS, results in OPV devices that achieve a PCE that is 85% of the PCE of PTQ10:Y6 devices prepared with organic solvents. From our knowledge, 9.98% PCE is the highest performance achieved for water-processed OPV

devices embedded nanoparticles prepared with mini-emulsion. Last analysis made with cryo-TEM have revealed the expected crystalline domain of Y6 in the nanoparticle. The same analysis on nanoparticles prepared with nanoprecipitation did not show the same feature as more amorphous nanoparticles were observed. This difference introduces the concept of hard and soft nanoparticles, which essential as we understand now that going from a nanoparticulate film to a BHJ-like film required nanoparticles that can be easily sintered without any phase segregation and by avoiding high temperature.

Chapter 5

Extension to other polymer and non-fullerene acceptor systems

5.1. Introduction

The previous chapter has illustrated that PTQ10:Y6 nanoparticles-based solar cells could reach unprecedent performances close to 10% PCE. The low interfacial energy of this donor:acceptor system is believed to be the driven factor to obtain an intimate morphology between the donor and the acceptor inside the nanoparticles. This type of morphology might be crucial to insure homogenous layers without grain boundaries and large domains upon thermal treatment. These encouraging findings were followed by thermal analysis revealing a melting of Y6 crystals hence allowing efficient sintering of the nanoparticles. Now, it is of great interest to study further a wider variety of donor:acceptor systems to continue the correlation with surface energies and morphology, as well as trying to decrease the optimal temperature to process the nanoparticulate film – a pre-requisite for scaling-up OPV manufacturing on thermally fragile flexible substrates such as PET. This annealing temperature is highly linked to the molecular arrangement of PTQ10 and Y6 in the nanoparticles, and more specifically of Y6. Therefore, changing the NFA might open the door to more insights on how the formation of the nanoparticles is influenced by the NFA, and what could be the features that impact the treatment process of the nanoparticles layer.

To this end, binary blend nanoparticles based on PTQ10 associated with IDIC and Y12 are studied in the present chapter. Y12 is another small molecule from the Y-series, that has shown over 10% of PCE in the literature when associated with PTQ10.[180],[198] The use of Y12 here is particularly interesting as it opens the door for studying a possible impact of the alkyl side chains on the formation of nanoparticles and the subsequent OPV process. It has the identical backbone of Y6, but instead of having 2-ethylhexyl side chains on the two nitrogen, it has the longer 2-butyloctyl side chains. Y12 has shown to be more soluble and in a wider variety of solvent than Y6. Following this study, the effect of the polymer's alkyl chain is also in the core of this chapter as PTQ10 is then replaced with a novel polymer donor FO6-T to form nanoparticles. This polymer is particularly interesting because it also allows the study of its derivatives FO4-T and FO8-T, which differ according to their alkyl side chains length. This series of polymer have been recently developed by Prof. Martin Heeney at Imperial College of London. Materials were nicely provided by this research group to ours in a collaborative mode.[199]

5.2. PTQ10 and non-fullerene acceptors

In this study, I have associated PTQ10 two other NFAs that are IDIC and Y12. The chemical structures and energy levels of the organic semiconductors used in this study are shown in **Figure 5-1**. In order to continue the correlation between the optoelectronic properties of the OPV devices and the interfacial energy of the blends, contact angles have been measured to extract the different surface energies of the NFAs. The resulting measurements and extracted value can be found in **Table 5-1** and Figure 5-2. The system PTQ10:IDIC has an interfacial energy of 7.0 mN m^{-1} which is interesting as it gives us the possibility to study an "intermediate $\gamma_{D:A}$ system", somewhere in the middle between PTQ10:Y6 (low $\gamma_{D:A}$) and PTQ10:PCBM (high $\gamma_{D:A}$). Interestingly for PTQ10:Y12, the longer alkyl chains is increasing its compatibility with PTQ10 as a lower $\gamma_{D:A}$ of 4.0 is obtained as compared to 4.5 mN m^{-1} for PTQ10:Y6. With these new results, the aim is to obtain some sort of figure of merit which could help to select the right system based on their interfacial energy to form nanoparticles for efficient water-based OPV.

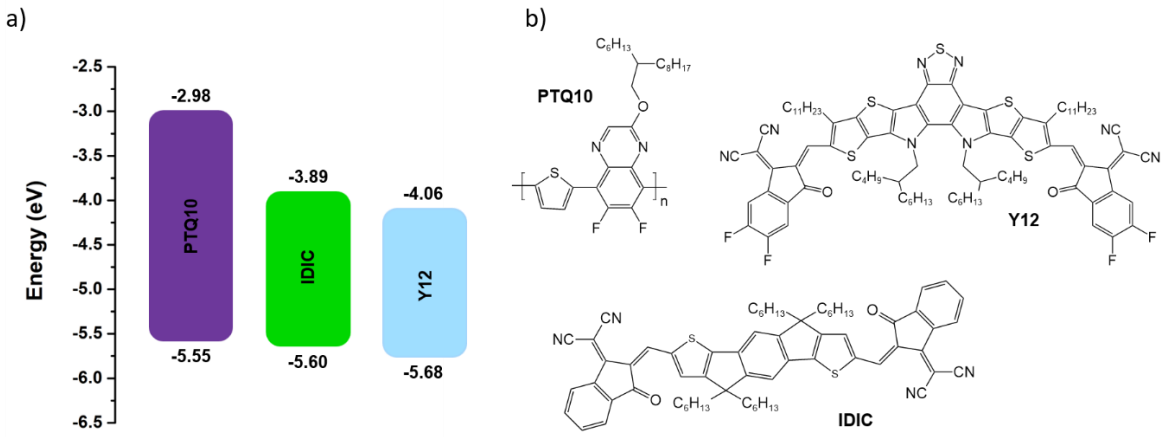

Figure 5-1: (**a**) Highest Occupied Molecular Orbital (HOMO) and Lowest Unoccupied Molecular Orbital (LUMO) of PTQ10, IDIC and Y12. (**b**) Chemical structures of PTQ10 donor polymer, IDIC and Y12 acceptor small molecules.

Table 5-1: Surface energies (polar, dispersive and total) of PTQ10, IDIC and Y12. $\gamma_{D:A}$ represents the interfacial energy between PTQ10 and the NFAs.

Material	γ_D (mN m^{-1})	γ_P (mN m^{-1})	γ (mN m^{-1})	$\gamma_{D:A}$ (mN m^{-1})
PTQ10	21.3	1.7	23.1	/
IDIC	16.9	10.7	27.6	7.0
Y12	18.3	7.7	25.9	4.0

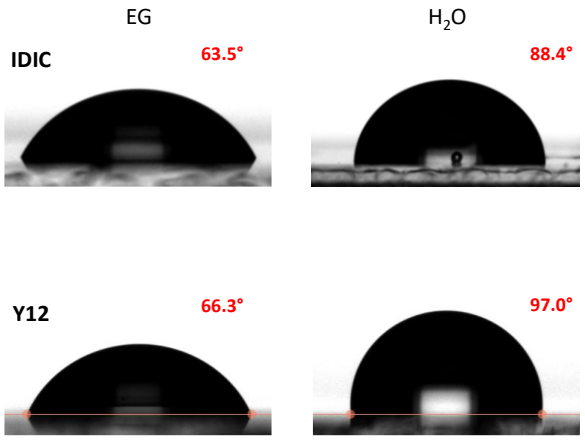

Figure 5-2: Goniometer pictures of contact angles and their values in red of ethylene glycol (left) and water (right) on IDIC and Y12 films deposited from chloroform.

5.2.1 PTQ10:IDIC and PTQ10:Y12 nanoparticles

Composite nanoparticles with PTQ10:IDIC and PTQ10:Y12 were synthesised following the usual procedure described in **Methods**: For the organic phase, 35 mg ml^{-1} of PTQ10:NFA [1:1.2] mixture was first dissolved in chloroform stirred for 2 h at 65 °C in a nitrogen-filled glovebox. For PTQ10:IDIC, the ratio has been chosen based on the optimal ratio reported in the literature.[46] Then, the same aqueous phases for both system were obtained by dissolving 5 mg ml^{-1} (17 mM) of SDS in deionised water and stirred for 30 min at room temperature. The concentration of both dispersions was adjusted in order to obtain a concentration of 60 mg ml^{-1}.

UV-visible spectroscopy and photoluminescence quenching measurements have been carried out on the two obtained dispersions (**Figure 5-3**). PTQ10:IDIC nanoparticles show a broad light absorption between 500 nm – 750 nm. The resulting fluorescence peak observed at 780 nm, as well as the shoulder emission at 850nm, after a photoexcitation at 540 nm is arising from the acceptor IDIC.[200] Meanwhile, the electron transfer from PTQ10

to IDIC seems to be very efficient as no fluorescence emission from PTQ10 is measured. Therefore, this result indicates the presence of large domains of IDIC which could lead to a relatively poor exciton dissociation in the nanoparticles. Concerning PTQ10:Y12, the system presents two narrow absorption bands between 500 nm – 750 nm and 750 nm – 850 nm that respectively correspond to PTQ10 and Y12. Just like for PTQ10:IDIC, the electron transfer from PTQ10 to NFA is very efficient as no radiative recombination from exciton formed in PTQ10 is observed. The emission of Y12 is, on the other hand, not totally quenched as the photo-absorption leads to an intense PL peak emission at 924 nm and a shoulder peak at 1050 nm. Similar to IDIC, it could indicate the presence of unfavourable morphology for the excitons to be dissociated efficiently. This shoulder have been reported to be the sign of a high degree of crystallinity and a large crystal size.[201] In order to fully assess the PL results, the same measurements should be done on pure IDIC and Y12 nanoparticles to quantify the PL quenching. Nonetheless, both absorption spectra displayed sharp vibronic peaks which could already assess the crystalline nature of the two particles which is consistent with the mini-emulsions process.

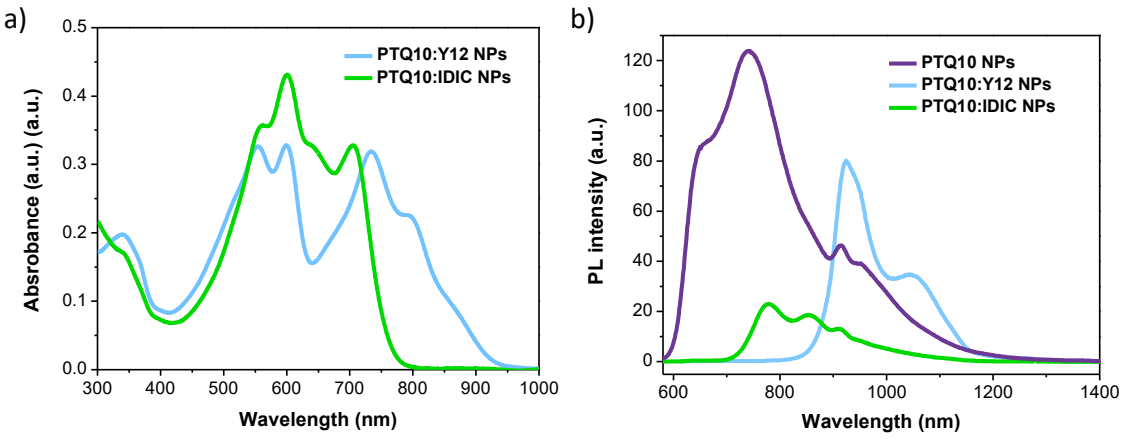

Figure 5-3: (**a**) Absorption spectra of PTQ10:Y12 NPs and PTQ10:IDIC NPs (dispersions) and (**b**) PL spectra of PTQ10 NPs, PTQ10:Y12 NPs and PTQ10:IDIC NPs (dispersions). (dispersions concentration = 0.03 mg ml^{-1})

Concerning the diameter of the nanoparticles, both systems present comparable average diameter of 63.2 nm and 59.2 nm for PTQ10:IDIC and PTQ10:Y12 respectively, which is consistent with the previous donor:acceptor systems studied (**Table 5-2**).

Table 5-2: Average diameter of PTQ10:IDIC NPs and PTQ10:Y12 nanoparticles measured with DLS

System	Z-average (d.nm)	PdI
PTQ10:IDIC	63.2	0.213
PTQ10:Y12	59.2	0.173

Organic solar cells have been fabricated from these two dispersions and their OPV performances are now presented and analysed. For each of them, a morphological investigation has also been made to determined how the donor and acceptor materials are internally arranged within the nanoparticles. Devices prepared from PTQ10:NFA nanoparticles dispersion concentrated at 60 mg ml^{-1} have been prepared as well as the PTQ10:NFA control devices made from chloroform solution concentrated at 14 mg ml^{-1}. For the *np-BHJ* solar cells, the dispersion has been spin-coated onto ZnO at a speed of 3000 rpm for 60 sec. The resulting nanoparticulate layers were then annealed at different temperature for 5 min and the measured thickness were around 165 nm. The reference *BHJ* devices were formed by spin coating the organic solution at a speed of 1000 rpm and subsequently annealed at 110 °C for 10 min resulting in a thickness of 118 nm.

5.2.2 PTQ10:IDIC

5.2.2.1. OPV performances

Table 5-3 and **Figure 5-4** are showing the evolution of OPV performances with varying the thermal annealing temperature. The observed trend is more similar to the previously studied PTQ10:$PC_{61}BM$ than it is for PTQ10:Y6 as the treatment did not drastically changed the performances. Nevertheless, an obvious optimal temperature of 140 °C with maximum PCE of 4.98% and a hero-cell of 5.23% (J_{SC} = 11.90 mA cm^{-2}, V_{OC} = 855 mV and FF = 0.52) is obtained. This maximum PCE is directly related to the maximum current density obtained with the same annealing temperature. Thereafter, increasing the temperature to 170°C and 200° negatively impacts the J_{SC} which drop to 9.25 mA cm^{-2} and 8.71 mA cm^{-2}. In the same way as for PTQ10:$PC_{61}BM$, this reduction of J_{SC} might be the sign of phase separation between PTQ10 and IDIC. Interestingly, one might remark here again the constant increase of FF correlated with the increase of annealing temperature previously observed with Y6 and PCBM, without yet an increase of PCE. The open-circuit

voltage also presents an increase at higher temperatures (170 °C) up to 902 mV, which is slightly reduced to 881 mV at 200 °C due to a possible excessive phase separation as seen in with $PC_{61}BM$.

Table 5-3: Average OPV performances of optimised PTQ10:IDIC *np-BHJ* extracted from a minimum of 8 devices with varying the annealing temperature (best devices are shown in brackets).

TA Temperature (°C)	V_{OC} (mV)	J_{SC} (mA cm^{-2})	FF	PCE (%)
100	857 ± 10 (863)	8.36 ± 0.14 (8.43)	0.48 ± 0.02 (0.50)	3.44 ± 0.19 (3.62)
140	851 ± 7 (855)	11.77± 0.07 (11.90)	0.50 ± 0.02 (0.52)	4.98 ± 0.24 (5.23)
170	902 ± 16 (908)	9.25 ± 0.26 (9.53)	0.52 ± 0.00 (0.52)	4.34 ± 0.16 (4.48)
200	881 ± 16 (891)	8.71 ± 0.26 (8.83)	0.54 ± 0.02 (0.55)	4.18 ± 0.17 (4.34)

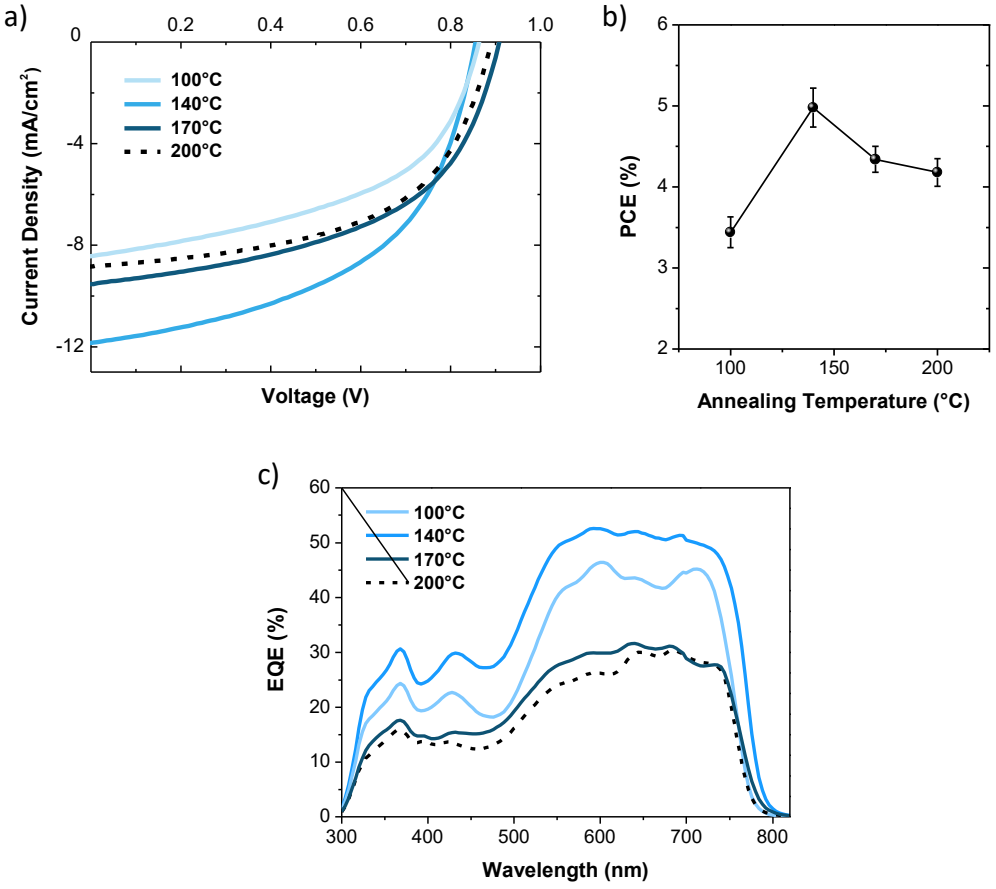

Figure 5-4: (**a**) J-V curves and (**c**) EQE curves for PTQ10:IDIC np-BHJ devices with varying the thermal annealing temperature from 100°C to 200°. (**b**) represents PCE vs thermal annealing temperature for PTQ10:IDIC np-BHJ OPV devices

While the overall efficiency of PTQ10:IDIC *np-BHJ* exhibits a notable strength by reaching one of the highest PCE (5.23 %) reported with the mini-emulsion method, it still falls short when compared to its counterpart processed from organic solvent, which achieves 10.98% PCE (**Figure 5-5** and **Table 5-4**). The difference in performances is mainly due to an important loss in FF (0.67 for *BHJ* devices and 0.50 for *np-BHJ* devices) as well as a low J_{SC} (18.12 mA cm^{-2} for *BHJ* devices and 11.77 mA cm^{-2} for *np-BHJ* devices). Concerning the V_{OC}, a non-negligible loss of 50 mV is observed when switching to the nanoparticles-based devices. Nonetheless, this loss can be suppressed with a higher annealing temperature, which might be in accordance with a reduction of the donor/acceptor interface area that allow longer charge carrier lifetime.[200] In order to reach high exciton dissociation rate together with high V_{OC}, intermediate temperature between 140 °C and 170°C should also be screened. Even though PTQ10:IDIC *np-BHJ* only reached half of the performances obtained with PTQ10:IDIC *BHJ*, we observe from the EQE measurement a much better photo-conversion with this water-based system than the PTQ10:PC_{61}BM system. Herein, the water-based devices are able to convert 53 % of absorbed photons into collected charges, which is only 28 % lower than for the organic solvent-based system (**Figure 5-5**). Therefore, having an $\gamma_{D:A}$ that is not as high as PTQ10:PC_{61}BM might be beneficial to the IDIC-based system in order to achieve an advantageous morphology for the photogeneration of charges.

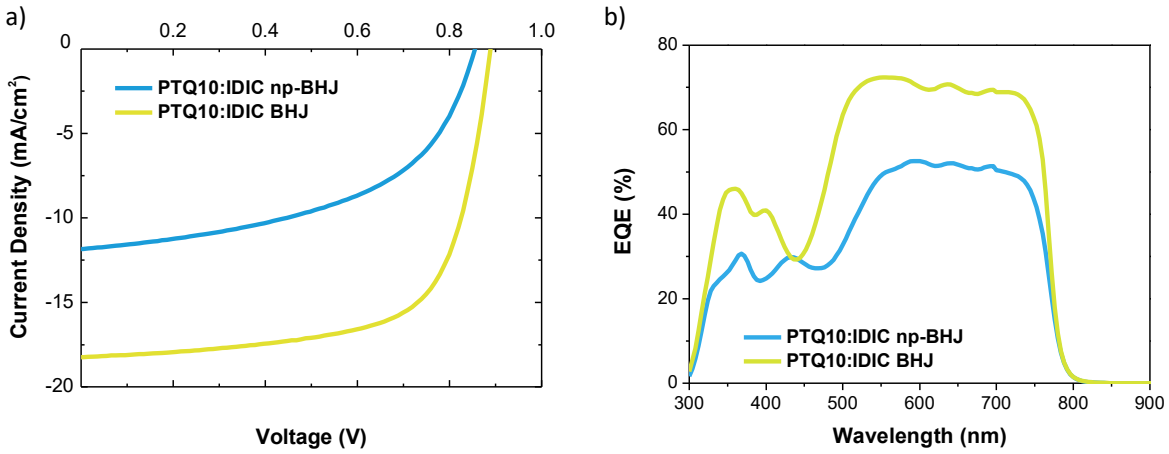

Figure 5-5: (**a**) J-V curves and (**b**) EQE for PTQ10:IDIC np-BHJ (blue) and PTQ10:IDIC BHJ (yellow) at the optimal thermal annealing temperature. Note that the selected curves have been chosen to be as close as the average performance shown in **Table 5-4**.

Table 5-4: Average OPV performances of optimised PTQ10:IDIC np-BHJ and BHJ extracted from a minimum of 8 devices at the optimal thermal annealing temperature (best devices are shown in brackets).

	V_{OC} (mV)	J_{SC} (mA cm^{-2})	FF	PCE (%)
PTQ10:IDIC *BHJ*	898 ± 10 (914)	18.12 ± 0.28 (18.30)	0.67 ± 0.00 (0.67)	10.98 ± 0.18 (11.27)
PTQ10:IDIC *np-BHJ*	851 ± 7 (855)	11.77 ± 0.07 (11.90)	0.50 ± 0.02 (0.52)	4.98 ± 0.24 (5.23)

5.2.2.2. Morphological investigation

From the analysis of the PV performances of PTQ10:IDIC np-BHJ, it seems that even if the measured interfacial energy of PTQ10:IDIC is lower than PTQ10:$PC_{61}BM$, this nanoparticle-based solar cells does not show an appropriate morphology to reach high efficiencies. Scanning transmission X-ray microscopy technique has shown a good capability to elucidate the nanoparticle morphology. We first performed the NEXAFS measurements on IDIC, and we plotted the results together with the previously obtained PTQ10's NEXAFS spectrum. From **Figure 5-6**, the choice of the key absorption energies had been made by testing different combination of energy, and the following three orthogonal energies have been selected: 284.3 eV (IDIC), 288 eV (PTQ10) and 291.8 eV (IDIC).

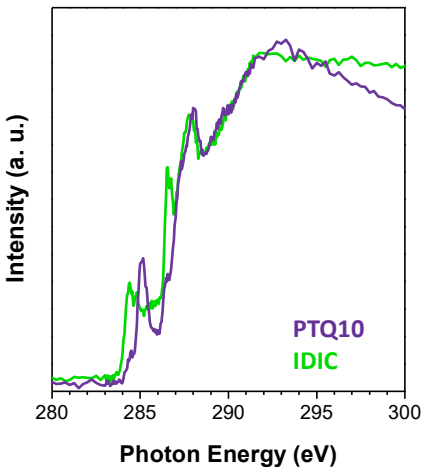

Figure 5-6: NEXAFS spectra for the pure materials PTQ10 and IDIC overlapped.

The **Figure 5-7** is showing the compositional maps extracted from STXM analysis for PTQ10:IDIC nanoparticles right after the synthesis as well as the average radial composition profiles.

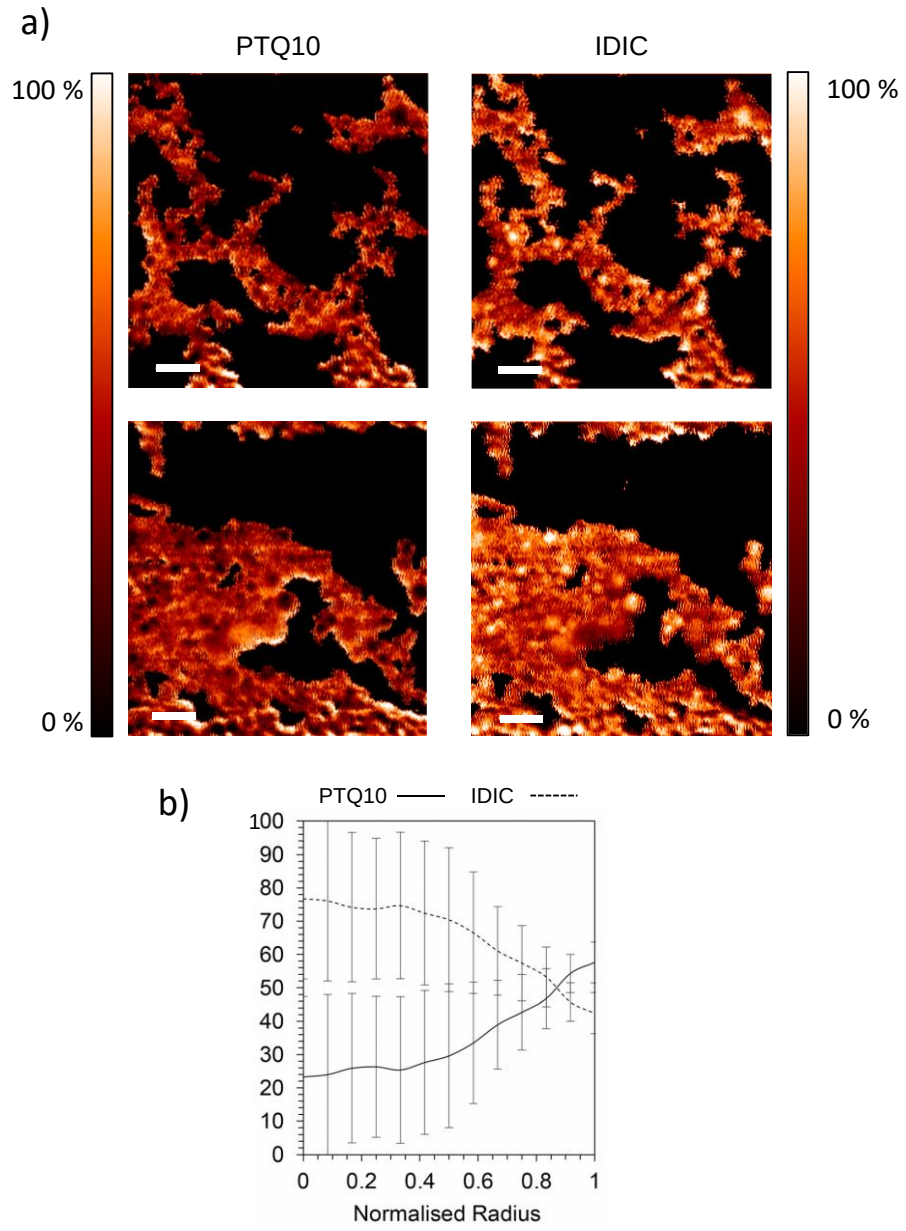

Figure 5-7: (**a**) STXM composition maps of PTQ10:IDIC NPs without thermal treatment: PTQ10 (left) and IDIC (right) All scale bars are 500 nm. The colour contrast is scaled such that light colours correspond to higher component concentrations. (**b**) *Average radial composition profiles*

From the $\gamma_{D:A}$ of this system (7.0 mN m^{-1}), the phase separation between the donor and acceptor was expected to be larger than PTQ10:Y6 having a lower $\gamma_{D:A}$. The internal morphology of PTQ10:IDIC is indeed found to be a core-shell like morphology, with a

PTQ10-rich shell and a IDIC-rich core. From the radial composition profile, only 24 % of PTQ10 is present in the core with a majority 76% of IDIC (**Figure 5-7b**). In the shell, we observed a majority of PTQ10 but the overall composition of the shell is much more intermixed than the core-shell composition of PTQ10:$PC_{61}BM$. This shows that the core and the shell are still more intermixed than what was found for PTQ10:$PC_{61}BM$ nanoparticles, which is consistent with the lower interfacial energy obtained with IDIC-based nanoparticles but not as intermixed than PTQ10:Y6 an even lower interfacial energy system. Therefore, this result highlights here again that is preferable to use systems with low $\gamma_{D:A}$ to achieve nanoparticles with more intermixed donor and acceptor phases. Yet core-shell, the OPV results of PTQ10:IDIC nanoparticles solar cells have shown loss with respect to their organic-solvent counterparts than PTQ10:$PC_{61}BM$ nanoparticles (55 % against 60 %). It is perhaps safer to argue that only low interfacial energies system can give well intermixed donor and acceptor composite nanoparticles such as PTQ10:Y6. Unfortunately, no images of the annealed PTQ10:IDIC nanoparticles have been recorded due to lack of STXM beam time. Nonetheless, we could expect that there is no dramatic change upon annealing, especially at high temperature as no significant losses have been observed on the different OPV parameters. Yet, the nanoparticles are likely to sintered when increasing the temperature which would explained the enhancement of the FF and the J_{SC} at 140 °C.

5.2.3 PTQ10:Y12

The results obtained with PTQ10:IDIC showed that even a donor/acceptor blend with an intermediate interfacial energy is not fully suitable for water-processed solar cells. Moving back now to a low interfacial energy system with PTQ10:Y12, we are expecting to confirm the previously observed OPV performances and morphology obtained with PTQ10:Y6.

5.2.3.1. OPV performances

The performances of PTQ10:Y12 nanoparticles-based devices are presented in **Table 5-5** and **Figure 5-8**. The data show the evolution of OPV performances with varying the thermal annealing temperature from 100 °C to 200 °C. As previously observed for PTQ10:Y6 *np-BHJ*, this np-BHJ with an NFA having longer alkyl chains is showing a similar

trend when annealed up to 150 °C. A simultaneous increase in V_{OC}, J_{SC} and FF allow the power conversion efficiency to raise from 4.15 % to 7.10 %. Beyond this optimal annealing temperature of 150 °C, an important drop of PCE is observed, which becomes dramatic at an annealing temperature of 200 °C. EQE spectra have been recorded for PTQ10:Y12 *np-BHJ* annealed at different temperature (**Figure 5-8c**). The results show that the overall loss is not related to any material degradation as both the donor and acceptor are still contributing equally to the charge generation and only to a lower extent for high annealing temperature.

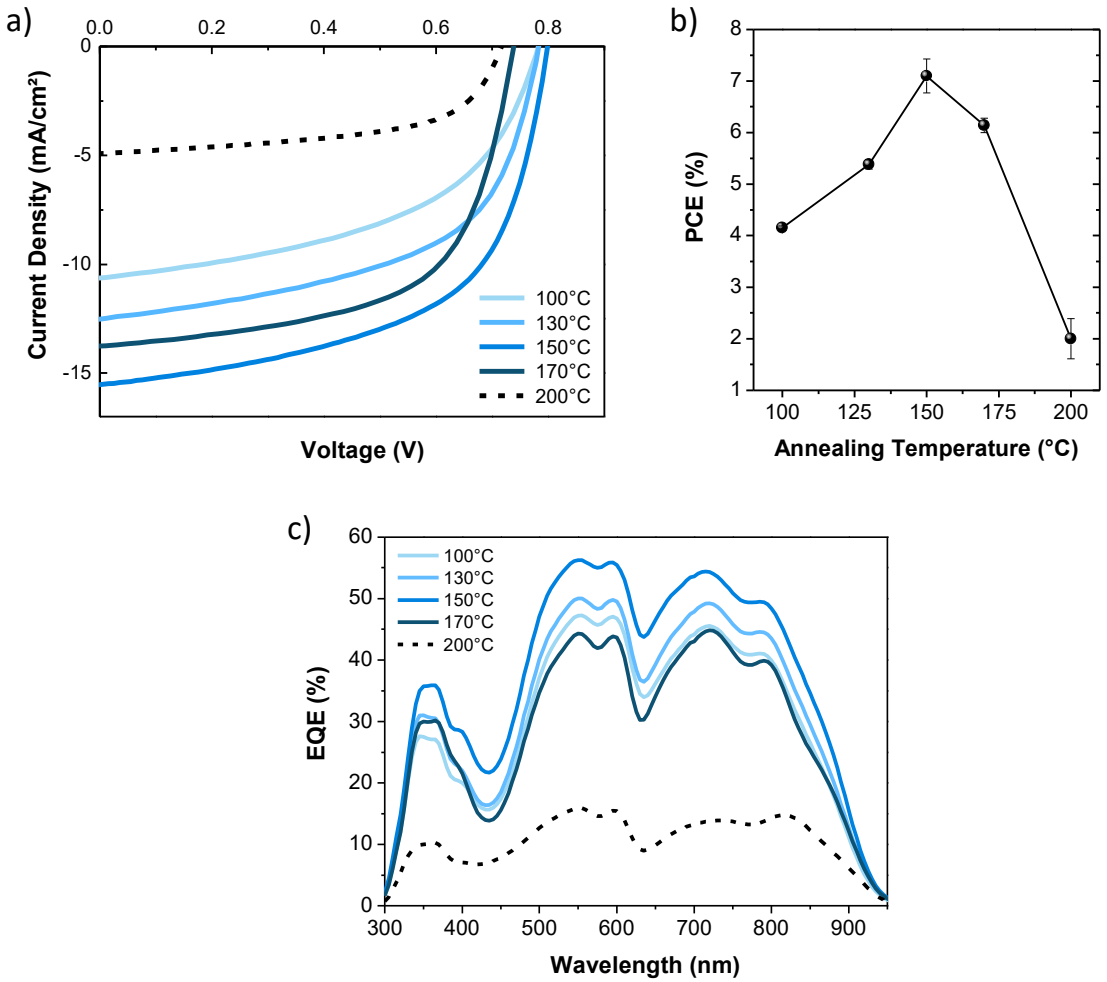

Figure 5-8: (**a**) J-V curves and (**c**) EQE curves for PTQ10:Y12 np-BHJ devices with varying the thermal annealing temperature from 100°C (light blue) to 200°C (dark dashed line). Note that the selected curves have been chosen to be as close as the average performance for each annealing temperature shown in **Table 5**. (**b**) represents PCE vs thermal annealing temperature for PTQ10:Y12 np-BHJ OPV devices

Table 5-5: Average OPV performances of PTQ10:Y12 *np-BHJ* extracted from a minimum of 4 devices with different thermal treatment (best devices are shown in brackets).

TA Temperature (°C)	V_{OC} (mV)	J_{SC} (mA cm^{-2})	FF	PCE (%)
100	778 ± 9 (782)	10.70 ± 0.23 (10.62)	0.50 ± 0.01 (0.51)	4.15 ± 0.04 (4.20)
130	780 ± 6 (775)	12.55 ± 0.13 (12.77)	0.55 ± 0.01 (0.55)	5.38 ± 0.09 (5.46)
150	797 ± 8 (804)	15.44 ± 0.32 (15.93)	0.58 ± 0.01 (0.59)	7.10 ± 0.33 (7.52)
170	751 ± 17 (775)	13.52 ± 0.17 (13.40)	0.60 ± 0.01 (0.61)	6.14 ± 0.14 (6.35)
200	690 ± 30 (709)	5.55 ± 0.60 (6.30)	0.52 ± 0.07 (0.60)	2.00 ± 0.39 (2.66)

Although relative high performances have been reached with this system, it only reaches 60% of the performances demonstrated by its organic-solvent counterpart PTQ10:Y12 *BHJ* prepared with chloroform (**Figure 5-9** and **Table 5-6**), mainly due to much lower shot-circuit current density. The direct correlation between the obtained performances and the interfacial energy is not verified as we would expect similar behaviour than PTQ10:Y6. Nevertheless, it is quite interesting to see that the optimal annealing temperature has been shifted to a lower temperature (150 °C) than the one needed for PTQ10:Y6 (200 °C), due to the extension of the alkyl chains of the NFA.

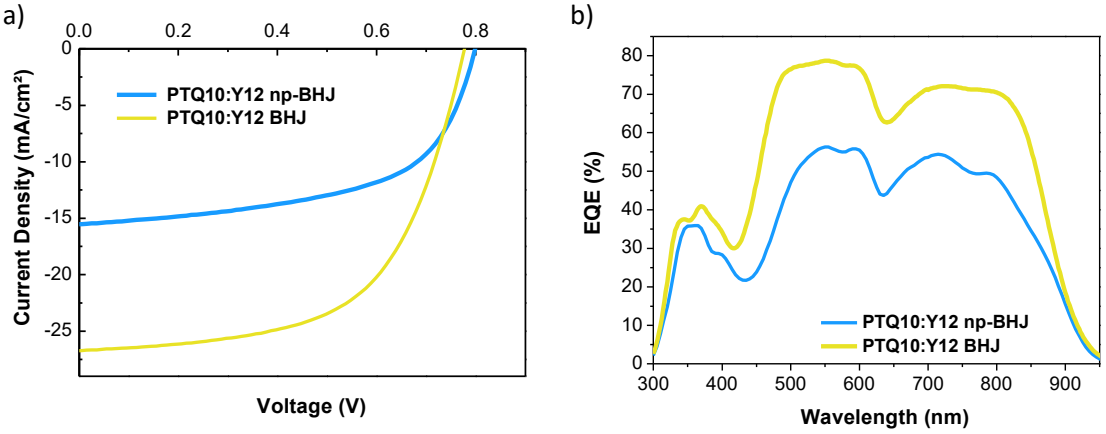

Figure 5-9: (**a**) J-V curves and (**b**) EQE for PTQ10Y12 np-BHJ (blue) and PTQ10:Y12 BHJ (yellow) at the optimal thermal annealing temperature. Note that the selected curves have been chosen to be as close as the average performance shown in **Table 5-6**.

Table 5-6: Average OPV performances of PTQ10:Y12 BHJ and PTQ10:Y12 np-BHJ extracted from a minimum of 8 devices with different thermal treatment (best devices are shown in brackets).

	V_{OC} (mV)	J_{SC} (mA cm^{-2})	FF	PCE (%)
PTQ10:Y12 *BHJ*	779 ± 12 (796)	25.41 ± 0.91 (25.9)	0.58 ± 0.00 (0.58)	11.54 ± 0.51 (11.96)
PTQ10:Y12 *np-BHJ*	797 ± 8 (804)	15.44 ± 0.32 (15.93)	0.58 ± 0.01 (0.59)	7.10 ± 0.33 (7.52)

5.2.3.2. Morphological investigation

To get further information on the temperature-dependence of the performances, AFM measurements have been performed and the **Figure 5-10** is showing the topography images of PTQ10:Y12 *np-BHJ* films annealed at 130, 150, 170 and 200°C for 5 min.

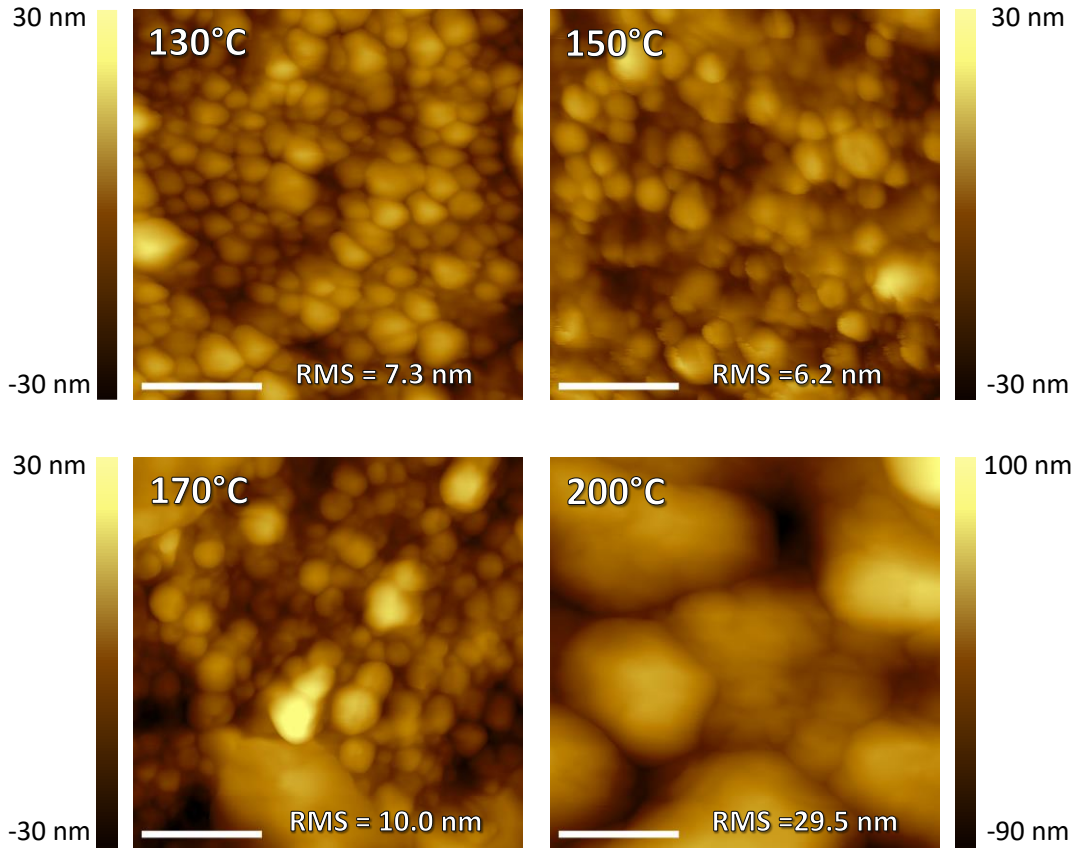

Figure 5-10: AFM topography images (height) of PTQ10:Y12 *np-BHJ* film annealed at various temperature. (Scale bar = 300nm)

For the first annealing at 130°C, nanoparticles can still be seen with an RMS roughness of 7.3 nm which is slightly decreased to 6.2 nm with an annealing of 150°C. This optimal annealing temperature does not completely sinter the nanoparticles as spherical shapes can still be seen, but much less than at 130°C. The higher temperature of 170°C already show some large phase separation illustrated by the larger domains at the bottom and top left of the AFM image with an RMS roughness rising to 10.0 nm. Meanwhile, some parts of the film are still formed from nanoparticles with grain boundaries. Therefore, the window to obtained a smooth and fully blended film does not seem to exist here which can be the reason for the limited J_{SC}. Upon annealing at 200°C, the Y12-based nanoparticule film seems to behave like the previously studied PTQ10:PC_{61}BM system, illustrated by a large phase separation. Large domains are observed (400 - 700 nm) and the roughness increases up to 29.5 nm. The formation of such clusters can explain the massive drop in J_{SC} observed at this temperature due to an increase of geminate recombination and poor charge extraction due to the presence of large cluster of PTQ10 and Y12 at the ETL and HTL interface respectively. However, this does not match with our previous assumption that low interfacial energy was beneficial for composite nanoparticles in order to form upon annealing a layer which possessed an intermixed donor/acceptor morphology.

That being said, these results point out the influence of alkyl side chains when processing nanoparticles-based OPV cells, and more specifically the influence on the optimal annealing temperature. Although no STXM measurements have been ran on this system to accurately determined its radial profile composition, cryo-TEM images have been collected and are now being presented and discussed (**Figure 5-11**).

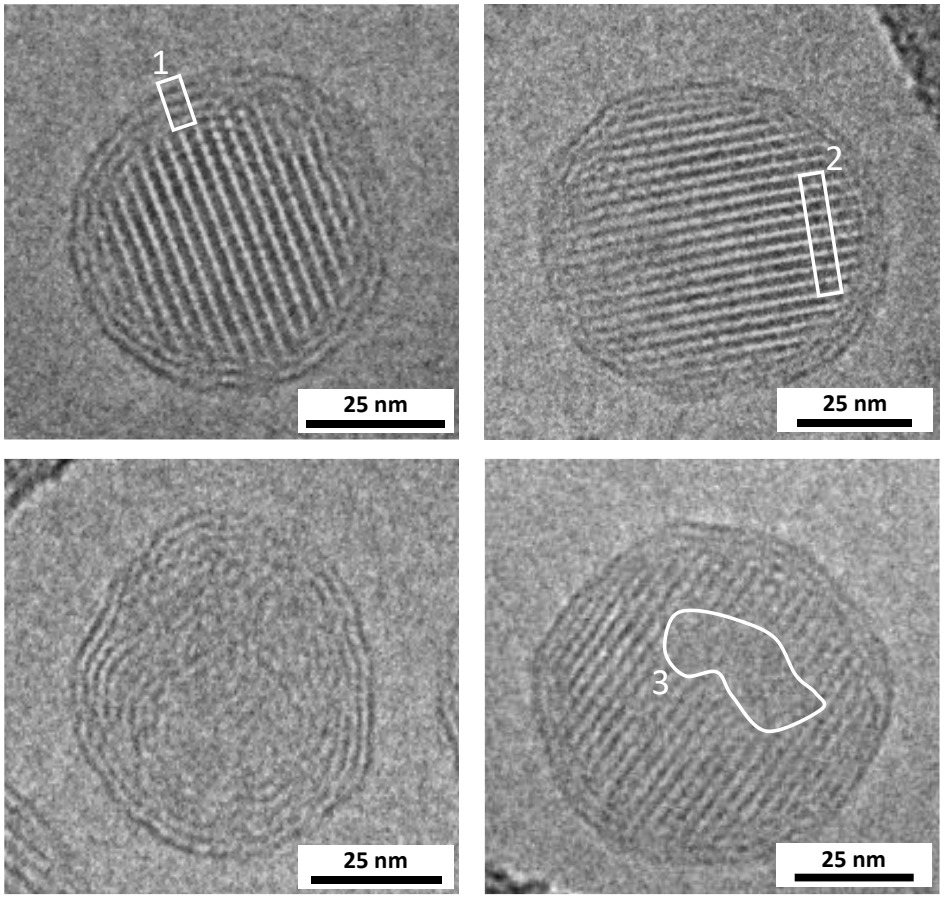

Figure 5-11: Cryo-TEM images of PTQ10:Y12 nanoparticles. The periodic spacings highlighted by the rectangle 1 and 2 corresponds to PTQ10 (d_z = 2.3 nm) and Y12 (d_z = 3.0 nm) respectively.

From the cryo-TEM images, it is obvious that no intimate morphology inside the nanoparticle is obtained with the PTQ10:Y12 system as we could expect from its low interfacial energy. Instead, PTQ10:Y12 nanoparticles consist of a monocrystalline domain in the core and another one with a different orientation in the shell of the particles, while PTQ10:Y6 nanoparticles had a polycrystalline structure with multiple lattice orientations. From the alternating high and low electron density lines, the lattice spacing d_z is easily accessible. The shell of the particles has a crystalline structure with a lattice spacing of 2.3 nm which is consistent with the diffraction peak of PTQ10 at q_z = 0.27 Å^{-1} reported with GIWAXS measurements.[202] Therefore, the periodic spacing in the core equal to 2.9 nm surely correspond to Y12, which match a similar value reported in the literature from GIWAXS measurements.[203] To confirm these observations, pure nanoparticles of PTQ10 and Y12 should be also analysed with cryo-TEM. Thought it seems on some images that the core is single Y12 crystal, further images are showing as well the presence amorphous domains of either PTQ10 or Y12 in the core as shown by the white area 3. Such an

observation might be in accordance with the low $\gamma_{D:A}$ of PTQ10:Y12 which allow the formation of more intermixed nanoparticles. Nonetheless, these results might explain the high photoluminescence intensity from Y12 molecules in composite PTQ10:Y12 nanoparticles (**Figure 5-3**), due to the large Y12 crystalline domains. The difference of arrangement between Y6 and Y12 under the same formation conditions certainly comes from the longer alkyl chains of Y12. A possible explanation would be that the higher solubility of Y12 in the organic phase during the mini-emulsion process gives to the NFA even more time for molecular self-assembly in the nanoparticles. A similar effect is observed in the formation of A-DA'D-A type SMAs-based film, deposited with a chloroform solution, and having different side chain length, where ordered molecular packing are formed even without a thermal treatment.[204] The explanation for the observed core-shell morphology could be explained in the same manner, where the radial phase separation is driven by the strong arrangement of Y12 which thus prevent the donor and acceptor to form mixed domains. In addition, the presence of the NFA in the core is consistent with the higher surface energy of Y12 as compare to PTQ10 ($\gamma_{Y12} > \gamma_{PTQ10}$).

5.2.3.3. V_{OC} loss: Y6 vs Y12

While most of the OPV parameters of PTQ10:Y12 *np-BHJ* devices can be understand through the morphological analysis, the fact that this system does not undergo any V_{oc} loss with respect to its organic counterpart, which is in contrast with the Y6-based nanoparticle system, was quite surprising. Such result suggests that the chains length has an influence on this V_{OC} drop. In order to gain some understandings of such difference, the evolutions of V_{OC} vs. light intensity for both PTQ10:Y6 and PTQ10:Y12 *np-BHJ* is plotted in **Figure 5-12**. Both *np-BHJ* devices exhibit large slops 1.37 ± 0.02 kT/q and 1.41 ± 0.01 kT/q for PTQ10:Y12 *np-BHJ* and PTQ10:Y12 *np-BHJ* respectively. These large values indicate that trap assisted recombination of less than 2nd order recombination is occurring in both systems. Though the slope is lower for Y12-based devices, it is unlikely that the V_{OC} loss observed with PTQ10:Y6 *np-BHJ* originates from non-radiative recombination energy loss only. From the monocrystalline domains observed with the cryo-TEM, we could have expected a lower trap density from the PTQ10:Y12 *np-BHJ* and thus less bimolecular recombination. More understandings are hence needed in order to probe the parameters affecting the V_{OC} PTQ10:Y6 *np-BHJ* devices.

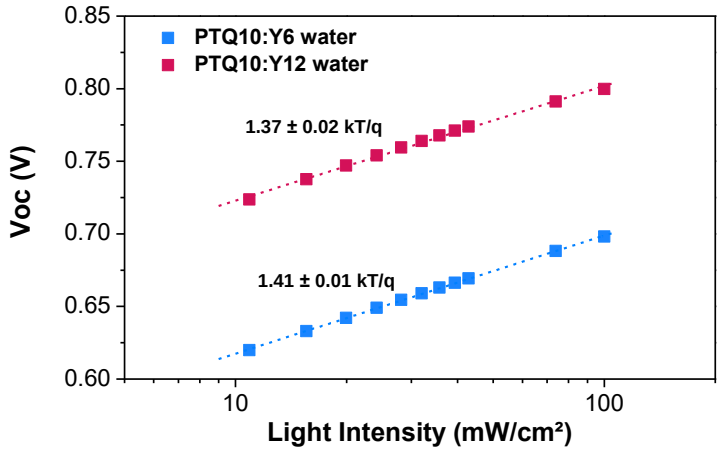

Figure 5-12: Open-circuit voltage (V_{OC}) as a function of light intensity for PTQ10:Y12 np-BHJ (red) and PTQ10:Y12 *np-BHJ* (blue) devices.

5.2.4 Conclusion

From the results obtained with PTQ10 and two additional NFAs, it was possible to extend the study of the impact of the interfacial energy of system when forming nanoparticles. With an intermediate $\gamma_{D:A}$, PTQ10:IDIC *np-BHJ* showed power conversion efficiency above 5 %, which is still half of the performances obtained with PTQ10:IDIC *BHJ* devices prepared with chloroform. The core-shell observed in the STXM analysis implies that the miscibility between the two material is not high enough to prevent the radial phase separation. Coming back to a low $\gamma_{D:A}$ system, devices with PTQ10:Y12 nanoparticles have been studied. The OPV performances obtained with these particles have shown a high dependence to the thermal treatment and increase continuously up to 150°C thermally. Surprisingly and contrary to PTQ10:Y6 np-BHJ, for higher temperatures, the performances drop dramatically down to 2.00 % for 200°C. Cryo-TEM images have highlighted a core shell morphology where both the donor and the acceptor exhibit highly crystalline structures. Upon annealing, the thin shell of PTQ10 might allow the Y12 to easily percolate and inevitably create large domain at a too high temperature. Nevertheless, the study of Y12 has introduced the notable effect of the acceptor side chains length on the morphology of the nanoparticles and subsequently on the OPV performances. More importantly for water-processed OPV, the increase of the side chains length seems to allow the use of lower temperature for the thermal treatment of the nanoparticulate film, while keeping relatively high efficiency. To carry on, and confirm the positive impact of longer side chains

on the formation and processing of nanoparticles, the study is now enlarged to the donor polymer with varying side chains.

5.3. Impact of polymer alkyl side chain with FOx-T:Y6

Following the results obtained on the effect of the side chain length of the acceptor (Y6 vs Y12), the logical next step is now to turn our attention to the alkyl chain length of the donor polymer. Like small molecules, alkyl side chains are essential for conjugated polymers in order to increase their solubility and consequently their processability. Other than that, their modification can have a strong impact on their proprieties and those of the devices based these polymers. For instance, even though longer chains are better for solubility, they are often problematic for charge transport and optimal phase segregation.[205–207] Nevertheless, side-chain engineering has also shown positive effect on mechanical proprieties, molecular aggregation, crystallinity and its orientation.[208–212] Therefore, it was also of great interest to assess the impact of such modification when forming nanoparticles out of these polymers. Other than the references previously mentioned, few examples can be found in the literature for organic solvent-based OPV, and no reported studies examining the influence of the side chain length on water-based OPV. Being able to perform a large screening of conjugated polymers with differing side chains is not an easy task due to their synthetic complexity and the lack of commercially available candidates. For this purpose, we have initiated during this PhD a collaboration with Dr. Martina Rimmele and Prof. Martin Heeney, following their recent published work on a new library of conjugated polymers with record-low synthetic complexity.[199] This library has enabled us to study the impact of the side chains on the formation of the nanoparticles and their integration in OPV devices.

5.3.1 FOx-T:Y6 nanoparticles

FOx-T is a family of conjugated polymers based on benzo[*c*]-[1,2,5]thiadiazole which is the electron acceptor unit and a thiophene being the electron donor unit.[199] A large library has been synthesised based on these combined units, allowing the screening of different alkyl side chains. One of the polymers, namely FO6-T, was especially attractive as

it reaches 15.4% PCE in a binary blend with L8-BO as the acceptor (processed from chloroform and DIO, at lab-scale, in the group of Prof. Gasparani in London). On top of being a performing polymer for OPV, its good solubility in non-chlorinated solvents and its low synthetic complexity make it a good candidate for potential upscaling.[201],[213] Herein, the study will focus on three different polymers, namely FO4-T, FO6-T and FO8-T, with different alkyl side chains which are 2-butyl-1-octyl, 2-hexyl-1-decyl and 2-octyl-1-dodecyl respectively (**Figure 5-13**). As we are now familiar with, and as it will also be interesting to compare the upcoming results with previous polymer:NFA system, Y6 is used as the acceptor small molecule to form composite nanoparticles with each of the FOx-T polymers.

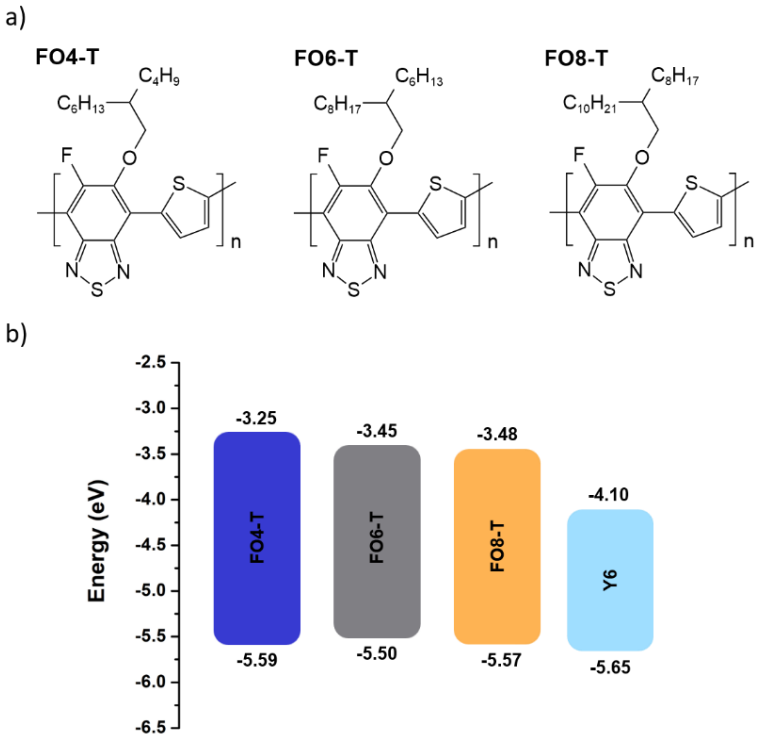

Figure 5-13: (**a**) Chemical structures of FO4-T, FO6-T and FO8-T donor polymers. (**b**) Highest Occupied Molecular Orbital (HOMO) and Lowest Unoccupied Molecular Orbital (LUMO) of FO4-T, FO6-T, FO6-T and Y6.

Composite nanoparticles with FOx-T:Y6 nanoparticles were synthesised following the usual procedure described in **Methods**: For the organic phase, 35 mg ml^{-1} of FOx-T:Y6 [1:1.5] mixture was first dissolved in chloroform stirred for 2 h at 65 °C in a nitrogen-filled glovebox. Aqueous phase was obtained by dissolving 5 mg ml^{-1} (17 mM) of SDS in

deionised water and stirred for 30 min at room temperature. The concentration of each dispersion was adjusted in order to obtain a concentration of 60 mg ml^{-1}.

UV-visible absorbance spectroscopy was then performed for each of the three dispersions and are plotted in **Figure 5-14**. All polymers are showing similar features which are a first absorption peak in the high energy region around 350–400 nm, and then two peaks in the lower energy region from 600–700 nm. Therefore, in these regions, the synthesised nanoparticles of FOx-T:Y6 have the same spectral signature. Looking more carefully at the Y6 region (700-850 nm), the composite nanoparticle FO8-T:Y6 presents a higher contribution of Y6 absorption. As the spectra are normalised to the maximum absorption in the FOx-T polymers region, the higher contribution from Y6 is probably due to a lower absorption coefficient of the FO8-T polymer as previously observed for polymers when increasing the side chain length.[205]

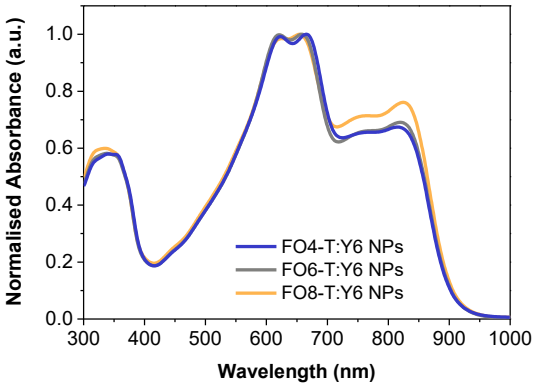

Figure 5-14: UV-visible absorption spectra of FO4-T:Y6 (blue line), FO6-T:Y6 (grey line), FO8-T:Y6 (orange line) nanoparticles dispersions. (dispersions concentration = 0.06 mg ml^{-1})

5.3.2 FOx-T nanoparticles films

The deposition of the aqueous dispersions was done following the optimised process described in **Chapter 3**. Nanoparticle layers were firstly formed on glass substrates in order to examine the absorbance behaviour of each blend upon different thermal annealing conditions. In **Figure 5-15**, the absorbance of the *np-BHJ* films as cast, and annealed at 140°C, 170°C and 200°C are shown. For each condition, an interesting trend is observed from the ratio between the Y6 peak (around 840 nm) and the FOx-T polymers peak (around 675 nm) which increases with the side chain length and for all annealing

temperature (**Figure 5-16a**). This trend is relatively consistent with what is observed in the absorption spectra of the dispersions as the Y6/FOx-T ratio was also higher for FO8-T based nanoparticles due to lower extinction coefficient for this polymer. Overall, for each nanoparticulate layer, an increase in the contribution of the Y6 absorption is observed as compare to the dispersions. With increasing annealing temperature, this ratio keeps rising as the Y6 peak gets even more pronounced at high temperatures. And for FO8-T:Y6 at 200°C, the contribution of Y6 becomes even sharper and intense as compare to FO4-T:Y6 and FO6-T:Y6 nanoparticulate layers. We note that the FOx-T peaks is also getting more intense as the temperature increases, but it is less impacted than the NFA peak (**Figure** 5-16**b** & **c**). These results indicate that upon thermal energy, both the polymer and the Y6 tend to have more mobility in the film when increasing the side chain. This increase is probably enhancing the intermolecular interaction and the crystallisation of Y6.

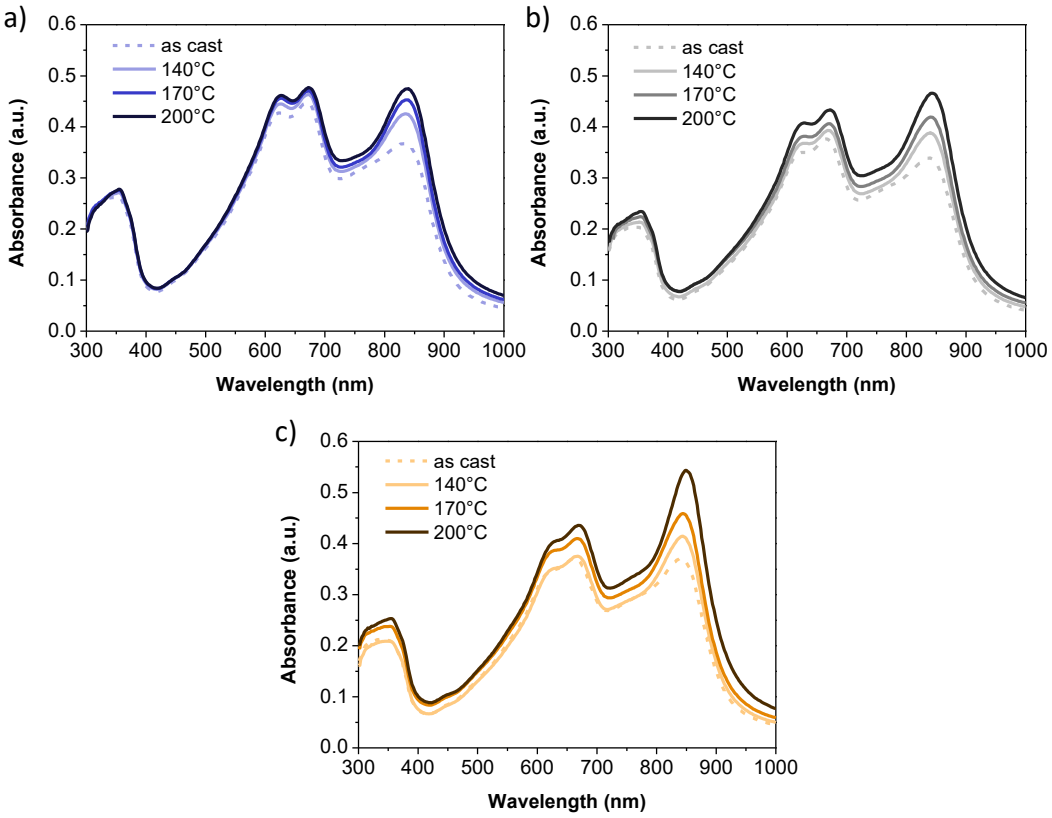

Figure 5-15: UV-visible absorption spectra of (**a**) FO4-T:Y6 *np-BHJ* films, (**b**) FO6-T:Y6 *np-BHJ* films and (**c**) FO8-T:Y6 *np-BHJ* films with varying thermal treatment.

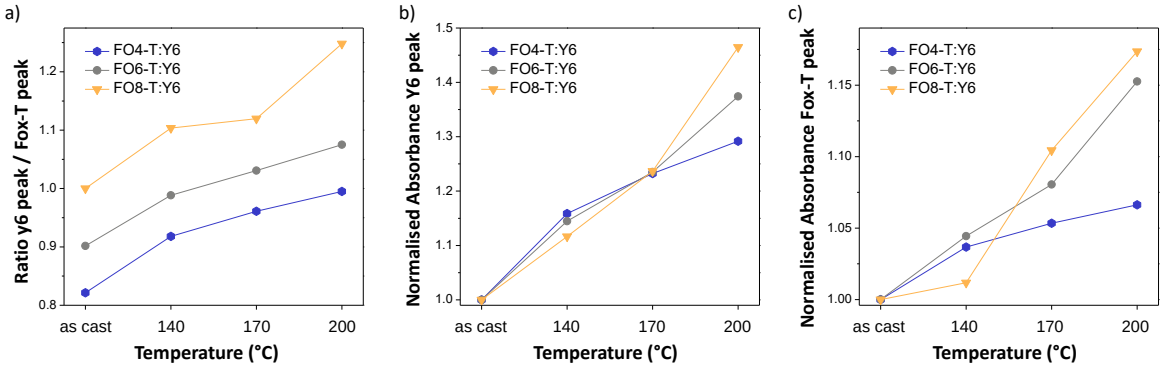

Figure 5-16: (**a**) Evolution of the ratio between the peak intensity of Y6 (at 840 nm) and FOx-T (at 675 nm) with varying temperature. Evolution of the peak intensity of (**b**) Y6 and (**c**) FOx-T with varying temperature

---

5.3.2.1. OPV performances

In order to evaluate the OPV performances of each nanoparticulate layer upon thermal annealing, solar cells prepared from FOx-T:Y6 nanoparticles dispersion concentrated at 60 mg ml^{-1} have been prepared. The dispersion has been spin-coated onto ZnO at a speed of 2500 rpm for 60 sec resulting in a nanoparticles layer thickness of around 160 nm. The resulting nanoparticulate layers were then annealed at different temperature for 5 min resulting in an active layer thickness of 160 nm. For the control devices, I have decided to use the references reported in the published work of Rimmele *et al.* due to the lack of reliable devices fabricated our lab.[214] J-V curves of the three donor:acceptor systems with varying thermal annealing are shown in **Figure 5-17a-c** along with the evolution of the average PCE extracted at each temperature (**Figure 5-17d**). When annealed at 140°C, the two FO4-T:Y6 and FO6-T:Y6 nanoparticles-based solar cells exhibit similar performances with an overall PCE of 6.65% and 6.77% respectively. Slightly higher performances are obtained with the FO8-T:Y6 system reaching a 7.34% PCE mainly due to a better V_{OC} as compare to the nanoparticles with shorter chain polymer. When increasing the annealing temperature to 170°C, the previous trend is magnified as the FO8-T:Y6 *np-BHJ* performances are significantly increased while for FO4-T:Y6 and FO6-T:Y6 *np-BHJ* the increase of PCE is barely noticeable (7.39 % and 7.28 % respectively). A simultaneous increase of FF, J_{SC} and V_{OC} allow FO8-T:Y6 *np-BHJ* to reach an impressive 10.40% PCE (**Table 5-7**). Now taking a look to the performances of all the three devices annealed at 200°C, the np-BHJ based on shorter alkyl side chains polymers FO4-T:Y6 and FO6-T:Y6

are reaching their optimal performances with an average PCE of 9.01% and 9.05% respectively. As it is often the case with these nanoparticles-based solar cells, the FF is the major parameter that was enhanced with the increase of thermal annealing temperature. Surprisingly, FO8-T:Y6 *np-BHJ* behaves differently. Instead of seeing the performances of get even higher, a large drop of all V_{OC}, J_{SC} and FF is observed, causing the PCE to decline to an average of 3.19%. From these results, the FO8-T:Y6 nanoparticles-based device stand out by its lower optimal annealing temperature surely arising from the longer chains of the FO8-T polymer. This is comparable to when the alkyl chains were extended from Y6 to Y12 earlier in the chapter. But in the case of the polymer the lower temperature also gave better performances as compare to the FO4-T and FO6-T based devices.

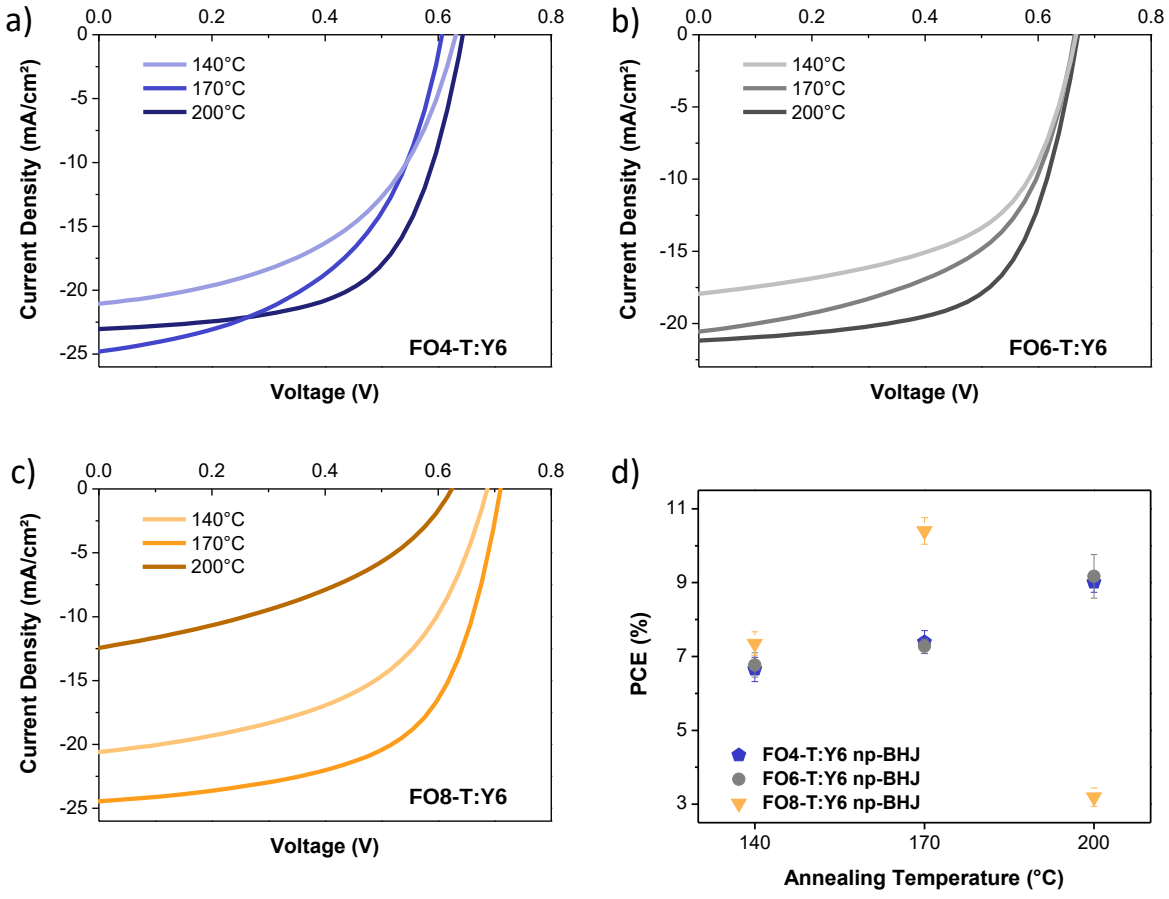

Figure 5-17: J-V curves of (**a**) FO4-T:Y6, (**b**) FO6-T:Y6 and (**c**) FO8-T:Y6 np-BHJ devices with varying thermal annealing. Note that the selected curves have been chosen to be as close as the average performance for each annealing temperature shown in **Table 5-7**. The graph (**d**) represents the average PCE vs. annealing temperature for each system.

The **Table 5-7** presents the details of the previous results as well as the OPV performances obtain with the same donor:acceptor systems but fabricated from a chloroform solution. Interestingly, the references do not show the same trend in performances as the water-processed devices. Indeed, the FO6-T:Y6 solar cells are clearly showing higher efficiency than FO4-T:Y6 and FO8-T:Y6. In this regard, a larger gap still remains between FO6-T:Y6 *np-BHJ* solar cells and their organic solvent-procced counterpart FO6-T:Y6 *BHJ* solar cells, 9.05% and 14.1% respectively. Concerning the devices prepared with FO8-T:Y6 nanoparticles, almost no difference with the organic solvent-processed device in the overall efficiency is observed with 10.4% and 10.7% PCE achieved respectively. Thought a V_{OC} loss of 83 mV could be detrimental, a larger FF allows the water-processed devices to compete with their organic solvent-processed counterpart. The V_{OC} loss concerns every FOx-T:Y6 *np-BHJ* devices and seems to be here again consistent with the presence of Y6 in the nanoparticles. The polymers should be associated with additional NFAs to definitely link this V_{OC} loss to the use of Y6, as has been done with PTQ10. Nevertheless, as previously shown for Y12, the longer side-chains of a polymer-based nanoparticles allow their processing at lower temperature while reaching PCE over 10%.

Table 5-7: Average OPV performances of optimised FOx-T:Y6 *np-BHJ* and *BHJ* devices extracted from a minimum of 8 devices with varying annealing temperature (best devices in brackets).

	TA temperature (°C)	V_{OC} (mV)	J_{SC} (mA cm^{-2})	FF	PCE (%)
FO4-T:Y6 *np-BHJ*	140	632 ± 9 (637)	20.80 ± 0.39 (21.02)	0.51 ± 0.02 (0.53)	6.65 ± 0.33 (7.05)
	170	609 ± 8 (619)	24.58 ± 0.62 (24.40)	0.49 ± 0.02 (0.52)	7.39 ± 0.31 (7.79)
	200	652 ± 12 (670)	22.43 ± 0.43 (22.25)	0.62 ± 0.01 (0.63)	9.01 ± 0.27 (9.45)
FO4-T:Y6 *BHJ*[a]	100	750	22.72	0.58	9.80
FO6-T:Y6 *np-BHJ*	140	665 ± 8 (661)	19.09 ± 1.33 (21.20)	0.53 ± 0.03 (0.52)	6.77 ± 0.33 (7.28)
	170	664 ± 7 (661)	20.05 ± 0.39 (19.96)	0.55 ± 0.01 (0.57)	7.28 ± 0.19 (7.52)
	200	656 ± 14 (657)	22.33 ± 0.83 (23.42)	0.62 ± 0.02 (0.63)	9.05 ± 0.34 (9.88)

FO6-T:Y6 *BHJ*[a]	100	790	26.70	0.67	14.10
FO8-T:Y6 *np-BHJ*	140	689 ± 11 (699)	20.88 ± 0.84 (20.86)	0.51 ± 0.02 (0.52)	7.34 ± 0.32 (7.64)
	170	707 ± 4 (713)	24.17 ± 0.48 (24.78)	0.61 ± 0.01 (0.60)	10.40 ± 0.17 (10.64)
	200	626 ± 4 (628)	12.75 ± 1.12 (11.90)	0.41 ± 0.01 (0.41)	3.19 ± 0.25 (3.68)
FO8-T:Y6 *BHJ*[a]	100	790	24.16	0.57	10.70

[a]*The references were made with chloroform and have been taken from ref* [199]

5.3.2.2. Morphological investigation

The singular behaviour of FO8-T:Y6 nanoparticles upon annealing is presuming to be due to an early morphological change as compared to FO4-T:Y6 and FO6-T:Y6. To have more insight this assumption, topological AFM images are shown in **Figure 5-18** for two different annealing temperature (i.e. 140 and 200 °C).

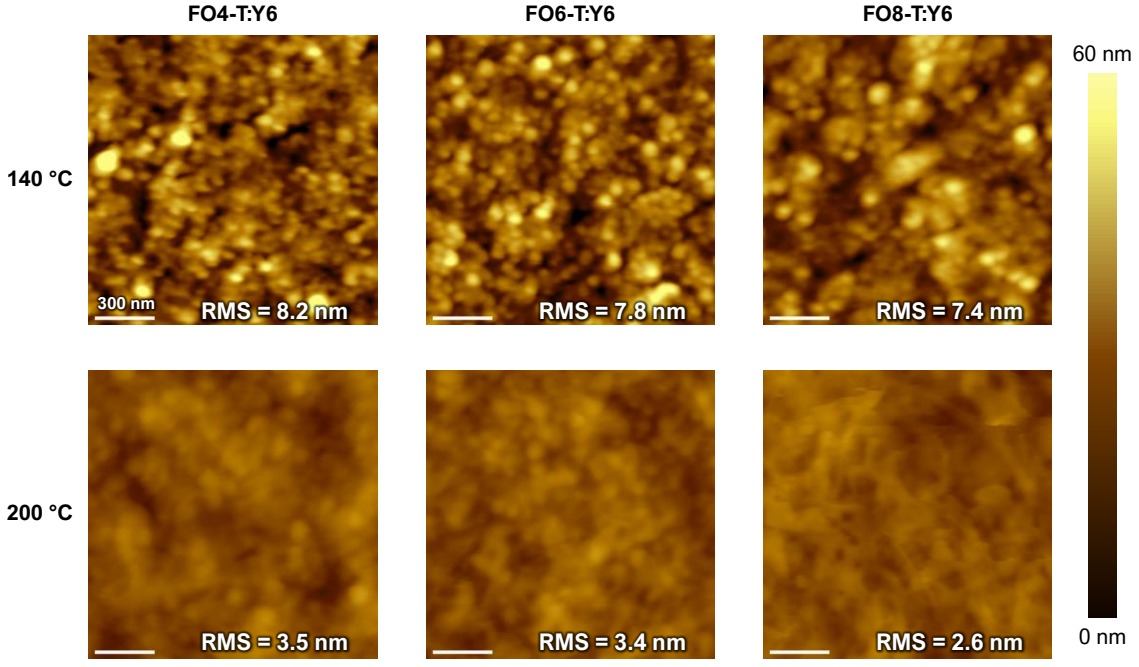

Figure 5-18: AFM topography images (height) of FO4-T:Y6, FO8-T:Y6 and FO8-T:Y6 (from left to right) np-BHJ film annealed at 140°C (top) and 200°C (bottom) for 5 min. (Scale bar = 300nm)

For each donor:acceptor system, nanoparticles are still visible even after a thermal annealing of 140 °C . The layers present also a relatively high roughness indicating that the sintering of nanoparticles is not totally done. However, even with the presence of a nanoparticulate films, a trend is observed when increasing the alkyl chains length as the RMS roughness is decreasing from 8.2 nm to 7.4 nm for FO4-T:Y6 and FO8-T:Y6 respectively. This result suggests that, with increasing side chain length, the sintering of the nanoparticles begins at lower temperature. At 200 °C, a similar behaviour observed for PTQ10:Y6 happens with a large decrease of the roughness which illustrates the total sintering of the nanoparticles. Although we could expect a large roughness and phase separation with FO8-T:Y6 because the performance dropped by more than 60 %, here again the RMS roughness is getting smaller with longer alkyl chains. Focusing now on the phase images (**Figure 5-19**), it is even clearer the nanoparticles are less and less visible when increasing the alkyl chains length. Side chains have the ability to create various distances between the polymer's backbone, leading to decrease the polymer backbone interaction. Although longer chains do not have an impact on the electronic properties, it can allow the polymer a necessary degree of mobility at lower temperature. This can be directly related to some transition temperature such as the T_g, which is known to be decreased when increasing the polymer side chains.[215],[216] With these preliminary results, we show that it is possible to design hard and soft nanoparticle with variation of the alkyl chains length. The longer the chains, the softer the particles. Unfortunately no reliable images have been extracted for the films annealed at 170 °C, the optimal temperature for FO8-T:Y6 nanoparticles-based OPV cells as it is expected to have the optimal sintering at this temperature. The height image at 200 °C do not give any clue to understand the drop of performances for FO8-T:Y6 np-BHJ devices. However, when looking at the phase images, larger phase segregation is observed for FO8-T:Y6 np-BHJ with large domains between 300 nm to more than 1 µm. Such morphological change at the nano/microscale can explain the drop of performances due to increased geminate recombination.

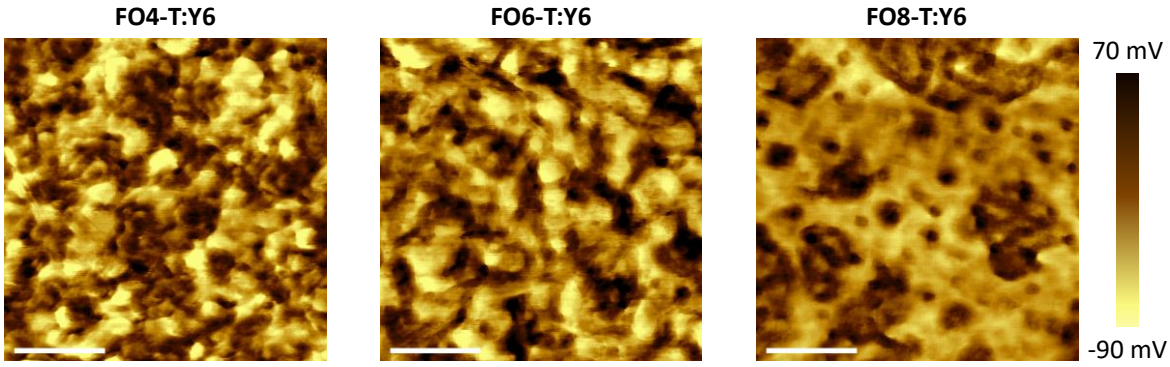

Figure 5-19: AFM images (phase) of FO4-T:Y6, FO8-T:Y6 and FO8-T:Y6 (from left to right) np-BHJ film annealed at 200°C for 5 min. (Scale bar = 300nm)

Since high OPV performances have been achieved with FOx-T:Y6 *np-BHJ*, comparable to what has been obtained with PTQ10:Y6 nanoparticles, an intimate donor:acceptor morphology is expected as internal morphology of the three FOx-T:Y6 nanoparticles. Unfortunately, no STXM mapping of the materials has been done to confirm this assumption. Nevertheless, cryo-TEM images have been recorded to analyse the internal morphologies of the nanoparticles and detect eventual differences to explain the different behaviour of the nanoparticles under thermal annealing (**Figure 5-20**). Indeed, the behaviours of the films upon annealing have some similarities with PTQ10:Y6 prepared with mini-emulsion and nanoprecipitation and FO8-T:Y6 nanoparticles seem to be softer than the nanoparticles prepared with the shorter side chains polymers. Therefore, we could expect from the FO4-T and FO6-T based nanoparticles more crystalline phase. However, the cryo-TEM images of the three type of particles are not showing much differences between each other. For all the nanoparticles, a strong crystalline nature is observed with mixed orientations which is very similar to what has been previously observed with PTQ10:Y6 prepared with mini-emulsion. Therefore, it seems that increasing the length of the polymer side chains do not have an effect on the crystallinity.

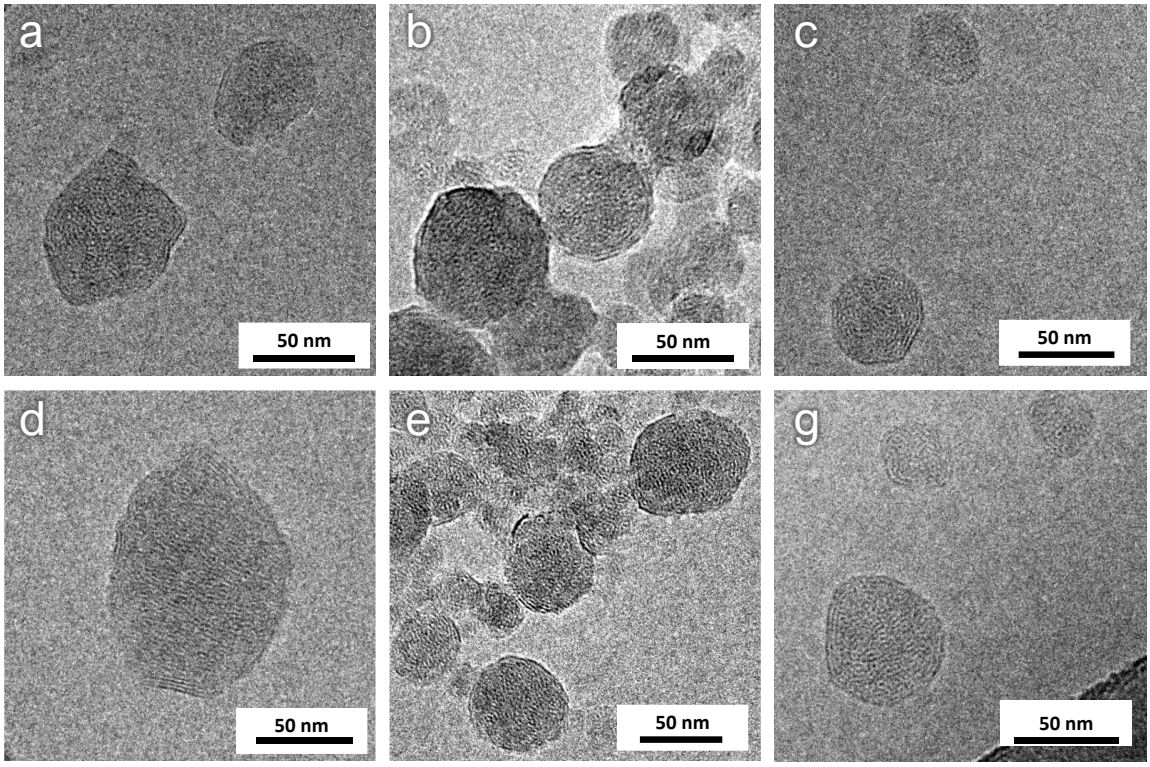

Figure 5-20: Cryo-TEM images of (**a,d**) FO4-T:Y6, (**b,e**) FO6-T:Y6 and (**c,g**) FO8-T:Y6 nanoparticles

5.3.3 Conclusion

Nanoparticles based on polymers FOx-T, which have different alkyl side-chain length, and the NFA Y6 have been studied to assess the effect of varying the polymer side-chains length. The absorption signature of the nanoparticulate films exposed to various annealing temperature already shown some contrast in term of absorption features. The contribution of Y6 is getting more and more dominant over the polymer when increasing the thermal annealing, and this phenomenon is enhanced when expanding the polymer side chain length. This result was a first indication that longer side chains could be more favourable to induce a change in the aggregation of both materials. Looking at OPV performances of the different nanoparticles-based BHJ, an important contrast is observed between FO8-T:Y6 and the two other systems. FO4-T:Y6 and FO6-T:Y6 nanoparticles-based solar cells need a high temperature (200°C) to reach their highest performances (9.01% and 9.05% respectively), while for FO8-T:Y6 a lower temperature was enough

(170°C) and achieved also a superior PCE (10.5%). Surface morphology analysis revealed that the sintering of FO8-T:Y6 nanoparticles needs less energy to happen with 170°C being the optimal temperature. Surprisingly, cryo-TEM images do not displayed any differences in term of molecular arrangement. Nevertheless, and despite the low interfacial energy of these three systems, the cryo-TEM images are showing that a thin crystalline shell is present on all the three nanoparticles. Further investigation are still ongoing such as DSC measurements and GIWAXS to understand the parameters that can induce the reorganisation of the FOx-T:Y6 nanoparticles based-active layer.

5.4. Conclusion of chapter 5

In this chapter, PTQ10 has been associated with additional NFAs to pursue the study of the impact of the interfacial energy between the donor and the acceptor on the morphology of nanoparticles and nanoparticles-based BHJ (*np-BHJ*). Blended with IDIC, the PTQ10:IDIC *np-BHJ* devices have shown a maximum PCE of 5.23 %. This donor:acceptor system, which has an intermediate $\gamma_{D:A}$ between PTQ10:Y6 and PTQ10:$PC_{61}BM$, also forms nanoparticles with a core-shell morphology. However, more intermixed domains were observed which could favour the formation. This result shows that the selection of a system with a low $\gamma_{D:A}$ allows the formation of a fully blended film where the nanoparticles are completely sintered. PTQ10 was also associated with Y12, a similar acceptor than Y6 with longer side-chain length. Although PTQ10:Y12 has a low $\gamma_{D:A}$, PTQ10:Y12 nanoparticles present a core-shell morphology with a thin shell composed of PTQ10. Nonetheless, this morphology is not preventing PTQ10:Y12 *np-BHJ* solar cells to reach a relatively high efficiency of 7.52 % PCE which is limited by a low J_{SC} due to high geminate recombination. In addition, the longer alkyl side chains of Y12 with respect to Y6 have impacted the process of the active layer as the optimal temperature was found to be lower. This is encouraging in view of reducing the thermal treatment of nanoparticule films to match the industrial processing requirements. Following these results, FOx-T donor polymers with different alkyl chain length have been studied in association with Y6. Increasing the length of the polymer side-chains allowed to decrease the optimal annealing temperature (170°C for FO8-T:Y6 *np-BHJ* vs 200°C for FO4-T:Y6 *np-BHJ* and FO6-T:Y6 *np-BHJ*) without concessions on the overall performances of FO8-T:Y6 *np-BHJ* solar cells. The resulting PCE was found to be as high as the PCE obtain for the same donor:acceptor

system but processed from chloroform solution bridging the gap between water processed and chlorinated solvent processed active layers. From the AFM measurements, such lower temperature is believed to come from the softer nanoparticles obtained by increasing the side chain length of the polymer. However, more morphological analysis such as GIWAXS are needed due to the lack of contrast revealed by the cryo-TEM images.

Chapter 6

Linking nano-morphology and charge transport with nano-gap devices

Part of the following chapter has been published in a peer-reviewed journal [217]:

H. Laval, Y. Tian, V. Lafranconi, M. Barr, P. Dastoor, M. M. Marcus, G. Wantz, N. P. Holmes, K. Hirakawa, **2024**, *2404112*, 1.

6.1. Introduction

Up to now, the morphology of the nanoparticles has proved to influence greatly nanoparticles-based OPV devices, and is closely linked to the final performances. In an effort to pursue our understanding on this dependency, it is crucial to explore charge transport in these nano-objects upon morphological differences. Diverse strategies are employed to study electronic transport in organic semiconductors. Among the experimental techniques used for this purpose; time-of-flight, field-effect transistor configuration, electron or hole only devices or charge extraction by linearly increasing voltage are the most widely spread.[82,112,138,218] However, all these techniques explored not only the charge transport in the nanoparticle itself but also between the nanoparticles since the properties of thin films, *i.e.* nanoparticles assemblies, have been studied. Therefore, in an effort to investigate the charge transport properties at the single nanoparticle scale, nanogap devices have been developed to probe the charge transport at the nanoparticle scale. Nanoscale devices were fabricated using clean-room technology, e-beam lithography and photo-lithography. A diode configuration with a sub micrometric gap of 100 nm was developed in order to characterise the waterborne organic semiconductor nanoparticles. Doing so, it allows us to get closer to the electronic properties of a single nanoparticle. Dielectrophoresis (DEP) has been used to insert nanoparticles in the nanogap. The final nanogap devices with nanoparticles trapped inside were analysed using hole-only devices and mobilities were extracted in space charge limited current regime. P3HT, P3HT:eh-IDTBR and P3HT:o-IDTBR nanoparticles have been synthetised by mini-emulsion and their morphology have been studied using STXM. These nanoparticles, having different composition and morphology have been inserted in the nanogap device and their mobility extracted. Such a comprehensive study allowed us to link the composition and morphology of the nanoparticle to understand their possible impact on the final OPV device performances.

6.2. Nano-gap devices fabrication

The nanogap structures have been built on silicon substrates with 230 nm thermally grown silicon oxide using clean-room techniques. First e-beam lithography was used to design the nanoscale gap between the two electrodes. Three kinds of nanoscale structures have been designed: trapezoid shaped electrodes with length and width of 100 nm, rectangular shaped electrodes with nanogap length of 100 nm and a width of 10 μm and interdigitated electrode with nanogap length of 100 nm and a width of 29 μm. Titanium (10 nm) and gold (50 nm) were thermally evaporated to form the electrodes followed by a lift-off process. Then photolithography was used to create the contacts, followed by a second evaporation of Ti/Au electrode and a lift-off process. The workflow of the design of such nanoscale electrode is schematised in **Figure 6-1** and the detailed experimental procedure is described in **Methods**. The resulting devices for the trapezoid shaped electrodes are shown in **Figure 6-2**.

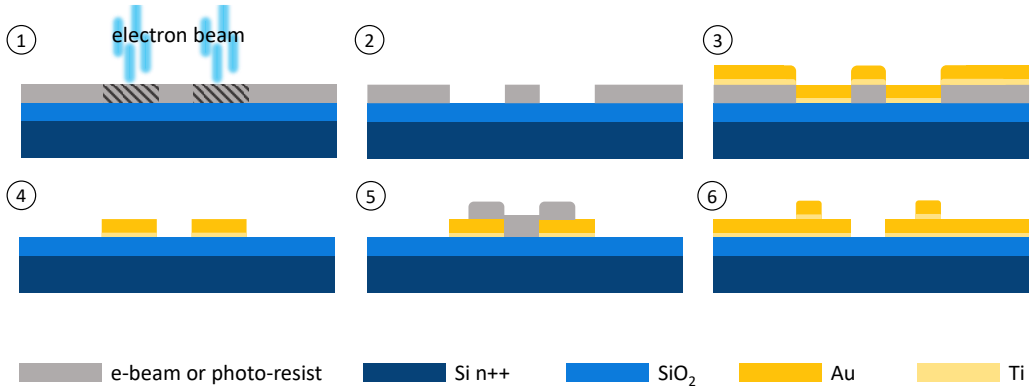

Figure 6-1: Fabrication of the nanoscale device (**1**) e-beam lithography (**2**) e-beam development (**3**) electrodes deposition (**4**) lift-off (**5**) photolithography (**6**) electrodes deposition + lift off.

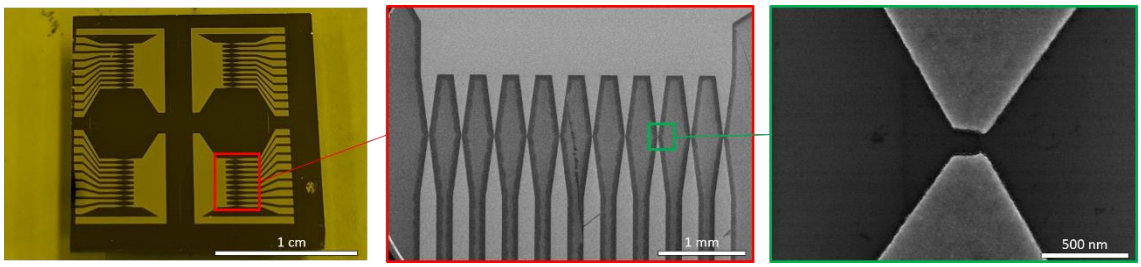

Figure 6-2: Photograph and scanning electron microscopy images of the nanogap devices.

6.3. DEP force: A tool to trap nanoparticles in the gap

After fabrication of the nanogap channels, nanoparticles have been incorporated using DEP technique. This technique has been widely used in biology to trap cells or proteins, and can also be used to attract dielectric particles as well as semiconductors or metallic particles.[219–223] DEP force is created when a particle is submitted to an alternative electric field, which creates a polarisation in the particle. Depending on the permittivity and conductivities of the medium and the object, the force can be attractive or repulsive. The process involves the deposition of a drop of nanoparticle dispersion on the nanogap. Then an alternative voltage is applied between the two electrodes to induce the dielectrophoresis force. Finally, the excess of water containing nanoparticles is removed and the substrate dried. **Figure 6-3** illustrated schematically the process of nanoparticles trapping. The dielectrophoresis force exerted to the nanoparticles depends a several parameters as described by the following equation (6.1):

$$F_{DEP} = 2\pi\varepsilon_m a^3 Re[K(\omega)]\nabla E^2 \tag{6.1}$$

Where a is the particle radius, ε_m is the permittivity of the suspending medium, E is the amplitude of the applied field (in case of AC field, root-mean-squared E) and $Re[K(\omega)]$ the real part of the Clausius-Mossotti factor (CM factor). The latter is dependent on the frequency of the applied alternative electric field and can be either positive or negative, which implies that the DEP force can be either positive or negative too. $Re[K(\omega)]$ is defined by the equation (6.2) where ε_p is the permittivity of the particle, σ_m is the conductivity of the suspending medium, σ_p is the conductivity of the particles, and ω is the angular frequency of the applied electric field:

$$\boldsymbol{Re[K(\omega)]} = \frac{\left[\left(\boldsymbol{\varepsilon_p} + \boldsymbol{2\varepsilon_m}\right) + \frac{\left(\boldsymbol{\sigma_p} - \boldsymbol{\sigma_m}\right)\left(\boldsymbol{\sigma_p} + \boldsymbol{2\sigma_m}\right)}{\boldsymbol{\omega^2}}\right]}{\left[\left(\boldsymbol{\varepsilon_p} + \boldsymbol{2\varepsilon_m}\right)^2 + \frac{\left(\boldsymbol{\sigma_p} + \boldsymbol{2\sigma_m}\right)^2}{\boldsymbol{\omega^2}}\right]} \tag{6.2}$$

The insertion of nanoparticles in trapezoid shaped electrodes using DEP force was performed on P3HT nanoparticles synthesised by mini-emulsion (see **Chapter 3** for experimental details) with 97 nm average diameter determined by DLS. The concentration of the dispersion was optimised to 0.05 mg ml^{-1} as well as some of the DEP conditions: the peak-to-peak voltage (V_{pp}) at 3 V and DEP time (t_{DEP}) equal to 5 seconds. The effect of the frequency of the electric field was studied.

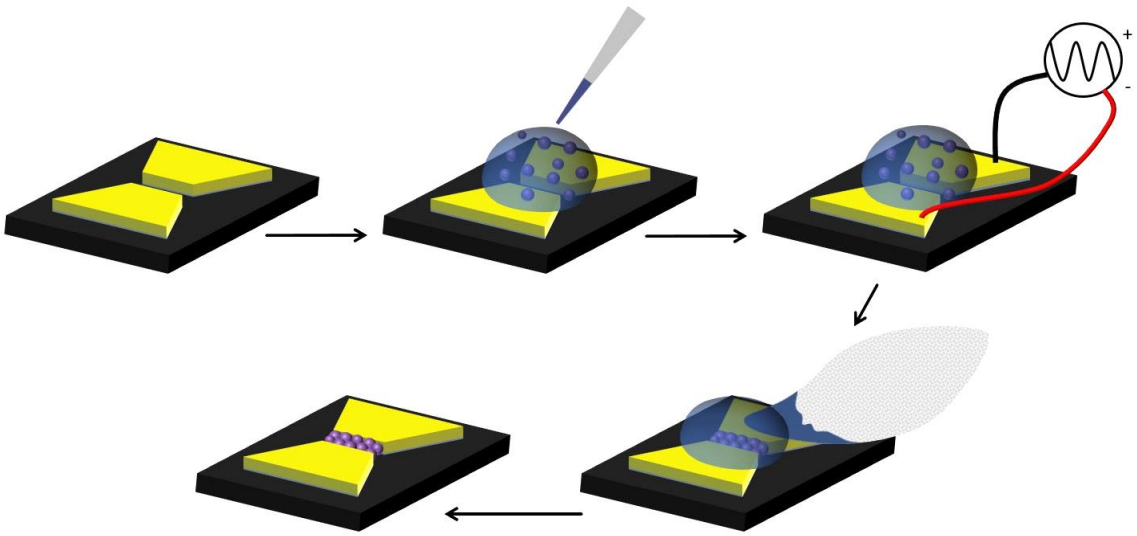

Figure 6-3: Different steps for the insertion of nanoparticles in the nanogap device.

The real part of the Clausius-Mossotti (CM) factor was calculated for different frequency of the applied electric field considering that $\varepsilon_p = 2.9\ \varepsilon_0$, $\varepsilon_m = 80\ \varepsilon_0$, $\sigma_m = 4\ 10^{-4}$ S m^{-1} and $\sigma_p = 10^{-3}$ S m^{-1} (**Figure 6-4a**).[222,224,225] The calculation shows that the DEP force can be either attractive or repulsive. At low frequencies, from 1 kHz to 20 kHz, the DEP force is attractive and the CM factor constant. Starting from 20 kHz and for higher frequencies, the CM factor decreases until it reaches zero around 170 kHz. For higher frequencies, the CM factor becomes negative and the DEP force turns repulsive. The impact of the frequency on the insertion of P3HT nanoparticles in trapezoid nanogaps is shown in **Figure 6-4b**. One can clearly see that for low frequency of applied electric field, from 3 to 10 kHz, the trapping is highly efficient, with nanoparticles in the channel, as well as on the sides of the electrodes. For frequencies of 30 and 60 kHz, the nanoparticles are more directed to the nanogap and

not around the electrodes, illustrating that the DEP force decreases while still being positive (attractive). However, starting from 100 kHz and up to 1 MHz, almost no NP are trapped in the channel, suggesting strongly that the DEP force became repulsive.

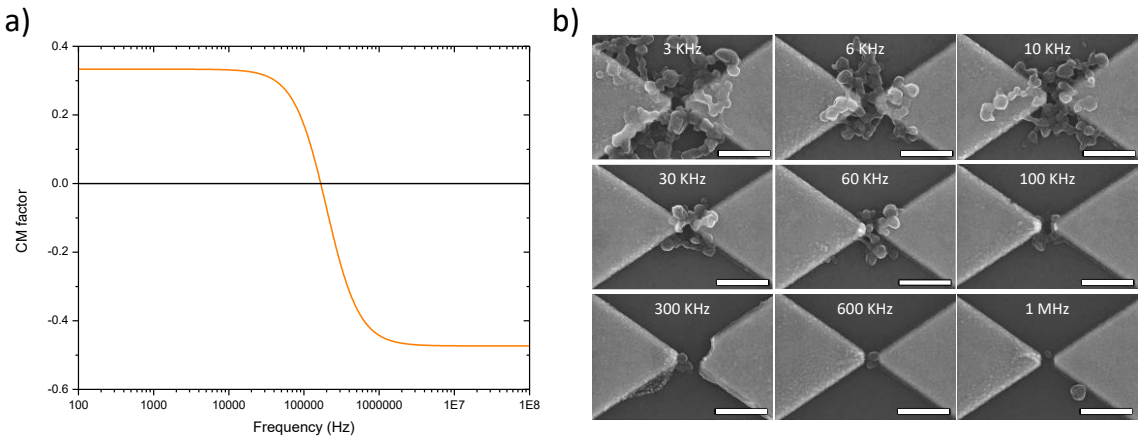

Figure 6-4: (**a**) Calculation of the CM factor for the applied conditions. (**b**) SEM images of the different nanogap after DEP process and for various applied AC electric field (scale bars: 500 nm).

6.4. Space charge limited current mobility

Now that the nanoparticles are trapped in the channel, the mobility can be extract by performing a simple I-V characterisation. In particular, the architecture developed is suitable for space-charge-limited-current (SCLC) measurements.[226] Doing so, the dependence of the measured current to an applied voltage can help to distinguish different charge transport regime (**Figure 6-5**). The first one is observed at low voltage and correspond to the ohmic regime, where the current evolves linearly with the voltage ($J \propto V$). Such a regime can generally emphasise a good ohmic contact. At a higher electric field, the current becomes space-charge limited and start to be quadratically dependent to the applied voltage ($J \propto V^2$). In this regime, a SCLC mobility can be extracted by the use equation (6.3), which represents the mathematical formulation of the Mott-Gurney law:

$$J_{SCLC} = \frac{9}{8}\varepsilon_0\varepsilon_r\mu\frac{V^2}{L^3} \quad (6.3)$$

In which ε_r is the relative permittivity of the organic semi-conductor, μ the charge carrier mobility (in our case the hole mobility μ_{h+} and L the distance between the two electrodes. The current density, J, was calculated using the section of the electrode as area: $A = W \times e$, with W and e as the width and the thickness of the electrodes. When increasing further the electric field, until a point called the trap-filled-limit SCLC where all the traps are filled. After that point, a new regime of trap-free is reached, where the mobility extracted generally represents the intrinsic mobility of the material. However, the organic semiconductors often have a high density of traps and this regime is only attained at high electric field. Therefore, the mobility extract from the SCLC trap-free regime do not represent the effective mobility in the active layer under the operating point of the organic solar cell and for this study, the mobility will be extracted from the shallow-trap SCLC.

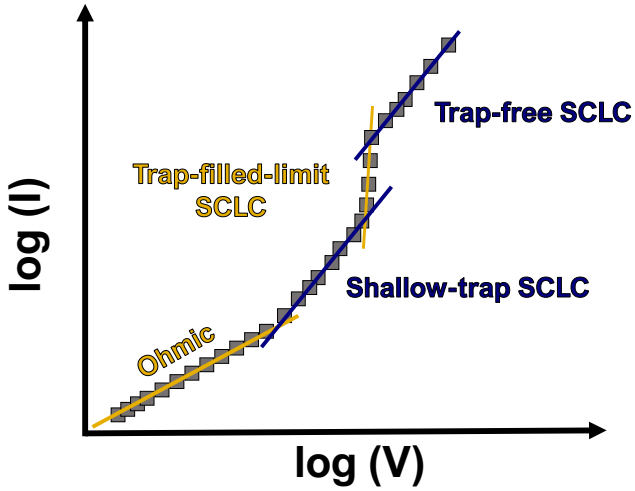

Figure 6-5: Typical I-V of SCLC in solids with different regime.

6.5. Device optimisation

In order to investigate the possibility to probe the charge transport using such nano-junction, different electrodes geometry have been investigated. Moreover, in addition to a

thermal treatment, different self-assembled monolayers (SAM) has been used as a surface treatment of the nanogap.

6.5.1 What electrodes?

In addition to the first design with trapezoid electrodes, P3HT nanoparticles have also been trapped in the nanogap with the rectangular and interdigitated geometry. For trapezoid configuration, the DEP conditions were V_{pp} = 3 V, t_{DEP} = 5 s and f = 60 kHz and for rectangular and interdigitated configuration, the same condition were used except for V_{pp} which was set to 5 V. After the DEP step, the excess of water is removed and the substrates dried in a nitrogen environment at 100°C for 10 min. The nanogap electrodes before and after DEP are presented in **Figure 6-6**.

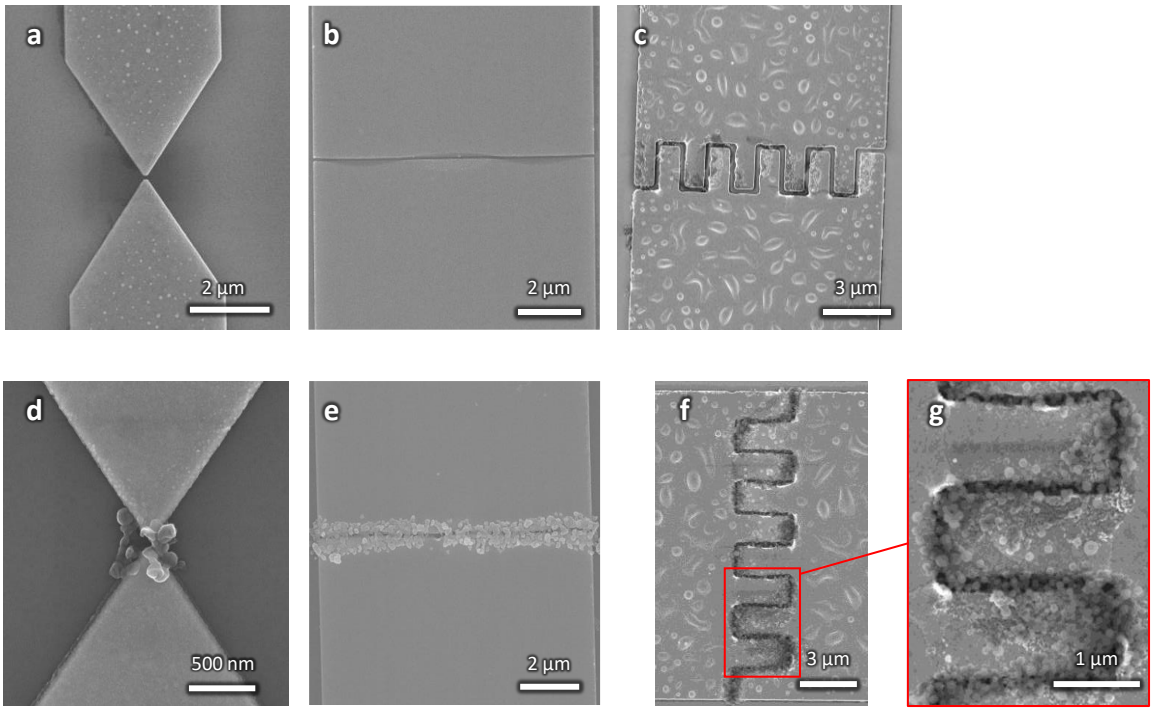

Figure 6-6: SEM images of the rectangular (a, d), trapezoid (b, e) and interdigitated (c, f, g) nanogap electrodes before (a-c) and after (d-g) dielectrophoresis step.

From the SCLC regime, hole mobilities were extracted for the rectangular and trapezoid geometries, 4.8 and 5.3 10^{-4} cm^2 V^{-1} s^{-1} respectively (in forward bias), a value commonly found for P3HT.[227] However, for the trapezoid configuration, a perfectly quadratic regime was not found, and only slopes around 1.63 were extracted, indicating that the SCLC regime might not have been reached for this structure. As one can see in

Figure 6-6d, nanoparticles are not only present inside the 100 nm gap but also around. In these side parallel pathways for charges, SCLC regime might not have been reached, resulting in I-V characteristic not purely quadratic. In addition, the error calculated for the trapezoid structure is large, on the order of magnitude as the mobility itself (**Table 6-1**). Therefore, mobility extracted from such device is not fully reliable. On the other hand, for the rectangular nanostructure, a slope of two could be found without and with a thermal annealing, which shows that the space charge limited current regime is reached. Furthermore, the error calculated on the mobility values for the rectangular configuration is lower than that of trapezoid configuration, indicating that the trapping of the nanoparticles in a rectangular geometry is more reproducible.

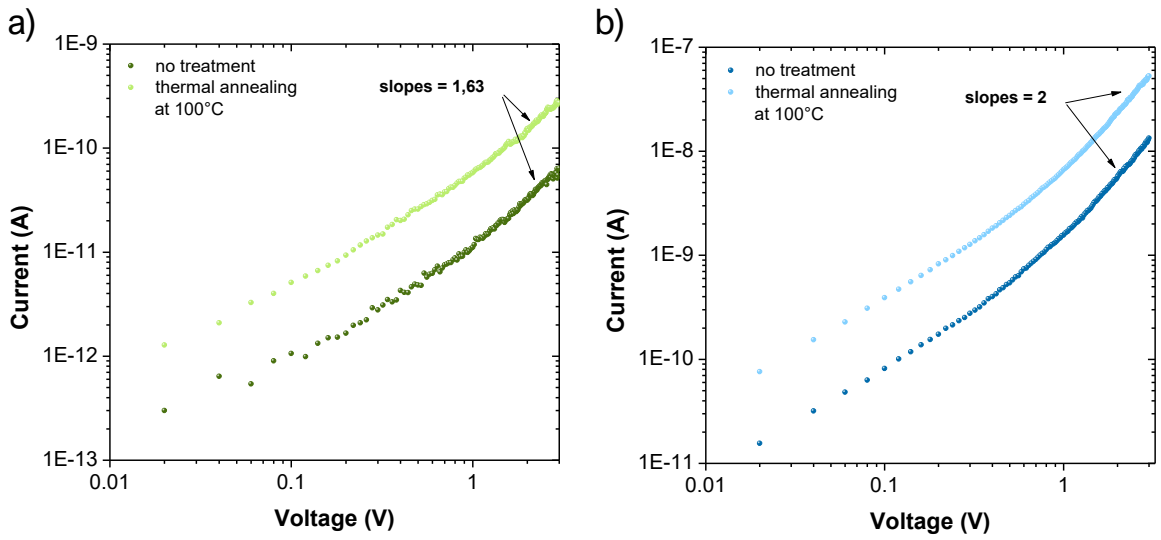

Figure 6-7: I-V characterisation plotted in logarithmic scale of the trapezoid (**a**) and rectangular (**b**) organic nano-junctions without and with thermal treatment.

Table 6-1: Hole mobilities (μ_{h+}) in $cm^2\ V^{-1}\ s^{-1}$ for various nanogap device configurations (trapezoid and rectangular) and different thermal treatments.

Architecture	Thermal treatment	μ_{h+} ($cm^2\ V^{-1}\ s^{-1}$)		Error ($cm^2\ V^{-1}\ s^{-1}$)	
		forward	reverse	forward	reverse
Trapezoid	no	4.3×10^{-4}	5.3×10^{-4}	$\pm 3.7 \times 10^{-4}$	$\pm 2.0 \times 10^{-4}$
	yes	2.7×10^{-3}	3.8×10^{-3}	$\pm 1.5 \times 10^{-3}$	$\pm 1.0 \times 10^{-3}$
Rectangular	no	4.8×10^{-4}	5.0×10^{-4}	$\pm 1.2 \times 10^{-4}$	$\pm 1.4 \times 10^{-4}$

	yes	2.3×10^{-3}	2.4×10^{-3}	$\pm 0.7 \times 10^{-3}$	$\pm 0.8 \times 10^{-3}$

Interdigitated electrodes geometry has been chosen to favour the signal-to-noise ratio as well as decrease the contact resistance.[228,229] However, the reproducibility of the results obtained with these electrodes was found to be poor and the mobility difficult to extract. Indeed, as shown in **Figure 6-8**, the SCLC regime is not always achieved with such architecture. The filling of nanoparticles might not efficient enough with the current DEP parameters applied, and further optimisation should be undertaken (**Figure 6-6g**).

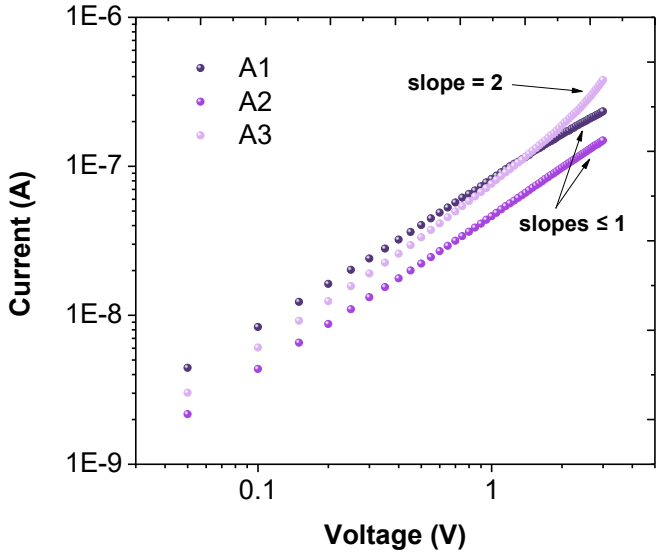

Figure 6-8: I-V curves of different interdigitated organic nano-junctions highlighting the poor reputability and the lack of SCLC regime.

6.5.2 What surface treatment?

In addition to the favourable thermal treatment, surface treatments with SAM have been investigated. The use of SAM to treat the surface and the electrodes can be beneficial to remove possible charge traps as well as improving the charge injection.[230–232] In the case of the DEP, we suspect that this treatment could also improve the insertion of nanoparticles in the gap. Three different molecules were used in this study, namely

octadecyltrichlorosilane (OTS), 1H,1H,2H,2H-perfluorodecyltrichlorosilane (FDTS) and phenethyltrichlorosilane (PETS). The I-V characteristics in logarithmic scales of the rectangular nanogap filled with P3HT nanoparticles and annealed at 100 °C for 10 min are shown in **Figure 6-9** for different SAM treatment. First, we observed an increase of almost two order of magnitude difference from the FDTS-treated device to the PETS-treated one. Secondly, these two SAM treatments seem to prevent the devices to reach the SCLC as no quadratic dependence with the applied voltage is observed. Interestingly, the increase of the current from the use of FDTS to PETS could be attributed to the decrease of hydrophobicity (less important for the PETS-treated device), which would result in a more effective trapping of the nanoparticles as illustrated with the SEM images in **Figure 6-10**.[233] Concerning the absence of a quadratic regime, the behaviour of the PETS-treated device curves seems to tend toward a SCLC, and a higher electric field might be necessary to finally reach it. Tests have been done by increasing the voltage but the signal-to-noise ratio became lower leading to unreliable results. For the FDTS treated devices, the poor filling is probably causing the absence of quadratic effect.

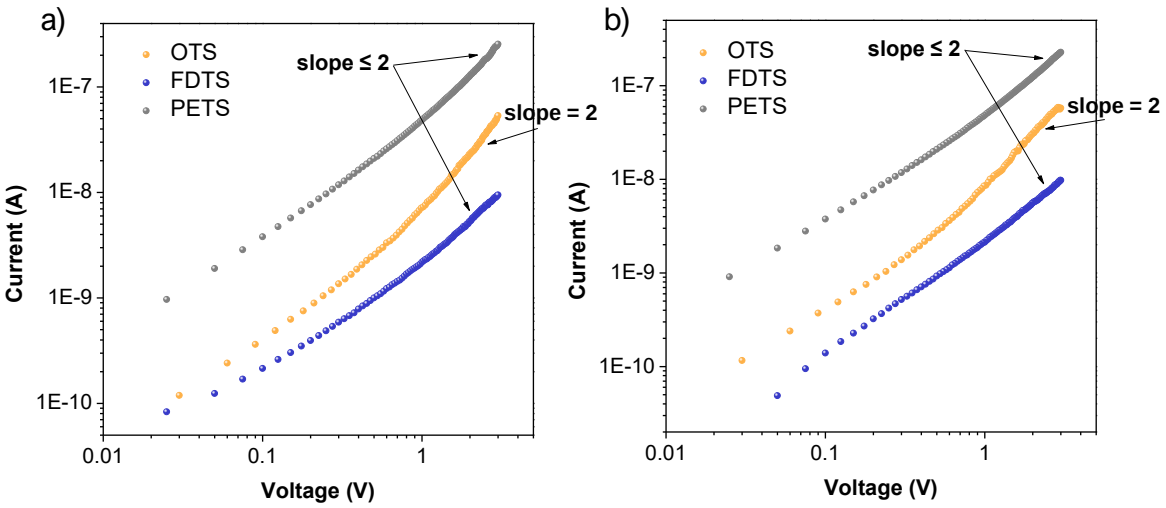

Figure 6-9: (**a**) Forward and (**b**) reverse I-V characterisation plotted in logarithmic scale of the organic nano-junctions for different SAM treatments applied (thermal annealing, OTS treatment).

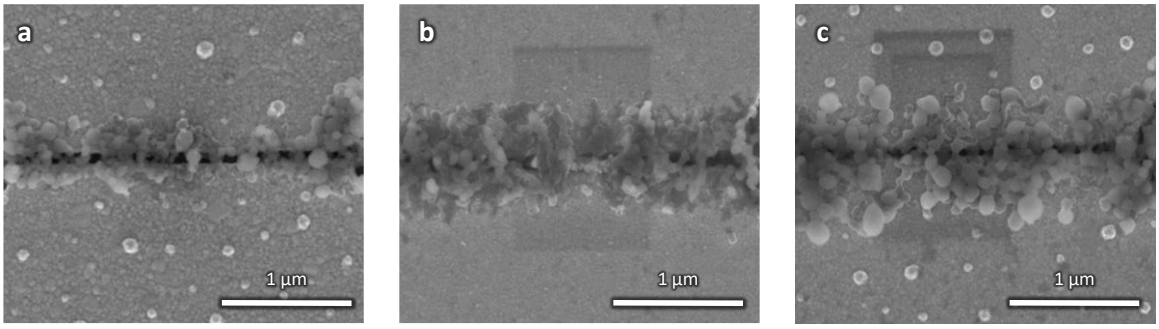

Figure 6-10: SEM images of the rectangular electrodes having different SAM treatment after dielectrophoresis step: (**a**) FDTS, (**b**) OTS, (**c**) PETS.

Concerning the OTS treatment, the SCLC regime was easily reached and the nano-gap devices present an optimal hole mobility of 2.4 10^{-3} cm^2 V^{-1} s^{-1}. Interestingly, this mobility is similar to that obtained when the devices were only submitted to a thermal annealing (2.3 10^{-3} cm^2 V^{-1} s^{-1}). These results suggest that both treatment (OTS treatment and thermal treatment) have a similar effect. One can suggest that both treatments lead to the improvement of charge transport between particles and/or between the particle and the electrode by improving the contact between nanoparticles and/or the electrodes. This effect can be explained since OTS treatment can get rid of morphological trap,[234] herein represented by interparticle spacing, grain boundaries or poor contact with the electrode, as the treatment can lead to a better uniformity in the channel. On the other hand, thermal annealing of P3HT nanoparticles on OTS treated substrates does not improve the mobility further, reaching also 2.4 10^{-3} cm^2 V^{-1} s^{-1}. This result is surprising as thermal annealing can improve the hole mobilities in P3HT thin films deposited from organic solvent due to enhanced crystallinity.[235] This difference between P3HT thin films deposited from organic solvents and P3HT nanoparticles can be explained by the fabrication method of the nanoparticles (mini-emulsion) which involves a thermal treatment for several hours and can enhance the crystallinity of P3HT already in the nanoparticle. UV-visible spectra of P3HT thin films fabricated from nanoparticles before and after thermal treatment have been recorded (**Figure 6-11**). One can clearly see the two vibronic peaks of P3HT at 554 nm and 604 nm, an indication of the crystallinity of P3HT, already at room temperature (without thermal treatment). The thermal annealing at 130°C did not lead to significant change in the position or intensity of these peaks, indicating that the crystallinity has not been improved. This result is in accordance with the absence of improvement of hole mobility upon thermal annealing at 100°C.

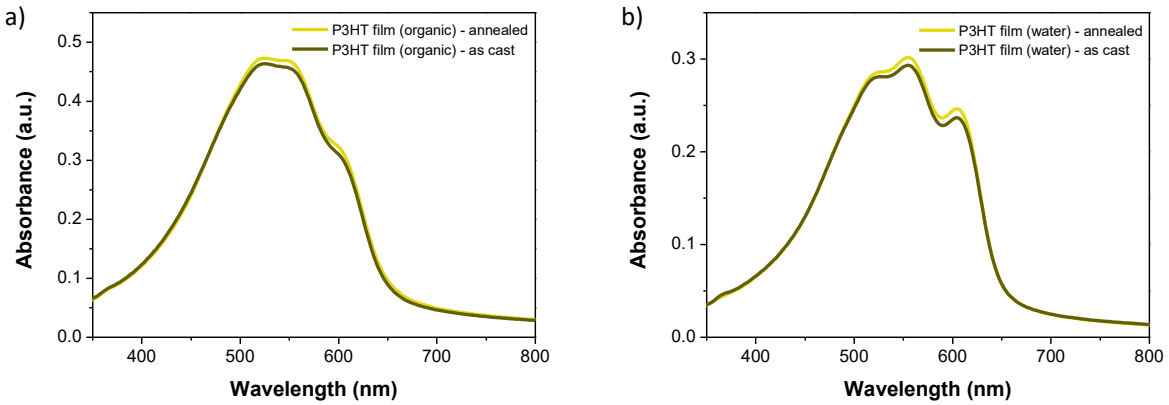

Figure 6-11: UV-vis absorbance of P3HT films deposited from (**a**) chlorobenzene solution and (**b**) aqueous dispersion as cast and after thermal annealing.

These first experiments on pure P3HT allowed to identify the conditions for fabrication of the nano-junctions (geometry, OTS treatment, 100°C thermal annealing) which will be used in the following part of the study.

6.6. P3HT:o-/eh-IDTBR nanoparticles: A case study

The primary objective with this nano-gap architecture is study the electronic transport in different kind of composite nanoparticles having various morphology type. From the literature survey in **Chapter 1** and the results obtained so far during this work, the core-shell is a morphology that is often observed when using the mini-emulsion. Such a morphology can have diverse aspects, either with a donor-rich shell and an acceptor-rich core, or the complete opposite with an acceptor-rich shell and a donor-rich core. These different spatial distributions of materials inside a nanoparticle have rarely been discussed from the standpoint of charge carrier mobility. In order to dive into this, the work of Barr *et al.* have been chosen as the bedrock to select the core-shell-like nanoparticles to study.[122] As a reminder, they have shown that the higher surface energy material of the blend is preferentially migrating in the nanoparticle core, while the one with the lower surface energy is forming the shell. This result was particularly clear with two similar systems, P3HT:eh-IDTBR and P3HT:o-IDTBR, where the donor material P3HT is respectively predominantly located in the core or in the shell. In order to investigate the impact of the morphology and the change in spatial distribution of the donor material

(P3HT) in the particle on the hole mobility of composites donor/acceptor particles, the nanogap structures previously developed have been used.

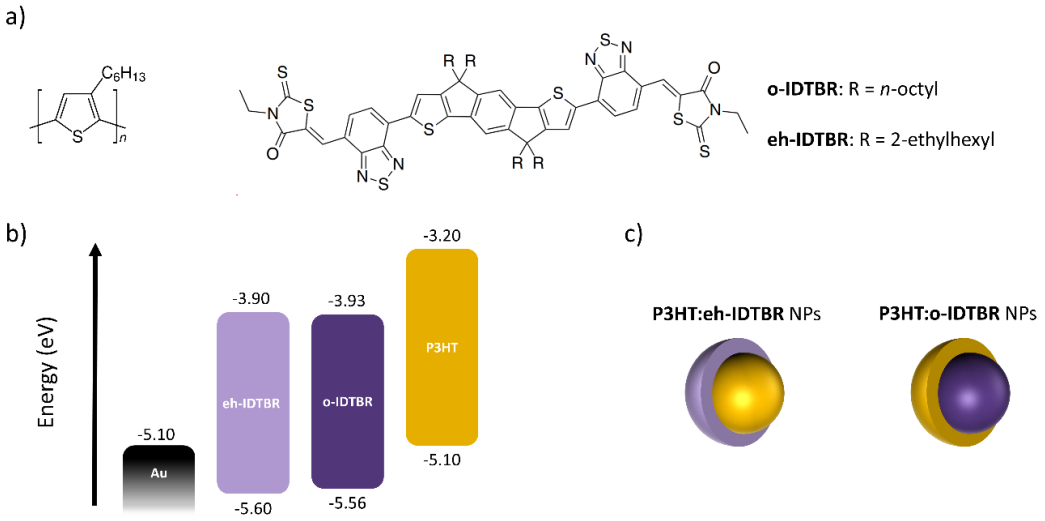

Figure 6-12: (**a**) Chemical structure of donor material P3HT and acceptor materials o-IDTBR and eh-IDTBR, (**b**) Energy level diagram of eh-IDTBR, P3HT and o-IDTBR and gold electrode, (**c**) Schematic representation of P3HT:eh-IDTBR NPs and P3HT:o-IDTBR NPs internal morphology.

6.6.1 Nanoparticles synthesis

P3HT:eh-IDBTR and P3HT:o-IDBTR nanoparticles have been synthesised with the procedure detailed in **Methods**. For the organic phase, 25 mg ml^{-1} of P3HT:eh-/o-IDBTR [1:1] mixture was first dissolved in chloroform stirred for 2 h at 65 °C in a nitrogen-filled glovebox. Final aqueous dispersions were obtained with a concentration adjusted at 0.05 mg ml^{-1} of active materials. Such low concentrations were used for optimal trapping of the nanoparticles using the dielectrophoresis method (Paragraph **6.3**).

6.6.2 Morphology investigation

Prior to investigation of the charge transport, the internal morphology for each system has been revealed using STXM. The resulting images of the measurements and the extracted radial profiles (**Figure 6-13** and **Figure 6-14**) show the distribution of each material inside the nanoparticle. A core-shell model is applied to extract the true core

composition based on the measured nanoparticle center composition and the core-shell dimensions, as reported by Holmes *et al*.[121] For P3HT:o-IDTBR nanoparticles, the donor material is driven to the shell as it has a slightly lower surface energy than the o-IDTBR (26.9 mN m^{-1} and 28.1 mN m^{-1} respectively). In the case of the P3HT:eh-IDTBR, because of the higher surface energy of P3HT as compare to eh-IDTBR (26.9 mN m^{-1} and 18.3 mN m^{-1} respectively), the P3HT is mainly driven to the core of the nanoparticles. However, since the two NFA materials do not have high surface energy as compared to fullerene acceptors (*i.e.* PCBM = 38.2 mN m^{-1} ; $PC_{71}BM$ = 39 mN m^{-1}), the compositions of shell and the core of the nanoparticles are more balanced than generally observed for fullerene based particles: the proportions of P3HT in the shell are 40% and 60% for P3HT:eh-IDTBR and P3HT:o-IDTBR respectively. Therefore, it is possible to conclude that P3HT:eh-IDTBR NP has an acceptor-rich shell while P3HT:o-IDTBR has a donor-rich shell. Such a difference in the composition of the NP may have an impact on the charge mobility and more specifically on the hole transport through the P3HT. One can argue that a better pathway for holes is obtained with the P3HT:o-IDTBR nanoparticle as the P3HT is mainly in the shell, whereas poor pathways might confine charges inside the core of the P3HT:eh-IDTBR nanoparticle.

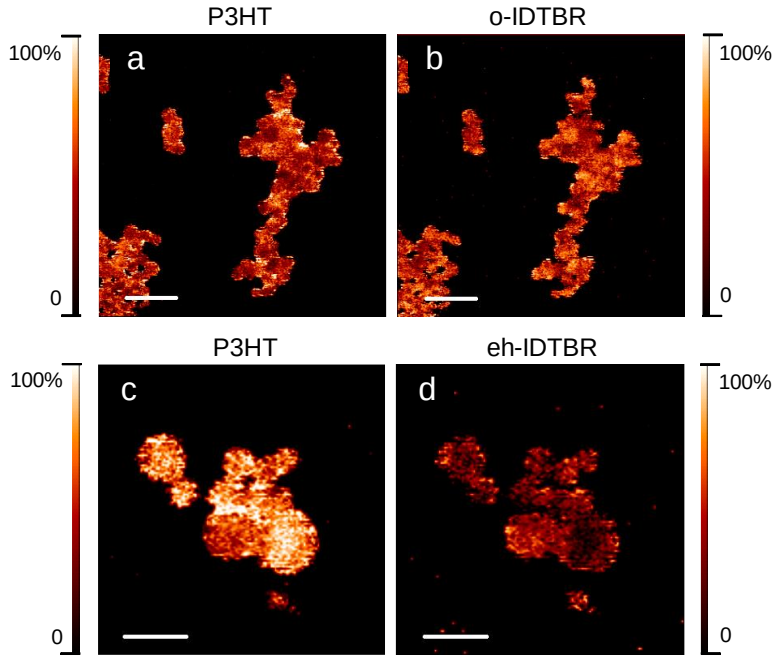

Figure 6-13: STXM fractional composition maps showing the concentration of (**a**) P3HT and (**b**) o-IDTBR for 1:1 P3HT:o-IDTBR nanoparticles and STXM fractional composition maps showing the concentration of (**e**) P3HT and (**f**) eh-IDTBR for 1:1 P3HT:eh-IDTBR nanoparticles. The scale bars in **a** and **b** are 1 µm, the scale bars in **e** and **b** are 500 nm. The colour contrast is scaled such that light colours correspond to higher component concentrations.

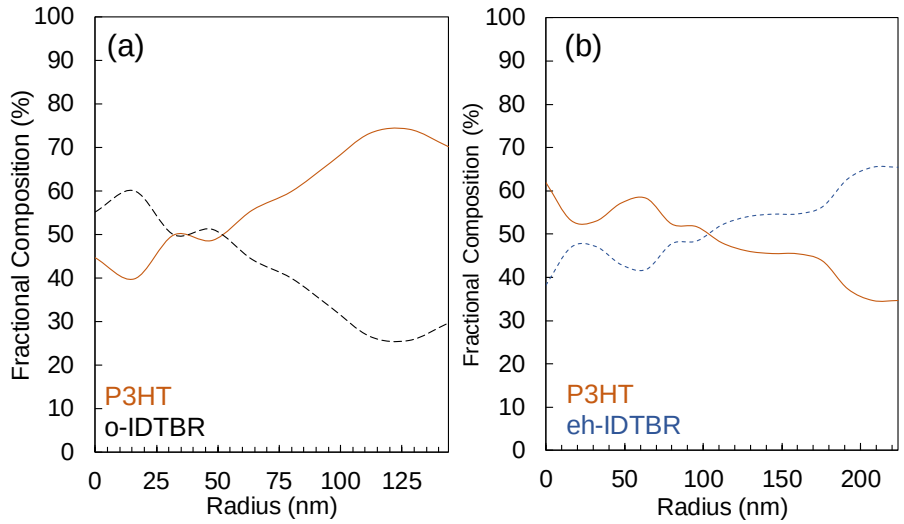

Figure 6-14: Radial composition profiles extracted from STXM maps of representative nanoparticles for (**a**) P3HT:o-IDTBR and (b) P3HT:eh-IDTBR.

6.6.3 Mobility studied through nanogap devices

To probe a possible impact of the P3HT spatial distribution in the nanoparticle on the hole mobility, the nano-gap device described earlier is used. The architecture was slightly improved in order to enhance the signal to noise ratio while keeping a geometrical ratio between channel length and width of at least 20 (W/L = 25 in our case). This factor is necessary to be able to probe the material in the channel and avoid artefacts coming from the edges that might induce overestimation of the mobility.[236] The architecture used had a L= 100 nm and W = 2.5 µm. The three different type of nanoparticles were successfully inserted in the nanogap channels: P3HT, P3HT:o-IDTBR and P3HT:eh-IDTBR using optimised DEP conditions (V_{pp} = 5 V, f = 60 kHz, t_{DEP} = 5 sec) as seen in **Figure 6-15**. As shown in the energy level diagram (**Figure 6-12b**), hole injection occurs from the Fermi level (E_F) of the gold electrode to the highest occupied molecular orbital (HOMO) of P3HT. The energy barrier between the E_F of the gold electrode and the HOMO of the two NFAs should be large enough to not be overcome even if they might present ambipolar transport.[237] To confirm these assumptions, and verify if the injection and the extraction of the holes is only happening through the P3HT, eh-IDTBR and o-IDTBR pure nanoparticles were inserted in the nano-gap devices as a control test and I-V characterisation was performed. As a result, no current above the noise level was extracted (**Figure 6-16**),

confirming either the lack of hole injection through the two NFAs or their poor ability to transport holes.

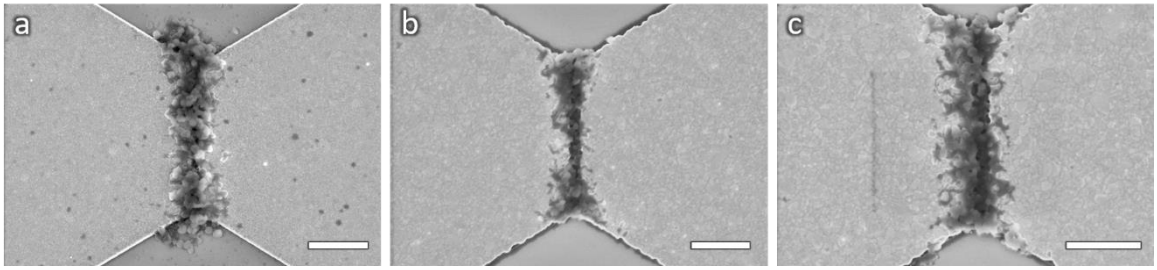

Figure 6-15: SEM images of the nanogap device with L = 100 nm and W = 2.5 µm after the dielectrophoresis step and filled with (a) P3HT NPs, (b) P3HT:eh-IDTBR NPs and (c) P3HT:o-IDTBR NPs (scale bars: 1 µm).

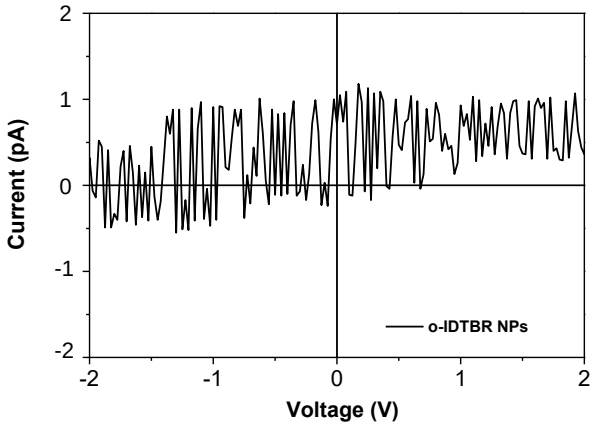

Figure 6-16: I-V characteristic of o-IDTBR pure nanoparticles in nanogap structure.

In **Figure 6-17a** the I-V characteristics in logarithmic scales of nanogap devices with either pure P3HT nanoparticles and the two blend nanoparticles (P3HT:o-IDTBR and P3HT:eh-IDTBR) are presented. One can observe from the log(I)-log(V) plots two distinct regimes. Similarly to what was previously observed for trapezoid and rectangular electrodes with P3HT nanoparticles, at low electric field (V ≤ 0.2 V) the first regime corresponds to the ohmic regime (slope of 1), thus confirming an ohmic injection and extraction for the holes, and ticking an important assumption for the use of the SCLC theory.[238] The second regime is seen at higher electric field (V ≥ 1 V) for each nanoparticle

system and is associated to the SCLC regime where the current depends quadratically on the applied voltage.

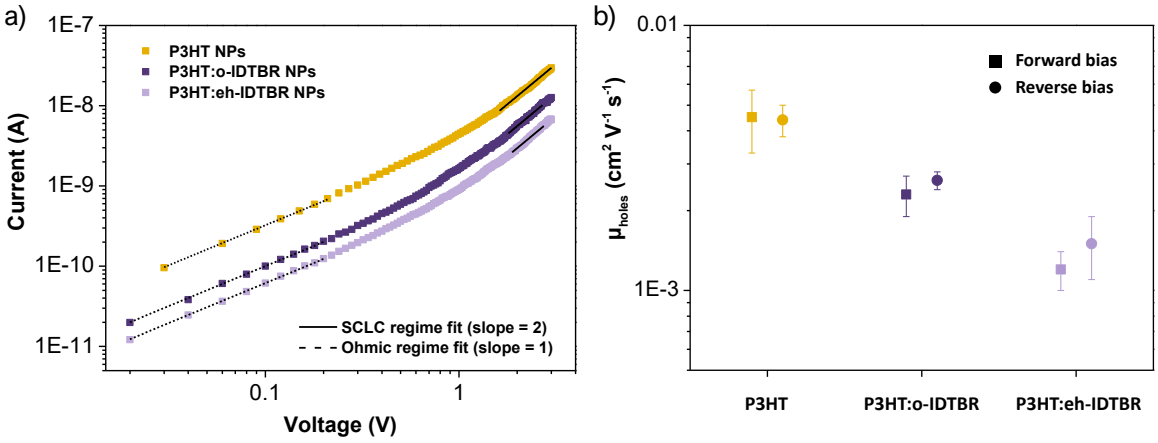

Figure 6-17: I-V characteristics plotted in logarithmic scales of P3HT, P3HT:o-IDTBR and P3HT:eh-IDTBR nanoparticles with their ohmic region fit (black dashed line) and SCLC region fit (black solid line). Figure (**b**) is showing the resulting hole mobility extracted at the forward and reverse bias.

Table 6-2: Summary of the μ_{h+} for P3HT, P3HT:o-IDTBR and P3HT:eh-IDTBR nanoparticles

Nanoparticle system	μ_{h+} ($cm^2\ V^{-1}\ s^{-1}$)		error ($cm^2\ V^{-1}\ s^{-1}$)	
	forward	reverse	forward	reverse
P3HT	4.5×10^{-3}	4.4×10^{-3}	$\pm 1.2 \times 10^{-3}$	$\pm 0.6 \times 10^{-3}$
P3HT:o-IDTBR	2.3×10^{-3}	2.6×10^{-3}	$\pm 0.4 \times 10^{-3}$	$\pm 0.2 \times 10^{-3}$
P3HT:eh-IDTBR	1.2×10^{-3}	1.5×10^{-3}	$\pm 0.2 \times 10^{-3}$	$\pm 0.4 \times 10^{-3}$

For P3HT:eh-IDTBR and P3HT:o-IDTBR, a hole mobility (forward bias) of 1.2 ± 0.4 10^{-3} $cm^2\ V^{-1}\ s^{-1}$ and 2.3 ± 0.2 10^{-3} $cm^2\ V^{-1}\ s^{-1}$ respectively was calculated, whereas a hole mobility of 4.5 ± 1.2 10^{-3} $cm^2\ V^{-1}\ s^{-1}$ is obtained for pure P3HT NPs. These results first confirm that the addition of the acceptor slightly disturbs the hole transport in the composite nanoparticles, the mobility decreasing by half compared to pure P3HT NP. In addition, this analysis can help understanding the possible impact on the hole mobility induced by a change of polymer content in the shell of the composite nanoparticles. However, only a very slight increase in the hole mobility in forward bias is observed for P3HT:o-IDTBR nanoparticles compared to P3HT:eh-IDTBR nanoparticles. Considering also the error calculated on the mobilities, these result suggest that the NP morphology and the P3HT

content in the shell (60% in P3HT:o-IDTBR NPs / 40% in P3HT:eh-IDTBR NPs) have no significant impact on the hole mobilities in P3HT:IDTBR composite nanoparticles. Even a limited amount of P3HT in the shell (here 40% for P3HT:eh-IDTBR NPs) is enough to transport holes efficiently through the nanoparticle.

6.6.4 P3HT:o-/eh-IDTBR nanoparticles solar cells

OPV devices prepared from P3HT:eh-IDTBR and P3HT:o-IDTBR nanoparticles dispersion concentrated at 60 mg ml^{-1} have been prepared as well as their control devices made with a solution of CB concentrated at 24 mg ml^{-1}. For the *np-BHJ* solar cells, the dispersion has been spin-coated onto ZnO at a speed of 3000 rpm for 60 sec. The resulting nanoparticulate layers were then annealed at an optimal temperature of 130 °C for 5 min. The reference *BHJ* devices were formed by spin-coating at a rotation speed of 800 rpm for 60 sec and subsequently annealed at 100°C for 10 min. More details about the solar cell fabrication protocol can be found in **Methods**.

Modest performances were obtained with power conversion efficiencies (PCE) of 1.86% and 1.62% for devices with P3HT:o-IDTBR and P3HT:eh-IDTBR respectively obtained for 130°C thermal annealing temperature. Increasing it up to 150°C led to a decrease of the performances of the devices down to 1.05% for P3HT:o-IDTBR. It has been shown that when nanoparticles are synthesised by mini-emulsion technique, the thermal annealing temperature necessary to achieve the nanoparticles sintering and reach optimal performances can be quite high, up to 200°C. However, concomitantly, phase segregation between the donor and the acceptor phase can also occur at such high temperature. One can suggest that for P3HT:IDTBR nanoparticles based active layer, a thermal annealing temperature of 130°C is not enough to efficiently sinter the nanoparticle but temperature above 130°C promotes large phase segregation leading to a drop of efficiency. In addition, two different nanoparticle diameters have been synthesised to assess its impact on the water-based OPV devices. Small nanoparticles diameter of around 53 nm and larger ones of 74 nm have been made for the two composite nanoparticles. For both donor:acceptor systems, having smaller nanoparticles enhanced the performances with a significant increase of V_{OC} and FF (**Table 6-3** & **Figure 6-18**). Interestingly, this is even more evident for P3HT:o-IDTBR nanoparticles. The NFA in this system shows high crystallinity upon

thermal annealing. Decreasing the nanoparticle size of P3HT:o-IDTBR is suspected to weakened the high crystallinity of o-IDTBR,[239] which can positively impact the V_{OC} and FF.[240] With such kind of NP size optimisation, optimal performances up to 1.86% PCE was achieved for P3HT:o-IDTBR OPV devices fabricated from water-based colloidal inks. Control devices fabricated from organic solvent have also been prepared as a comparison (**Figure 6-18c**).

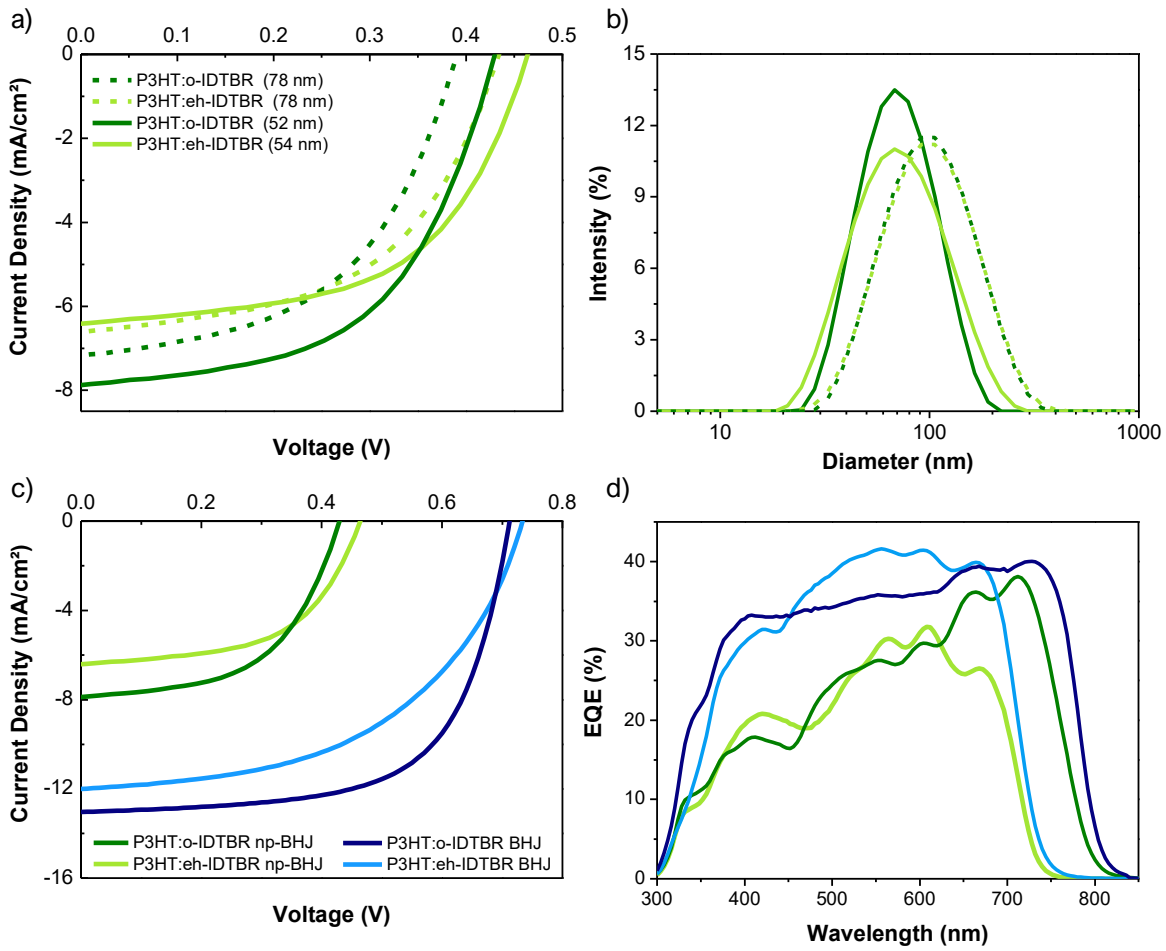

Figure 6-18: (**a**) J-V characteristics of OPV devices with active layers fabricated P3HT:o-IDTBR and eh-IDTBR from water-based nanoparticles inks with varying the nanoparticles diameter and (**b**) the DLS measurements of the nanoparticles (**c**) J-V and (**d**) EQE characteristics of OPV devices with active layers fabricated from P3HT:o-IDTBR and eh-IDTBR water-based nanoparticles inks (*np-BHJ*) and from organic solvents inks (*BHJ*).

Table 6-3: Average OPV performances of P3HT:o-IDTBR and P3HT:eh-IDTBR *np-BHJ* (thickness = 230 nm) extracted from a minimum of 8 devices with different nanoparticles diameter. Performances of control devices P3HT:o-IDTBR and P3HT:eh-IDTBR *BHJ* (thickness = 130 nm) are also shown.

	NPs size (nm)	J_{SC} (mA cm^{-2})	V_{OC} (V)	FF	PCE (%)
P3HT:o-IDTBR *np-BHJ*	78	7.36 ± 0.21	0.38 ± 0.02	0.51 ± 0.02	1.43 ± 0.14
	52	7.90 ± 0.17	0.43 ± 0.01	0.55 ± 0.01	1.86 ± 0.10
P3HT:o-IDTBR *BHJ*	/	13.19 ± 0.15	0.71 ± 0.01	0.62 ± 0.05	5.8 ± 0.40
P3HT:eh-IDTBR *np-BHJ*	78	6.64 ± 0.20	0.43 ± 0.01	0.53 ± 0.00	1.52 ± 0.04
	54	6.43 ± 0.17	0.46 ± 0.01	0.55 ± 0.01	1.62 ± 0.27
P3HT:eh-IDTBR *BHJ*	/	11.17 ± 0.76	0.72 ± 0.02	0.53 ± 0.03	4.21 ± 0.19

The devices fabricated from water suffer from very low V_{oc} compared to the reference fabricated from organic solvent, with a loss of 260 to 280 mV. A possible explanation for the large difference in V_{OC} could be the higher crystallinity of the acceptor and/or the donor in the case of nanoparticle-based thin films. UV-visible absorbance spectra of P3HT:eh-IDTBR and P3HT:o-IDTBR films deposited with chloroform and water are shown in **Figure 6-19**. The thin film made of nanoparticles present sharper and more intense red-shifted vibronic peaks which could indicate higher crystallinity of both the donor and the acceptor, compared to that of thin film processed from organic solvent. The formation of large crystalline domains of either donor and acceptor has already been shown to decrease the energy of the charge transfer state (E_{CT}) and, as a consequence, the V_{OC}. Decrease of 100 to 150 mV of the V_{OC} have been reported upon crystallisation of PCBM and P3HT respectively.[173,241] Another explanation might come from the difference of crystallisation between the donor and the acceptor which was found to increase the non-radiative energy loss ($\Delta V_{OC\ non\text{-}rad}$) and thus reduce the V_{OC}.[242,243] In particular, such mechanism has been observed when increasing the crystallinity of o-IDTBR with respect to the donor material, thus reducing the V_{OC} of 100 mV due to non-radiative recombination. The strong aggregation of the donor and/or the acceptor could result in a strong decrease of the E_{CT} or an increase of $\Delta V_{OC\ non\text{-}rad}$, and as a consequence, explain the drop of 260-280 mV in V_{OC}. More investigations are necessary to confirm (or infirm) this hypothesis and gain understandings on the V_{OC} loss in water-processed OPV devices. In addition, we

compared our results with the literature, Xie *et al.* fabricated OPV devices based on P3HT:o-IDTBR nanoparticles prepared by mini-emulsion. These researchers reported higher performances, with 2.53% PCE.[74] The lower PCE obtained in our study is mainly due to a significant decrease of the V_{OC}, 430 mV for this study compared to 750 mV reported by Xie *et al.* Several hypotheses could explain such discrepancy. First, it has been shown that the P3HT molar mass can impact the V_{OC} of P3HT-based nanoparticles OPV devices.[160] Moreover, as mentioned before, higher crystallinity of either P3HT or IDTBR molecules could also be the reason of such decrease, as aggregation of donor and/or acceptor has been shown to lead to V_{OC} losses. Nevertheless, when comparing P3HT:eh-IDTBR and P3HT:o-IDTBR devices prepared for water-based nanoparticles dispersions annealed at 130°C, no significant difference is observed in the performances of the devices, with 1.62% and 1.86% PCE respectively. In particular, the fill factor, particularly sensitive to charge transport, is identical for both kind of active layer: 0.55 for P3HT:eh-IDTBR and P3HT:o-IDTBR. Such result can be related to the hole mobilities obtained using nanogap devices in which no significant difference in hole transport has been observed between the two kind of particles, 1.2 10^{-3} cm^2 V^{-1} s^{-1} and 2.3 10^{-3} cm^2 V^{-1} s^{-1} for P3HT:eh-IDTBR and P3HT:o-IDTBR nanoparticles respectively.

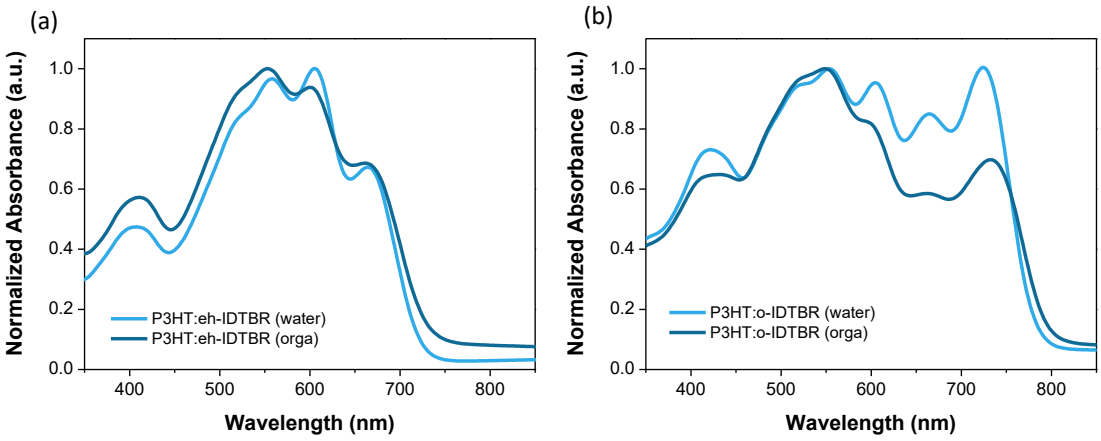

Figure 6-19: UV-vis absorbance spectra of (**a**) P3HT:eh-IDTBR and (**b**) P3HT:o-IDTBR films deposited from chloroform (dark blue) and water (light blue).

6.7. Conclusion of chapter 6

Devices with nanogap electrodes have been developed in which either pure donor NP (P3HT) or composite NP (P3HT:eh-IDTBR and P3HT:o-IDTBR) have been inserted using dielectrophoresis technique. It resulted in planar organic nanojunctions, from which we managed to extract hole mobilities. The analysis showed that the hole mobility in composite P3HT:IDTBR nanoparticles decreases by a factor two compared to pure P3HT NP. However, no significant difference was observed between the two kind of composite nanoparticles (P3HT:eh-IDTBR and P3HT:o-IDTBR) although the proportion of P3HT in their shell was different. It suggests that conduction pathways for the positive charges could be efficiently found even for proportion as low as 40%. Such similarity in the charge transport at the nanoscale could also be observed on OPV devices with active layers made of either P3HT:eh-IDTBR and P3HT:o-IDTBR NP (from water-based inks). Indeed, similar photovoltaic performances was measured in both cases with 1.62% and 1.86% PCE respectively. To conclude, this study helped to create a link between the performances of macro-scale OPV devices and the properties at the nanoscale of organic semiconductor nanoparticles. This development also opens the route to widen the understandings of the nanoscale properties of organic semiconductor nanoparticles using nanoscale devices such as organic nano-junctions.

Chapter 7

Conclusion and outlook

7.1. Conclusion

The successful development of water-processed organic solar cells in this work was made possible through a meticulous optimisation of the nanoparticulate layer formation. Forming homogenous and pin-hole free layers with an aqueous dispersion is challenging, and this work has laid the foundations to control this coating process via spin-coating. Such an outcome allowed us to progress in our understanding of the OPV performances achieved with different kind of organic semiconductor nanoparticles.

This work has demonstrated how the surface energies of the donor and acceptor material play a major role in the formation of a composite nanoparticle synthesised with the mini-emulsion method. In particular, the interfacial energy between the donor and acceptor influences the internal morphology of nanoparticles, as well as the conditions to process a nanoparticulate film. Achieving intricately mixed nano-domains was made possible through the surface energy matching of PTQ10 and Y6, resulting in a low interfacial energy system. Upon an optimised thermal treatment, this closely mixed morphology was found to be maintained while merging the nanoparticles to form a layer with transport pathways. When Y6 was replaced with other acceptors, $PC_{61}BM$ or IDIC, having a higher interfacial energy with PTQ10, the phase separation inside the nanoparticle increased, giving rise to a core-shell-like morphology. However, the impact of the lower interfacial energy of PTQ10:IDIC as compared to PTQ10:$PC_{61}BM$ could be observed via a much better photo-conversion achieved by the IDIC-based nanoparticle devices. Yet core-shell, PTQ10:IDIC nanoparticles showed a more intermixed shell and core than PTQ10:$PC_{61}BM$ nanoparticles due to a lower donor/acceptor interfacial energy.

Nonetheless, this interfacial energy concept has shown its limits when the alkyl side chain of Y6 were elongated to Y12. When the latter was associated with PTQ10, the resulting composite nanoparticles formed a core-shell-like morphology with highly crystalline Y12 rich-core. Although the reason for the morphological contrast between a Y6 and Y12-based nanoparticle is yet not totally clear, this contrast is surely the cause of the different behaviours upon thermal annealing. The optimal temperature for PTQ10:Y12 *np-BHJ* (150 °C) was much lower than the one for PTQ10:Y6 *np-BHJ* (200 °C) approaching acceptable temperature ranges for industrialisation. Based on these results, the study has been extended to the donor polymer material, where the alkyl side chain length has shown

a similar influence on the processing of the nanoparticulate film. By switching from a polymer with short side chains (FO4-T) to a polymer with longer side chains (FO8-T), it was possible to consider lower temperatures to achieve similar and even higher efficiencies that those obtained with the FO4-T. Doing so, water-processed organic solar cells based on nanoparticles prepared with the mini-emulsion have for the first time shown an efficiency surpassing the 10 % power conversion efficiency milestone.

With the aim of establishing a direct link between the nanomorphology and the charge transport inside a nanoparticle, the development of nano-gap devices has been carried out. The dielectrophoresis force has been showed to be a great tool for the precise trapping of nanoparticle inside a sub-micrometre gap. The study of IDTBR-based core-shell nanoparticles having different spatial distribution has shown that the shell composition does not have an important influence neither on the mobility of the charge carriers in the nanoparticle nor on the final OPV performances of the water-processed devices.

7.2. Outlook

Although much efforts have been made to form thin films with nanoparticle dispersions with a good coating, this process induces a lot of variability, which has led to time and materials consumption. The spin coating is a technique that has some parameters set by the operator's motions (speed of the dispense, height from the substrate, angle of the micro-pipette) which are relatively hard to control precisely. These parameters are impacting greatly the quality of the coating, especially in the case of water-based inks, and small variations could lead to a non-working device due to dewetting and aggregates formation. Therefore, moving on to techniques such as blade coating and slot-die coating could allow the precise optimisation and setting of each deposition parameters, and lead to a better reproducibility. Indeed, it is important to continue advancing toward a better control of this nanoparticulate layer formation, in order to render this process more compatible with this upscaling. To continue towards the improvement of the nanoparticulate thin film formation, different treatments other than UV-O_3 should be investigated on the ZnO surface in order to favour the coating of the aqueous ink. In particular, the use of a self-assembled monolayer (SAM) could be a good way to tune the surface properties of a surface. Although

SAMs often present a hydrophobicity propriety, some molecules can have a hydrophilic head group such as 3-aminopropanoic acid (C3-SAM) with its $-NH_2$ hydrophilic head group or [3-(N,N-dimethylamino)propyl]trimethoxysilane (NTMS-SAM) with its amine group. The former has been shown to be a good ETL modifier, and the latter to favour the unipolar behaviour of a n-type OFET.[244,245] The option of changing the ZnO layer with another electron transport layer is also to be considered, as the former is showing a hydrophobic surface.

Along this PhD work, an interesting observation was made on devices prepared with Y6-based nanoparticles. As shown in **Figure 7-1**, every water-processed organic solar cell prepared with Y6-base system experienced a notable Voc loss (80 – 140 mV) as compared to the same system but prepared with organic solvents. When using other acceptors, no Voc loss was noted between the two process. Therefore, it seems that forming nanoparticles from Y6 induces a change in some energetic levels which is directly seen on the measured Voc. Some preliminary investigations have been performed to probe the origin of such a loss. In particular, the presence of lower CT states could explain this loss as well as a broadening of the Y6 LUMO density of state. Future works would be helpful to properly understand the origin of this loss in order to find strategies to reduce it.

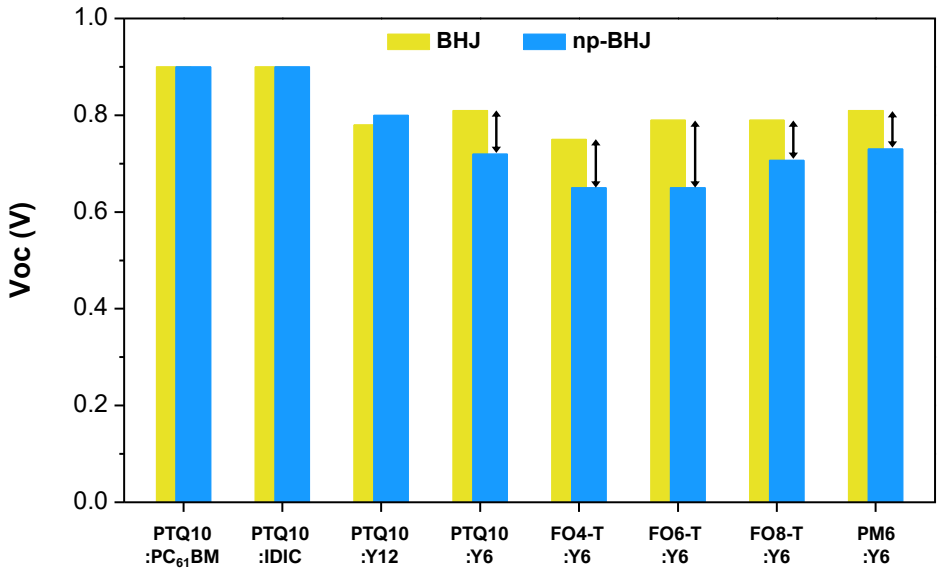

Figure 7-1: Open-circuit voltage of different water-processed devices (*np-BHJ*) and their organic solvent-processed counterparts (*BHJ*).

Thanks to this work, we have opened the door to the role and impact of the chemical structure on the formation and processing of composite nanoparticles. In particular, the **Chapter 5** and its promising results coming from the elongation of the side chains length of both donor (FO8-T) and acceptor (Y12) is expecting to be continued to acquire deeper understandings. Morphological analysis such as GIWAXS combined with DSC measurements could further throw some light on the impact of the side chain length on the molecular arrangement of the blend upon different annealing temperature. The use of such data could guide the community in the optimisation of these nanoparticle system, as well as in the choice of new materials to simultaneously decrease the annealing temperature while achieving high efficiencies. In addition to side chains, the impact of other chemical groups should be investigated such as end-groups of both donor and acceptor materials, as well the acceptor fused-ring skeleton.

It is worth noting that the use of additives during the nanoparticle formation has rarely been explored in the community. When looking at the highest PCE (11 %) reported in the literature achieved by Xie *et al.,* such results has been obtained thanks to DIO as an additive in the organic phase.[73] Even though this solvent it not the best example in term of sustainability (high toxicity) and is known to impact long-term ageing of solar cells[246], its impact on the morphology demonstrates the advantage of additives for nanoparticles formation. In the case of the mini-emulsion, additives could be beneficial to facilitate the processing of the highly crystalline nanoparticles. This strategy has been explored for organic solvent-processed OPV to regulate the crystal nucleation and crystal growth of Y6.[247,248] While additives could help softening nanoparticles for better processability, their role in the phase separation during the nanoparticle formation should be investigated. Indeed, additives might be a good way to tune the different surface energy involved in the arrangement of the materials within the nanoparticles. Further pushing the concept of solid additive, ternary blended nanoparticles can be seen as the next big investigation. For solvent-processed OPV, this ternary strategy is currently giving the best efficiencies reported in the literature as it allows a broader spectral coverage as well as an energy cascade alignment that improves the charge separation and transport.[249] The interest for ternary organic solar cells also comes from the possibility of regulating the morphology (crystallinity, phase separation, molecular orientation…).[250] Therefore, the internal morphology of a binary blended nanoparticle could be greatly influenced upon the addition

of a third component, with the aim of cancelling the large phase separation inside the nanoparticle and during the annealing of the film while sintering the nanoparticles.

The following **Figure 7-2** aimed to place this work within the stat-of-the-art of the water-processed OPV. Undeniably, our results demonstrate the capacity of the mini-emulsion method to produce nanoparticles that can compete with the ones produced with the nanoprecipitation despite the use of an anionic surfactant. With our contribution to the encouraging trend showing the increasing of the efficiency over the years, we hope to see again a fresh momentum in the community.

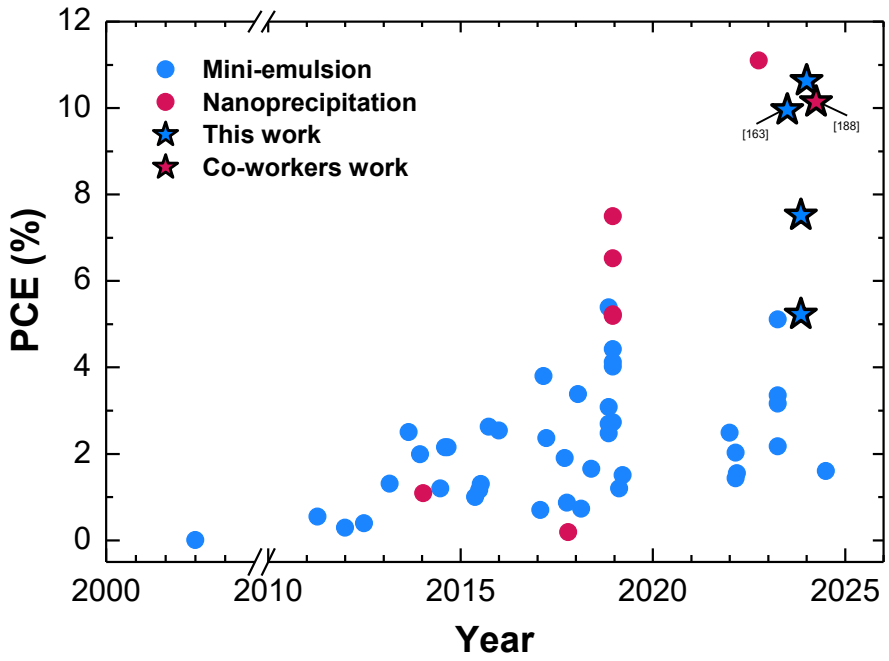

Figure 7-2: Evolution of the PCE obtained from water-based organic solar cells (this work included) prepared via different method over the years.

Methods

1. Materials

The following section is listed the materials used during my PhD thesis:

Chloroform (≥99%),1,2,4-trimethylbenzene TMB (≥98%), ethanolamine (≥99.5%), ethanol (≥99.8%), zinc acetate dihydrate, sodium dodecyl sulfate (SDS), sodium dodecyl benzene sulfonate (SDBS), trichloro(octadecyl)silane (OTS) and Pluronic F127 were purchased from *Sigma Aldrich*. 1H,1H,2H,2H-perfluorodecyltrichlorosilane (FDTS) and phenethyltrichlorosilane (PETS) were purchased from *Tokyo Chemical Industry*. MoO_3 powder was purchased from *NEYCO*. Deionised water was obtained from a *PURELAB* Flex system (≈15 MΩ). PTQ10 (M_w = 60 kDa), Y6 and Y12 were purchased from *Brillant Matters*. P3HT (M_W = 53 kDa) and $PC_{61}BM$ were purchased from *Solaris Chem Inc*. o-IDTBR and eh-IDTBR were purchased from *1-Material*. IDIC was purchased from *Ossila*. The donor polymers FO4-T, FO6-T and FO8-T were prepared by Dr. Martina Rimmele following the procedure reported in the article from Rimmele *et al.*[251] All the materials were used as received without further purification

2. Nanoparticles fabrication

Unless otherwise specified, here is described the synthesis of nanoparticles via the mini-emulsion method reported by Landfester *et al.*[91,140]: For the preparation of the organic and aqueous phase, the reader is referred to the section of interest. A macro-emulsion is then obtained by adding the organic phase into the aqueous phase (1:5 volume ratio) and stirred for 1 h at 40 °C (1000 rpm). The mini-emulsion dispersion was formed by sonicating the macro-emulsion using a *BRANSON* Digital Sonifier 450 in an ice-water bath for 2 min. Once the sonification done, chloroform evaporation was done by stirring the mini-emulsion for a minimum of 3 h at 65 °C. Centrifugal dialysis was carried out by using Amicon Ultra-15 centrifuge filter (cut-off 100 kDa) and *Hettich* Universal 320 centrifugal. Four centrifugation cycles were done at 2200 rpm for 9 min. The retentate was raised to 15 ml with deionised water between each step. Final aqueous dispersions were obtained with a concentration adjusted to the desire concentration of active materials.

3. Devices fabrication

3.1. Organic solar cells

Organic solar cells were fabricated with an inverted architecture glass/ITO/ZnO/ active layer/MoO_3/Ag, where ZnO and MoO_3 were used as electron transport (ETL) and hole transport (HTL) interlayer, respectively. The ITO covered glasses (1.5 x 1.5 cm², 10 Ω sq^{-1}, *VisionTek*) were cleaned by sequential ultrasonic treatments: diluted soap *Hellmanex*™ III, deionised water and isopropanol. The ZnO precursor solution was prepared by mixing zinc acetate dihydrate (165 mg) and ethanolamine (90 µl) with ultrapure ethanol (5 ml). The solution was then stirred at 55 °C in air for 30 min and left at room temperature under continuous stirring prior to deposition. Before depositing the ETL, the substrates were dried and treated by UV-ozone for 15 min. ZnO precursor solution was then spin-coated to form 40 nm thin films. The substrates were then thermally annealed in air at 180 °C for 30 min. For *np-BHJ* active layers, substrates were treated by UV-ozone for 20 min before deposition in order to increase the hydrophilicity of the surface. The *np-BHJ* active layers were obtained by spin coating on ZnO-covered substrates the nanoparticle dispersions with variable rotation speed. For *BHJ* active layers, deposited from organic solvents, the details are shown in each chapter depending of the donor:acceptor system. Afterwards, for both type of devices (water-processed and organic solvent-processed) vacuum evaporation (P = 10^{-6} mbar) was used to deposit HTL MoO_3 (7 nm thick with a rate of 0.5 Å s^{-1}) and electrode Ag (80 nm thick with a rate of 2 Å s^{-1}). The area of OPV devices was set by the shadow mask at 10.5 mm^2 and the pattern is shown in **Figure M0-1**.

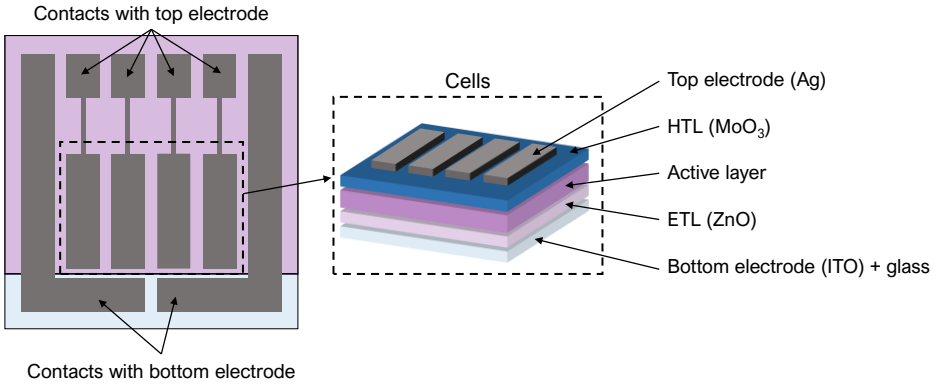

Figure M0-1: Structure of an OPV cell fabricated at the IMS laboratory during this PhD work.

3.2. Nano-gap devices

The nano-gap electrodes were fabricated on Si/SiO_2 substrates. Prior the deposition of the e-beam lithography resist polymethyl methacrylate (PMMA), the substrates were cleaned by sequential ultrasonic treatments: acetone and isopropanol. Consecutively, the substrates were dried for 10 min at 110°C in an oven containing Ar flow. A solution of PMMA in anisole (wt% 6) was spin coated onto the substrate at 4000 rpm for 50 sec resulting in a 300 nm thick PMMA layer. PMMA resist film was then dried for 5 min at 180°C in an oven containing Ar flow. Subsequently, the e-beam lithography JEOL JBX-6300SG was used to transfer the pre-defined pattern of the nano-gap electrode onto the substrate, employing the current of 300pA and accelerating voltage of 100kV. The dose value used in writing process was $1100\mu C\ cm^{-2}$. Next, the exposed pattern was developed by immersion in MIBK:IPA (1:3) solution for 45 sec, and then rinsed in IPA for 30 sec, followed by drying in a N_2 flow. Metal deposition was carried out using e-beam evaporation of Ti/Au (10/50 nm). Subsequently, the lift-off for e-beam evaporated metal electrodes was performed in hot acetone followed by IPA rinsing and N_2 drying. In order to performed electrical characterisation using a probe station, the nano-gap electrodes were extended by using photolithography with the Karl Suss MA6 Mask Aligner and thermal evaporation of Ti/Au (10/50 nm).

4. Nanoparticles and films characterisation

4.1. UV-visible absorption spectroscopy

UV–visible–NIR absorption spectra were acquired on a *Jasco* V-570 or *Shimadzu* UV-3600 Plus spectrophotometer from 300 to 1000 nm with 0.5 nm step. For the measurements of dispersions, the nanoparticle inks were diluted in D.I. water in a 4-sided quartz cuvette with 1 cm optical path. The blank was done using D.I. water in the same type of cuvette. For the absorbance of thin-films, the solution or dispersion were spin coated onto a clean glass substrate and the blank was done using the same substrate.

4.2. Photoluminescence (PL) spectroscopy

PL emission spectra were acquired on a *Jasco* FP-8700 spectrophotometer (**Chapter 4** & **5**) and on a *Photon Technology International Quantmaster* 40 setup (**Chapter 3**). Excitation wavelength was set at an energy within the absorption range of the material of interest, and the emission was recorded up to 1400 nm with a step of 1 nm and a scan speed of 100 nm min^{-1}. The nanoparticle inks were diluted in water in a 4-sided quartz cuvette with 1 cm optical path and the absorbance at the excitation wavelength was set at 0.3 a.u.

4.3. Atomic force microscopy (AFM)

During this PhD work, I used the Bruker Innova AFM to record the height and phase images in tapping mode. Oxford Instruments cantilevers with 160 microns lengths were used (AC-160-TS) were used at their resonant frequency (around 300 kHz). Scan speed was set between 0.7 and 1 Hz with a resolution of 512 or 1024 lines/image was used.

4.4. Scanning electron microscopy (SEM)

The SEM images were collected with a *Hitachi* SU8000 field emission scanning electron microscope by setting the accelerating voltage at 3 kV with an emission current of 5 µA. For the images of the nano-gap electrodes, a conductive carbon tape was placed on one side of each electrodes in order to extract the excess of electron induced by the beam.

4.5. Cryo Transmission electron microscopy (Cryo-TEM)

Prior imaging the particles, the vitrification of the samples was carried out in a homemade vitrification system. The chamber was maintained at 22 °C, and the relative humidity was 80 %. A 5 µL drop of the sample was deposited onto a lacey carbon film covered with a 300 mesh Cu grid (*Ted Pella*) rendered hydrophilic using an ELMO glow discharge unit (*Cordouan Technologies*, Pessac, France). The grid was automatically

blotted to form a thin film and plunged in liquid ethane at −190 °C, as maintained by liquid nitrogen. Thus, a vitrified film was obtained in which the native structure of the vesicles was preserved. The grid was mounted onto a cryo holder (*Gatan* 626-Pleasanton, CA, USA) and observed under low-dose conditions (10 e A^{-2}) in a Tecnai G2 microscope (*FEI*, Eindhoven, Netherlands) at 200 kV. Images were acquired using an Eagle slow scan CCD camera (FEI).

4.6. X-ray spectromicroscopy

The STXM characterisation of the internal morphology of the nanoparticles presented in this work were performed at two different synchrotron beamlines: the PolLux beam line (X07DA) at the Swiss Light Source (SLS) (Villigen, Switzerland), and the Polymer STXM 5.3.2.2 beamline of the Advanced Light Source (ALS) (Berkeley, USA).[252,253] Second- and third-order light was removed, at the SLS, by an order sorting aperture and higher order suppressor and at the ALS by an order sorting aperture and an N2 gas filter. The transmitted X-ray beam was detected by a scintillator and a photomultiplier tube. The STXM Fresnel zone plate (Ni at SLS, Au at ALS) had an outer most zone width of 25 nm, setting the spatial resolution limit of the measurement.

4.6.1. Near-edge X-Ray absorption fine structure (NEXAFS)

The NEXAFS spectroscopy is a powerful tool to extract the X-ray fingerprint absorption spectrum of each component of a blend system. In our case, with organic materials, the carbon K-edge is the most important absorption edge and it requires to operate with X-ray energies around 285 eV. The different spectral features obtained in this region correspond to the transition of a carbon core 1s electron to an antibonding state (π^* or σ^*). Different transitions are possible depending on the chemical bonding environments of carbon atoms, which are specific to each material. Therefore, such a measurement needs to be performed on pristine films of each organic semiconductor material. The latter were prepared by spin coating chloroform or chlorobenzene solutions of each material onto PEDOT:PSS (Clevios PH from Heraeus) coated glass substrates. 2×2 mm^2 sections were scored on the films using a scalpel, followed by floating off the film sections onto a deionised water surface, which was made possible by dissolving the PEDOT:PSS sacrificial layer under the semiconductor material films. 2×2 mm^2 film sections were subsequently collected

onto 300 mesh Cu grids (20 µmbar, 63 µm hole and 3 mm diameter, purchased from ProSciTech Pty. Ltd.) as shown in **Figure M2**. Samples were air dried at room temperature. NEXAFS lines scans were performed for each pristine material film, and the energy of the X-ray beam was varied between 278 and 390 eV, spanning the carbon K-edge region. Orthogonal energies for later STXM mapping were selected by overlaying NEXAFS spectra of each donor:acceptor material combination.

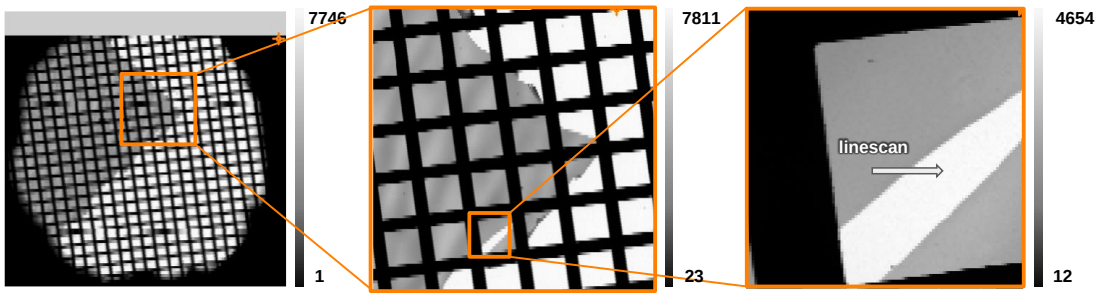

Figure M2: Section of a thin film floated off onto the mesh copper grid for NEXAFS linescan.

4.6.2. Scanning transmission X-ray microscopy (STXM)

For STXM measurements, composite nanoparticle samples were prepared for by spin coating 2.5 µL of aqueous dispersions (< 10 mg ml^{-1}) onto low stress silicon nitride (Si_3N_4) membrane windows (window dimensions 1×1 mm^2, window thickness 30 nm, silicon frame dimensions 5×5 mm^2, purchased from *Silson*, UK) at 3000 rpm, 1 min, low acceleration. These conditions were set in order to obtain a nanoparticle monolayer. Next, the resulting samples were loaded in the STXM sample chamber and a zone of interest was selected by performing an image scan at 290 eV (**Figure M3**). Then, the selected orthogonal energies were successively used and their corresponding image scan were obtained. Singular value decomposition (SVD) was used to fit a sum of the pristine material NEXAFS spectra to the measured blend spectrum of the nanoparticles, at each pixel in the STXM images. Prior to singular value decomposition (SVD) fitting, the pristine material NEXAFS spectra were normalised to film thickness. The method of reference spectrum normalisation involves dividing the real spectrum by a theoretical spectrum calculated based on the material's chemical formula using henke.lbl.gov/optical_constants/filter, in

order to convert the absorbance spectrum into the mass absorption coefficient. The aXis2000 package (unicorn.mcmaster.ca/aXis2000.html) was used to perform image analysis of STXM maps. Correlative TEM was used post-STXM to reimage the same nanoparticles for collecting position-matched micrographs. The Si3N4 membrane substrates with deposited nanoparticles were transported back to the University of Sydney (Australia) to measure TEM on a JEOL JEM-1400 at an accelerating voltage of 120 kV, using a Norcada custom TEM holder for Si3N4 membrane substrates (NTS-J-NX5-001).

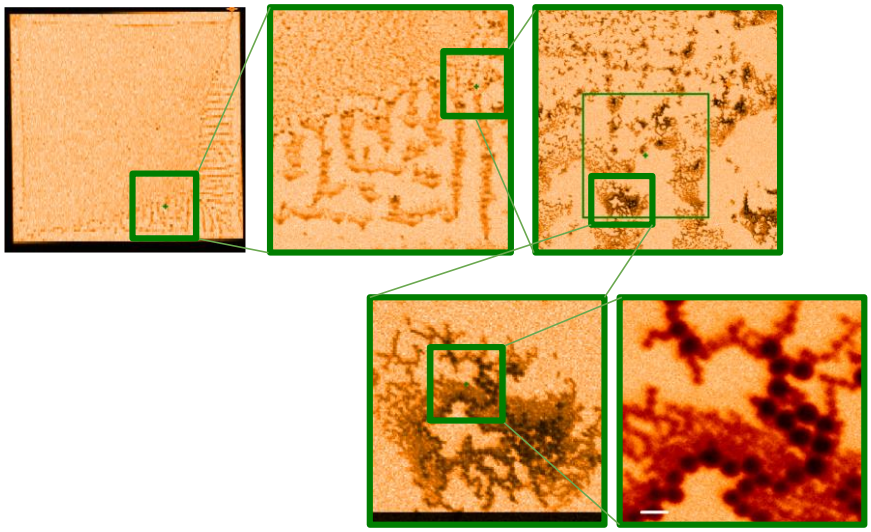

Figure M3: Si3N4 membrane substrates with deposited nanoparticles and an example of a region of interest.

4.7. Thermal gravimetric analysis (TGA)

TGA was performed on a TGA 2, Mettler Toledo STAR system with a heating rate of 10 °C min^{-1} under nitrogen atmosphere. The nanoparticle dispersions were first freeze-dried using a CRIOS-80, Cryotec in order to remove the aqueous dispersant. The nanoparticles were then recovered in an alumina crucible and characterised in TGA. For the sample annealed prior to any characterisation, annealing was performed directly inside of the crucible in glove box for 2 and 5 min.

4.8. Differential scanning calorimetry (DSC)

DSC measurements were per formed on a DSC 3, Mettler Toledo STAR system under a nitrogen atmosphere. For each sample, the temperature was increased from 25 to 200 °C at 10 °C min^{-1}, then cooled down to 25 °C following the same ramp. This process was repeated for a second cycle. For PTQ10:Y6 nanoparticles, only one cycle was performed, representative of the processing conditions used during device preparation.

4.9. Contact angle

The surface energies of the different materials were determined using a Krüss DSA 100 goniometer by the method proposed by Wu *et al.*[165] based on the contact angle measurements of two different liquids on the substrate surface at 20 °C in static mode. The results correspond to the mean of at least 3 measurements.

5. Electrical characterisations

5.1. Current-Voltage measurement of the OPV cells

To extract the photovoltaic parameters, a solar simulator using a xenon source and AM1.5G filters (*Newport* LCS-100) was used. The spectrum of the lamp is plotted in **Figure** M4 and is over plotted with the theoretical AM1.5G spectrum for comparison. The light intensity of the lamp was set at 100 mW cm^{-2} (1 sun) using a calibrated silicon reference cell from *Newport Co.* The J–V curves were recorded in the dark and under 1 sun with single voltage sweeps from -1 V to +1 V using a *Keithley* 2400 source meter unit, and parameters were directly extracted via a *LabVIEW* program based in the equation presented in **Chapter 1**. J–V characterisation was done in a nitrogen-filled glovebox at room temperature. Stability test was performed under continuous light illumination (xenon source, UV filter with cut-off at 400 nm, 100 mW cm^{-2}) and under open-circuit voltage conditions. Prior every measurement, solar cells were exposed to light from the solar simulator for 20 sec in order to induce a “light soaking” effect. More specifically, the UV

region of the solar simulator spectrum acts as a photo-dopant for the ZnO layer (ETL) and greatly improves its conductivity through an electron traps passivation.[254],[255] This quick light soaking was found to be essential to minimise as possible the series resistance R_s.

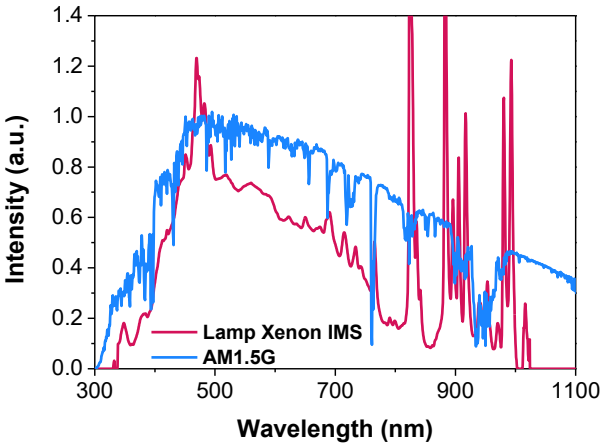

Figure M4: Emission spectrum of the solar simulator used in this work, as well as the reference AM1.5G spectrum.

5.2. External Quantum Efficiency measurement (EQE)

EQE measurements were carried out using a PVE300 Photovoltaic EQE system from *Bentham Co.* EQE was performed in ambient atmosphere and all OPV devices were encapsulated to avoid any degradation. J–V curves were re-recorded afterward to verify the good encapsulation. A Silicon (300 nm – 900 nm) and a Germanium (900 nm – 1800 nm) reference cells were used to create a data correction file (calibration). The J_{SC} was calculated according the equation in **Chapter 1**.

5.3. Space Charge Limited Current measurement (SCLC)

The nano-gap devices were measured in the dark and in air under a probe station and using an *Agilent* B1500A semiconductor device parameter analyser. Single voltage sweeps from -3 V to +3 V were done to extract the I-V curves of each device. The hole

mobilities of the different materials placed in the gap were extracted following the fitting and the equation defined in **Chapter 5**.

5.4. Light intensity measurement

These linearity measurements were recorded by using a high-power green LED (528 nm) supplied by *Intelligent LED Solutions*, calibrated with a calibrated integrated sphere (*Labsphere*), and double checked with a silicon diode (*Centronic Ltd*). A *Keithley* 2604B dual channel source measure unit was used to power the LED, bias the photodetector and record data. All devices were shielded in a Faraday cage.

Glossary

A.U.	Arbitrary Unit
AFM	Atomic Force Microscopy
Ag	Silver
AM1.5G	Air Mass 1.5 Global
Au	Gold
BHJ	Bulk Heterojunction
D:A	Donor:Acceptor
CM	Clausius-Mossotti
DEP	Dielectrophoresis
DLS	Dynamic Light Scattering
DSC	Differential Scanning Calorimetry
e-beam	Electron beam
E_{CT}	Charge Transfer Energy
E_g	Bandgap Energy
eh-IDTBR	(5Z)-3-Ethyl-2-sulfanylidene-5- [[4-[9,9,18,18-tetrakis(2-ethylhexyl)-15-[7-[(Z)-(3-ethyl-4-oxo-2-sulfanylidene-1,3-thiazolidin-5-ylidene)methyl]-2,1,3-benzothiadiazol-4-yl]-5,14-dithiapentacyclo[10.6.0.03,10.04,8.013,17]octadeca-1(12),2,4(8),6,10,13(17),15-heptaen-6-yl]-2,1,3-benzothiadiazol-7-yl] methylidene]-1,3-thiazolidin-4-one
EQE	External Quantum Efficiency
ETL	Electron Transport Layer
FDTS	1H,1H,2H,2H-perfluorodecyltrichlorosilane
FF	Fill Factor
HOMO	Highest Occupied Molecular Orbital
HTL	Hole Transport Layer
IDIC	2,2'-((2Z,2'Z)-((4,4,9,9-tetrahexyl-4,9-dihydro-s-indaceno[1,2-b:5,6-b'] dithiophene -2,7-diyl)bis(methanylylidene))bis(3-oxo-2,3-dihydro-1H-indene-2,1-diylidene))dimalononitrile
ITO	Indium Tin Oxide
J_{dark}	Dark Current Density
J_{MPP}	Current Density at Maximum Power Point

J_{SC}	Short Circuit Current Density
J_{ph}	Photo Current Density
J-V	Current Density-Voltage
L	Channel length
LED	Light Emitted Diode
LUMO	Lowest Unoccupied Molecular Orbital
MoO_3	Molybdenum Oxide
NEXAFS	Near Edge X-ray Absorption Spectroscopy
NFA	Non-Fullerene Acceptor
NP	Nanoparticle
NREL	National Renewable Energy Laboratory
o-IDTBR	(5Z,5'Z)-5,5'-((7,7'-(4,4,9,9-tetraoctyl-4,9-dihydro-s-indaceno[1,2-b:5,6-b'] dithiophene-2,7-diyl)bis(benzo[c][1,2,5]thiadiazole-7,4-diyl)) bis (methanylylidene))bis(3-ethyl-2-thioxothiazolidin-4-one)
OPV	Organic Photovoltaic
OSC	Organic Semiconductor
OTS	Octadecyltrichlorosilane
P3HT	Poly(3-hexylthiophene-2,5-diyl)
P_{MAX}	Maximum Power Point
$PC_{61}BM$	Phenyl-C61-Butyric-Acid-Methyl-Ester
PCE	Power Conversion Efficiency
PdI	Polydispersity Index
PETS	Phenethyltrichlorosilane
PMMA	Poly(methyl 2-methylpropenoate)
PL	Photo Luminescence
PTQ10	Poly[(thiophene)-alt-(6,7-difluoro-2-(2-hexyldecyloxy)quinoxaline)]
PV	Photovoltaic
PVT	Poly(1-vinyl-1,2,4-triazole)
RT	Room Temperature
R_S	Series Resistance
R_S	Shunt Resistance
SAM	Self-Assembled Monolayer

SCLC	Space Charge Limited Current
SDS	Sodium Dodecyl Sulfate
SEM	Scanning Electron Microscopy
STXM	Scanning Transmission X-ray Microscopy
TA	Thermal Annealing
TEM	Transmission Electron Microscopy
TGA	Thermo Gravimetry Analysis
Ti	Titanium
UV	Ultraviolet
V_{MPP}	Voltage at Maximum Power Point
V_{PP}	Peak-to-Peak Voltage
V_{OC}	Open-Circuit Voltage
W	Channel width
Y6	2,2'-((2Z,2'Z)-((12,13-bis(2-ethylhexyl)-3,9-diundecyl-12,13-dihydro-[1,2,5]thiadiazolo[3,4-e]thieno[2",3'':4',5']thieno[2',3':4,5]pyrrolo[3,2-g]thieno[2',3':4,5]thieno[3,2-b]indole-2,10-diyl)bis(methanylylidene))bis(5,6-difluoro-3-oxo-2,3-dihydro-1H-indene-2,1-diylidene))dimalononitrile
Y12	2,2'-((2Z,2'Z)-((12,13-bis(2-butyloctyl)-3,9-diundecyl-12,13-dihydro-[1,2,5]thiadiazolo[3,4-e]thieno[2",3'':4',5']thieno[2',3':4,5]pyrrolo[3,2-g]thieno[2',3':4,5]thieno[3,2-b]indole-2,10-diyl)bis(methanylylidene))bis(5,6-difluoro-3-oxo-2,3-dihydro-1H-indene-2,1-diylidene))dimalononitrile
ZnO	Zinc Oxide
μ_{h+}	Hole mobility

References

[1] J. Rockström, W. Steffen, K. Noone, Å. Persson, F.S. Chapin, E. F. Lambin, T. M. Lenton, M. Scheffer, C. Folke, H. J. Schellnhuber, B. Nykvist, C. A. de Wit, T. Hughes, S. van der Leeuw, H. Rodhe, S. Sörlin, P. K. Snyder, R. Costanza, U. Svedin, M. Falkenmark, L. Karlberg, R. W. Corell, V. J. Fabry, J. Hansen, B. Walker, D. Liverman, K. Richardson, P. Crutzen, J. A. Foley, *Nature* **2009**, 461, 472−475.

[2] K. Richardson, W. Steffen, W. Lucht, J. Bendtsen, S. E. Cornell, J. F. Donges, M. Drüke, I. Fetzer, G. Bala, W. von Bloh, G. Feulner, S. Fiedler, D. Gerten, T. Gleeson, M. Hofmann, W. Huiskamp, M. Kummu, C. Mohan, D. Nogués-Bravo, S. Petri, M. Porkka, S. Rahmstorf, S. Schaphoff, K. Thonicke, A. Tobian, V. Virkki, L. Wang-Erlandsson, L. Weber, J. Rockström, *Sci. Adv.* **2023**, *9*, eadh2458.

[3] H. Lee, K. Calvin, D. Dasgupta, G. Krinner, A. Mukherji, P. Thorne, C. Trisos, J. Romero, P. Aldunce, K. Barret, **2023**.

[4] "IEA (2024), CO2 Emissions in 2023, IEA, Paris https://www.iea.org/reports/co2-emissions-in-2023, Licence: CC BY 4.0," **2024**. Accessed 08 August 2024.

[5] H. Ritchie, P. Rosado, M. Roser, *Our world data* **2024**.

[6] R. Perez, M. Perez, *Int. Energy Agency SHC Program. Sol. Updat.* **2009**, *50*, 4.

[7] EMBER, "Electricity Data Explorer," can be found under https://ember-climate.org/data/data-tools/data-explorer/, **2024**. Accessed 08 August 2024.

[8] J. Pastuszak, P. Węgierek *Materials* **2022**, *15*, 5542.

[9] NREL, "Best research-cell efficiency chart," can be found under https://www.nrel.gov/pv/cell-efficiency.html, **2024**. Accessed 08 August 2024.

[10] M. P. Tsang, G. W. Sonnemann, D. M. Bassani, *Sol. Energy Mater. Sol. Cells* **2016**, *156*, 37.

[11] A. E. Becquerel, *C. R. Acad. Sci. Paris* **1839**, *9*, 561.

[12] W. Smith, *Nature* **1873**, *7*, 303.

[13] C. E. Fritts, *Am. J. Sci.* **1883**, *26*, 465.

[14] A. Pochettino, *Acad. Lincei Rend* **1906**, *15*, 355.

[15] J. Koenigsberger, K. Schilling, *Ann. Phys.* **1910**, *337*, 179.

[16] H. Inokuchi, H. Akamatu, *Solid State Phys.* **1961**, *12*, 93.

[17] D. M. Chapin, C. S. Fuller, G. L. Pearson, *J. Appl. Phys.* **1954**, *25*, 676.

[18] J. J. M. Halls, C. A. Walch, N. C. Greenham, E. A. Marseglia, R. H. Friend, S. C. Moratti, A. B. Holmes, *Nature* **1995**, *376*, 498.

[19] G. Yu, A. J. Heeger, *J. Appl. Phys.* **1995**, *78*, 4510.

[20] J. J. M. Halls, K. Pichler, R. H. Friend, S. C. Moratti, A. B. Holmes, *Appl. Phys. Lett.*

1996, *68*, 3120.

[21] G. Yu, J. Gao, J. C. Hummelen, F. Wudl, A. J. Heeger, *Science* **1995**, *270*, 1789-1791.

[22] S. E. Shaheen, C. J. Brabec, N. S. Sariciftci, F. Padinger, T. Fromherz, J. C. Hummelen, *Appl. Phys. Lett.* **2001**, *78*, 841.

[23] W. Shockley, *J. Appl. Phys* **1961**, *32*, 510.

[24] A. Köhler, H. Bässler, *Electron. Process. Org. Semicond.* **2015**, 1.

[25] A. J. Heeger, S. Kivelson, J. R. Schrieffer, W. P. Su, *Rev. Mod. Phys.* **1988**, *60*, 781.

[26] J. Frenkel, *Phys. Rev.* **1931**, *37*, 17.

[27] P. Peumans, A. Yakimov, S. R. Forrest, *J. Appl. Phys.* **2003**, *93*, 3693.

[28] Y. Firdaus, V. M. Le Corre, S. Karuthedath, W. Liu, A. Markina, W. Huang, S. Chattopadhyay, M. M. Nahid, M. I. Nugraha, Y. Lin, A. Seitkhan, A. Basu, W. Zhang, I. McCulloch, H. Ade, J. Labram, F. Laquai, D. Andrienko, L. J. A. Koster, T. D. Anthopoulos, *Nat. Commun.* **2020**, *11*, 5220.

[29] T. M. Clarke, J. R. Durrant, *Chem. Rev.* **2010**, *110*, 6736.

[30] G. Lakhwani, A. Rao, R. H. Friend, *Annu. Rev. Phys. Chem.* **2014**, *65*, 557.

[31] M. H. Jao, H. C. Liao, W. F. Su, *J. Mater. Chem. A* **2016**, *4*, 5784.

[32] S. Guan, Y. Li, C. Xu, N. Yin, C. Xu, C. Wang, M. Wang, Y. Xu, Q. Chen, D. Wang, L. Zuo, H. Chen, *Adv. Mater.* **2024**, *36,* 2400342.

[33] Z. Chen, J. Ge, W. Song, X. Tong, H. Liu, X. Yu, J. Li, J. Shi, L. Xie, C. Han, Q. Liu, Z. Ge, *Adv. Mater.* **2024**, *36*, 2406690.

[34] S. Li, L. Ye, W. Zhao, S. Zhang, S. Mukherjee, H. Ade, J. Hou, *Adv. Mater.* **2016**, *28*, 9423.

[35] J. Zhao, Y. Li, G. Yang, K. Jiang, H. Lin, H. Ade, W. Ma, H. Yan, *Nat. Energy* **2016**, *1*, 1-7.

[36] W. Zhao, S. Li, H. Yao, S. Zhang, Y. Zhang, B. Yang, J. Hou, *J. Am. Chem. Soc.* **2017**, *139*, 7148.

[37] J. Yuan, Y. Zhang, L. Zhou, G. Zhang, H. L. Yip, T. K. Lau, X. Lu, C. Zhu, H. Peng, P. A. Johnson, M. Leclerc, Y. Cao, J. Ulanski, Y. Li, Y. Zou, *Joule* **2019**, *3*, 1140.

[38] J. Jin, Q. Wang, K. Ma, W. Shen, L. A. Belfiore, X. Bao, J. Tang, *Adv. Funct. Mater.* **2023**, *33*, 2213324.

[39] C. Li, J. Zhou, J. Song, J. Xu, H. Zhang, X. Zhang, J. Guo, L. Zhu, D. Wei, G. Han, J. Min, Y. Zhang, Z. Xie, Y. Yi, H. Yan, F. Gao, F. Liu, Y. Sun, *Nat. Energy* **2021**, *6*, 605.

[40] M. T. Dang, L. Hirsch, G. Wantz, *Adv. Mater.* **2011**, *23*, 3597.

[41] P. L. T. Boudreault, A. Najari, M. Leclerc, *Chem. Mater.* **2011**, *23*, 456.

[42] M. C. Scharber, D. Mühlbacher, M. Koppe, P. Denk, C. Waldauf, A. J. Heeger, C. J.

Brabec, *Adv. Mater.* **2006**, *18*, 789.

[43] M. Zhang, X. Guo, W. Ma, H. Ade, J. Hou, *Adv. Mater.* **2015**, *27*, 4655.

[44] Z. C. Wen, H. Yin, X. T. Hao, *Surfaces and Interfaces* **2021**, *23*, 100921.

[45] S. Shoaee, H. M. Luong, J. Song, Y. Zou, T. Q. Nguyen, D. Neher, *Adv. Mater.* **2024**, *36*, 2302005.

[46] C. Sun, F. Pan, H. Bin, J. Zhang, L. Xue, B. Qiu, Z. Wei, Z. Zhang, Y. Li, *Nat. Commun.* **2018**, *9*, 743.

[47] F. Zhao, J. Zhou, D. He, C. Wang, Y. Lin, *J. Mater. Chem. C* **2021**, *9*, 15395.

[48] X. Kong, J. Zhang, L. Meng, C. Sun, S. Qin, C. Zhu, J. Zhang, J. Li, Z. Wei, Y. Li, *CCS Chem.* **2023**, *5*, 841.

[49] P. Cheng, X. Zhan, *Chem. Soc. Rev.* **2016**, *45*, 2544.

[50] Q. Lu, Z. Yang, X. Meng, Y. Yue, M. A. Ahmad, W. Zhang, S. Zhang, Y. Zhang, Z. Liu, W. Chen, *Adv. Funct. Mater.* **2021**, *31*, 2100151.

[51] P. Ding, D. Yang, S. Yang, Z. Ge, *Chem. Soc. Rev.* **2024**, *53*, 2350.

[52] M. O. Reese, S. A. Gevorgyan, M. Jørgensen, E. Bundgaard, S. R. Kurtz, D. S. Ginley, D. C. Olson, M. T. Lloyd, P. Morvillo, E. A. Katz, A. Elschner, O. Haillant, T. R. Currier, V. Shrotriya, M. Hermenau, M. Riede, K. R. Kirov, G. Trimmel, T. Rath, O. Inganäs, F. Zhang, M. Andersson, K. Tvingstedt, M. Lira-Cantu, D. Laird, C. McGuiness, S. Gowrisanker, M. Pannone, M. Xiao, J. Hauch, R. Steim, D. M. Delongchamp, R. Rösch, H. Hoppe, N. Espinosa, A. Urbina, G. Yaman-Uzunoglu, J. B. Bonekamp, A. J. J. M. Van Breemen, C. Girotto, E. Voroshazi, F. C. Krebs, *Sol. Energy Mater. Sol. Cells* **2011**, *95*, 1253.

[53] NREL, "Champion Photovoltaic Module Efficiency Chart," can be found under https://www.nrel.gov/pv/module-efficiency.html, **n.d.**

[54] M. A. Green, E. D. Dunlop, M. Yoshita, N. Kopidakis, K. Bothe, G. Siefer, X. Hao, *Prog. Photovoltaics Res. Appl.* **2024**, *32*, 3.

[55] J. Wu, J. Luke, H. K. H. Lee, P. Shakya Tuladhar, H. Cha, S. Y. Jang, W. C. Tsoi, M. Heeney, H. Kang, K. Lee, T. Kirchartz, J. S. Kim, J. R. Durrant, *Nat. Commun.* **2019**, *10*, 5159.

[56] J. Jing, Y. Dou, S. Chen, K. Zhang, F. Huang, *eScience* **2023**, *3*, 100142.

[57] G. Wang, M. A. Adil, J. Zhang, Z. Wei, *Adv. Mater.* **2019**, *31*, 1970324.

[58] R. Basu, F. Gumpert, J. Lohbreier, P. O. Morin, V. Vohra, Y. Liu, Y. Zhou, C. J. Brabec, H. J. Egelhaaf, A. Distler, *Joule* **2024**, *8*, 970.

[59] I. McCulloch, M. Chabinyc, C. Brabec, C. B. Nielsen, S. E. Watkins, *Nat. Mater.* **2023**, *22*, 1304.

[60] R. Po, J. Roncali, *J. Mater. Chem. C* **2016**, *4*, 3677.

[61] Z. Ngagoum, H. Vijayakumar, S. Alpert, C. Schmid, *Sol. Energy* **2024**, *270*, 112379.

[62] R. Sun, X. Yuan, X. Yang, Y. Wu, Y. Shao, X. Wu, C. J. Brabec, J. Min, *Joule* **2024,**

8(9), 2523-2538.

[63] G. Bernardo, T. Lopes, D. G. Lidzey, A. Mendes, *Adv. Energy Mater.* **2021**, *11*, 2100342.

[64] R. R. Søndergaard, M. Hösel, F. C. Krebs, *J. Polym. Sci. Part B Polym. Phys.* **2013**, *51*, 16.

[65] T. Shimura, S. Sato, P. Zalar, N. Matsuhisa, *Adv. Electron. Mater.* **2023**, *9*, 2200512.

[66] S. Lee, D. Jeong, C. Kim, C. Lee, H. Kang, H. Y. Woo, B. J. Kim, *ACS Nano* **2020**, *14*, 14493.

[67] D. Corzo, D. Rosas-Villalva, A. C, G. Tostado-Blázquez, E. B. Alexandre, L. H. Hernandez, J. Han, H. Xu, M. Babics, S. De Wolf, D. Baran, *Nat. Energy* **2022**, *8*, 62.

[68] F. P. Byrne, S. Jin, G. Paggiola, T. H. M. Petchey, J. H. Clark, T. J. Farmer, A. J. Hunt, C. Robert McElroy, J. Sherwood, *Sustain. Chem. Process.* **2016**, *4*, 1-24.

[69] C. M. Alder, J. D. Hayler, R. K. Henderson, A. M. Redman, L. Shukla, L. E. Shuster, H. F. Sneddon, *Green Chem.* **2016**, *18*, 3879.

[70] X. Xu, W. Jing, H. Meng, Y. Guo, L. Yu, R. Li, Q. Peng, *Adv. Mater.* **2023**, *35*, 2208997.

[71] L. Shang, S. Qu, Y. Deng, Y. Gao, G. Yue, S. He, Z. Wang, Z. Wang, F. Tan, *J. Mater. Chem. C* **2022**, *10*, 506.

[72] C. Kim, H. Kang, N. Choi, S. Lee, Y. Kim, J. Kim, Z. Wu, H. Y. Woo, B. J. Kim, *J. Mater. Chem. C* **2020**, *8*, 15224.

[73] C. Xie, S. Liang, G. Zhang, S. Li, *Polymers* **2022**, *14*, 4229.

[74] C. Xie, T. Heumüller, W. Gruber, X. Tang, A. Classen, I. Schuldes, M. Bidwell, A. Späth, R. H. Fink, T. Unruh, I. McCulloch, N. Li, C. J. Brabec, *Nat. Commun.* **2018**, *9*, 5335.

[75] K. Jiang, J. Zhang, C. Zhong, F. R. Lin, F. Qi, Q. Li, Z. Peng, W. Kaminsky, S. H. Jang, J. Yu, X. Deng, H. Hu, D. Shen, F. Gao, H. Ade, M. Xiao, C. Zhang, A. K. Y. Jen, *Nat. Energy* **2022**, *7*, 1076.

[76] C. Yang, M. Jiang, S. Wang, B. Zhang, P. Mao, H. Y. Woo, F. Zhang, J. liang Wang, Q. An, *Adv. Mater.* **2024**, *36*, 2305356.

[77] S. Luo, C. Li, J. Zhang, X. Zou, H. Zhao, K. Ding, H. Huang, J. Song, J. Yi, H. Yu, K. S. Wong, G. Zhang, H. Ade, W. Ma, H. Hu, Y. Sun, H. Yan, *Nat. Commun.* **2023**, *14*, 6964.

[78] D. Wang, G. Zhou, Y. Li, K. Yan, L. Zhan, H. Zhu, X. Lu, H. Chen, C. Z. Li, *Adv. Funct. Mater.* **2022**, *32*, 2107827.

[79] S. Pang, Z. Chen, J. Li, Y. Chen, Z. Liu, H. Wu, C. Duan, F. Huang, Y. Cao, *Mater. Horizons* **2022**, *10*, 473.

[80] D. Liu, B. Yang, B. Jang, B. Xu, S. Zhang, C. He, H. Y. Woo, J. Hou, *Energy Environ. Sci.* **2017**, *10*, 546.

[81] F. Manger, K. Fischer, P. Marlow, H. Röhm, C. Sprau, A. Colsmann, *Adv. Energy*

Mater. **2023**, *13*, 2202820.

[82] C. Xie, X. Tang, M. Berlinghof, S. Langner, S. Chen, A. Späth, N. Li, R. H. Fink, T. Unruh, C. J. Brabec, *ACS Appl. Mater. Interfaces* **2018**, *10*, 23225.

[83] I. Burgués-Ceballos, F. Machui, J. Min, T. Ameri, M. M. Voigt, Y. N. Luponosov, S. A. Ponomarenko, P. D. Lacharmoise, M. Campoy-Quiles, C. J. Brabec, *Adv. Funct. Mater.* **2014**, *24*, 1449.

[84] C. Duan, K. Zhang, C. Zhong, F. Huang, Y. Cao, *Chem. Soc. Rev.* **2013**, *42*, 9071.

[85] T. T. Filate, S. Lee, L. R. Franco, Q. Chen, Z. Genene, C. F. N. Marchiori, Y. Lee, M. Araujo, W. Mammo, H. Y. Woo, B. J. Kim, E. Wang, *ACS Appl. Mater. Interfaces* **2024**, *16*, 12886.

[86] T. Liu, J. Heimonen, Q. Zhang, C. Y. Yang, J. Da Huang, H. Y. Wu, M. A. Stoeckel, T. P. A. van der Pol, Y. Li, S. Y. Jeong, A. Marks, X. Y. Wang, Y. Puttisong, A. Y. Shimolo, X. Liu, S. Zhang, Q. Li, M. Massetti, W. M. Chen, H. Y. Woo, J. Pei, I. McCulloch, F. Gao, M. Fahlman, R. Kroon, S. Fabiano, *Nat. Commun.* **2023**, *14*, 8454.

[87] Z. He, C. Zhong, S. Su, M. Xu, H. Wu, Y. Cao, *Nat. Photonics* **2012**, *6*, 591.

[88] A. Holmes, E. Deniau, C. Lartigau-Dagron, A. Bousquet, S. Chambon, N. P. Holmes, *ACS Nano* **2021**, *15*, 3927.

[89] M. Rammal, P. Lévêque, G. Schlatter, N. Leclerc, A. Hébraud, *Mater. Chem. Front.* **2020**, *4*, 2904.

[90] T. Kietzke, D. Neher, K. Landfester, R. Montenegro, R. Güntner, U. Scherf, *Nat. Mater.* **2003**, *2*, 408.

[91] T. Piok, S. Gamerith, C. Gadermaier, H. Plank, F. P. Wenzl, S. Patil, R. Montenegro, T. Kietzke, D. Neher, U. Scherf, K. Landfester, E. J. W. List, *Adv. Mater.* **2003**, *15*, 800.

[92] Ugelstad, *Polym. Lett.* **1973**, *11*, 503.

[93] L. D'Olieslaeger, M. Pfannmöller, E. Fron, I. Cardinaletti, M. Van Der Auweraer, G. Van Tendeloo, S. Bals, W. Maes, D. Vanderzande, J. Manca, A. Ethirajan, *Sol. Energy Mater. Sol. Cells* **2017**, *159*, 179.

[94] M. Bag, T. S. Gehan, D. D. Algaier, F. Liu, G. Nagarjuna, P. M. Lahti, T. P. Russell, D. Venkataraman, *Adv. Mater.* **2013**, *25*, 6411.

[95] B. Tan, Y. Li, M. F. Palacios, J. Therrien, M. J. Sobkowicz, *Colloids Surfaces A Physicochem. Eng. Asp.* **2016**, *488*, 7.

[96] Y. J. Kim, R. D. Schaller, H. C. Fry, *Small* **2019**, *15*, 1803563.

[97] S. Subianto, R. Balu, L. De Campo, A. Sokolova, N. K. Dutta, N. R. Choudhury, *ACS Appl. Mater. Interfaces* **2018**, *10*, 44116.

[98] J. Cho, S. Yoon, K. Min Sim, Y. Jin Jeong, C. Eon Park, S. K. Kwon, Y. H. Kim, D. S. Chung, *Energy Environ. Sci.* **2017**, *10*, 2324.

[99] C. Ceriani, M. Scagliotti, T. Losi, A. Luzio, S. Mattiello, M. Sassi, N. Pianta, M. Rapisarda, L. Mariucci, M. Caironi, L. Beverina, *Adv. Electron. Mater.* **2023**, *9*,

2201160.

[100] C. Xie, X. Zeng, C. Li, X. Sun, S. Liang, H. Huang, B. Deng, X. Wen, G. Zhang, P. You, C. Yang, Y. Han, S. Li, G. Lu, H. Hu, N. Li, Y. Chen, *Energy Environ. Sci.* **2024**, *17*, 2441.

[101] C. Xie, H. Huang, Z. Li, X. Zeng, B. Deng, C. Li, G. Zhang, S. Li, *Polymers (Basel).* **2024**, *16*, 91.

[102] R. Sun, Q. Wu, J. Guo, T. Wang, Y. Wu, B. Qiu, Z. Luo, W. Yang, Z. Hu, J. Guo, M. Shi, C. Yang, F. Huang, Y. Li, J. Min, *Joule* **2020**, *4*, 407.

[103] H. Kasai, H. S. Nalwa, H. Oikawa, S. Okada, H. Matsuda, N. Minami, A. Kakuta, K. Ono, A. Mukoh, H. N. H. Nakanishi, *Jpn. J. Appl. Phys.* **1992**, *31*, L1132.

[104] S. Gärtner, M. Christmann, S. Sankaran, H. Röhm, E. Prinz, F. Penth, A. Pütz, A. E. Türeli, B. Penth, B. Baumstümmler, A. Colsmann, *Adv. Mater.* **2014**, *26*, 6653.

[105] K. Fischer, P. Marlow, F. Manger, C. Sprau, A. Colsmann, *Adv. Mater. Technol.* **2022**, *7*, 2200297.

[106] F. Manger, P. Marlow, K. Fischer, M. Nöller, C. Sprau, A. Colsmann, *Adv. Funct. Mater.* **2022**, *32*, 2202566.

[107] P. Marlow, F. Manger, K. Fischer, C. Sprau, A. Colsmann, *Nanoscale* **2022**, *14*, 5569-5578.

[108] K. Fischer, P. Marlow, K. Bitsch, C. Sprau, A. Colsmann, *Sol. RRL* **2024**, *8*, 2400132.

[109] C. Wu, C. Szymanski, J. McNeill, *Langmuir* **2006**, *22*, 2956.

[110] Z. Hu, A. J. Gesquiere, *Chem. Phys. Lett.* **2009**, *476*, 51.

[111] Z. Hu, D. Tenery, M. S. Bonner, A. J. Gesquiere, *J. Lumin.* **2010**, *130*, 771.

[112] J. E. Millstone, D. F. J. Kavulak, C. H. Woo, T. W. Holcombe, E. J. Westling, A. L. Briseno, M. F. Toney, J. M. J. Fréchet, *Langmuir* **2010**, *26*, 13056.

[113] D. Darwis, N. Holmes, D. Elkington, A. L. David Kilcoyne, G. Bryant, X. Zhou, P. Dastoor, W. Belcher, *Sol. Energy Mater. Sol. Cells* **2014**, *121*, 99.

[114] T. Kietzke, D. Neher, M. Kumke, R. Montenegro, K. Landfester, U. Scherf, *Macromolecules* **2004**, *37*, 4882.

[115] T. Kietzke, D. Neher, M. Kumke, O. Ghazy, U. Ziener, K. Landfester, *Small* **2007**, *3*, 1041.

[116] K. B. Burke, A. J. Stapleton, B. Vaughan, X. Zhou, A. L. D. Kilcoyne, W. J. Belcher, P. C. Dastoor, *Nanotechnology* **2011**, *22*, DOI 10.1088/0957-4484/22/26/265710.

[117] S. Ulum, N. Holmes, D. Darwis, K. Burke, A. L. David Kilcoyne, X. Zhou, W. Belcher, P. Dastoor, *Sol. Energy Mater. Sol. Cells* **2013**, *110*, 43.

[118] S. Ulum, N. Holmes, M. Barr, A. L. D. Kilcoyne, B. Bin Gong, X. Zhou, W. Belcher, P. Dastoor, *Nano Energy* **2013**, *2*, 897.

[119] S. Chambon, C. Schatz, V. Sébire, B. Pavageau, G. Wantz, L. Hirsch, *Mater. Horizons* **2014**, *1*, 431.

[120] K. N. Schwarz, S. B. Farley, T. A. Smith, K. P. Ghiggino, *Nanoscale* **2015**, *7*, 19899.

[121] N. P. Holmes, K. B. Burke, P. Sista, M. Barr, H. D. Magurudeniya, M. C. Stefan, A. L. D. Kilcoyne, X. Zhou, P. C. Dastoor, W. J. Belcher, *Sol. Energy Mater. Sol. Cells* **2013**, *117*, 437.

[122] M. G. Barr, S. Chambon, A. Fahy, T. W. Jones, M. A. Marcus, A. L. D. Kilcoyne, P. C. Dastoor, M. J. Griffith, N. P. Holmes, *Mater. Chem. Front.* **2021**, *5*, 2218.

[123] J. Kosco, M. Bidwell, H. Cha, T. Martin, C. T. Howells, M. Sachs, D. H. Anjum, S. Gonzalez Lopez, L. Zou, A. Wadsworth, W. Zhang, L. Zhang, J. Tellam, R. Sougrat, F. Laquai, D. M. DeLongchamp, J. R. Durrant, I. McCulloch, *Nat. Mater.* **2020**, *19*, 559.

[124] R. Chowdhury, N. P. Holmes, N. Cooling, W. J. Belcher, P. C. Dastoor, X. Zhou, *ACS Omega* **2022**, *7*, 9212.

[125] J. Yang, A. Garcia, T. Q. Nguyen, *Appl. Phys. Lett.* **2007**, *90*, 103514.

[126] Y. Du, Y. Li, O. Aftenieva, T. Tsuda, P. Formanek, T. A. F. König, A. Synytska, *Adv. Opt. Mater.* **2022**, *10*, 2101922

[127] Y. Du, Y. Wang, V. Shamraienko, K. Pöschel, A. Synytska, *Small* **2023**, *19*, 2206907.

[128] O. Ghazy, B. Freisinger, I. Lieberwith, K. Landfester, *Nanoscale* **2020**, *12*, 22798.

[129] F. Almyahi, T. R. Andersen, N. A. Cooling, N. P. Holmes, M. J. Griffith, K. Feron, X. Zhou, W. J. Belcher, P. C. Dastoor, *Beilstein J. Nanotechnol.* **2018**, *9*, 649.

[130] F. J. M. Colberts, M. M. Wienk, R. A. J. Janssen, *ACS Appl. Mater. Interfaces* **2017**, *9*, 13380.

[131] M. Bag, T. S. Gehan, L. A. Renna, D. D. Algaier, P. M. Lahti, D. Venkataraman, *RSC Adv.* **2014**, *4*, 45325.

[132] N. A. D. Yamamoto, M. E. Payne, M. Koehler, A. Facchetti, L. S. Roman, A. C. Arias, *Sol. Energy Mater. Sol. Cells* **2015**, *141*, 171.

[133] T. S. Gehan, M. Bag, L. A. Renna, X. Shen, D. D. Algaier, P. M. Lahti, T. P. Russell, D. Venkataraman, *Nano Lett.* **2014**, *14*, 5238.

[134] G. Prunet, L. Parrenin, E. Pavlopoulou, G. Pecastaings, C. Brochon, G. Hadziioannou, E. Cloutet, *Macromol. Rapid Commun.* **2018**, *39*, 1870005.

[135] M. M. Rammal, P. Nizet, G. Layrac, S. Swaraj, B. Heinrich, J. Jing, É. Steveler, T. Heiser, N. Leclerc, P. Lévêque, A. Hébraud, *Synth. Met.* **2024**, *305*, DOI 10.1016/j.synthmet.2024.117599.

[136] N. P. Holmes, M. Marks, P. Kumar, R. Kroon, M. G. Barr, N. Nicolaidis, K. Feron, A. Pivrikas, A. Fahy, A. D. de Z. Mendaza, A. L. D. Kilcoyne, C. Müller, X. Zhou, M. R. Andersson, P. C. Dastoor, W. J. Belcher, *Nano Energy* **2016**, *19*, 495.

[137] N. P. Holmes, M. Marks, J. M. Cave, K. Feron, M. G. Barr, A. Fahy, A. Sharma, X. Pan, D. A. L. Kilcoyne, X. Zhou, D. A. Lewis, M. R. Andersson, J. Van Stam, A. B. Walker, E. Moons, W. J. Belcher, P. C. Dastoor, *Chem. Mater.* **2018**, *30*, 6521.

[138] C. Xie, A. Classen, A. Späth, X. Tang, J. Min, M. Meyer, C. Zhang, N. Li, A. Osvet, R.

H. Fink, C. J. Brabec, *Adv. Energy Mater.* **2018**, *8*, 1702857.

[139] L. Parrenin, G. Laurans, E. Pavlopoulou, G. Fleury, G. Pecastaings, C. Brochon, L. Vignau, G. Hadziioannou, E. Cloutet, *Langmuir* **2017**, *33*, 1507.

[140] K. Landfester, R. Montenegro, U. Scherf, R. Güntner, U. Asawapirom, S. Patil, D. Neher, T. Kietzke, *Adv. Mater.* **2002**, *14*, 651.

[141] T. M. Riddick, *Control of Colloid Stability through Zeta Potential*, Livingston Wynnewood, PA, **1968**.

[142] G. V. Lowry, R. J. Hill, S. Harper, A. F. Rawle, C. O. Hendren, F. Klaessig, U. Nobbmann, P. Sayre, J. Rumble, *Environ. Sci. Nano* **2016**, *3*, 953.

[143] P. J. Brown, D. S. Thomas, A. Köhler, J. S. Wilson, J. S. Kim, C. M. Ramsdale, H. Sirringhaus, R. H. Friend, *Phys. Rev. B - Condens. Matter Mater. Phys.* **2003**, *67*, 064203.

[144] X. M. Jiang, R. Österbacka, O. Korovyanko, C. P. An, B. Horovitz, R. A. J. Janssen, Z. V. Vardeny, *Adv. Funct. Mater.* **2002**, *12*, 587.

[145] F. Almyahi, T. R. Andersen, A. Fahy, M. Dickinson, K. Feron, W. J. Belcher, P. C. Dastoor, *J. Mater. Chem. A* **2019**, *7*, 9202.

[146] T. S. Gehan, C. L. C. Ellis, D. Venkataraman, M. Bag, *ACS Appl. Mater. Interfaces* **2020**, *12*, 8183.

[147] E. Destouesse, S. Chambon, S. Courtel, L. Hirsch, G. Wantz, *ACS Appl. Mater. Interfaces* **2015**, *7*, 24663.

[148] T. A. M. Ferenczi, C. Müller, D. D. C. Bradley, P. Smith, J. Nelson, N. Stingelin, *Adv. Mater.* **2011**, *23*, 4093.

[149] M. Abbas, G. Cakmak, N. Tekin, A. Kara, H. Y. Guney, E. Arici, N. S. Sariciftci, *Org. Electron.* **2011**, *12*, 497.

[150] S. Van Bavel, E. Sourty, G. De With, K. Frolic, J. Loos, *Macromolecules* **2009**, *42*, 7396.

[151] N. Li, B. E. Lassiter, R. R. Lunt, G. Wei, S. R. Forrest, *Appl. Phys. Lett.* **2009**, *94*, 023307.

[152] J. M. Frost, F. Cheynis, S. M. Tuladhar, J. Nelson, *Nano Lett.* **2006**, *6*, 1674.

[153] D. T. W. Toolan, S. Fujii, S. J. Ebbens, Y. Nakamura, J. R. Howse, *Soft Matter* **2014**, *10*, 8804.

[154] A. Sánchez-Díaz, X. Rodríguez-Martínez, L. Córcoles-Guija, G. Mora-Martín, M. Campoy-Quiles, *Adv. Electron. Mater.* **2018**, *4*, DOI 10.1002/aelm.201700477.

[155] M. Le Berre, Y. Chen, D. Baigl, *Langmuir* **2009**, *25*, 2554.

[156] G. A. Berriman, N. P. Holmes, J. L. Holdsworth, X. Zhou, W. J. Belcher, P. C. Dastoor, *Org. Electron.* **2016**, *30*, 12.

[157] E. B. L. Pedersen, M. C. Pedersen, S. B. Simonsen, R. G. Brandt, A. P. L. Böttiger, T. R. Andersen, W. Jiang, Z. Y. Xie, F. C. Krebs, L. Arleth, J. W. Andreasen, *J. Mater.*

Chem. A **2015**, *3*, 17022.

[158] W. Ma, J. Y. Kim, K. Lee, A. J. Heeger, *Macromol. Rapid Commun.* **2007**, *28*, 1776.

[159] N. P. Holmes, N. Nicolaidis, K. Feron, M. Barr, K. B. Burke, M. Al-Mudhaffer, P. Sista, A. L. D. Kilcoyne, M. C. Stefan, X. Zhou, P. C. Dastoor, W. J. Belcher, *Sol. Energy Mater. Sol. Cells* **2015**, *140*, 412.

[160] N. P. Holmes, S. Ulum, P. Sista, K. B. Burke, M. G. Wilson, M. C. Stefan, X. Zhou, P. C. Dastoor, W. J. Belcher, *Sol. Energy Mater. Sol. Cells* **2014**, *128*, 369.

[161] X. Wu, Y. Li, Y. Wang, M. Zhang, Q. Zhu, X. Huang, B. Li, Y. Y. Xue, J. Qing, W. Cai, *Sol. RRL* **2024**, *8*, 2300812.

[162] T. Wang, J. Q. Liu, X. T. Hao, *Sol. RRL* **2020**, *4*, 2000539.

[163] H. Laval, A. Holmes, M. A. Marcus, B. Watts, G. Bonfante, M. Schmutz, E. Deniau, R. Szymanski, C. Lartigau-Dagron, X. Xu, J. M. Cairney, K. Hirakawa, F. Awai, T. Kubo, G. Wantz, A. Bousquet, N. P. Holmes, S. Chambon, *Adv. Energy Mater.* **2023**, *13*, 2300249.

[164] C. B. Nielsen, S. Holliday, H. Y. Chen, S. J. Cryer, I. McCulloch, *Acc. Chem. Res.* **2015**, *48*, 2803.

[165] S. Wu, *J. Polym. Sci. Part C Polym. Symp.* **1971**, *34*, 19.

[166] T. Young, *Philos. Trans. R. Soc. London* **1997**, *95*, 65.

[167] Robin Szymanski. Vers l'industrialisation des cellules solaires organiques ternaires. Electronique. Université de Bordeaux, **2020**. Français. ⟨NNT : 2020BORD0298⟩. ⟨tel-03150355⟩

[168] C. Sun, F. Pan, S. Chen, R. Wang, R. Sun, Z. Shang, B. Qiu, J. Min, M. Lv, L. Meng, C. Zhang, M. Xiao, C. Yang, Y. Li, *Adv. Mater.* **2019**, *31*, 1.

[169] T. Ameri, T. Heumüller, J. Min, N. Li, G. Matt, U. Scherf, C. J. Brabec, *Energy Environ. Sci.* **2013**, *6*, 1796.

[170] A. Baumann, T. J. Savenije, D. H. K. Murthy, M. Heeney, V. Dyakonov, C. Deibel, *Adv. Funct. Mater.* **2011**, *21*, 1687.

[171] K. Vandewal, K. Tvingstedt, A. Gadisa, O. Inganäs, J. V. Manca, *Nat. Mater.* **2009**, *8*, 904.

[172] B. Qi, J. Wang, *J. Mater. Chem.* **2012**, *22*, 24315.

[173] F. Piersimoni, S. Chambon, K. Vandewal, R. Mens, T. Boonen, A. Gadisa, M. Izquierdo, S. Filippone, B. Ruttens, J. D'haen, N. Martin, L. Lutsen, D. Vanderzande, P. Adriaensens, J. V. Manca, *J. Phys. Chem. C* **2011**, *115*, 10873.

[174] C. W. Chu, H. Yang, W. J. Hou, J. Huang, G. Li, Y. Yang, *Appl. Phys. Lett.* **2008**, *92*, DOI 10.1063/1.2891884.

[175] Y. Fu, T. H. Lee, Y. Chin, R. A. Pacalaj, C. Labanti, S. Y. Park, Y. Dong, H. W. Cho, J. Y. Kim, D. Minami, J. R. Durrant, J. Kim, **2023**, DOI 10.1038/s41467-023-37234-0.

[176] J. Stöhr, in (Ed: J. Stöhr), Springer Berlin Heidelberg, Berlin, Heidelberg, **1992**, pp.

114–161.

[177] C. N. Hoth, S. A. Choulis, P. Schilinsky, C. J. Brabec, *J. Mater. Chem.* **2009**, *19*, 5398.

[178] N. Camaioni, C. Carbonera, L. Ciammaruchi, G. Corso, J. Mwaura, R. Po, F. Tinti, *Adv. Mater.* **2023**, *35*, 2210146.

[179] D. Zhang, B. Fan, L. Ying, N. Li, C. J. Brabec, F. Huang, Y. Cao, *SusMat* **2021**, *1*, 4-23.

[180] S. Riera-Galindo, M. Sanz-Lleó, E. Gutiérrez-Fernández, N. Ramos, M. Mas-Torrent, J. Martín, L. López-Mir, M. Campoy-Quiles, *Small* **2024**, *20*, 2311735.

[181] S. Xiong, K. Fukuda, S. Lee, K. Nakano, X. Dong, T. Yokota, K. Tajima, Y. Zhou, T. Someya, *Adv. Sci.* **2022**, *9*, 2105288.

[182] H. Shimizu, M. Yamada, R. Wada, M. Okabe, *Polym. J.* **2008**, *40*, 33.

[183] T. Zhang, M. Moser, A. D. Scaccabarozzi, H. Bristow, P. Jacoutot, A. Wadsworth, T. D. Anthopoulos, I. McCulloch, N. Gasparini, *J. Phys. Mater.* **2021**, *4*, 045001.

[184] J. Yuan, Y. Zhang, L. Zhou, G. Zhang, H. Yip, T. Lau, X. Lu, C. Zhu, H. Peng, P. A. Johnson, M. Leclerc, Y. Cao, J. Ulanski, Y. Li, Y. Zou, *Joule* **2019**, *3*, 1140.

[185] J. Kosco, S. Gonzalez-Carrero, C. T. Howells, T. Fei, Y. Dong, R. Sougrat, G. T. Harrison, Y. Firdaus, R. Sheelamanthula, B. Purushothaman, F. Moruzzi, W. Xu, L. Zhao, A. Basu, S. De Wolf, T. D. Anthopoulos, J. R. Durrant, I. McCulloch, *Nat. Energy* **2022**, *7*, 340.

[186] G. Yao, Y. Ge, X. Xiao, L. Zhang, N. Yi, H. Luo, S. Yuan, W. Zhou, *ACS Appl. Energy Mater.* **2022**, *5*, 1193.

[187] M. J. M. Wirix, P. H. H. Bomans, H. Friedrich, N. A. J. M. Sommerdijk, G. De With, *Nano Lett.* **2014**, *14*, 2033.

[188] A. Holmes, H. Laval, M. Guizzardi, V. Maruzzo, G. Folpini, N. Barbero, E. Deniau, M. Schmutz, S. Blanc, A. Petrozza, G. M. Paternò, G. Wantz, S. Chambon, C. Lartigau-Dagron, A. Bousquet, *Energy Environ. Sci.* **2024**, *17*, 1107.

[189] F. Qin, W. Wang, L. Sun, X. Jiang, L. Hu, S. Xiong, T. Liu, X. Dong, J. Li, Y. Jiang, J. Hou, K. Fukuda, T. Someya, Y. Zhou, *Nat. Commun.* **2020**, *11*, 4508.

[190] K. Zhang, H. Hu, S. Li, Y. He, J. Guo, *Int. J. Adhes. Adhes.* **2020**, *98*, 102539.

[191] J. J. Lai, Y. J. Lin, Y. H. Chen, H. C. Chang, C. J. Liu, Y. Y. Zou, Y. T. Shih, M. C. Wang, *J. Appl. Phys.* **2011**, *110*, DOI 10.1063/1.3603033.

[192] A. Soultati, A. Fakharuddin, E. Polydorou, C. Drivas, A. Kaltzoglou, M. I. Haider, F. Kournoutas, M. Fakis, L. C. Palilis, S. Kennou, D. Davazoglou, P. Falaras, P. Argitis, S. Gardelis, A. Kordatos, A. Chroneos, L. Schmidt-Mende, M. Vasilopoulou, *ACS Appl. Energy Mater.* **2019**, *2*, 1663.

[193] K. C. Lee, N. G. An, S. M. Lee, J. Heo, D. S. Kim, J. Y. Kim, C. Yang, *Sol. RRL* **2018**, *2*, 1700235.

[194] H. Hu, M. Ghasemi, Z. Peng, J. Zhang, J. J. Rech, W. You, H. Yan, H. Ade, *Adv. Mater.* **2020**, *32*, 2005348.

[195] P. W. M. Blom, V. D. Mihailetchi, L. J. A. Koster, D. E. Markov, *Adv. Mater.* **2007**, *19*, 1551.

[196] K. An, W. Zhong, F. Peng, W. Deng, H. Wu, N. Li, F. Huang, L. Ying, *Nat. Commun.* **2023**, *14*, 2688.

[197] J. Smith, H. Miyauchi, S. I. Stupp, T. J. Marks, **2013**, 16456.

[198] A. Saboor, O. Stroyuk, O. Raievska, C. Liu, J. Hauch, C. J. Brabec, *Adv. Funct. Mater.* **2024**, 2400453.

[199] M. Rimmele, Z. Qiao, J. Panidi, F. Furlan, C. Lee, W. L. Tan, C. R. McNeill, Y. Kim, N. Gasparini, M. Heeney, *Mater. Horizons* **2023**, *10*, 4202.

[200] S. Chandrabose, K. Chen, A. J. Barker, J. J. Sutton, S. K. K. Prasad, J. Zhu, J. Zhou, K. C. Gordon, Z. Xie, X. Zhan, J. M. Hodgkiss, *J. Am. Chem. Soc.* **2019**, *141*, 6922.

[201] J. Panidi, E. Mazzolini, F. Eisner, Y. Fu, F. Furlan, Z. Qiao, M. Rimmele, Z. Li, X. Lu, J. Nelson, J. R. Durrant, M. Heeney, N. Gasparini, ACS Energy Letters **2023**, *8*, 3038-3047.

[202] H. C. Wang, C. H. Chen, R. H. Li, Y.-C. Lin, C. S. Tsao, B. Chang, S. Tan, Y. Yang, K. H. Wei, *Sol. RRL* **2020**, *4*, 2000253.

[203] F. Eller, C. R. McNeill, E. M. Herzig, *Adv. Energy Mater.* **2024**,14, 2304455.

[204] B. Zhang, M. Jiang, P. Mao, S. Wang, R. Gui, Y. Wang, H. Y. Woo, H. Yin, J. L. Wang, Q. An, *Adv. Mater.* **2024**, *36*, 2405718.

[205] W. Yue, Y. Zhao, S. Shao, H. Tian, Z. Xie, Y. Geng, F. Wang, *J. Mater. Chem.* **2009**, *19*, 2199.

[206] H. J. Cho, S. J. Kang, S. M. Lee, M. Jeong, G. Kim, Y. Y. Noh, C. Yang, *ACS Appl. Mater. Interfaces* **2017**, *9*, 30755.

[207] C. Duan, R. E. M. Willems, J. J. Van Franeker, B. J. Bruijnaers, M. M. Wienk, R. A. J. Janssen, *J. Mater. Chem. A* **2016**, *4*, 1855.

[208] C. Liu, C. Xiao, J. Wang, B. Liu, Y. Hao, J. Guo, J. Song, Z. Tang, Y. Sun, W. Li, *Macromolecules* **2022**, *55*, 5964.

[209] L. Ye, W. Li, X. Guo, M. Zhang, H. Ade, *Chem. Mater.* **2019**, *31*, 6568.

[210] C. H. Lee, Y. Y. Lai, J. Y. Hsu, P. K. Huang, Y. J. Cheng, *Chem. Sci.* **2017**, *8*, 2942.

[211] M. Li, P. J. Leenaers, M. M. Wienk, R. A. J. Janssen, *J. Mater. Chem. C* **2020**, *8*, 5856.

[212] D. Yuan, G. Qin, L. Zhang, F. Pan, R. Qiu, S. Lei, S. Deng, J. Chen, *ACS Appl. Mater. Interfaces* **2021**, *13*, 57654.

[213] R. Po, G. Bianchi, C. Carbonera, A. Pellegrino, *Macromolecules* **2015**, *48*, 453.

[214] M. Rimmele, Z. Qiao, J. Panidi, F. Furlan, C. Lee, W. L. Tan, C. R. McNeill, Y. Kim, N. Gasparini, M. Heeney, *Mater. Horizons* **2023**, *10*, 4202.

[215] B. Friedel, C. R. McNeill, N. C. Greenham, *Chem. Mater.* **2010**, *22*, 3389.

[216] H. K. Reimschuessel, *J Polym Sci Polym Chem Ed* **1979**, *17*, 2447.

[217] H. Laval, Y. Tian, V. Lafranconi, M. Barr, P. Dastoor, M. M. Marcus, G. Wantz, N. P. Holmes, K. Hirakawa, **2024**, 2404112.

[218] M. Bag, T. S. Gehan, D. D. Algaier, F. Liu, G. Nagarjuna, P. M. Lahti, T. P. Russell, D. Venkataraman, *Adv. Mater.* **2013**, *25*, 6411.

[219] D. Kim, M. Sonker, A. Ros, *Anal. Chem.* **2019**, *91*, 277.

[220] R. Pethig, *Biomicrofluidics* **2010**, *4*, 022811.

[221] N. G. Green, H. Morgan, *J. Phys. Chem. B* **1999**, *103*, 41.

[222] Q. Zhao, W. Wang, J. Shao, X. Li, H. Tian, L. Liu, X. Mei, Y. Ding, B. Lu, *Adv. Mater.* **2016**, *28*, 6337.

[223] R. J. Barsotti, M. D. Vahey, R. Wartena, Y. M. Chiang, J. Voldman, F. Stellacci, *Small* **2007**, *3*, 488.

[224] M. P. Hughes, K. D. Rosenthal, N. A. Ran, M. Seifrid, G. C. Bazan, T. Q. Nguyen, *Adv. Funct. Mater.* **2018**, *28*, 1801542.

[225] K. Yim, G. L. Whiting, C. E. Murphy, J. J. M. Halls, J. H. Burroughes, R. H. Friend, J. Kim, *Adv. Mater.* **2008**, *20*, 3319.

[226] G. T. WRIGHT, *Nature* **1958**, *182*, 1296.

[227] K. Yang, Y. Wang, A. Jain, L. Samulson, J. Kumar, *J. Macromol. Sci. Part A* **2007**, *44*, 1261.

[228] Y. J. You, D. Y. Kim, S. C. Shin, J. W. Shim, *IEEE Access* **2018**, *6*, 64569.

[229] J. W. Jeong, J. W. Huh, J. I. Lee, H. Y. Chu, J. J. Pak, B. K. Ju, *Thin Solid Films* **2010**, *518*, 6343.

[230] M. Devynck, P. Tardy, G. Wantz, Y. Nicolas, L. Vellutini, C. Labrugère, L. Hirsch, *Appl. Phys. Lett.* **2012**, *100*, 053308.

[231] S. Sreekumar, M. Heidari, Z. Cheng, H. Maddali, K. House, H. Frei, E. Galoppini, D. M. O'Carroll, *ACS Appl. Mater. Interfaces* **2022**, *14*, 38270.

[232] H. B. Ouerghemmi, F. Kouki, P. Lang, H. Ben Ouada, H. Bouchriha, *Synth. Met.* **2009**, *159*, 551.

[233] D. Janssen, R. De Palma, S. Verlaak, P. Heremans, W. Dehaen, *Thin Solid Films* **2006**, *515*, 1433.

[234] L. A. Majewski, J. W. Kingsley, C. Balocco, A. M. Song, *Appl. Phys. Lett.* **2006**, *88* (22).

[235] A. Zen, J. Pflaum, S. Hirschmann, W. Zhuang, F. Jaiser, U. Asawapirom, J. P. Rabe, U. Scherf, D. Neher, *Adv. Funct. Mater.* **2004**, *14*, 757.

[236] K. Pei, M. Chen, Z. Zhou, H. Li, P. K. L. Chan, *ACS Appl. Electron. Mater.* **2019**, *1*, 379-388.

[237] A. F. Paterson, R. Li, A. Markina, L. Tsetseris, S. MacPhee, H. Faber, A.-H. Emwas, J. Panidi, H. Bristow, A. Wadsworth, D. Baran, D. Andrienko, M. Heeney, I. McCulloch, T. D. Anthopoulos, *J. Mater. Chem. C* **2021**, *9*, 4486.

[238] K. P. Goetz, O. D. Jurchescu, *Conductivity Measurements of Organic Materials Using Field-Effect Transistors (FETs) and Space-Charge-Limited Current (SCLC) Techniques*, Elsevier Ltd., **2019**, 453-487.

[239] H.-B. Fu, J.-N. Yao, *J. Am. Chem. Soc.* **2001**, *123*, 1434.

[240] K. Vandewal, K. Tvingstedt, A. Gadisa, O. Inganäs, J. V. Manca, *Phys. Rev. B - Condens. Matter Mater. Phys.* **2010**, *81*, 125204.

[241] K. Vandewal, A. Gadisa, W. D. Oosterbaan, S. Bertho, F. Banishoeib, I. Van Severen, L. Lutsen, T. J. Cleij, D. Vanderzande, J. V. Manca, *Adv. Funct. Mater.* **2008**, *18*, 2064.

[242] Z. H. Chen, P. Q. Bi, X. Y. Yang, M. S. Niu, K. N. Zhang, L. Feng, X. T. Hao, *J. Phys. Chem. C* **2019**, *123*, 12676.

[243] Q. He, W. Sheng, M. Zhang, G. Xu, P. Zhu, H. Zhang, Z. Yao, F. Gao, F. Liu, X. Liao, Y. Chen, *Adv. Energy Mater.* **2021**, *11*, 2003390.

[244] S. Zhang, L. Zuo, J. Chen, Z. Zhang, J. Mai, T. K. Lau, X. Lu, M. Shi, H. Chen, *J. Mater. Chem. A* **2016**, *4*, 1702.

[245] Y. Wang, T. Hasegawa, H. Matsumoto, T. Michinobu, *J. Am. Chem. Soc.* **2019**, *141*, 3566.

[246] N. Y. Doumon, G. Wang, X. Qiu, A. J. Minnaard, R. C. Chiechi, L. J. A. Koster, *Sci. Rep.* **2019**, *9*, 14454.

[247] S. Bao, H. Yang, H. Fan, J. Zhang, Z. Wei, C. Cui, Y. Li, *Adv. Mater.* **2021**, *33*, 2105301.

[248] C. Fan, H. Yang, Q. Zhang, S. Bao, H. Fan, X. Zhu, C. Cui, Y. Li, *Sci. China Chem.* **2021**, *64*, 2017.

[249] A. A. Mohapatra, V. Tiwari, S. Patil, *Energy Environ. Sci.* **2021**, *14*, 302.

[250] J. Liu, X. Liu, J. Xin, Y. Zhang, L. Wen, Q. Liang, Z. Miao, *Small* **2024**, *20*, 2308863.

[251] M. Rimmele, Z. Qiao, J. Panidi, F. Furlan, C. Lee, W. L. Tan, C. R. McNeill, Y. Kim, N. Gasparini, M. Heeney, *Mater. Horizons* **2023**, *10*, 4202.

[252] J. Raabe, G. Tzvetkov, U. Flechsig, M. Böge, A. Jaggi, B. Sarafimov, M. G. C. Vernooij, T. Huthwelker, H. Ade, D. Kilcoyne, T. Tyliszczak, R. H. Fink, C. Quitmann, *Rev. Sci. Instrum.* **2008**, *79*, 113704.

[253] A. P. Hitchcock, L. Yang, T. Warwick, H. Ade, *J. Synchrotron Radiat.* **2003**, *10*, 125-136.

[254] J. Gilot, M. M. Wienk, R. A. J. Janssen, *Appl. Phys. Lett.* **2007**, *90*, 143512.

[255] Y. Jin, J. Wang, B. Sun, J. C. Blakesley, N. C. Greenham, *Nano Lett.* **2008**, *8*, 1649.

Publication and Presentation List

Publications in international peer-reviewed journals:

- **H. Laval**, Y. Tian, V. Lafranconi, M. Barr, P. Dastoor, M. M. Marcus, G. Wantz, N. P. Holmes, K. Hirakawa, *Small* **2024**, 2404112.

- A. Holmes, **H. Laval**, M. Guizzardi, V. Maruzzo, G. Folpini, N.Barbero, E. Deniau, M. Schmutz, S. Blanc, A. Petrozza, G. M. Paternò, G. Wantz, S. Chambon, C. Lartigau-Dagron, A. Bousquet, *Energy Environ. Sci.* **2024**, 17, 1107.

- A. Holmes, **H. Laval**, E. Deniau, M. Schmutz, S. Blanc, G. Wantz, S. Chambon, C. Lartigau-Dagron, A. Bousquet, *Sol. Energy Mater. Sol. Cells* **2024**, *266*, 112656.

- **H. Laval**, A. Holmes, M. A. Marcus, B. Watts, G. Bonfante, M. Schmutz, E. Deniau, R. Szymanski, C. Lartigau-Dagron, X. Xu, J. M. Cairney, K. Hirakawa, F. Awai, T. Kubo, G. Wantz, A. Bousquet, N. P. Holmes, S. Chambon, *Adv. Energy Mater.* **2023**, *13*, 2300249.

- I. Persson, **H. Laval**, S. Chambon, G. Bonfante, K. Hirakawa, G. Wantz, B. Watts, M. A. Marcus, X. Xu, L. Ying, G. Lakhwani, M. R. Andersson, J. M. Cairney, N. P. Holmes, *Nanoscale* **2023**, *15*, 6126.

- A. Holmes, **H. Laval**, M. Schmutz, S. Blanc, J. Allouche, B. Watts, G. Wantz, N. P. Holmes, K. Hirakawa, E. Deniau, S. Chambon, C. Lartigau-Dagron, A. Bousquet, *Mater. Today Chem.* **2022**, *26*, 101229.

Presentation:

- International Conference on Science and Technology of Synthetic Electronic Materials, **2024**, Dresden, Germany, *oral presentation*.

- International Symposium on Functional-pi Electron Systems, **2023**, Raleigh, USA, *oral presentation*.

- Sustainable Energy Materials and Technologies for a Low Carbon Future **2023**, Thuwal, Saudi Arabia, *poster presentation*.

Titre : Contrôle de la morphologie de nanoparticules de semi-conducteurs organiques pour des cellules solaires photovoltaïques fabriquées par encres aqueuses

Résumé : Pour rendre le procédé de fabrication des cellules solaires organiques plus écoresponsable, l'utilisation de solvants toxiques doit être remplacée par une solution plus propre. Cette thèse aborde cette problématique en explorant l'utilisation de l'eau comme alternative. La stratégie pour surmonter cette contrainte consiste à former des nanoparticules à partir de ces matériaux, qui peuvent ainsi être dispersées dans l'eau. Deux méthodes principales sont utilisées dans la communauté pour obtenir de telles dispersions aqueuses : la mini-émulsion et la nano-précipitation. Les nanoparticules synthétisées par cette dernière présentent une morphologie interne plus favorable entre les matériaux donneurs et accepteurs par rapport à la mini-émulsion. De ce fait, les cellules solaires fabriquées à base de dispersions aqueuses préparées par nano-précipitation montrent des rendements beaucoup plus élevés. Le travail entrepris dans cette thèse vise à comprendre et à surmonter les limitations liées à la morphologie interne des nanoparticules préparées par mini-émulsion. En particulier, nous avons étudié l'influence de l'énergie interfaciale entre les matériaux donneurs et accepteurs sur la morphologie interne des nanoparticules ainsi que la longueur des chaînes alkyles de polymères et petites molécules. Cette thèse a aussi exploré le lien entre la morphologie et le transport des porteurs de charges au sein des nanoparticules en développant dispositifs à canal nanométrique. Dans ces canaux, nous avons réussi à piéger des nanoparticules de type cœur-écorce à l'aide de la force diélectrophorétique. Ce résultat a montré que la morphologie des nanoparticules et la composition de l'écorce n'ont pas d'impact significatif ni sur la mobilité des charges dans les nanoparticules, ni sur les performances finales des cellules solaires.

Mots-clés : Photovoltaïque, Organique, Nanoparticules, Morphologie, STXM, Nanotechnologie.

Title: Control of organic semiconductor nanoparticles morphology for water-processable photovoltaic solar cells

Abstract: In order to improve the sustainability of the organic photovoltaics, the use of toxic solvents for processing organic solar cells needs to be replaced by a cleaner alternative. The present thesis tackles this issue by exploring a way of replacing these solvents by water. The strategy is to form nanoparticles from these materials, that are thus able to be dispersed in water. Two main methods are employed in the community to obtain such an aqueous dispersion, the miniemulsion and the nanoprecipitation. Nanoparticles synthesised with the latter method are known to present a more favourable internal morphology between the donor and acceptor materials as compared to the former method. As a result, water-processable organic solar cells prepared from nanoprecipitation demonstrate much higher efficiencies. The work undertaken in this thesis aims to understand and overcome the limitations arising from the internal morphology of the nanoparticles prepared by miniemulsion. In particular, we studied the influence of the interfacial energy between the donor and acceptor material on the nanoparticle internal morphology as well as the length of the alkyl chains of polymers and small molecules. Moreover, this work explores the link between nanomorphology and charge transport within nanoparticles by developing nanogap devices. Dielectrophoresis force has been successfully used to insert core-shell nanoparticles in the nanogap. This result shows that nanoparticle morphology and shell composition do not have a dramatic impact on the charge mobility within the nanoparticle or the overall performance of the solar cells.

Keywords: Photovoltaic, Organic, Nanoparticles, Morphology, STXM, Nanotechnology.